

Statistical and Non-Statistical Processes in Polycyclic Aromatic Hydrocarbons and their Derivatives under Charged Particle Interaction

*A thesis submitted
in partial fulfillment for the degree of*

Doctor of Philosophy

by

NAJEEB P. K.



**DEPARTMENT OF PHYSICS
INDIAN INSTITUTE OF SPACE SCIENCE AND TECHNOLOGY
THIRUVANANTHAPURAM - 695547, INDIA**

SEPTEMBER 2017

Certificate

This is to certify that the thesis entitled “**Statistical and non-statistical processes in polycyclic aromatic hydrocarbons and their derivatives under charged particle interaction**” submitted by **Najeeb P. K.**, to the Indian Institute of Space Science and Technology, Thiruvananthapuram, in partial fulfillment for the award of the degree of **Doctor of Philosophy**, is a bonafide record of the research work carried out by him under my supervision. The contents of this report, in full or in parts, have not been submitted to any other Institute or University for the award of any degree or diploma.

Dr. Umesh R. Kadhane

Associate Professor

Department of Physics

Dr. S. Muruges

Head of the Department

Department of Physics

Place: Thiruvananthapuram

September 2017.

Declaration

I hereby declare that this thesis entitled “**Statistical and non-statistical processes in polycyclic aromatic hydrocarbons and their derivatives under charged particle interaction**” submitted in partial fulfillment of the Degree of “**Doctor of Philosophy**” is a record of original work carried out by me under the supervision of **Dr. Umesh R. Kadhane**, and has not formed the basis for the award of any degree, diploma, associateship, fellowship, or other titles in this or any other Institution or University of higher learning. In keeping with the ethical practice in reporting scientific information, due acknowledgments have been made wherever the findings of others have been cited.

Place: Thiruvananthapuram
September 2017.

Najeeb P. K.
Research Scholar
Department of Physics
Roll No.: SC12D012

Acknowledgments

My Ph.D. journey was made easy and enjoyable through the constant support from many people. I would like to acknowledge and sincerely thank them at this moment.

First of all, I would like to express my sincere gratitude to **Dr. Umesh R. Kadhane** for his valuable guidance and constant support throughout my Ph.D. tenure. It was of great help, and I was immensely benefited from the subjective discussions with him. He helped me a lot in shaping my career as a researcher, and I must appreciate his patience. He had always inspired me to think out of the box and become an independent researcher. His insight and knowledge on the subject has always admired me to urge for a broader understanding. I am deeply grateful to him for his involvement in my Ph.D. work. Apart from the professional relation, his advice helped me a lot in my personal life too. I must acknowledge him for being extremely supportive, and I wish to thank him for his efforts to make my Ph.D. journey wonderful.

I gratefully acknowledge the role of my Doctoral committee members, Prof. C. S. Narayanamurthy, Dr. S. Muruges, Dr. C. P. Safvan, Dr. Anil Shaji, Dr. Jobin Cyriac and Dr. Rakesh Kumar Singh for their suggestions, advice and constant support which has definitely improved the quality of my research work. I thank them for their trust they had in me, and for standing by me till the end of my Ph.D. work.

I thank Dr. K. S. Dasgupta, former Director of IIST, for the academic support and the facilities provided to carry out the research work at IIST even during the time of budget restrictions. I also thank the present Director of IIST, Dr. Vinay Kumar Dadhwal for the constant support to carry out the research to the next level. I express my gratitude to Dr. Raju K. George, Dean, Research and Development and Prof. A. Chandrasekhar, Dean, Academics, for their encouragement and support. I also thank the Research Council of IIST for their support at various phases of the Ph.D. program. I thank the faculty of IIST for their help whenever it was needed, especially during the experimental development. I

also thank the faculty of Physics Department, Dr. C. Sudheesh, Dr. Naveen Surendran, Dr. K. B. Jinesh, Dr. S. Jayanthi, Dr. Apoorva Nagar, Dr. Solomon Ivan and Dr. Kuntala Bhattacharjee for all the interactions and academic discussions. I also do acknowledge the help and support from the IIST administrative staff. I extend my thanks to the staff at IIST workshop (Dept. of Aerospace) for their help to finish the experimental setup instrumentation fast.

I extend my sincere thanks to our collaborators Dr. Sarita Vig, Dept. of Earth and Space Sciences, IIST, Thiruvananthapuram, and Dr. C. P. Safvan, Dr. Pragya Bhat and Dr. T. Sairam, IUAC, New Delhi, for the fruitful discussions, and the help during the beam time at IUAC. It would not have been possible to carry out my Ph.D. work beyond the boundary of IIST without their help. I wish to thank the project students, Anitha, Minna and Susmitha for their help during the experimental setup upgradation, and while performing the experiment. I gratefully acknowledge the help I received from Sujay (SAC, Ahmedabad) and Anudit (ISAC, Bengaluru) during their B.Tech project at IIST, as well as the help received from Saurabh Chatterjee, Ph.D. student, Dept. of Aerospace, IIST and Abishek Chakraborty, Ph.D. student, Dept. of Avionics at IIST.

I thank Prof. Shiromaru for giving the opportunity to visit Japan under SAKURA science exchange program. I thank faculties and staff of Physics and Chemistry Department, Tokyo Metropolitan University (TMU), Japan, for the support during the SAKURA science program. I am also thankful to Prof. T. Azuma for the opportunity and extensive support to visit Atomic and Molecular Physics lab, RIKEN, and for letting me work independently with the Riken Electrostatic Ion Storage Ring (RICE). I extend my thanks to Science and Engineering Research Board (SERB) for granting me the partial funding under international travel support (ITS) scheme to attend the 30th International Conference on Photonic, Electronic and Atomic Collisions (ICPEAC-XXX) held in Cairns, Australia, from 26th July to 1st August, 2017.

I would like to thank the Department of Space (DoS), Government of India, for supporting me with the JRF and SRF fellowship. It has helped me in completing my Ph.D. without bothering about financial issues, and this support was very instrumental for the achievement of this work. Moreover, I must thank the scientists from Indian Space Re-

search Organisation (ISRO) for the help during the calibration of the experimental setup at IIST.

I sincerely thank Dr. Umesh and Dr. Sarita, and their family, where the doors were always open for me. They fed me with the great flavor of food in many of the holidays during my stay at their home. Our research team had many lunches and dinner parties at their place which enhanced the bondage between us. Their support encourages us to do experimentation in cooking too. These meetings were very much helpful to overcome the stress during the high time of my Ph.D.

Extra curricular activities play an important role in making the life smooth and more wonderful. I got a very good company of research team in my lab where I really didn't feel that the time passes so fast. I thank Mr. Narasimha Murthy for the help during the experiment, Dr. Priyanka B. for the help during the experiment as well as thesis writing, Shalina, Keerthi, Vinitha M. V, Vinitha M. R, Gowri Shankar, Aarathi, and Swethank for their company. I am very much grateful to my friends at IIST, especially, Abhishek, Rakesh, Sujith, Vinu and Swagat for the encouraging supports at each level of my Ph.D. life. Their helping hands, whenever I was in need, should be greatly acknowledged. I thank my friends at IIST especially Resmi, Devi, Karthika, Meegle, Rahul, P. M. Mishra, Rohit, Raneesh and Arun for their company during the initial stages of my research. I would like to thank all other IIST friends, but this space will not be enough to name all. My research life was made easy with the support from scientific, technical, and administrative staff members of IIST and I specially thank the IIST canteen staff for feeding me during the last 5 years. I am grateful to the technical staff of IIST who helped me in all the possible way they can.

I believe our friends are the one who shapes our character and I am lucky enough to have a number of such good friends from my childhood. I thank my school and college friends, who gave motivation and unconditional support in every aspect during my education. Friends from my village stood by my side at hard times as pillars of strong support helping me in every situation and made it lighter than they seem to be, and thus filled my life with love and laughter. Let me convey my sincere thanks to my friends and people from my village, as they give a lot of value for the education, and support for my career

development.

Last but not least, I gratefully thank my parents Mr. Abdulla and Mrs. Kunhamina, without whose moral support it would not have been possible for me to finish the task. I am eternally grateful to my mother, who always soothed me with her kind words and gave comfort with love and support, whenever I was low. My parents guided me and gave constant support at each step of my career, with care. I am very much thankful to my sister Sareena for the extra care she had taken throughout my research. I am also thankful to my brother Noushad and my elder sister Saira for their support. I am thankful to Shajeera, my better half, who came into my life during the final phase of my research. I must thank her for choosing me as her life partner even though I was in my struggling stage. I extend my thanks to my family and relatives for their love and care which helped me to overcome several stressful situations during my Ph.D. I gratefully acknowledge and extend my heartfelt thanks to all my teachers and people I met in my life, who encouraged me to build a career in Physics.

Above all, I thank 'GOD-the almighty' for granting me the opportunity to undertake this Ph.D. research problem, and for making the path feasible to become a 'Scientist'.

Najeeb P. K.

Thiruvananthapuram, India.

Abstract

Abundant occurrence of polycyclic aromatic hydrocarbons (PAHs) and their nitrogen derivatives, polycyclic nitrogen heterocycles (PANHs) in nature in general, and in the astrophysical environment in particular, has intrigued researchers in recent decades. The functionality and survivability of these molecules in the ecosystem is entirely governed by their ability to discharge and accumulate smaller molecular subunits to and from their surroundings. The thermodynamics of their internal excitation modes and its correlation with the excitation mechanism is of utmost significance in deciding the role of these molecules. The time scale of internal rotational-vibrational oscillation of these molecules are in picoseconds and the relative magnitude of unimolecular dissociation timescales in comparison with this will decide whether it is a statistical or a nonstatistical which envisage the survivability of these molecules. Thus the excitation of these molecules by high-energy radiation and resulting statistical dissociation processes have been at the center stage of many research campaigns. Particularly of interest are the statistical dissociation processes leading to the formation of molecular hydrogen, acetylene or hydrogen cyanide molecules. The interest in these channels is not only driven by the intriguing molecular dynamics but also due to their pivotal role in deciding the biochemistry in astronomical environments. The correlation of the decay channels and internal energy is very important to completely understand these aspects. The decay constant is governed by the internal energy of the molecule which is strongly dependent on the collision parameters. To this end, electron spectroscopy and mass spectroscopy have been the most commonly used tools to investigate their dynamics, but they are seldom used together in coincidence. Typical linear ToF mass spectrometry measurements are on microsecond time scales. Thus if the effect of thermal velocity is mitigated on the time scale of first few microseconds, it is possible to probe the time evolution of the unimolecular dissociation channels of these molecules which fall in this decay time range. Moreover, electron-ion coincidence measurement can give a correlation of the internal energy and a given dis-

sociation channel. The inherent complexity of the design, implementation, and analysis make such experiment technically very challenging and time-consuming. Moreover, generally, such instruments are used with high energy photon collisions due to very selective excitation energetics, simplifying the selection scheme of coincidence. Charged particle interaction, in spite of being of great significance for PAHs and their derivatives, are rarely studied using such elucidative technique. This work addresses such a challenging task of designing and realizing a full instrumentation to probe the electron impact excitation in PAHs and PANHs in three different modes, namely, electron spectroscopy, mass spectrometry and most significantly, energy selective secondary electron-ion coincidence mode. After realizing the instrument it was used to elucidate the role of molecular structure in statistical dissociation channels, especially C_2H_2 and HCN loss in basic PAH and PANH.

The higher sensitivity of the projectile electron below 250 eV restricted our ability to do measurement below 4 a.u., the velocity of the charged particle. Therefore, to probe the energy loss in this velocity regime where we expect the charged particle to deposit more energy in electronic energy loss model, we perform the experiment with proton beam at lower velocity. But when this is done, the proton beam itself introduces additional complications due to the electron capture (EC) and capture ionization (CI) processes. Using multi-coincidence technique we have isolated as many contributions as possible. Using this data it was possible to identify the extent to which the structural randomisation can happen at a given projectile velocity. This method has also helped to compare the rate of evaporation from mono and di-cation. A detailed comparison of energetics and resulting statistical dissociation of C_2H_2 and HCN loss is done in the two complementary cases of proton and electron impact measurements. This work quantifies the structural randomization process and positional identity of carbon and nitrogen in collision-induced excitation of PAHs and PANHs.

Table of Contents

List of Tables	xvii
List of Figures	xix
Abbreviations	xxv
1 An Overview	1
1.1 Collision Processes and Energy Loss Mechanisms	2
1.2 Plasmon or Collective Excitation	3
1.3 Statistical and Non-statistical Decay Processes	4
1.4 Theoretical Methods	5
1.5 Experimental Techniques	7
1.6 Polycyclic Aromatic Hydrocarbons and their Derivatives	11
1.7 Electron-Ion Coincidence Measurements on PAHs and PANHs	12
1.8 Thesis Outline	14
2 Theoretical Methodology	17
2.1 Quantum Chemistry Calculation	18
2.2 Structure Calculations	20
2.3 Conclusion	27
3 Principles of Electron Spectroscopy and Ion Mass Spectrometry	29
3.1 Requirements for Experimental Study	30
3.2 Electron Spectrometers	31

3.2.1	Retarding Field Energy Analyzer	32
3.2.2	Parallel Plate Analyzer	33
3.2.3	Cylindrical Analyzer	35
3.2.4	Hemispherical Analyzer	37
3.2.5	Toroidal Analyzer	38
3.2.6	Time-of-Flight Energy Analyzer	39
3.3	Ion Spectrometers	41
3.3.1	Magnetic Sector Analyzer	41
3.3.2	Quadrupole Mass Analyzer	42
3.3.3	Time-of-Flight Mass Spectrometer	43
3.3.4	Reflectron Time-of-Flight Mass Spectrometer	45
3.4	Detection Systems	47
3.4.1	Faraday Cup	47
3.4.2	Channel Electron Multiplier	48
3.4.3	Microchannel Plate Detector	48
3.4.4	Position Readout	51
4	Experimental Methodology	55
4.1	e, 2e Experiment	56
4.2	Simulation and Design	56
4.3	Electron Gun	58
4.4	Electron Spectrometer	60
4.5	Mass Spectrometer	64
4.6	Pulsed Extraction ToF	66
4.7	Projectile Energy Loss Analyzer	68
4.8	High Voltage MOSFET Switch	70
4.9	Electron and Ion Detectors	72

4.10	Electron-Ion Coincidence Experimental Setup	74
4.11	Fabrication	75
4.12	Operational Modes of the Setup	76
4.12.1	Electron Spectrum	76
4.12.2	Mass Spectrum with Synchronized Switching	78
4.12.3	Electron-Ion Coincidence Measurement	79
4.13	Data Acquisition System	80
5	Testing and Calibration	83
5.1	Testing for Vacuum	83
5.2	Fast High Voltage MOSFET Switch Test for Electro-Optic Application	85
5.2.1	Electro-Optic Modulator Experiment	86
5.2.2	Calibration and Testing of Cylindrical Mirror Analyser	91
5.2.3	Calibration and Testing of Time-of-Flight Mass Spectrometer	98
5.3	Multi Coincidence Experiment	101
6	Electron Impact on PAHs and PANHs	106
6.1	Delayed Extraction Time-of-Flight	108
6.2	DEToF Experimental Setup Details	109
6.3	Analysis and Results	111
6.3.1	Normalisation and Beam Energy Dependence	116
6.3.2	HCN Loss Channel in Quinoline and Isoquinoline	120
6.3.3	HCN+C ₂ H ₂ Loss Channel in Quinoline and Isoquinoline	121
7	Ion Impact on PAHs and PANHs	125
7.1	Experimental Details	126
7.2	Mass Spectrum	127
7.3	Plasmon Excitation in Charged Particle Collision	134

7.4	Stability of PAHs and PANHs under Charged Particle Interaction	142
7.5	Metastable Decay Dynamics of PANHs upon HCN Loss	144
8	Conclusion and Future Scope	147
8.1	Instrumentation and Setup Development	148
8.2	Calibration and Testing	149
8.3	Investigation of Structural Effects in Napthalene and its Derivatives . . .	150
8.4	Future Scope	151
A	LUA Program Code Used in SIMION8.0 for Time Varying Electric Field	153
B	Arduino Program for Electron Spectrometer Operation and DAQ Automation	154
C	Function Fit Program for Metastable Decay Life-time Measurement	158
	Bibliography	159
	Publications Based on the Thesis	181

List of Tables

2.1	Hatree-Fock (HF) calculation for bond length by using GAUSSIAN09 with 3-21G basis set (bond labels are give as in Figure 2.1)	25
4.1	Typical voltage settings used for MCP and DLA (electron detector) . . .	73

List of Figures

2.1	Structure of (a) Naphthalene ($C_{10}H_8$) (b) Quinoline (C_9H_7N) (c) isoquinoline (C_9H_7N) (different colours refers to the individual atoms : grey - Carbon, blue - Nitrogen, white - Hydrogen)	22
2.2	Charge density of (a) Naphthalene ($C_{10}H_8$) (b) Quinoline (C_9H_7N) (c) isoquinoline (C_9H_7N)	24
2.3	Similarity of molecular orbital energy eigenvalues for quinoline and isoquinoline (dotted line shows a straight line with slope 1)	26
3.1	Schematic of an RFEA	33
3.2	Parallel plate analyzer schematic with electron trajectory	34
3.3	127^0 Cylindrical sector analyzer schematic	36
3.4	Cylindrical mirror analyzer schematic	37
3.5	2D schematic view of hemispherical analyzer	38
3.6	Double toroidal analyzer schematic with detector	39
3.7	Time of flight energy analyzer with pulse processing and data acquisition schematic	40
3.8	Principal components of a magnetic sector ion mass analyzer	42
3.9	Schematic of quadrupole mass analyzer	43
3.10	Layout of a Wiley-McLaren type ion ToF analyzer	45
3.11	Principle of reflectron mass analyzer	46
3.12	Faraday cup with secondary electron suppressor	48
3.13	Channel electron multiplier (a) Schematic (b) Dynode working principle	49
3.14	Microchannel plate detector (a) Schematic of MCP assembled (b) Dynode with potential working principle	50

3.15	MCP detector with CCD/CMOS imaging camera	51
3.16	Quadrant anode, where the position is obtained from the relative charge in the four quadrants	52
3.17	Wedge and strip detector	53
3.18	Delay line anode detector (a) Assembled with MCP (b) DLA with MCP working principle	54
4.1	3D view of electron-ion coincidence setup (CAD design with assembly of electron, ion spectrometer and electron gun)	57
4.2	Electron gun simulation (a) Trajectory of electron beam (b) Beam source region (Red colour: Electric fields lines, Blue colour: Electron trajectory)	59
4.3	Electron gun assembled on CF-63 flange with aperture (0.1 mm) and X- Y deflectors	60
4.4	(a) Secondary electron trajectory through CMA (Red colour: Electric fields lines, Blue colour: Electron trajectory) (b) CMA mechanical design . . .	61
4.5	CMA assembled with MCP along and delay line anode detector	62
4.6	Simulated CMA image obtained for electron energy 335 eV with standard deviation 0.42 and FWHM=1, projected at an angle $42^{\circ} 18''$ (a) from a point source (b) from an extended source having diameter of 4 mm . . .	62
4.7	Wiley-McLaren type ToF Schematic	65
4.8	Cut view of mechanical design (CAD) of time-of-flight mass spectrometer with provisional reflectron	66
4.9	(a) Simulated ion trajectories (in colored) through time-of-flight mass spectrometer (Red contours are electric field lines) (b) Interaction and acceleration region of the time-of-flight mass spectrometer shows field uniformity for smooth acceleration of the molecular ions	67
4.10	Time-of -flight mass spectrometer with ion detector assembled	67
4.11	3D cut view of parallel plate electrostatic energy analyser with frames (frame thickness and larger slits are for illustration purpose)	69

4.12	Parallel plate electrostatic analyser with electrostatic filed lines (shown as red lines) and the particle trajectory (various coloured trajectory corresponds to different initial energies of the electron beam)	69
4.13	High voltage MOSFET switch (push-pull) schematic	70
4.14	High voltage MOSFET switch (push-pull) along with the pulse rise time (<50 ns) and fall time in push-pull mode	70
4.15	MCP detector (a) Assesmbled on CF-160 flange, (b) Electrical connection schematic	72
4.16	CEM detector (a) With electrical connection (b) Standard electrical connection schematic for ion detection	73
4.17	Electron-ion coincidence experiment schematic	74
4.18	Mechanical alignment of the interaction region electron-ion coincidence experiment	75
4.19	Pulse processing schematic for electron energy spectrum using CMA	77
4.20	ARDUINO DUE with OP-AMP	78
4.21	Pulse processing schematic for ion ToF	79
4.22	Pulse processing electronics for electron-ion coincidence measurement	79
4.23	Pulsing sequence for electron-ion coincidence measurement	81
4.24	Electron-ion coincidence experimental setup with all electronics and DAQ system under working in Atomic and Molecular Physics Lab at IIST, Thiruvananthapuram	82
5.1	Detector pulse from (a) CEM for the ion detection (b) MCP for the electron detection	84
5.2	A steady electric field applied to an electro-optic material changes its refractive index	86
5.3	Image of (a) Single polarity HVFMOS (b) Single polarity HVFMOS under test	87
5.4	Electro-optic modulator (a) Schematic (b) Experimental setup	88

5.5	(a) Optic axis of SBN crystal is found to be 40° (the intensity without crystal (yellow) matches with SBN crystal 40° (green) data) (b) Angle and voltage graph for finding the proper operation of the setup	89
5.6	Switching performance (yellow color represents the output of HVFMS and blue color gives the output of switching of laser beam)	91
5.7	Calibration curve for CMA drawn from Auger electron spectrum of Xenon	92
5.8	Secondary electron (Auger) spectrum of atomic targets	93
5.9	Secondary electron spectrum of diatomic molecular target (KLL Auger reported in the literature)	94
5.10	Secondary electron spectrum of molecular targets	95
5.11	Secondary electron spectrum from Xe projected on PSD kept at (a) Focal point of CMA (b) 10 mm away from focal point of CMA	96
5.12	Differential cross section for Argon at (a) 500 eV electron impact (b) 300 eV electron impact (inset data are the DDCS of argon reported)	97
5.13	(a) Calibration curve for ToFMS drawn from Xenon ($Xe^+ - Xe^{6+}$) time of flight (b) ToF mass spectrum of Xe under 1000 eV electron impact	99
5.14	ToF mass spectrum of molecular targets	100
5.15	$\frac{Xe^{2+}}{Xe^+}$ as a function of projectile electron beam current	101
5.16	ToF mass spectrum of Xenon in coincidence with secondary electron	102
5.17	Naphthalene ($C_{10}H_8$) (a) Secondary electron spectrum (b) ToF mass spectrum in coincidence with energy selective secondary electron	103
6.1	DEToF experimental schematic (first acceleration region: region between P_1 and P_2 , second acceleration region: region between P_2 and D)	109
6.2	Pulsing sequence for DEToF	111
6.3	Typical Mass Spectrum of (a) Naphthalene ($C_{10}H_8$) (b) Quinoline (C_9H_7N) (c) isoquinoline (C_9H_7N) at 1000 eV electron impact (Inset:in figure (a) fragments of naphthalene, (b) fragments of quinoline, (c)fragments of isoquinoline)	112

6.4	Energy dependence of different decay channels with zero delay time extraction (a) Naphthalene (b) Quinoline (c) Isoquinoline molecules . . .	117
6.5	Various dissociative and violent decay channels with delay time extraction (a) Quinoline (b) Isoquinoline molecules under 250 eV electron impact .	118
6.6	Various violent and dissociative decay channels with delayed extraction time for naphthalene under 250 eV electron impact	119
6.7	HCN/C ₂ H ₂ loss channel in naphthalene, quinoline and isoquinoline . .	120
6.8	HCN+C ₂ H ₂ loss channel in quinoline and isoquinoline	121
6.9	HCN+C ₂ H ₂ loss channel overlapped mass spectrum in quinoline and isoquinoline	122
7.1	Typical Mass Spectrum of (a) Naphthalene (C ₁₀ H ₈) (b) Quinoline (C ₉ H ₇ N) (c) isoquinoline (C ₉ H ₇ N) at 50 keV proton impact in EE mode	128
7.2	Typical Mass Spectrum of (a) Naphthalene (C ₁₀ H ₈) (b) Quinoline (C ₉ H ₇ N) (c) isoquinoline (C ₉ H ₇ N) at 50 keV proton impact in EC mode	129
7.3	Typical Mass Spectrum of (a) Naphthalene (C ₁₀ H ₈) (b) Quinoline (C ₉ H ₇ N) (c) isoquinoline (C ₉ H ₇ N) at 50 keV proton impact in CI mode	130
7.4	Projectile proton beam energy dependence of C ₂ H ₂ loss channel in naphthalene, HCN loss channel in quinoline and isoquinoline in (a) EE mode (b) EC mode	132
7.5	The ratio of partial cross section for (a) ionisation (σ_i) to capture (σ_c) (b) double ionisation (σ_{ee}) to capture ionisation (σ_{ci}) for naphthalene (C ₁₀ H ₈) quinoline (C ₉ H ₇ N) isoquinoline (C ₉ H ₇ N) with different proton beam energies	135
7.6	Projectile proton beam energy dependence of C ₁₀ H ₈ ⁺⁺ channel in naphthalene, C ₉ H ₇ N ⁺⁺ channel in quinoline and isoquinoline in (a)EE mode (b) EC mode	138
7.7	Projectile proton beam energy dependence of C ₁₀ H ₈ ⁺⁺ – C ₂ H ₂ channel in naphthalene, C ₉ H ₇ N ⁺⁺ – HCN channel in quinoline and isoquinoline in (a) EE mode (b) EC mode	140

7.8 Top: The tail structure shown is formed when lifetime of parent $C_8H_6^{2+}$ has lifetime comparable to the time of flight of the fragments. Bottom: Shows the experimental intensity distribution as the function of ToF difference. 145

Abbreviations

AMP	Atomic and molecular physics
amu	Atomic mass unit
AO	Atomic orbitals
Ar	Argon
a.u.	Atomic unit
BE	Binding energy
BO	Born-Oppenheimer
C	Carbon
CCD	charged couple device
CEM	Channel electron multiplier
CFD	Constant fraction discriminator
CI	Capture ionization
CO	Carbon monoxide
COB	Coulomb over the barrier
CMA	Cylindrical mirror analyzer
CMOS	Complementary metal-oxide-semiconductor
CRT	Cathode ray tube
CSA	Cylindrical sector analyzer
DAQ	Data acquisition
DFT	Density functional theory
DIB	Diffuse interstellar band
DLA	Delay line anode
DLD	Delay line anode detector
DNA	Deoxyribonucleic acid
EA	Electron affinity
EC	Electron capture
ECR	Electron cyclotron resonance
EE	Electron emission
EELS	Electron energy loss spectroscopy
ESI	Electrospray Ionization
eV	Electron Volt
FC	Franck-Condon
FEL	Free electron laser
FFT	Fast Fourier Transform
FUV	Far ultra violet
GTF	Gaussian type function
H	Hydrogen atom

He	Helium atom
HDA	Hemispherical deflection analyzer
HF	Hartree-Fock
HOMA	Harmonic Oscillator Model of Aromaticity
HOMO	Highest occupied molecular orbital
HT	Herzberg-Teller
IR	Infrared
ISM	Interstellar medium
IVR	Intravibronic rotational
KER	Kinetic energy release
LCAO	Linear combination of atomic orbital
LDA	Local (electron) Density Approximation
LUMO	Lowest occupied molecular orbital
MC	Monte Carlo
MCP	Microchannel plate
meV	Milli-electron Volt
MO	Molecular orbital
MOSFET	Metal oxide semiconductor field effect transistor
MR	Membered ring
Ne	Neon
NIM	Nuclear Instrumentation Module
OVGF	Outer valence Green's function
PAH	Polycyclic aromatic hydrocarbon
PANH	Polycyclic aromatic nitrogen heterocycle
PE	Photoelectron
PEPICO	Photoelectron-photoion coincidence
PES	Photoelectron spectroscopy
PIMS	Photoionization mass spectrometry
PPA	Parallel plate analyzer
RF	Radio frequency
RPEA	Retarding potential analyzer
PSD	Position sensitive detector
RFA	Retarding Field Analyzer
RNA	Ribonucleic acid
SCF	Self consistent field
TDC	Time-to-digital converter
TD-DFT	Time-dependent density functional theory
ToF	Time-of-Flight
ToFMS	Time-of-flight mass spectrometer
TPES	Threshold photoelectron spectroscopy
TPEPICO	Threshold photoelectron-photoion coincidence
TTL	Time-to-time logic
UV	Ultraviolet
V	Volt
Xe	Xenon

Chapter 1

An Overview

Atoms and molecules are the most fundamental building blocks of all the matter that surround us. Biomolecules like amino acids, DNAs, RNA etc. are considered to be the basic building blocks of life, which are available in the terrestrial medium. Interestingly, their presence has been confirmed in the interstellar environment as well [1]. Interstellar molecular clouds and circumstellar envelopes act as factories of complex molecular synthesis. Moreover, a high number of molecules that are used in contemporary biochemistry on the Earth is found in the interstellar medium, planetary atmospheres and surfaces, comets, asteroids and meteorites and interplanetary dust particles. Therefore monitoring the formation and evolution of organic matter in space is crucial in order to determine the prebiotic reservoirs available on the prehistoric Earth [2]. In past centuries, researchers tried to explore the structure and dynamics of atoms and molecules [3–5]. When the molecules are exposed to the charged particle or photon interaction, they absorb energy in their internal degrees of freedom and become unstable. These energetically excited molecules will find different pathways to reduce the energy content either by ionizing themselves or by breaking them into pieces. A number of processes are available for the parent molecular ions to relax into a stable configuration. The understanding of such processes is important in wide areas of physical sciences, ranging from planetary and interstellar space [6, 7]. The main goal of this work is to investigate the structure and dynamics of a class of large molecules called PAHs and its derivatives named as PANHs by probing their dissociation pathways. These molecules show similarity to bio-molecules and are considered as a model system which helps in designing the tools and methods, which on longer time scale can be applied to more complex and important systems like biomolecules, aggregates, and clusters.

1.1 Collision Processes and Energy Loss Mechanisms

Generally, molecular ions are produced by using photon or charged particle interaction. For charged particle-molecule interaction, depending upon the projectile velocity as well as the impact parameter, there are two types of interactions. First, in the case of typical projectile velocities lower than 1 a.u., the interaction is more effective to perturb the nuclear coordinates of the molecule, where electrons in the target molecule accommodate the changing field due to the projectile adiabatically. Second, in the case of the projectile with velocities higher than this, which interact with the target faster than the vibrational time scale so that the energy exchange to the target will happen only within the electronic cloud. Electron, as well as the proton, are used as the projectile in this work. In the case of electron impact, when the energy of the electron is very low (e.g. thermal electrons), it could be captured by the neutral molecule to form a negative radical ion. If the energy is sufficient to excite one of the electrons of a molecule to any higher electronic state, the process is termed as electronic excitation. When the energy of an electron is high enough, it can ionize the molecule by removing an electron from it and is possible to have single, double and higher degree of ionization. Similarly, depending on the target and the energy of the primary electrons, various other processes can take place like molecular dissociation/fragmentation, ion-pair (positive and negative ions) formation and dissociative re-arrangement processes [8].

The projectile energy dependence of the electron impact ionization process is very commonly known to peak at about 70 eV to 100 eV, particularly for low-Z targets like hydrocarbons. At higher energy, the cross section varies as $\ln E/E$. Electron impact studies on PAHs in the low energy regime (energy lower than 100 eV) have been reported for few PAHs and PANHs [9–13]. But a detailed and higher energy electron impact study has not been done for PAHs and PANHs. Heavy charged particle-molecule collisions at intermediate velocities (velocity comparable to less tightly bound target electron) is relatively complex due to competing magnitudes of ionization and electron transfer cross section in this regime. Interaction of intermediate velocity (~ 1 a.u.) charged particle like proton with molecules will give the possible understanding of how the low-energy cosmic ray charged particle interacts with PAHs or PANHs in the interstellar medium.

In this type of collision, the energy deposited into the molecule due to a light ion (e.g. proton) is dominated by electronic processes since the electronic stopping power is much larger than the nuclear one. In ion-molecule collision experiments, the impact parameter and the molecular orientation cannot be controlled experimentally. To understand projectile velocity dependence and the orientation of target molecule, both theoretical and experimental studies have been performed in the case of proton-naphthalene collision [14]. Charged particle interaction with atoms and molecules are extensively studied so far at various impact energy regime [15–26]. Such kind of study is rarely performed for PANHs but few experimental studies have been done for PAHs at low and high projectile velocity [27–31]. Photoionization studies have shown that in PAHs the collective excitation plays an important role and it is unexplored in the case of charged particle interaction except naphthalene and fullurene [32–35].

1.2 Plasmon or Collective Excitation

When projectile interacts with the dense cloud of electrons in the molecule with low impact parameter, the energy is transferred to the electrons locally, since the other charges will be screened by Coulomb screening effect. At higher impact parameters the screening effect is less significant and the delocalized electron cloud of the molecule responds to the Coulombic interaction collectively. Such excitation is often observed not only in molecules but also in metallic, non-metallic clusters and some atomic species as well. Fundamentally, similar oscillation is also very common in nuclei. These excitations are characterized by integrated oscillator strength well beyond one. C_{60} , for example, is known to have a 21 eV plasmon excitation with an integrated oscillator strength of effective participation of 71 electrons in the collective excitation [36]. Thus the excitation process deposits very small amount of energy per electron but the total energy deposited is much larger than the ionization potential of the species. Such collective excited states were first discovered in nuclei (proton-neutron oscillation) [37] and were called giant dipole resonances [38, 39].

The energy of giant resonance peaks varies from 2 eV in metal clusters to 20 MeV in nuclei making it 7 orders of magnitude higher. In the case of C_{60} , an analogous feature

appears nearly at 21 eV with width 11.5 eV, close to the one observed in graphite at about 25 eV [36]. Considering the two-dimensional structure of PAHs, this feature is expected nearly at 17 eV and has been observed in electron energy loss spectroscopy studies of PAH films and photoion yield studies in the gas phase [36,40]. The collective excitations are of interest, because of their very large cross sections compared to typical single particle processes and to know what follows after such excitations. In the case of molecules, this kind of excitation not only leads to single ionization but it also causes a significant amount of evaporation of smaller neutral fragments from the parent molecule [41]. Collective excitation is shown to play a major role in the photoionization of naphthalene and related compounds [32]. Similarly, it is very significant in the case of fullerene under charged particle interaction [42]. Plasmon excitation on PAHs has been less explored, whereas, in the case of PANHs such studies have not been reported till date to the extent of our knowledge.

1.3 Statistical and Non-statistical Decay Processes

In a charged particle-molecule collision, energy deposited by the projectile will be stored in the molecular internal rotational-vibrational mode [8,43]. Once the molecular ion is formed, the electron charge generally gets localized over the whole molecular ion [44–46]. So molecular ions are not generated with a specific internal energy but have a broad energy distribution. There will be a randomization of internal energy over all the vibrational modes of a molecular ion prior to any fragmentation and the resulting mass spectra would show a statistical bond breaking. Such processes favor the lowest-energy dissociation channels. The timescale of internal rotational-vibrational oscillation of the molecules is in picoseconds, with respect to which the unimolecular dissociation time scale is considerably larger, and will decide whether the process is a statistical or non-statistical one and which decides the survivability of these molecules. Typically, non-statistical fragmentation processes are fast (femtosecond time scales) and there is no time for the excitation energy to re-distribute itself over all the degrees of freedom of the molecule before the initial fragmentation step. Statistical and non-statistical fragmentation processes often compete. After a non-statistical fragmentation, the molecule may still have high enough

internal energy to decay further via secondary statistical fragmentation. In general, the balance between processes in which energy is transferred to the electronic degrees of freedom (electronic stopping processes) and processes in which energy is transferred directly to the vibrational modes (nuclear-stopping processes) affects the balance between statistical and non-statistical fragmentation processes. Few studies on statistical and non-statistical process has been reported in the case PAHs [47–52]

Larger molecules generally produce a very complex mass spectrum, mainly due to (i) the numerous possible dissociation channels and (ii) the complex isomerization followed by unimolecular dissociation which is statistical in nature with a variable decay constant. The decay constant itself is governed by the internal energy of the molecule which is strongly dependent on the collision parameters. These statistical processes make the molecular dynamics very significant in areas like biochemistry, astrochemistry, life sciences, etc. For the dissociation product ion to appear in the mass spectrum, they must have a very specific range of dissociation time constant for the parent ion. For linear time-of-flight mass spectrum (ToFMS), it is typically 10^6 s^{-1} . For PAHs and PANHs, specific channels like C_2H_2 loss and HCN loss occur with time constants of the order of 10^6 s^{-1} . In this work, the focus is to investigate the statistical processes since the molecular dynamics of our interest is in this regime.

1.4 Theoretical Methods

The understanding of high energy-molecule collision processes and chemical reactions/pathways will be an incomplete study without a complementary contribution from experimental and theoretical work. The theoretical calculation of molecules must address two parts. One is the static part, i.e. structure calculation, and the other is its dynamics. Structure calculation includes bond structure, binding energies, wave function and so on. Generally, such calculations are very accurate for small molecules (molecules having few atoms). But for larger molecules, it is difficult to get very accurate estimation due to the large basis sets. Still, fairly accurate estimations are possible for the ground state of large molecules as well, particularly for PAHs it is easy, because of the symmetries. It also calculates electron affinity, proton affinity with fairly good accuracy. But when it comes to

calculating transition strength, transition probabilities that are for the spectroscopy, mass spectroscopy, and fragmentation, the calculations of the transition states and the Arrhenius parameters becomes extremely difficult, because the excited states involved in such processes are not stable.

In statistical dissociation experiment, it is important to understand first, what particular dissociation channel one is interested in, followed by the different ways in which a system can go into a state of that fragmentation channel. Thus, for example, there could be two ways in which C_2H_2 loss can happen in the case of naphthalene and azulene as reported [53]. From these kinds of transition state calculations, one gets the probabilities and lifetimes/decay constants. Photon interaction with molecules gives photoelectron spectrum (PES) and the peaks represent the binding energy for molecular orbitals (MOs) in which the measured electron is coming out. Such interaction also alters the nuclear coordinates upon removal of an electron and hence gives rise to vibrational transitions due to Franck-Condon (FC) overlap. The PES of a molecule is typically associated with a broadening due to Franck-Condon overlap of vibrational states. Advanced calculations that take care of the electron-electron correlation as well as the relaxation energy correction to represent the PES peak positions with a reasonable accuracy include configuration interaction techniques, perturbation techniques, and Green's function methods like outer valence Green's function (OVGF) [54–56]. Such calculation is done for few PAH molecules in the case of photoionization spectra [29, 57, 58]. But in the case of charged particle interaction, such calculations have not been done in which the electron spectra have broad energy distribution, and additionally, configuration integral calculation make it more complex. In the present case to obtain various stability parameters for PAHs and PANHs the structure calculation has been performed. There are different methods in quantum chemistry to find the molecular properties like Hartree-Fock self-consistent, density functional theory (both are *ab initio* methods), semiempirical method etc.

1.5 Experimental Techniques

Typically in an ionization process, an electron and recoil ion are formed. The energetics of the ionization process can be traced back by measuring the properties of recoil ion as well as the properties of the outgoing electron. Energy and angular distribution of the outgoing electron carry the information of the structure of the target. Due to the low mass of electron even the smallest amount of stray magnetic/electric fields like earth magnetic field or stray electric field due to charges sitting on the insulating surface or even the insulating patch on the conducting surface itself will completely distort the information carried by the secondary electron. Moreover, while trying molecular studies, the outgoing electron will typically have few electron volts of kinetic energy. Therefore these electrons are more prompt in responding to the stray electric field. In the case of photoionization, a known energetic photon is used and the outgoing electron energy is predicted. But when it comes to charged particle interaction, the energy transfer to the outgoing electron is decided not only by the initial energy of the particle but also by the impact parameter.

Photoionization using synchrotron sources radiation is now a very commonly used technique and a lot of experimental as well as theoretical analysis for most of the molecules are already done. In fact, the technology is even commercialized. Most commonly known techniques for such measurements are the photoelectron-photoion coincidence (PEPICO) and the threshold photoelectron-photoion coincidence (T-PEPICO) spectroscopy [36]. In this experiment, with the help of the energy analysis of emitted electrons, a precise value of the internal energy and therefore a very narrow range of decay constants can be experimentally obtained. On the other hand charged projectiles would deposit a broad range of energies, hence making the process of estimating the internal energy very complex, even if the secondary electron energy is tracked. In the context of PEPICO spectroscopy, the excess energy left in the molecule after the photo-ionization process plays a vital role in deciding the decay pathways of the molecular ions [59]. Similarly, in the case of charged particle interactions, the mechanism of energy loss decides the internal energy of the recoil ions and possible decay channels [14, 60]. The sensitivity of the spectrometer is more critical in the case of charged particle interaction because the electron from the same molecular orbital can come at variable energies and the spectrometer should have

uniform sensitivity over this energy range.

It is equally important to understand the details of the recoil ion produced in such collision process. There it is also essential to thoroughly analyze the properties of the emitted ion which itself adds complication since these ions are heavy and cannot use their kinetic energy to analyze. Moreover, the change in their recoil kinetic energy will be comparable to the thermal energies, and negligible in comparison to their original momentum. An extremely cooled target can be used so that such recoil effects will be studied. But such a technique cannot be used for large molecules since these molecules can't really cool them down to such an extent to see the recoil effects. When the mass is so large, the momentum transfer will have an even lower change in their velocity. In case of a molecule, only when a multiply charged molecules fragments are produced the Coulomb repulsion between them only give rise to substantially a large momentum. So for singly charged molecular ion or a molecular fragment which is produced due to a monocation, one has to really rely on the mass detection. The detection of mass is perhaps the most important task to start, and the other measurements like momentum recoil ion momentum spectroscopy (RIMS) [61] and cold target recoil ion momentum spectroscopy (COLTRIMS) [62] are not really applicable here. For such mass measurement various techniques can be used like quadrupole mass analyzer, Penning trap, Paul's trap [63–65]. Penning trap and Paul's would make it is difficult to measure the electron energy due to the permanent magnetic field, closed geometry and RF field. Whereas the linear ToFMS is easy to build and it offers a possibility of having a completely field-free region for the electron emission [66]. It gives 2π accessibility for the emitted electron in principle so that a suitable electron spectrometer can be placed on the other side of ToFMS. In that sense, time-of-flight (ToF) is a very convenient technique for the recoil ion measurement. It measures the ToF of the particle after imparting an equal amount of energy per charge state. A two-stage Wiley-Maclaren geometry tries to correct for the spread due to velocity and spatial distribution [67]. But this comes at the cost of having some electric field in the interaction region. Therefore if any electron spectroscopic measurement is to be done then it is essential to do pulsing of the extraction field for the recoil ion.

Generally, such experiments utilize electrostatic and in some rare cases magnetic electron energy analyzer. The sensitivity of the measurement techniques requires very accu-

rate geometry and field free interaction region. Since the electron spectrometers provide angle and energy differential yields, it can detect an extremely small fraction of the total number of the electrons produced in the target.

A combination of a secondary electron spectrometer and a recoil ion mass spectrometer gives much more detailed information compared to the separate use of these instruments. Thus energy selective secondary electron-ion coincidence technique is an extremely powerful tool. The energetics in this whole process is very accurately known if it is due to photoionization. The major issue with such measurement is the very strong dissimilarity in the count rates, which causes extremely demanding conditions on the coincidence rate. A large count rate for ions is found compared to extremely low electron count rate. Generally, for any good quality electron spectrometer, the acceptance will be of the order of 10^{-3} , depending on the resolution of the spectrometer and will be able to detect 10^{-4} . That is, the total rate dissimilarity will be of the order of 10^{-6} or so. Moreover, for such a large dissimilarity in count rate and cannot afford to have large ion production rate. This increases the probability of chance coincidence detection for the uncorrelated event. Therefore such experiments are generally very long experiments and very focused. In case of photoionization, at least state selectivity can be assured by knowing what would be the energy of electron coming from a given molecular orbital by knowing the photon energy. State selectivity in case of charged particle collision becomes extremely complicated, so the experiment will be much more time-consuming than PEPICO. Therefore even though such a measurement is though expected to be very rewarding, it is very challenging by itself.

Since electrons are very sensitive to the stray field the instrument should make sure that no electric field is in the interaction region when the electron beam is interacting with molecules. But if the interaction region is kept field free and allow the recoil ion to slowly drift into the acceleration region (where a constant potential is applied) it will lead to delay in detection of recoil ion in the coincidence. For example, at thermal velocities (for naphthalene ~ 100 meters per second), the molecular ion will take hundreds of microseconds if not milliseconds to cross the distance of 1 cm field free interaction region and enter into the acceleration region. Moreover, before the extraction of the molecular ion from interaction region for the corresponding electron detection, further ionization

causes false coincidence. Adding to this, with overall collision rate of 1kHz, are producing one electron per millisecond ($1/10^{-6}$), which means that one out of 10^6 electrons produced will be detected on average and in 1000 seconds and get one true coincidence for the electron. To speed up the process for increasing the true coincidence rate, that means one has to accelerate the ions by applying potential in the interaction region. If a constant electric field is used in the interaction field for this purpose, it will affect the primary as well as the secondary electron. So the only way to solve this problem is to have an electron spectrometer and detect the electron till that time so as to ensure the electric field in the interaction region is zero (i.e, interaction region should be field-free during interaction and till detection of a secondary electron). After detecting the electron, switch the projectile electron beam OFF and field in the interaction region ON before the ion gets too much drift, otherwise, the resolution will be spoiled. Now how fast this is done is decided by the electronics entirely and therefore designing such electronics, pulse processing electronics and high voltage switches put a very demanding condition on such instruments.

Though the photoionization is a very powerful technique, considering there are several environments where charged particles are interacting with the molecule, that understanding is also very important. Investigations using such techniques are very rare due to the extreme complication resulting due to such conglomeration. The first and foremost is the contradictory requirement of the extraction fields in the interaction region for the instrument which forbids the use of constant voltages onto the extraction electrodes. At the same time, pulsed electric field affects the mass resolution adversely. Moreover, the double differential nature of secondary electron detection gives orders of the magnitude of dissimilarity in the count rate on electron and ion detector and therefore demands extremely low count rate resulting in an extension of data acquisition time.

1.6 Polycyclic Aromatic Hydrocarbons and their Derivatives

Polycyclic aromatic hydrocarbons (PAHs) are a group of organic compounds consisting of two or more fused aromatic rings. These are a family of hydrocarbons consisting of molecules where carbon (C) atoms are arranged in a honeycomb lattice type structure of fused six-member aromatic rings with H atoms located at the periphery of the ring, on the other hand polycyclic aromatic nitrogen heterocycles (PANHs) are species with one or more CH groups substituted by a nitrogen atom in PAHs. The proposed widespread existence of PAHs in the interstellar medium (ISM) has driven recent investigations of their spectroscopic and photophysical attributes [68,69]. Cations or protonated species of PAHs have been linked with the diffuse interstellar bands (DIBs) [70]. Since nitrogen is the fourth most abundant element in space, it has been proposed that PANHs should also be present in the ISM [68]. The spectroscopy of PANHs is motivated by their possible involvement in pre-biotic chemistry as well as eventual transformation into the nitrogen-containing aromatic systems that are essential ingredients in biomolecules apart from an astrobiological importance [71–76]. The presence of PANHs has been reported in the extraterrestrial meteoroids, in the atmosphere of Titan and they could be involved in the chemical origin of life [77, 78]. Small PANHs like quinoline readily dissociate under exposure to interstellar radiation [79]. Moreover, it produces reactive photo products that may contribute to the composition of the ISM; of particular significance is the HCN loss in these systems [80]. The incomplete combustion of fossil fuels, coal, wood, cigarette smoke etc generates PAHs on earth environment and it is carcinogenic [81,82]

Considering the abundance of high-energy radiation in the interstellar medium, it remains an interesting endeavor to understand the mechanisms behind the survivability of PAHs and PANHs in such harsh environments. The molecular structure of PAHs is strongly affected by shock processing in the interstellar medium [83, 84]. Micelotta *et al* demonstrated that the interstellar PAHs (with the number of carbon atom = 50) do not survive in shocks with velocities greater than 100 km s^{-1} and larger PAHs (with the number of carbon atom = 200) are destroyed for shocks with velocities 125 km s^{-1} [85]. Electronic excitation by impacting ions or electrons may lead to isomerization into stable

pure-C species such as fullerenes. But, nuclear interactions in interstellar shocks may be a viable pathway to the formation of nitrogen-containing PAHs [85]. Amongst the numerous interaction mechanisms between energetic radiation and PAHs, plasmon excitation dominates due to its large oscillator strength. With intermediate velocity proton impact on naphthalene, it has been shown that the plasmon excitation mode in PAHs contributes almost exclusively to the evaporation of H or C_2H_2 [86]. The existence of plasmon excitation in PANHs has not been investigated so far. In addition, PANHs have been associated with functional materials such as organic photovoltaics, where a clear understanding of their photochemistry and spectroscopy is necessary [87]. Very few investigations have been carried out in the context of HCN formation apart from the formation and dissociation of quinoline and isoquinoline [88]. The other ionization and dissociation channels have been largely ignored. In this work, statistical and non-statistical processes in these molecules have been focused on charged particle interaction.

1.7 Electron-Ion Coincidence Measurements on PAHs and PANHs

Considering the complexities involved in the case of electron-ion coincidence studies for molecules, it has been very difficult to make a focused study of large molecules like PAHs using such a technique, particularly while using charged particle as a projectile. If charged particle interaction has to be studied spectrometrically, it is very important that the particular channel is identified and is used as a tool to understand the dynamics of these molecules. It is also important that such an identified channel should have no cross channels because multiple processes give rise to same products and using such coincidence techniques to separately study each channel is impractical. Moreover, it will not be possible to do a very large set of measurements at many different ranges of electron energies and many different projectile configurations.

For PAHs and PANHs, it is known that the H_2 loss and the C_2H_2 loss channels are the important statistical channels. Due to the limited resolution of the spectrometer one can have due to pulsed extraction, it is hard to detect the H_2 and H loss process in a simple lin-

ear ToFMS, but C_2H_2 loss is clearly separable. An instrument with provisions to perform electron spectroscopy and simple ToF spectroscopy separately along with electron-ion coincidence measurement is a very useful tool for electron impact studies. Moreover, since the extraction and the excitation process is also pulsed, then by varying the delay between the excitation pulse and extraction pulse, the statistical nature of fragmentation process can be probed. Generally, high energy photon source facility like synchrotron facilities are large facilities and not easily available. High energy ion beam facilities are also sufficiently large that they are also not easily accessible or they have restricted access. An electron gun, on the other hand, is a very convenient tool while designing a setup of this kind of experiment. Moreover, the setup with such excitation source like electron gun makes whole instrument compact and portable. After completion of the development, of course, the setup can be installed at the facilities like Synchrotron Radiation Source (SRS) or at high energy ion beam facility. Then they can be used to study the different modes like electron emission mode pure ionization modes like ToF mode or coincidence mode. The sensitivity of the electron to the electric or magnetic field causes additional complications in the experiment. Therefore while using electron beam it becomes imperative that one should pulse the electron beam. This automatically provides an opportunity to study a special technique called delayed extraction time-of-flight mass spectrometry.

Typically the development of a mass spectrometry and electron spectrometry setup involves a substantial amount of simulation and design followed by a planning of the instrument, all the while keeping in mind various considerations which have mechanical engineering aspects as well as vacuum technology, after which the instrument has to be fabricated, integrated, tested and calibrated for its performance for all the different modes. Only after successful completion of such calibration and testing the instrument can be used to perform the physics experiment of interest. Pulse processing electronics in general plays very significant role in the performance of the instrument of this nature. Moreover, since one expects to use a pulsed extraction and pulsing of the electron beam itself, that means it involves not only the regular analog and digital pulse processing of low amplitude pulses but also high voltage extremely fast pulses which in itself is a complicated task. Generally, such instrumentation is extremely expensive and very specialized.

Such electron-ion coincidence studies under electron impact have been done mainly

in the case of atoms, where the Auger electron-ion coincidence measurements have been done extensively [89]. But for molecules, such studies are done under photon interaction using techniques like PEPICO [36, 90]. In the case of molecules, this kind of study was mainly focused on the dicationic states of molecules like N_2 , CO_2 and their dissociation dynamics [91–93]. Even though such studies are limited in the case of electron impact experiments on nitrogen, tetrachloromethane molecules have been reported [94, 95] by using Auger electron-ion coincidence measurements. These kinds of molecular, structural or dynamical studies are very rare in the case of large mole molecules like PAHs and PANHs.

1.8 Thesis Outline

This thesis concerns the electron and mass spectroscopy of large molecules under charged particle interaction. A very energy selective secondary electron-ion coincidence setup is designed, fabricated and tested. The instrumentation is then used to study electron impact ionization and statistical dissociation dynamics of three basic types of PAHs and PANHs. These dynamics are then compared with proton impact on the same set of molecules.

Chapter 1: An Overview:- In this chapter, a brief introduction to collision process and energy loss mechanism in charge particle-molecule collision is given. Various theoretical and experimental techniques are discussed briefly to understand the importance and role of PAHs and PANHs of the terrestrial and extraterrestrial environment. Further, this chapter explains the significance of plasmon/collective excitation (a peculiar property associated with PAHs and PANHs), dissociation process and their importance in statistical and non-statistical decay processes.

Chapter 2: Theoretical Methodology:- In this chapter, the various theoretical calculation methods used in this work have been discussed to understand the molecular, structural and dynamical properties. The quantum chemistry *ab initio* calculations performed to study the structural variations of PAHs and PANHs and their relevance under charged particle-PAH/ PANH interaction described in detail.

Chapter 3: Principles of Electron Spectroscopy and Ion Mass Spectrometry :-

This chapter introduces the basics of experimental techniques used in electron and ion spectroscopy. A detailed study on different experimental components is described including various spectrometric techniques, detection mechanism, and data acquisition system.

Chapter 4: Experimental Methodology:- This chapter describes the development of experimental setup at Atomic and Molecular Physics Laboratory, IIST, Thiruvananthapuram for electron impact ionization and electron-ion coincidence measurement. The simulation, instrumentation, and construction of e, 2e setup in detail is described.

Chapter 5: Testing and Calibration:- This chapter presents the testing for the functionality of individual components of the experimental setup including spectrometers and detectors. Further, calibration of spectrometers and detectors are discussed. Demonstration of electron spectra, mass spectra, electron-ion coincidence spectra of various atomic and molecular targets are shown as the preliminary test results.

Chapter 6: Electron Impact on PAHs and PANHs:- This chapter explains the interaction of the electron with PAHs and PANHs and the statistical dissociation process. The delayed extraction time-of-flight mass spectrometric technique is used in this work to study the statistical dissociation and neutral evaporation mechanisms.

Chapter 7: Ion impact on PAHs and PANHs:- This chapter discusses the interaction of the ion with PAHs and PANHs and the related structural effects. It also focuses on energy deposition and the effects of collective/ plasmon excitation in PAHs and PANHs. Further, metastable decay dynamics studies on dicationic molecules are discussed.

Chapter 8: Conclusion and Future Scope:- This chapter summarizes and concludes the work performed. The setup built under this work has excellent potential in molecular physics studies. This chapter also discusses the further possible extension of the work.

Chapter 2

Theoretical Methodology

The quantum states of the molecule play a very critical role in the energy exchange process when a proton or charged particle interacts with the target. Therefore for a complete understanding of the problem, a proper assessment of such quantum mechanical properties of the target molecule is essential to make the correlation between the experimental results and the properties of the molecules. Such electronic states of the system must be computed using various existing and time-tested models. For this purpose particularly in molecular physics, quantum chemical computational approaches are used, which are based on various theories like Hartree-Fock self-consistent method, density functional theory, semi-empirical method etc. By using these methods the wave functions of the states as well as the eigenvalues can be calculated. With the help of this information, the models can be devised, which will help in finding the excitation and de-excitation and so on. When it comes to the process of dissociation or fragmentation, the structure details like bond properties become important and they can be, in principle, calculated from the above-mentioned methods.

Theoretical study to explain the energetic radiation interaction with the molecule to a very good accuracy is difficult due to the simultaneous involvement of several collisional processes during the experiment, which are results of the many-body interaction processes. The experimental results become multidimensional in nature due to complexity in the potential energy surface and associated many degrees of freedom ($3N-6$, where N is the number of atoms in the molecule) for large molecules. The wavefunction for polyatomic systems is a function of several parameters simultaneously like bond distances, bond angles, dihedral angles of rotation etc. Hence a quantum chemical approach based on approximations helps in giving results with reasonable accuracy for nuclear coordinates, vibrational modes, potential energy surface and the electronic wavefunction. This chapter reviews various established methods of quantum computation of molecular structure with more stress on the models used as part of this work.

2.1 Quantum Chemistry Calculation

Quantum mechanics is required to properly describe the electronic structures of atoms and molecules. Let us consider the simplest case of the hydrogen atom. To obtain time-independent solution for hydrogen atom problem with quantum mechanics one must solve the following equation which is written as

$$E\psi = \hat{H}\psi \quad (2.1)$$

where ψ is the wave function that describes an atom or molecule. The Hamiltonian operator, \hat{H} , is the sum of the kinetic (\hat{T}) and potential (\hat{V}) energy operators:

$$\hat{H} = \hat{T} + \hat{V} = \frac{\hbar^2}{2\mu}\nabla^2 + \hat{V}(r) \quad (2.2)$$

where μ is the reduced mass of the system, and \hbar is the reduced Planck constant. The potential energy operator $\hat{V}(r)$ in Eq. (2.2) is the potential describing the attraction between the electron and nucleus due to the Coulomb interaction. Solving the Schrodinger equation (Eq.(2.1)) involves finding both the wave function ψ , as well as the corresponding energy of the system, E . For a two-body system like the H atom, this is a straightforward procedure. On the other hand, analytical solutions for systems with three or more non-constrained interacting particles (e.g. electrons or protons) do not exist. Therefore a number of numerical methods which are used for calculating the wave function of an arbitrary many-body system and its energy.

The first approximation that is usually made when solving Schrodinger equation for a molecule is the Born-Oppenheimer approximation [96], in which one assumes that the motions of electrons and nuclei are decoupled, i.e. that the electrons instantaneously adapt to any movement of the nuclei, and that the nuclei are therefore considered to be stationary when calculating electronic wavefunctions. This simplification generally only introduces a small error to the calculation of ground-state structures because the mass of a proton is about 1836 times greater than that of an electron, and it is therefore used in all of the methods that are commonly used.

A well-known method for numerically calculating the wave function of atoms and molecules is the Hartree-Fock method. In the Hartree-Fock model, explicit pairwise interactions between the electrons are neglected. Instead, each electron moves in the mean field of the other electrons in the system. By only considering such mean-field effects, the HF method lacks a description for most types of explicit correlations between the motion of the electrons. Despite these limitations, HF, can in many cases, still produce reasonably accurate results and perhaps more importantly, act as the first step to more advanced models. Because the effective Hamiltonian (the Fock operator) for an electron in the HF method depends on the averaged coordinates of the other electrons, the calculations are performed iteratively. Using a trial wave function, the HF equations are solved which result in a new wave function. The Fock operator is regenerated with this new function and the processes are repeated until the wave function and Fock operator converge in a self-consistent way. Because of this process, the HF method is often referred to as one of the self-consistent field (SCF) method. Building upon the foundation of the HF method, there is a number of more advanced models, known as post-HF methods. In one way or another, these do away with the biggest limitation of HF: the mean field approximation. While increasing the computational cost, in some cases significantly, these methods improve the accuracy of the results from HF through the inclusion of electron correlation.

An alternative to HF and post-HF methods is Density Functional Theory (DFT) [97]. In DFT, one uses the electron density to determine the energy of a system, in contrast to the wave-functions based HF method. This is possible due to the Hohenberg-Kohn theorem [98] which states that there is a direct one-to-one correspondence between any observable quantity of a stationary many-electron system and the ground state electron density of a system. This means that the problem of solving the N-body Schrodinger equation with $3N$ degrees of freedom is reduced to solving a problem only dependent on the three spatial coordinates ($r = (x, y, z)$). Up to this point, DFT is an exact theory, but there is a limitation to this scheme. While many of the components of the DFT method are well-defined, the exact functions of the density function that describes the exchange-correlation energy are unknown. The approach (functional) used to describe exchange-correlation energy is what sets different DFT methods apart. A plethora of different DFT functionals exists, from purely theoretical models to empirically fitted forms, and combinations of

these in semi-empirical models. One of the functionals widely used as a DFT functional for different isolated molecular systems is the B3LY (Becke, three-parameter, Lee-Yang-Parr) [99]. For clusters and other large systems where long-range dispersion forces are important, long-range corrected (LC) hybrid density functional, ω B97X-D [100] and local density functional, M06-L [101] are often used as the lack of such interactions is a shortcoming of most other DFT methods [102]. The quantum mechanical calculations for molecular structure and dynamics are critical to this work and the quantum mechanical computations are done with help of GAUSSIAN09 packages [103].

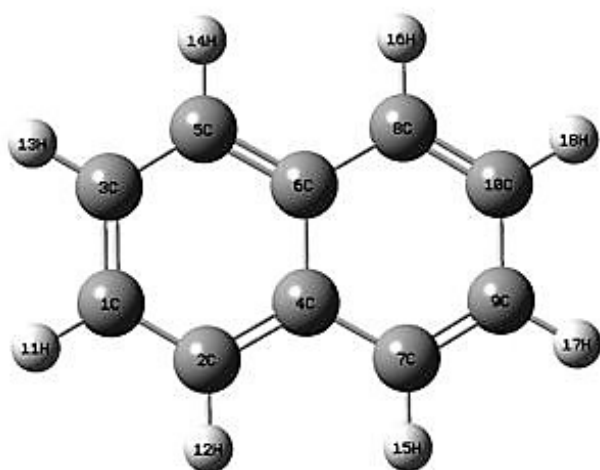
2.2 Structure Calculations

The work presented in this thesis focuses on three representative examples of PAHs and PANHs family mainly naphthalene, quinoline, and isoquinoline. The interest comes from the fact that these three molecules are structurally similar and two of them are isomers. Therefore it is interesting to explore how their properties differ due to the difference in the structure. These properties could include bond parameters in general, binding energies and ionization potentials. Of course, there are more properties which could calculate, which are dynamic in nature and would require more complicated methodologies, so this work is not focusing on that. Moreover, for the process of charged particle energy loss, the average electron density is the parameter which is critical. Therefore it is not expected that the HF and DFT method would give the total electron density very differently even though the binding energy value itself may change within a few fractions of electron volts. So, therefore, HF level calculation is performed for the three molecules to obtain the electron density distribution and the binding energies as well as ionization potential.

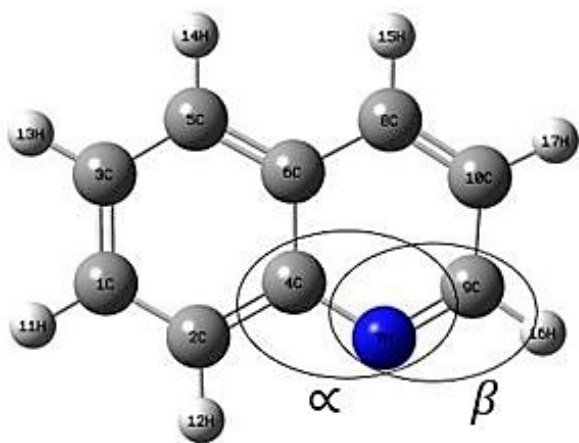
It is known that electron or ion impact ionization and fragmentation of the molecules is mainly driven by the specific vacancy production by the projectile. Furthermore, under Born approximation, the exact details of the molecular orbital weakly affect the overall cross sections. For all the cases considered here, the valence structure is dominated by s and p orbitals and hence it is expected that naphthalene and its nitrogen-containing derivatives will have similarity in terms of vacancy production. It has been seen and stud-

ied in detail that C_2H_2 loss in PAHs and loss of HCN in the corresponding PANHs are statistical decay channels. The decay constant of these processes strongly depends on the intra-vibronic redistribution of the energy upon vacancy creation and electronic rearrangements. Therefore, significant importance is given to the analysis of the possible statistical loss of HCN while understanding the structure calculation results. In addition, as seen earlier, the most prominent fragmentation channels are accompanied by HCN loss, and therefore any influence on the probability of HCN loss in PANHs will directly impact the fragmentation yields of various fragmentation channels. Thus, it becomes essential that the variation of the statistical channels like HCN loss is understood in terms of the detailed difference in the bond structure of these molecules. At this juncture, one must consider the variation of individual bond structure and associated structural attributes deciding the propensity of specific fragmentation channels. The three examples taken up here obviously fall into two categories namely (i) naphthalene and (ii) quinoline and isoquinoline. The large structural difference between the two groups and the well-known activation barriers for the two cases [87, 104] imply that naphthalene may show different intensities of specific fragmentation channel, compared to the corresponding ones in the second group. However, a certain similarity in the fragmentation process of quinoline in comparison to isoquinoline is expected. This aspect is explored in more details in the following section.

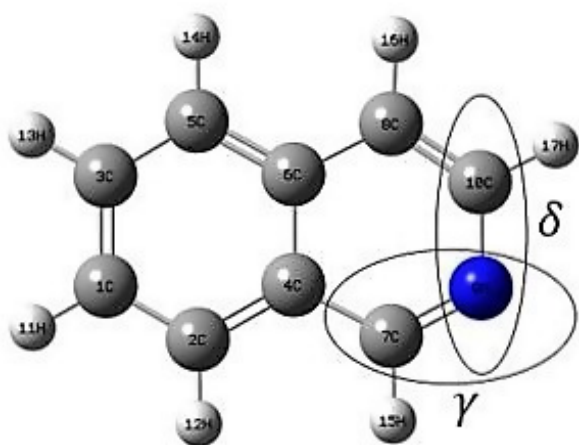
In order to understand the structural variations, the optimized geometry, as well as the ionization potential and bond length changes, were computed for the three target molecules using the HF method. The computations were performed with the help of the quantum chemistry packages GAUSSIAN09 [105] by using 3-21G [106] basis. To assess the consistency of these calculations, the ionization potential of each species is compared. The similarities and differences between the three species in terms of their structural attributes are analyzed based on the computational results. The calculated ionization potentials for naphthalene, quinoline, isoquinoline were found to be 7.97 eV, 8.55 eV, 8.45 eV. These values compare well with the database value of 8.144 ± 0.001 eV, 8.63 ± 0.02 eV, 8.534 ± 0.02 eV [107] respectively. From the HF calculation, highest occupied molecular orbital(HOMO) value for the ionization potential(with opposite sign) have been taken [108]. The similarity in the ionization potential for quinoline and iso-



(a)



(b)



(c)

Figure 2.1: Structure of (a) Naphthalene ($C_{10}H_8$) (b) Quinoline (C_9H_7N) (c) isoquinoline (C_9H_7N) (different colours refers to the individual atoms : grey - Carbon, blue - Nitrogen, white - Hydrogen)

quinoline are due to very similar structures electronically. Naphthalene, on the other hand, is much easier to ionize. Figure 2.3 shows the similarity of molecular orbital energy eigenvalues for quinoline and isoquinoline. The next aspect of importance is the energy loss mechanism during the interaction of the electron beam with the molecules. It is well understood that in this collision regime with the electron as the projectile, the only mechanism which is of significance is the electronic energy loss to the target. Thus the electron density distribution in the molecule can be used as a measure of such energy loss. Two targets with identical electronic energy density distribution would directly imply identical energy loss in the collision process in consideration here. To this end, the total valence electron density distribution in three dimensions is obtained from the calculation and the density is integrated for a given orientation of the molecule. The electron density seen by the projection in the planar orientation of the target (which offers the largest area and hence the cross section) is shown for the three targets in Figure 2.2. The projected electron density appears to have a small enhancement near the nitrogen atom. Considering the overall active area where the energy loss is expected to be significant, this difference around the nitrogen atom would affect the energy loss process marginally. A similar conclusion has been shown to be correct for various examples using energy loss calculation by *Monte-Carlo* simulation [109], except that there is a small difference near the N atom for quinoline and isoquinoline as seen in figure 2.1. Thus it is reasonable to assume that the electronic energy loss in these three cases will be identical.

A variation in the bond length is observed when one carbon-hydrogen pair is replaced in naphthalene by nitrogen to make CN bond in the quinoline and isoquinoline. In quinoline, 4C-7N(α) bond shrinks by 0.058 a.u and 7N-9C(β) shrinks by 0.072 a.u. compared to the corresponding atoms in naphthalene. Similarly, in the case of isoquinoline 7C-9N(γ) bond shrinks by 0.075 a.u and 9N-10C(δ) is reduced by 0.050 a.u ($\alpha, \beta, \gamma, \delta$ bond are referred as in Figure 2.1). Due to the resonance structure, it is expected that corresponding bond lengths will only interchange amongst α and β as well as amongst γ and δ as seen in Figure 2.1. It is observed that the quinoline system is left with the only option in the form HCN fragment. This is achieved by keeping the β bond intact and thus the nitrogen atom pairs with one of the neighboring carbon atoms. The pairing with carbon while keeping the bond α intact would require the breaking of a larger number

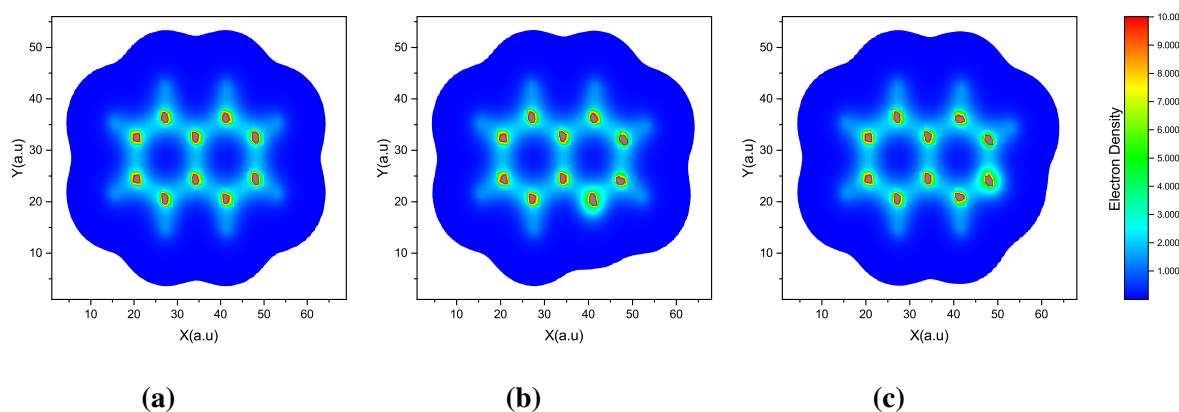


Figure 2.2: Charge density of (a) Naphthalene ($C_{10}H_8$) (b) Quinoline (C_9H_7N) (c) isoquinoline (C_9H_7N)

of bonds thus requiring larger internal energy. As can be seen from the Figure 2.1, as well as Table 2.1, the bonds labeled as α , are very unlikely to contribute in the forming HCN fragment. On the other hand for isoquinoline, there could be two possibilities of, either (i) bond γ or (ii) bond δ . Hence one expect that the intensity yield of HCN should be approximately doubled in favor of isoquinoline for identical collision conditions. Of course, a small deviation due to the slight difference in the actual cross-sections as well as threshold energies in the two cases is expected. Thus for quinoline, bond β itself is the only possibility. The difference would be due to the resonance structure, both γ and δ bonds can contribute equally to the HCN formation. This is quantitatively clear by the fact that the bond alteration in both cases is identical. And the roles of bond β and bond γ or δ are also identical. Thus, with the help of HF calculation it is expected that at higher energy electron impact, the branching ratios in quinoline and isoquinoline should vary by a factor of two in favor of isoquinoline.

Generally, a considerable amount of complex computational efforts are required to calculate various intermediate and transition state structure. Such detailed calculations have been carried out for naphthalene [87] and for quinoline and isoquinoline [104]. But such calculations are done in the context of photoionization measurements where the internal energy distribution is known very accurately. In the case of charged particle impact, the energy deposition process is complex and the internal energy covers a very broad

Table 2.1

Hartree-Fock (HF) calculation for bond length by using GAUSSIAN09 with 3-21G basis set (bond labels are give as in Figure 2.1)

Naphthalene (C ₁₀ H ₈)		Quinoline (C ₉ H ₇ N)		Isoquinoline (C ₉ H ₇ N)	
Bond Length (a. u.)	Bond Label	Bond Length (a. u.)	Bond Label	Bond Length (a. u.)	Bond Label
1.414	1C – 3C	1.415	1C – 3C	1.416	1C – 3C
1.373	1C – 2C	1.373	1C – 2C	1.373	1C – 2C
1.419	2C – 4C	1.418	2C – 4C	1.417	2C – 4C
1.431	4C – 6C	1.429	4C – 6C	1.425	4C – 6C
1.419	5C – 6C	1.418	5C – 6C	1.418	5C – 6C
1.373	3C – 5C	1.373	3C – 5C	1.373	3C – 5C
1.419	4C – 7C	1.364	4C – 7N	1.421	4C – 7C
1.373	7C – 9C	1.314	7N – 9C	1.313	7C – 9N
1.414	9C – 10C	1.416	9C – 10C	1.361	9N – 10C
1.373	8C – 10C	1.371	8C – 10C	1.372	8C – 10C
1.419	6C – 8C	1.416	6C – 8C	1.475	6C – 8C
1.084	3C – 13H	1.084	3C – 13H	1.084	3C – 13H
1.085	5C – 14H	1.085	5C – 14H	1.084	5C – 14H
1.084	1C – 11H	1.084	1C – 11H	1.083	1C – 11H
1.084	2C – 12H	1.083	2C – 12H	1.084	2C – 12H
1.085	7C – 15H	1.085	8C – 15H	1.089	7C – 15H
1.084	9C – 17H	1.083	10C – 17H	1.085	10C – 17H
1.084	10C – 18H	1.087	9C – 16H	1.084	8C – 16H
1.085	8C – 16H				

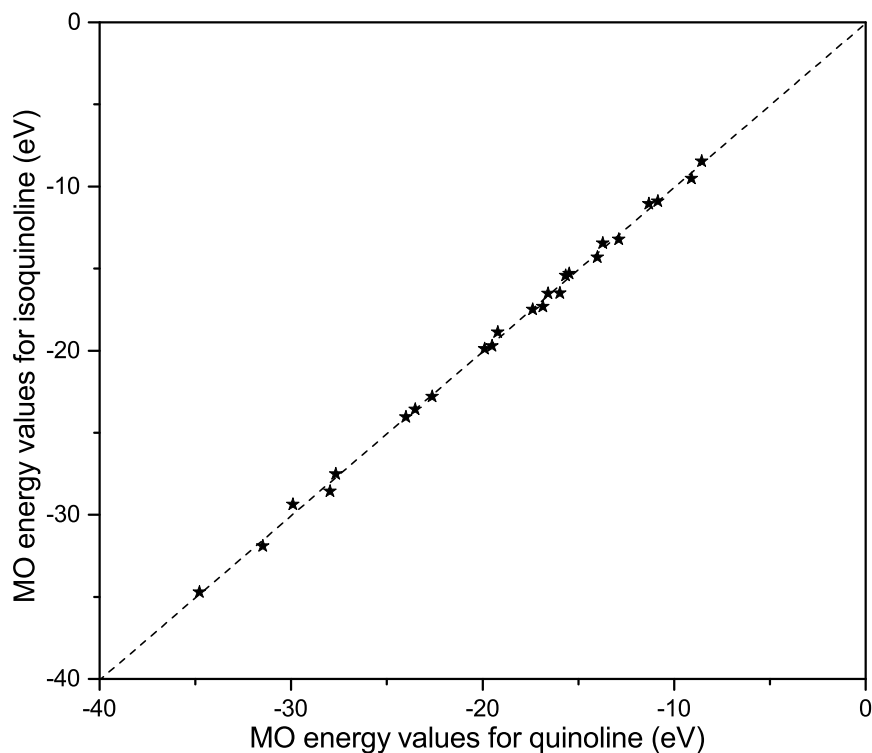


Figure 2.3: Similarity of molecular orbital energy eigenvalues for quinoline and isoquinoline (dotted line shows a straight line with slope 1)

range of values. So the above analysis carried out only on the basis of the bond parameter is very simplistic. Therefore to put the present analysis in perspective, the work is done on the neutral atom and low energy electron impact measurements on quinoline and isoquinoline with isotopic labeling are referred [12, 13]. In these studies, it was found that with 70 eV electron collision with isoquinoline, nearly 70% of the HCN loss stems from the carbon adjacent to the nitrogen atom and the rest comes from the structural isomerization and hence randomization of the carbon-nitrogen pairing in HCN emission. A similar analysis of quinoline shows that only 33% contribution comes from the nitrogen pairing with adjacent carbon. In low-energy electron collisions, the HCN loss is seen to originate entirely from the pairing of adjacent carbon atoms with nitrogen. The photodissociation studies reported recently covers a very small range [104] of internal energies and hence cannot be used in the present context to conclude about the dissociation yield propensity in electron impact case.

2.3 Conclusion

Using HF method calculation the structural properties of three molecules of PAHs have been compared. There are several similarities in the structure is observed with a minor difference in the bond length due to the replacement of CH with nitrogen. The electron energy distribution will have same distribution everywhere except the location of nitrogen, as expected. Therefore, it is expected that the electronic energy loss in the intermediate velocity charged particle should be same. Since one of carbon-hydrogen pair is replaced by nitrogen it is bound to have some small differences like the minor change in the bond length. Considering that quinoline and isoquinoline are isomers, the exact location of nitrogen does not influence, very strongly. Therefore, if there is bond dissociation process it expected that it should be favorable in the case of isoquinoline compared to quinoline and a probability which is twice that of isoquinoline than quinoline is also expected. Experimentally it is shown that there is some amount of structural randomization in the case of two isomers but such an estimate has not been performed theoretically. Though the ratio to be two is expected, under certain operating conditions it has not been two; but such measurement has not been done in detail. Baldwin *et al.* [12, 13] have shown this randomization in low electron energy impact. The process is different than the usual energy loss mechanism in the case of fast charged particle collision, so it is yet to study how this ratio is getting affected as the function of projectile energy.

Chapter 3

Principles of Electron Spectroscopy and Ion Mass Spectrometry

Spectroscopy, in general, is used to determine the identity, quantity, structure, and the environment of atoms, molecules, and ions by analyzing the particles (photons, neutrons, charged particles) emitted, absorbed or scattered by them. Electron spectroscopy, in particular, analyzes the electrons emitted or scattered by the sample and ion spectroscopy determines the properties of ions created in various ionizing/fragmentation processes. During the past few decades, the development of electron spectroscopy has been vital both in the instrumentation and in the theoretical aspect of the spectra. The state-of-the-art electron spectrometers can achieve sub-meV energy resolution over a broad range of electron kinetic energy. It can be used to measure a number of other parameters characterizing the emitted electrons, such as their angular distribution and spin. Similarly, ion spectroscopy has developed rapidly in the last decades. Modern spectrometer designs are suitable not only for determining the chemical constituents of the sample but also for precise studies of molecular dynamics and dissociation processes. The capability of this instrument is substantially augmented by the technique of coincidence. This technique is based on recording multi measured parameter in a correlated manner.

A crucial component in experimental studies of electron and ion spectroscopy is always the method and the source of ionization. Here, a broad variety of sources is available, suitable for different techniques and for probing different properties of the electronic structure of the matter. The sample can be bombarded by electrons (electron guns), ions, ultraviolet radiation (gas discharge lamps) or x-rays (x-ray tubes). A revolutionary new source for electron spectroscopy was found in 1947 with the discovery of synchrotron radiation [110]. As for future radiation sources for atomic/molecular spectroscopy, free electron lasers are currently being developed [111]. Spectrometers are essential for the measurement of energy and angular distribution of electrons and ions. Finally, the detec-

tion mechanism and data acquisition are required for completing the precise experimental measurement of electron and ion properties, and dynamics. Main areas of application of electron and ion mass spectrometry are atomic and molecular physics, solid state physics, chemistry, biology, materials science and other industrial applications.

3.1 Requirements for Experimental Study

To realize the design of a charged particle interaction/collision experimental system, it is necessary to create an environment where a stream of particles can travel without loss of momentum, and make electrodes and pole pieces that faithfully produce the electrical and magnetic fields necessary to deflect the particles. Moreover, the cost-based instrumentation feasibility is also to be considered. Here the discussion is the basic requirement for experimental construction of ion/electron spectroscopy.

When an atom, molecule or charged particle travels in the atmospheric pressure (of the order of 1 bar), it can travel tens of nanometers (mean free path) between successive impacts (collisions), which modify its direction, or energy, or other particle properties. If the pressure is reduced to 1 millibar, the mean free path increases to a few micrometers. So it follows that high vacuum ($\sim 10^{-7}$ millibar) is required for the operation of a charged-particle experimental system with minimal probability of collision with background gas.

An oil-free vacuum system with turbomolecular pumps, ion pumps, or sorption pumps is most desirable, although a system evacuated with a properly trapped oil diffusion pump is adequate in many cases. For high vacuum, the experimental chamber surfaces must be kept clean, since contamination with an insulating material will result in evaporation and reduce the vacuum capability. Moreover, the buildup of surface charges causes an unpredictable deflection of charged particles passing nearby. Clean electrode surfaces are particularly important for particles of energy less than 100 eV and when high spatial resolution is required. All electrodes must be clean and free of hydrocarbon contamination before installation in the vacuum system. Baking the chamber will improve the vacuum quality as well as electrode surface conductivity. Electrode surface quality and stability are often improved by a coating of carbon black. These techniques were followed for

the e, 2e experimental setup.

The very important factor in the instrumentation is to choose the right material for constructing the experimental chamber, electrodes, electrical shielding, wiring etc. Stainless steel is widely used for chamber making because it has the advantage of being bakeable, strong, and easy to machine. The materials used to construct electrode elements must be such that the equipotential surfaces near the electrodes faithfully follow the contours of the electrode surfaces. The refractory metals such as tungsten, tantalum, molybdenum, and oxygen free high conductivity copper are probably the best electrode materials. These metals have a low and uniform surface potential, do not oxidize at ordinary temperatures, and are also bakeable. Electrodes and other electric lenses must be mounted on non-conducting materials. Glass, ceramic, mica and Teflon are the best option for this purpose.

In the coming sections, the principle of operation of the spectrometers widely used in electron and ion spectroscopy will be discussed. As a detailed discussion of the many types of mass/energy analyzers that have been developed is beyond the scope of this thesis, the principles of operation of a few representative electron and ion analyzers will only be described.

3.2 Electron Spectrometers

The main purpose of electron spectrometers is to separate free electrons according to their kinetic energy and to record their energy distribution (i.e. to record the number of electrons having a certain kinetic energy). Additionally, other parameters like electron angular distribution or the electron spin can also be recorded. The main goal in designing electron spectrometers is to achieve high energy resolution (the minimum energy difference between two electrons which can be separated) and high transmission (the effective electron collection by the spectrometer). However, these two contradict each other; increasing the transmission of the spectrometer leading to lower energy resolution and vice versa. Practical spectrometer designs compromise between these requirements, depending on the specific application. In electron energy analyzers, the electrons with different energy

follow a different path and can be separated in space. The path separation is achieved using the Lorentz force,

$$\vec{F} = e\vec{E} + (e\vec{v} \times \vec{B}), \quad (3.1)$$

where e is the charge of the electron, E is the electric field vector, v is the velocity of the electron and B is the magnetic field vector. Depending on the type of analyzer, one can obtain the energy distribution, the mass distribution or both. In practice, it is sufficient to use only either electric or magnetic field analyzers and only in some rare cases, both fields are used simultaneously. In the present work, electrostatic analyzers are used since the trajectory of primary (projectile), secondary electron should not be affected by the magnetic field. So in the section below, discussing the familiar electrostatic analyzers common in electron spectrometry have been discussed.

3.2.1 Retarding Field Energy Analyzer

The most commonly used energy analyzer is the retarding field energy analyzer (RFEA) also known as retarding potential energy analyzer (RPEA) or multi-grid analyzer, where the kinetic energy of the particles is deduced from the height of a potential barrier that they can just surmount with a series of grids used to select particles having a given charge sign and to analyse the energy distribution of these particles. Depending on the grid biasing, the analyzer using (at least) three grids and a collector can be configured to measure either ions or electrons [112–114]. A typical design of the RFEA is shown in Figure 3.1.

The current at the collector is the integrated current of particles whose energy exceeds the potential established by the grid. As the grid potential is reduced from that at which all current is cut off, the collector current increases. To obtain the energy distribution, the integrated current as a function of retarding potential must be differentiated. One drawback of this method is that only the component of velocity normal to the retarding grid is selected. There are also a number of practical difficulties. The ratio of the initial energy to the energy at the potential barrier varies rapidly for particles near the threshold for penetrating the retarding barrier. This gives rise to rapidly varying focusing effects

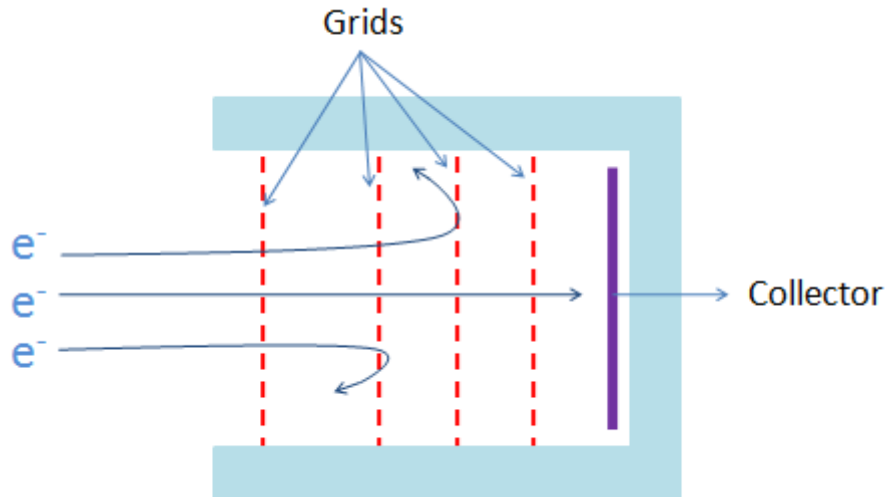


Figure 3.1: Schematic of an RFEA

near the threshold so that the particles approaching slightly off axis are often deflected away from the collector. As a result, the transmission of the analyzer is unpredictable near the threshold. Another problem with retarding potential analyzers is that the low-energy particles near the retarding grid are seriously affected by space charge and by stray electric and magnetic fields. These analyzers are very easy to construct and are very compact, but the vagaries of their performance suggest that their use for high-resolution energy analysis be avoided if possible.

The deflection of the charged particle in an electric or magnetic field can be recorded as a function of the particle energy per unit charge, or momentum per unit charge. These are called energy dispersive analyzers, which offers much more effective performance when compared to RPEA. Parallel plate analyzer (PPA), cylindrical mirror analyzer (CMA), a hemispherical analyzer (HDA) are the examples for dispersive energy analyzers.

3.2.2 Parallel Plate Analyzer

A PPA is one of the simplest electrostatic analyzers which employ a uniform field created by placing a potential difference across a pair of plane-parallel plates, as shown in Figure 3.2 with slits for allowing particles to enter and exit [115].

The separation of electrons with different kinetic energy is achieved in a static electric field ε between two parallel plates as shown in Figure 3.2. The Lorentz force acts along

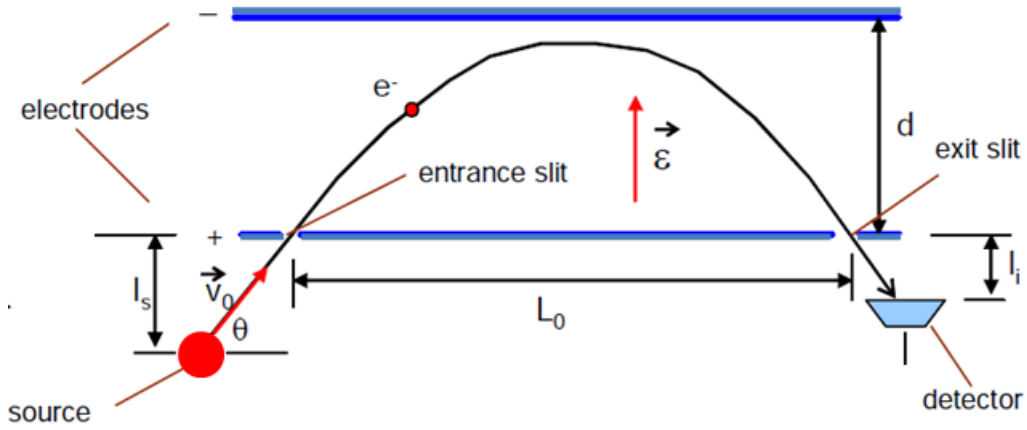


Figure 3.2: Parallel plate analyzer schematic with electron trajectory

the y-axis giving the acceleration $a = \frac{eE}{m}$. The velocity along the x-axis is constant. The electron follows a parabolic path between the plates,

$$y = -\frac{a}{2v_0 \cos^2 \theta} x^2 + \tan \theta, \quad (3.2)$$

here, v_0 is the initial velocity at the angle θ from the x-axis. The distance travelled between the plates along the x-axis is $x = tv_0 \cos \theta$. After calculating the flight time t , the distance L_0 can be obtained.

The deflection potential V_d (V), in relation to the incident energy E (eV), the plate spacing d , and the slit separation L is given by

$$V_d = \left(\frac{E}{q}\right) \frac{2d}{L}, \quad (3.3)$$

and the energy resolution is,

$$\frac{\Delta E}{E} = \frac{w}{L} + (\Delta\alpha)^2 + \frac{1}{2}(\Delta\beta)^2, \quad (3.4)$$

where w is the entrance and exit slit width, α is the angle in the plane of deflection and β is the angle in the perpendicular plane of deflection.

Although the parallel plate is an attractive design because of its simple geometry, there are several problems. The entrance apertures or slits in the front plate are at the

boundary of a strong field and hence act as lenses to produce unwanted aberrations. This problem can be alleviated for the design with the energy-resolving slits in a field-free region by placing a fine wire mesh over these entrance apertures to mend the field. A large electrical potential must be applied to the back plate, creating a strong electrostatic field outside the analyzer. The apparatus in which the analyzer is installed must often be shielded from this field. In addition, as the gap between the plates is large, the fringing field at the edges of the plates can penetrate into the deflection region. This problem can be solved by extending the edges of the plate well beyond the deflection region, or by placing compensating electrodes at the edges of the gap.

3.2.3 Cylindrical Analyzer

There are two types of cylindrical analyzer (i) cylindrical sector analyzer (ii) cylindrical mirror analyzer

Cylindrical Sector Analyzer

The cylindrical sector analyzer (CSA) consists of a pair of curved plates (as shown in Figure 3.3), such that the electric field is radial [116]. It is designed with the electric field E perpendicular to V so that the energy of the particles remains constant. Particles are injected midway between the electrodes in a direction approximately tangent to the circular arc of radius R_0 .

Assuming a charged particle that originates at ground potential with essentially no kinetic energy, and a mean pass energy $E = -qV$ (the energy of the particle that travels along the central path of radius R_0), the potentials to be applied to the outer (R_2) and inner (R_1) cylindrical elements are:

$$V_{outer} = V\left(1 - 2\ln\frac{R_2}{R_0}\right), \quad (3.5)$$

$$V_{inner} = V\left(1 - 2\ln\frac{R_1}{R_0}\right), \quad (3.6)$$

The energy resolution of CSA is,

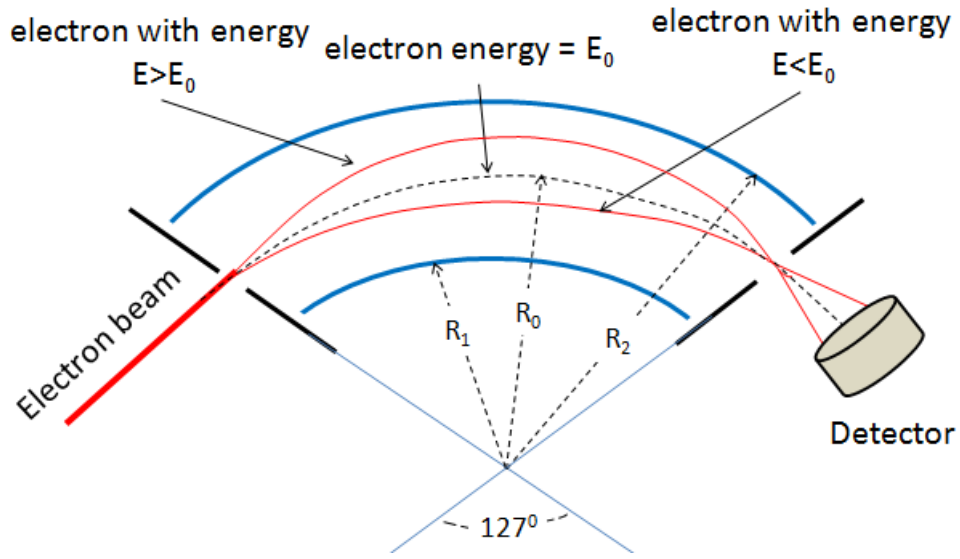


Figure 3.3: 127° Cylindrical sector analyzer schematic

$$\frac{\Delta E}{E} = \frac{w}{R_0 + \frac{2}{3}(\Delta\alpha)^2 + \frac{1}{2}(\Delta\beta)^2}, \quad (3.7)$$

where w is the slit width, α is the angle in the plane of deflection and β is the angle in the perpendicular plane of deflection.

Cylindrical Mirror Analyzer

The cylindrical-mirror analyzer is similar to the parallel plate analyzer except that the deflection plates are coaxial cylinders (2D projection of CMA is shown in Figure 3.4). This analyzer is symmetrical around the z -axis, which means that the charged particle in a cone can be focused on the same spot, which in turns gives the space focusing. An obvious advantage of this analyzer is that particles at any azimuthal angle can be collected [117].

For optimum performance the entry angle $\alpha = 42.3^\circ$, in which case the distance from the source to detector is $L = 6.12r_1$. The inner cylindrical plate is at the same potential as the source, and the potential on the outer cylinder, relative to the inner cylinder, is

$$V_{outer} = 0.763 \left(\frac{E}{q} \ln \left(\frac{r_2}{r_1} \right) \right) \quad (3.8)$$

The resolution of the axial-focusing cylindrical mirror analyzer is,

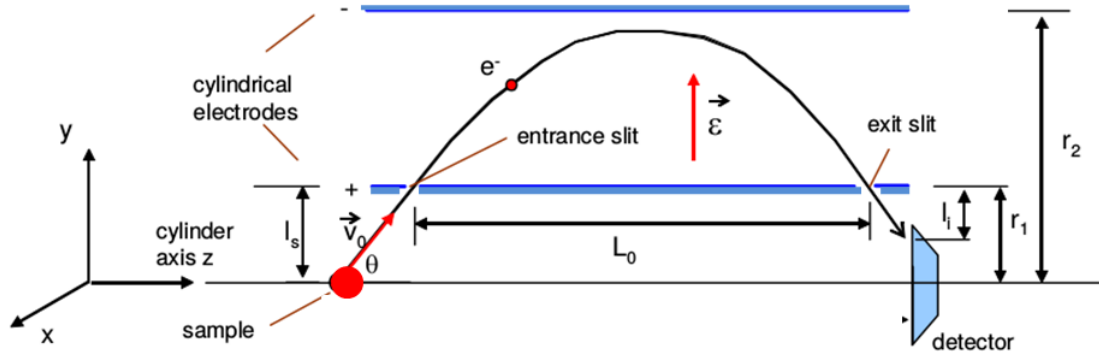


Figure 3.4: Cylindrical mirror analyzer schematic

$$\frac{\Delta E}{E} = 1.09\left(\frac{w}{L}\right), \quad (3.9)$$

for a source of axial extent w and an energy-resolving aperture of diameter $w' = w \sin \alpha$ perpendicular to the axis. Moreover, if the source is not small and well-defined, the entry and exit slots in the inner cylinder can be used to define the resolution of the cylindrical mirror analyzer.

3.2.4 Hemispherical Analyzer

A hemispherical analyzer is a type of dispersive analyzer, where the deflecting electric field is created between two half-spheres with a common center (as shown in Figure 3.5). As with the cylindrical mirror, the spherical analyzer can also be used to collect all particles emitted from a point source at or near a particular polar angle.

Assuming a charged particle that originates at ground potential with essentially no kinetic energy, and a mean pass energy $E = -qV$ (the energy of the particle that travels along the central path of radius r_0), the potential to be applied to the outer and inner spherical elements are

$$V_{outer} = V\left(2\frac{r_0}{r_2} - 1\right) \quad (3.10)$$

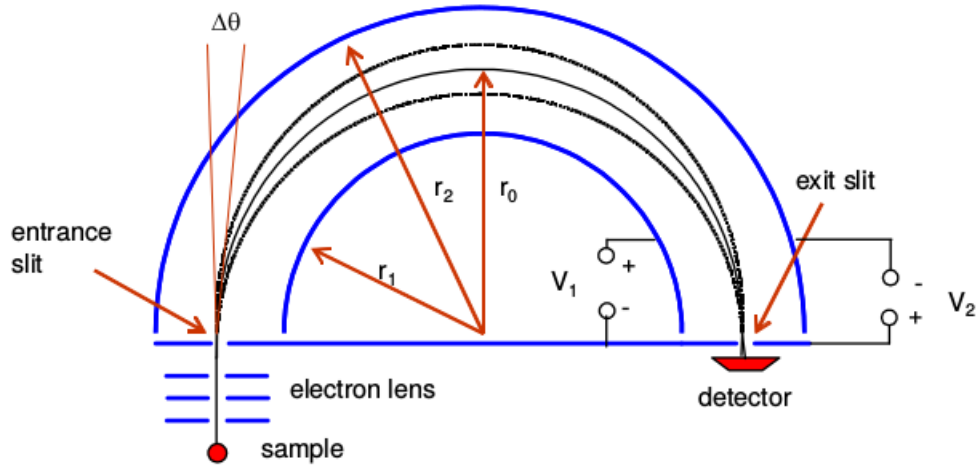


Figure 3.5: 2D schematic view of hemispherical analyzer

$$V_{inner} = V \left(2 \frac{r_0}{r_1} - 1 \right) \quad (3.11)$$

where r_1 and r_2 are the radius of inner and outer spheres, respectively

The resolution of the 180° spherical sectors is,

$$\frac{\Delta E}{E} = \frac{w}{2r_0} + \frac{1}{2}(\Delta\alpha)^2 \quad (3.12)$$

where w is the slit width, α is the angle in the plane of deflection and β is the angle in the perpendicular plane of deflection.

In comparison with the parallel-plate or cylindrical mirror analyzers, the spherical analyzer has the advantage of requiring relatively low electrical potentials on the electrodes. Because the electrodes are closely spaced in the spherical analyzer, fringing fields are less of a problem and more easily controlled. The chief drawback of this type of analyzer is the difficulty of fabrication and mounting, and more importantly the collection efficiency.

3.2.5 Toroidal Analyzer

In the toroidal electron analyzer, the electrons in a certain energy range traverse the gap between the toroidal sectors, where they will be deflected and dispersed at the exit as shown in Figure 3.6 [118] ensuring the parallel-to-point focusing in the axial plane which

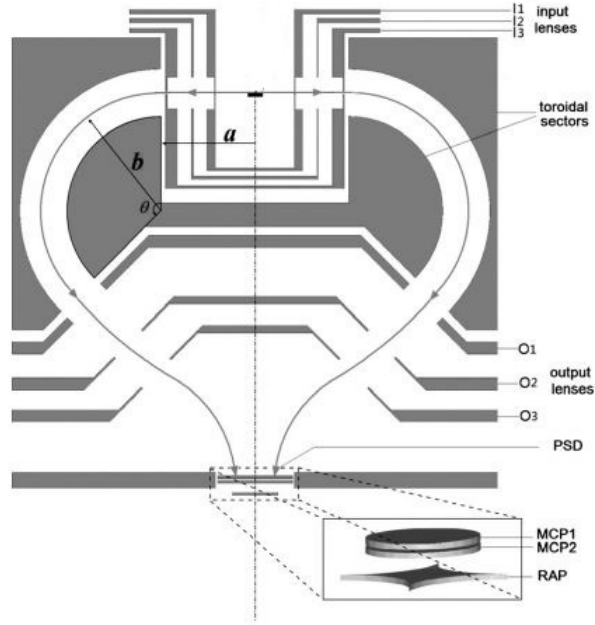


Figure 3.6: Double toroidal analyzer schematic with detector

is perpendicular to the central axis [119]. The potential applied to the inner and outer toroidal sectors could be expressed as

$$V_{r_1, r_2} = \frac{2V_p}{\pi a} (\pi a + 2b) \left[\ln \frac{b(2r_{1,2} + \pi a)}{r_{1,2}(2b + \pi a)} \right] \quad (3.13)$$

where cylindrical radius a (as shown in Figure 3.6) and r_1 , r_2 are the spherical radii of the inner and outer toroidal surfaces, respectively. The zero potential is chosen to lie on the central path of the radius $b = \frac{(r_1 + r_2)}{2}$.

Toroidal electron spectrometer has high resolution and efficiency compared to conventional electron spectrometers, but it adds the complexity of fabrication.

3.2.6 Time-of-Flight Energy Analyzer

In a time of flight electron analyzer, the electrons with different energy are not separated in space, but in time. All electrons follow the same flight path, but more energetic electrons arrive at the detector before those electrons which are having comparatively less energy.

The instrument contains a retardation/acceleration region, where the initial kinetic en-

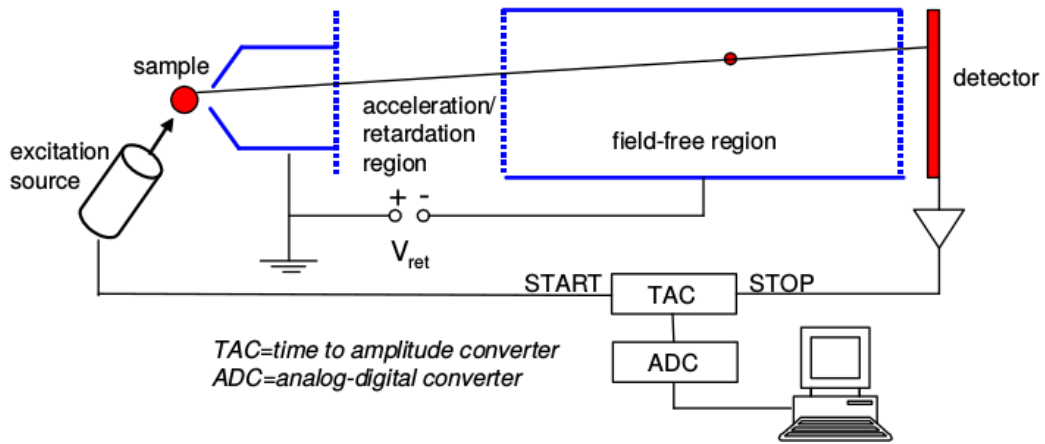


Figure 3.7: Time of flight energy analyzer with pulse processing and data acquisition schematic

ergy of the electrons are shifted so that the flight time falls into the time measurement range of the instrument (Figure 3.7). Typically, fast electrons are decelerated before entering the field-free drift tube, a long tube where electrons with different velocity become sufficiently separated in time before reaching the detector. For an electron with an energy E_k after deceleration/acceleration, the flight time to the detector is,

$$t = L \sqrt{\frac{m}{2E_k}} \quad (3.14)$$

where L is the length of the field free drift tube. For example, for $E_k = 10$ eV and $L=100$ mm, $t \approx 50ns$.

The flight time is measured electronically, using the ionization event as the START pulse and the electron's arrival at the detector as STOP. The ionization source must operate in a pulsed mode so that the electrons produced by one pulse have time to reach the detector before the next ionization pulse. The time and energy resolution of the ToF analyzers depends on the time spread of electrons that follow a different flight path to the detector, the duration of the ionization pulse and on the accuracy of the time measurement electronics.

ToF analyzers are relatively simple and have a high transmission. Moreover, it has the ability to detect electrons over a broad energy range simultaneously. But in ToF analyzers it is difficult to achieve as high resolution as with dispersive analyzers and it requires

pulsed mode sources. Conversion from ToF spectrum to the energy spectrum is non-linear, and the energy resolution is not constant across the spectrum.

3.3 Ion Spectrometers

In ion mass spectroscopy, the mass to charge ratio of the ions is determined, which allows in determining the chemical composition of the sample, and also a number of additional properties such as the kinetic energy distribution, the angular distribution and the correlation with other particles that originate from the same ionization event. Three main categories of modern ion mass spectrometers exist (i) magnetic sector analyzers (ii) quadrupole mass analyzers (iii) time-of-flight analyzers.

3.3.1 Magnetic Sector Analyzer

In a magnetic deflection mass spectrometer, ions leaving the ion source are accelerated to a high velocity. The ions then pass through a magnetic sector in which the magnetic field is applied in a direction perpendicular to the direction of ion motion. When acceleration is applied perpendicular to the direction of motion of an object, the object's speed remains constant, but the object travels in a circular path. Therefore, the magnetic sector follows an arc; the radius and angle of the arc vary with different ion optical designs.

The ions enter the magnetic field with B perpendicular to their velocity. While in the constant magnetic field, the ions follow a circular path with radius r_0 so that, the mass by charge ratio is given as,

$$\frac{m}{q} = \frac{B^2 r_0^2}{2V} \quad (3.15)$$

In order to obtain a spectrum over a range of m/q values, either voltage V in the acceleration region or magnetic field strength B must be scanned. According to the spatial focusing properties of the equipment, there are single focusing analyzers, where a circular beam path of 180, 90, or 60 degrees can be used, and double focusing analyzers, where an electrostatic analyzer is added to separate particles with the difference in kinetic ener-

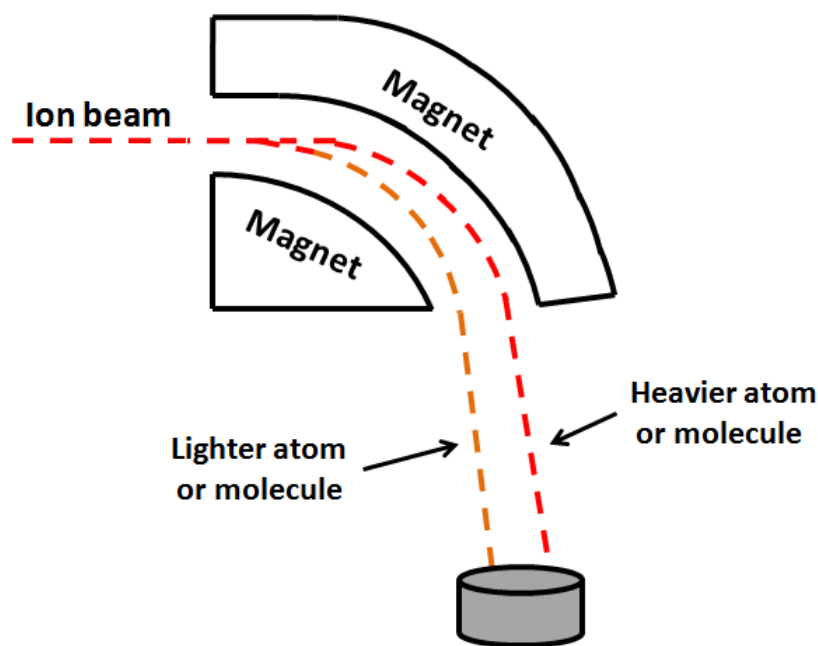


Figure 3.8: Principal components of a magnetic sector ion mass analyzer

gies. In a single-focusing magnetic sector instrument, there is a lack of uniformity in ion energies, since the accelerating potential experienced by an ion depends on the region at which it is formed in the ionization chamber.

3.3.2 Quadrupole Mass Analyzer

A quadrupole field is formed by four electrically conducting parallel rods, as shown in Figure 3.9 [120]. Opposite pair of electrodes is electrically connected. One diagonally opposite pair of rods is held at $+U_{dc}$ volts and the other pair at $-U_{dc}$ volts. An RF voltage supplies a signal $(+V \cos \omega t)$ to the first pair of rods and $(-V \cos \omega t)$ to the second pair of rods, which appear as oscillating hyperbolic potentials between the four rods [120]. Ions from the ion source are injected into the quadrupole through a circular aperture. As the ions move down the quadrupole, they undergo transverse motion in X-Y planes.

The applied voltages affect the trajectory of ions traveling down the flight path centered between the four rods. For a given DC/AC voltage, only those ions of a certain mass-to-charge ratio pass through the quadrupole filter, and all the other ions are thrown out of their original path. A mass spectrum is obtained by monitoring the ions passing

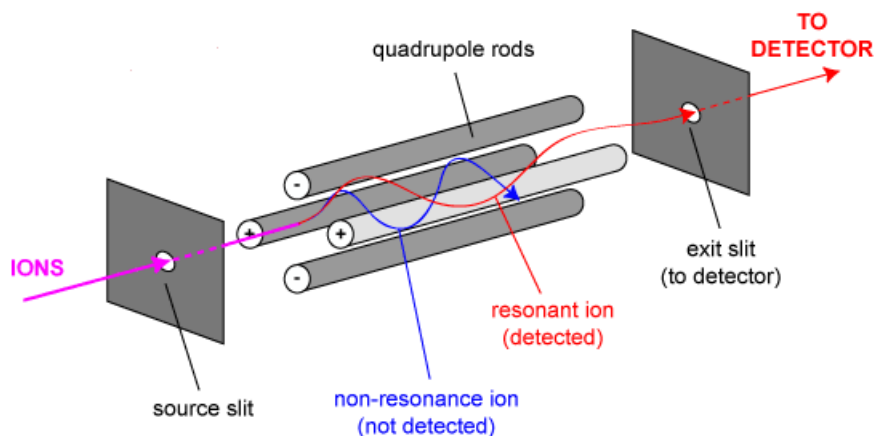


Figure 3.9: Schematic of quadrupole mass analyzer

through the quadrupole filter as the voltages on the rods are varied. There are two methods: varying ω and holding U and V constant, or varying U and V fixed for a constant ω .

3.3.3 Time-of-Flight Mass Spectrometer

Time-of-flight mass spectrometer (ToFMS) is one of the simplest mass analyzing devices, which separates ions after their initial acceleration by uniform electric fields, according to their velocities when they drift in a field-free region (as shown in Figure 3.10). The time differences resulting from the initial spatial distribution of the ions along the axis of the flight tube is commonly minimized by incorporating the two field acceleration geometry and space focusing principles introduced by Wiley and McLaren [67]. The focus condition given by Wiley and McLaren makes the flight time of ions independent of their generating points in the ionization region to first order. Two main modes of operation of ion ToF analyzers are the constant extraction field mode and pulsed extraction field mode. In the constant field mode, all voltages applied to the instrument are kept constant. The ion extraction starts at the moment it is created. The electric field strength in the extraction region should be sufficient to direct all the created ions into the acceleration region before they leave the extraction region. Whereas, in the pulsed mode, during the interaction, the extraction field will not be present. Immediate after the ion formation, with the help of fast response, switch the interaction field will be applied and extract the ions to the acceleration region before they drift in the field free interaction region. This

requires additional complexity in the instrument.

The primary information to be obtained from the ion ToF spectra is the mass/charge ratio of the ions. The kinetic energy of the ions can be obtained in some instruments with additional hardware. The velocity of positive ions is typically much smaller than that of electrons. To obtain the mass resolved ToF spectra, ions must first be extracted from the sample region and then accelerated before entering the field-free drift region.

In order to measure the flight time, the moment of the ion detection must be determined with respect to the ion creation. One possibility is to use a pulsed ionization source. Since electrons travel much faster than ions, these pulses correspond closely to the time of possible ionization events and can be used as a START pulse for the timing electronics. The STOP pulse or pulses are obtained, as usual, from the ion detector. The second possibility is also to detect the electrons from the ionization events to perform coincidence measurements. For this, an electron detector is placed at the opposite side of the extraction region. Again, since the electron flight time is much shorter than the ion flight time, the detected electrons provide a suitable START pulse for the ion ToF measurement. To derive the flight time of ions, consider an ion created in interaction region having charge q and mass m with initial energy U_0 and increases to U when it accelerates.

$$U = U_0 + qsE_s + qdE_d \quad (3.16)$$

and time-of-flight,

$$T(U_0, s) = T_s + T_d + T_D, \quad (3.17)$$

$$T_s = \frac{\sqrt{2m[U_0 + qE_s]} \pm \sqrt{2mU_0}}{qE_s}, \quad (3.18)$$

$$T_d = \frac{\sqrt{2mU}}{qE_d} - \frac{\sqrt{2m[U_0 + qE_s s]}}{qE_d}, \quad (3.19)$$

$$T_D = \frac{D}{2} \sqrt{\frac{2m}{U_0 + qE_d}}, \quad (3.20)$$

where, T_s , T_d and T_D is the time-of-flight in interaction region, extraction region and

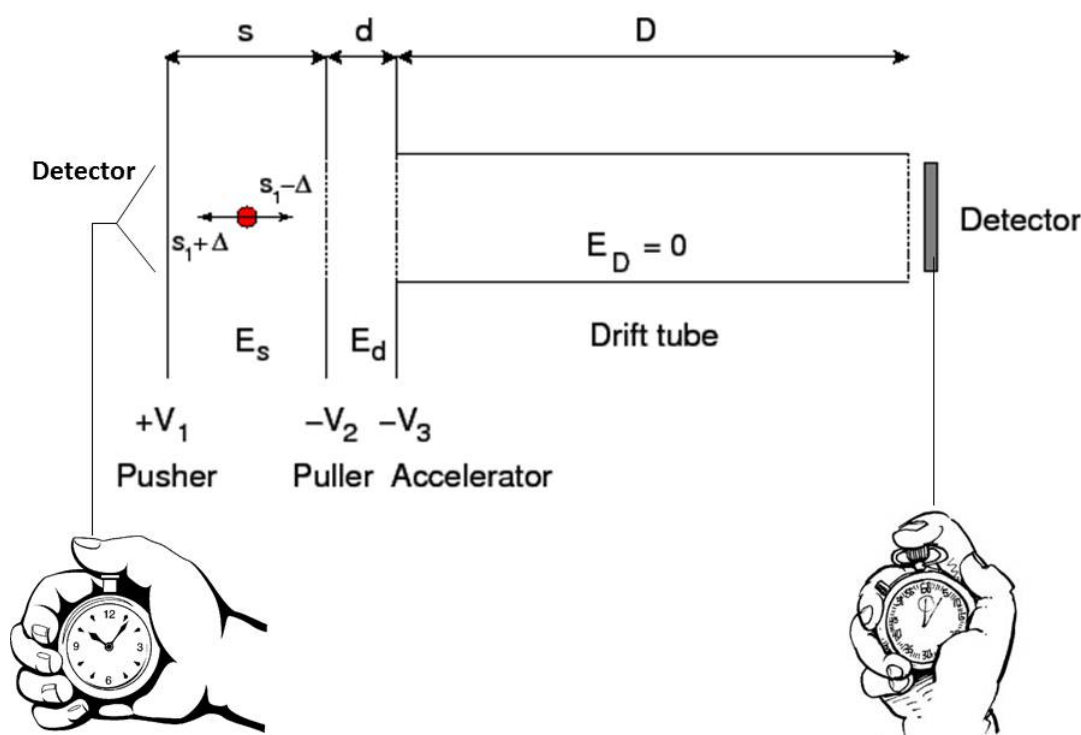


Figure 3.10: Layout of a Wiley-McLaren type ion ToF analyzer

drift tube respectively. The \pm sign in T_s corresponds to initial velocity directed respectively away from and towards the extraction field. This equation is the general flight time equation in which most of the experimental quantity such as D , s , d , E_s and E_d are known.

3.3.4 Reflectron Time-of-Flight Mass Spectrometer

In order to achieve very high mass resolution, the time spread due to the kinetic energy of the ions must be eliminated, in addition to the space focusing. Wiley-McLaren geometry is correct for these parameters only to first order. This second order correction can be achieved by using a reflection of ions. In reflectron, the drift region is separated into two parts, with a reflection region in between. The electric field between the grids in the reflection region is chosen to stop the ions and eventually accelerate them backward to the same kinetic energy, as shown in Figure 3.11. In the usual "linear" ToF, ions with initial velocity towards the acceleration region (and the detector) arrive earlier. In reflectron ToF,

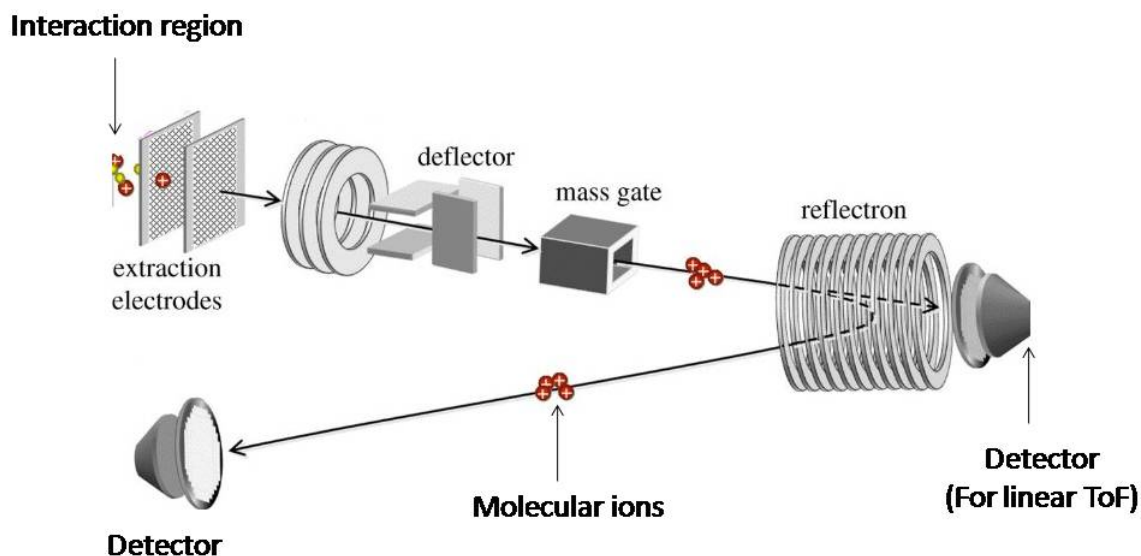


Figure 3.11: Principle of reflectron mass analyzer

these ions penetrate further into the reflection region (between U_F and U_R) and thus their total flight path increases.

Ions with initial velocity away from the acceleration region have slightly less kinetic energy when arriving at the reflection region and are "turned back" at an earlier point, thus their flight path is shorter. The differences in the flight path can be used to compensate for the different velocities at which the ions travel. For calculating the reflection voltages needed for the exact compensation of the initial kinetic energy effects, the following equation can be used,

$$t_R = \frac{2d_R}{U_R - U_F} \sqrt{\frac{2qE_k}{m}}, \quad (3.21)$$

where, t_R is the time spent in the reflection region, d_R is the length of the reflection region and E_k is the exact kinetic energy of the ions. For two ions with kinetic energies E_{k1} and E_{k2} the time difference $t_{R1} - t_{R2}$ must be equal to $t_{D2} - t_{D1}$, where t_D is the

flight time in the drift region.

3.4 Detection Systems

Once the electron energy and ion mass selection are performed with the help of spectrometers, one needs to detect these particles. In this section, the details of the detection techniques used in spectroscopy will be discussed. For particle energies up to a few tens of keV, a stream of charged particles of sufficient intensity can be collected and measured directly as an electrical current. Charged particles can also be detected with photographic emulsions, scintillators, and various solid-state devices. For the charged particle detection, there are two ways of detection (i) the particles can be collected at a metal surface and the resultant electrical current measured directly (ii) they can be detected by collecting the slower secondary electrons that are ejected from a metal surface by impact of the primary particle. Here few major detectors in use for electron/ion detection are described.

3.4.1 Faraday Cup

The collector for the direct detection of a current of a charged particle is called a Faraday cup (FC) (Figure 3.12). The electric current of the FC is dependent on the incident particle beam current. These simple collectors are connected directly to a current-measuring device and are useful at currents down to the detection limits of modern electrometers about 10^{-14} A. In the case of ion beam or high-energy electron beam detection, care must be taken because backscattered and secondary electrons may be ejected from the interior surface of the cup when the charged particles strike. These electrons may escape from the FC aperture. This results in the current overestimation for positively charged particle beams and current underestimation for electrons and other negative charged particle beams from the true values of current. To prevent the escape of secondary electrons, the depth of a Faraday cup should be at least five times its diameter. A suppressor aperture or grid biased to about -30 V in front of a Faraday cup effectively prevents the escape of most secondary electrons. The Faraday cup is a direct current measurement detector and relatively insensitive but, very robust.

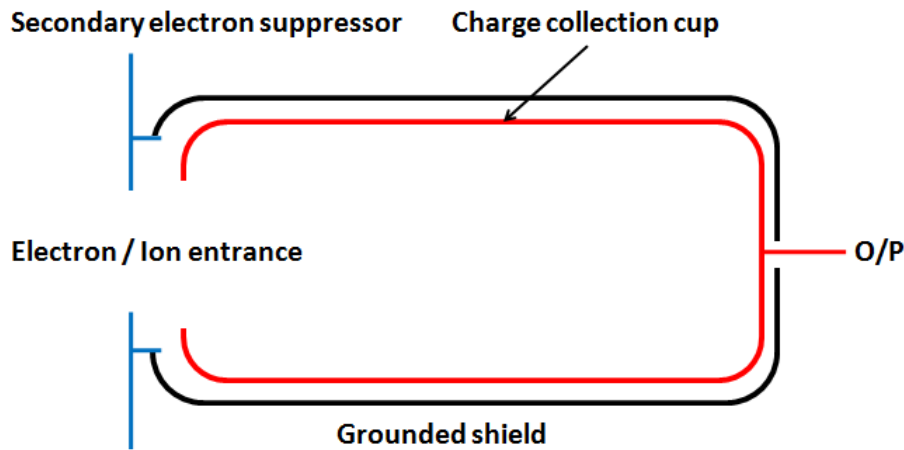


Figure 3.12: Faraday cup with secondary electron suppressor

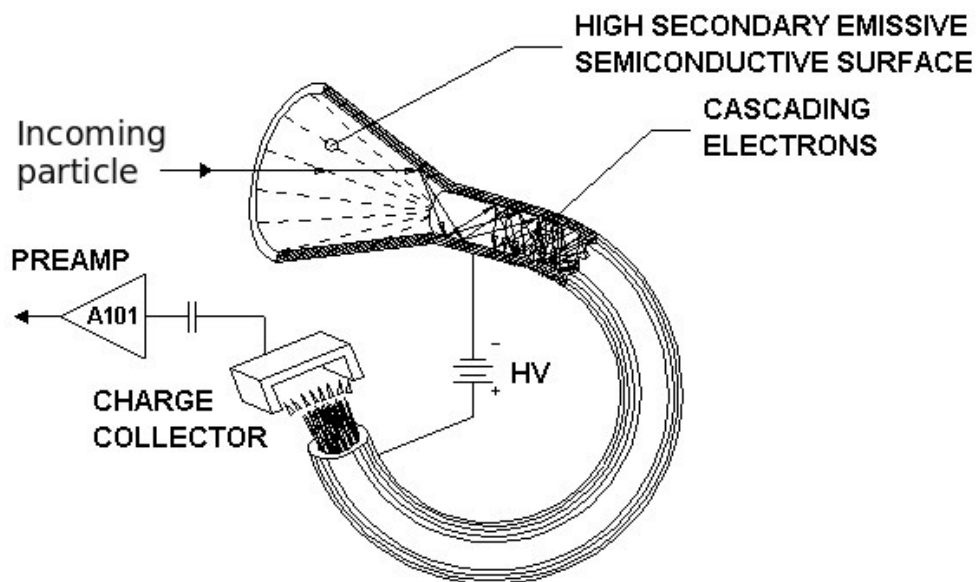
3.4.2 Channel Electron Multiplier

A channel electron multiplier/channeltron (CEM) has a high surface resistance which forms a continuous dynode (as in Figure 3.13a) when a potential is applied between the input and output end of the CEM [121]. Dynode has the property of emitting secondary electrons when primary particles impinge upon it (Figure 3.13b).

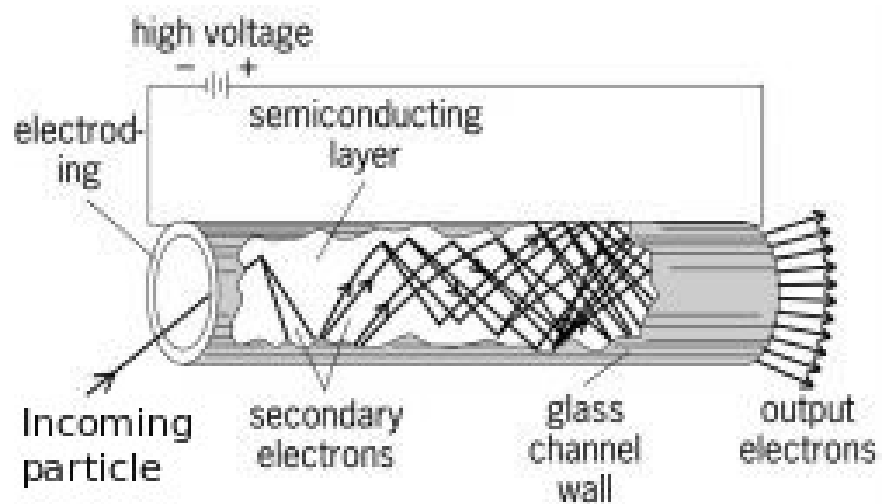
When a charged particle or photon strikes the input aperture of the channeltron, it produces secondary electrons, and these electrons are accelerated down the channel by a positive bias. The electrons strike the channel walls, producing additional electrons (and so on) from the surface with multiple collision, and amplifies the electrons to $10^6 - 10^8$ times. Biasing of the CEM depends upon the amplification and operation voltage threshold. Typically for detection of positive ions, the input is at a negative potential of 1200 to 3000 volts and the output is on the ground. For detection of negative ions, the input is generally on the ground or some positive potential, and the output is at a high positive voltage. The standard CEMs are capable of detecting a maximum of 5 million particles per second.

3.4.3 Microchannel Plate Detector

Microchannel plate detector (MCP) is a two-dimensional periodic array of very-small diameter glass capillaries (channels) fused together and sliced in a thin plate that amplifies



(a)



(b)

Figure 3.13: Channel electron multiplier (a) Schematic (b) Dynode working principle

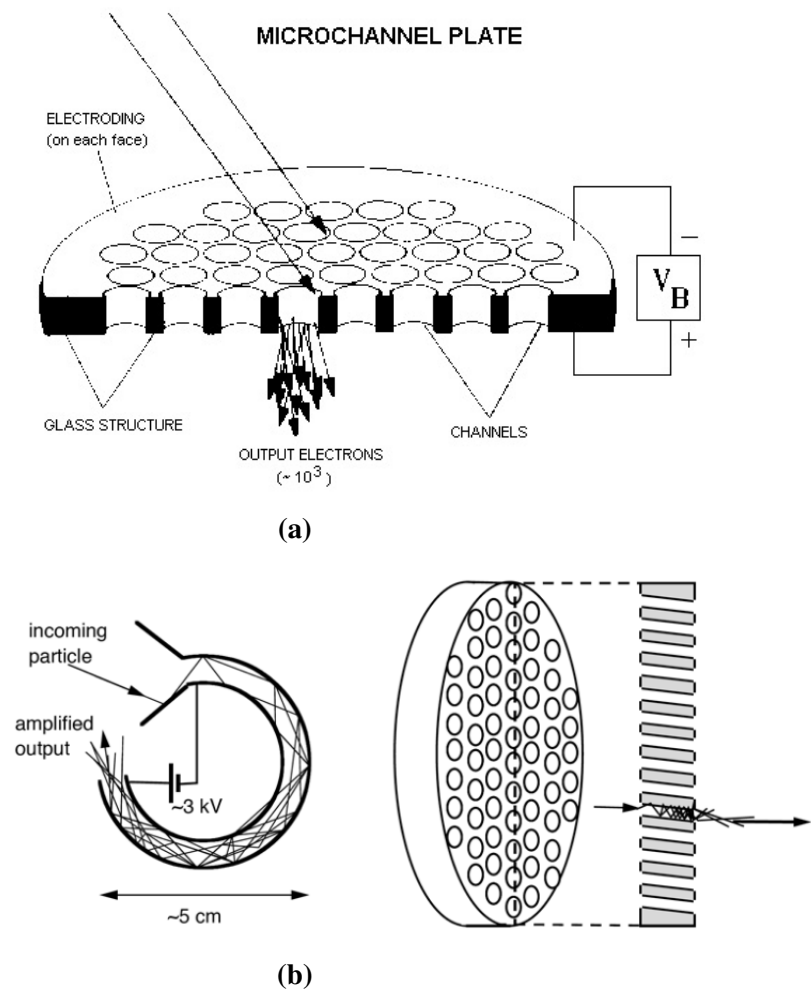


Figure 3.14: Microchannel plate detector (a) Schematic of MCP assembled (b) Dynode with potential working principle

electron signal similar to CEM. One can consider MCP as an assembly of millions of miniature CEMs in micron scale (Figure 3.14)

An incident particle (ion, electron, photon etc.) enters a channel and emits an electron from the channel wall. Secondary electrons are accelerated by an electric field developed by a voltage applied across both the ends of the MCP. These electrons travel along their parabolic trajectories until they, in turn, strike the channel surface, thus producing more secondary electrons. This process is repeated many times along the channel; as a result, this cascade process yields a cloud of several thousand electrons, which emerge from the rear of the plate. The efficiency of MCP for various kinds of particle detection has been discussed in detail by Wiza *et al.* [122]. Generally, two or more MCPs are operated in series and for a single particle hit it can generate a pulse of 10^8 or more electrons at the

output. The output signals are typically collected in any of several ways, including metal or multi-metal anodes, the resistive anode (1D or 2D), wedge and strip anode, delay line anode or on a phosphor screen deposited on a fiber-optic or other substrate. Microchannel plates have a combination of unique properties like high gain, high spatial resolution, and high temporal resolution. They can be used in a large variety of applications including, imaging spectroscopy, electron spectroscopy, and electron microscopy, mass spectrometry, astronomy, molecular and atomic collision studies, cluster physics etc.

3.4.4 Position Readout

By using microchannel plate detector it is possible to get the position information (imaging) of charged particles by using different kinds of position enabled detection techniques like phosphorous screen, charged coupled device (CCD), the wedge and strip anode, delay line anode etc. Position encoding is achieved in the second stage, where a coordinate is assigned to the centroid of the electron cloud emerging from the back of the MCP.

CCD/CMOS Camera

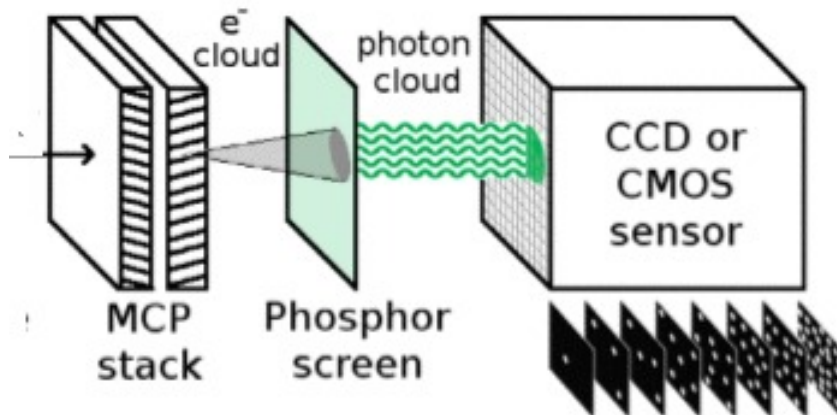


Figure 3.15: MCP detector with CCD/CMOS imaging camera

The CCD/CMOS camera detector comprises a phosphorous screen along with charged coupled device (CCD) or complementary metal-oxide-semiconductor (CMOS) camera in the back of an MCP (as shown in Figure 3.15 [123]). When the electron cloud created by the MCP falls on a semi-transparent phosphor screen, it is transformed into a localized

photon shower [124–126]. These intensified photon events are bright enough to be detected with a normal CCD or CMOS camera, and can, in fact, be observed with the naked eye. Due to the slow electronic readout of the optical image with its microsecond time resolution, it is not very useful for obtaining timing information or rapid readouts.

2D Resistive Anode Readout

Resistive anode readout consists of a square sheet of insulating material with resistivity coating and a contact at each corner. The pulse amplitudes and rise-times are proportional to the event distance from the contact, and the event location can be determined from either the charge division or the difference in the signal timing between opposing contacts [127, 128]

Quadrant Anode

In a quadrant anode, the anode is divided into quarters and placed behind the MCPs, such that for each photon/ charged particle event, part of the electron cloud hits each of the four quadrants [129]. The event position can then be calculated from relative amounts of charge collected by each quadrant (Figure 3.16). Some designs have a ring-shaped fifth anode around the detector inside to help spread out the electron cloud over the four quadrants [130–132].

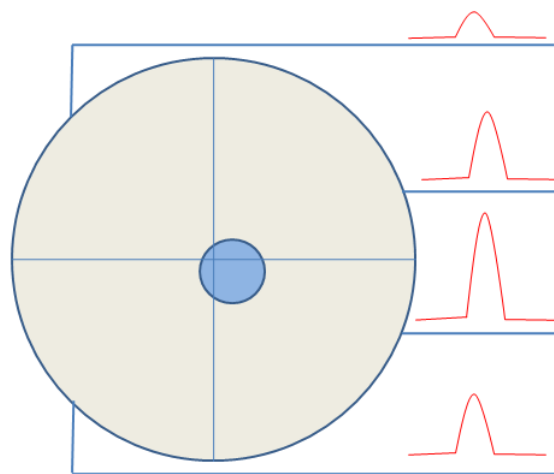


Figure 3.16: Quadrant anode, where the position is obtained from the relative charge in the four quadrants

Wedge and Strip Anode

The most common wedge and strip anode design have three electrode elements (as shown in Figure 3.17 [123]). The relative charge in the wedge is related the event position in the direction parallel to the wedges, and the strips are not of equal width and thus the charges are collected by the strip [133, 134]. The anode can be used for the calculation of the event position in the direction perpendicular to the strip. Wedge and strip anodes provide a simple but effective means of imaging through linear position dependent charge division amongst several conductive electrode elements [135].

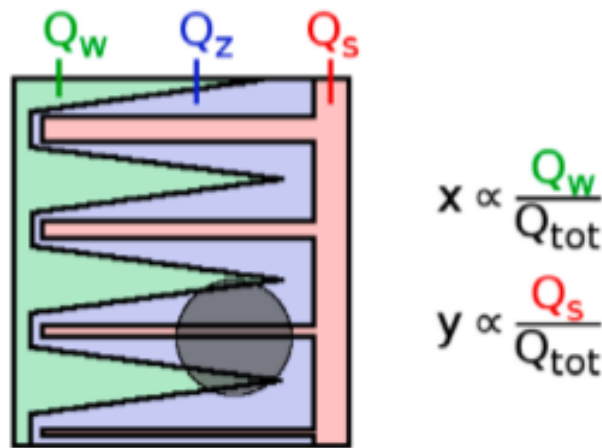


Figure 3.17: Wedge and strip detector

Delay Line Anode

A delay line anode (DLA) is a position (x , y) and time (t) sensitive microchannel plate area detector for imaging of single counted particles with or without temporal resolution in the picosecond range [136]. The anode consists basically of two meander structured delay lines (a bare copper wire wound); one rotated by 90° with respect to the other and both isolated from each other (as shown in Figure 3.18a [137]). The electron cloud from the MCP stack output is drawn to the detector anode by a positive potential difference between the anode and back side of MCP stack, where it induces electrical pulses into the delay line by capacitive coupling. The pulses are traveling to both ends of the meander within a time determined by the hitting position (Figure 3.18b [137]). The position of

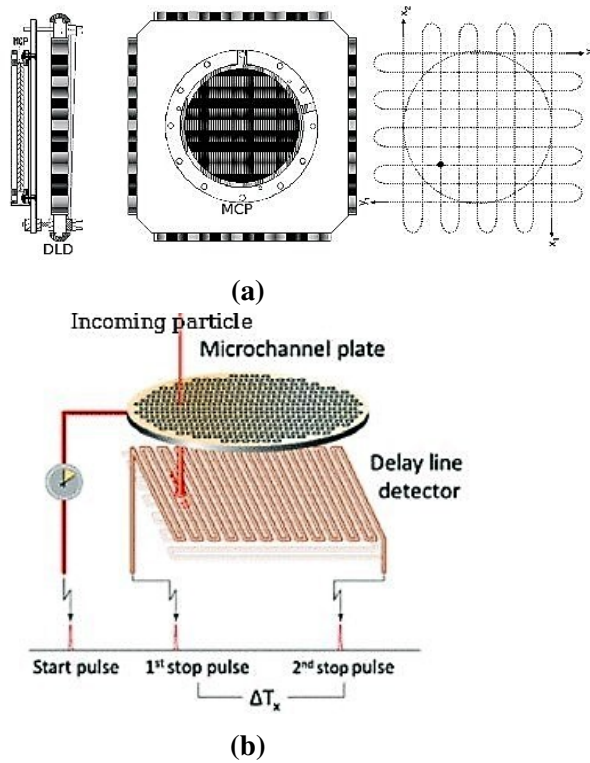


Figure 3.18: Delay line anode detector (a) Assembled with MCP (b) DLA with MCP working principle

a charge pulse is encoded by the signal arrival time differences at opposite ends of the delayline [138].

In order to determine the time difference between an outer time marker and the particle impact, the signal from MCP can be used as a reference (the time zero signal). In this way it possible to deduce the particle impact time from the delay line signals, by using the sum values,

$$\text{sumx} = x_1 + x_2 \quad (3.22)$$

$$\text{sumy} = y_1 + y_2 \quad (3.23)$$

These sum values are constant within resolution less than 1 nS.

For completing the experimental set-up for electron and ion spectroscopic studies, there are other important factors like electronics, data acquisition, data analysis etc. should be involved. These topics will be discussed in detail in the instrumentation and associated electronics for e,2e experiment section in Chapter 4.

Chapter 4

Experimental Methodology

There are three very important aspects of the coincidence experimental setup, which are to be taken care, namely, the source of excitation which in the present context is the electron beam, the electron spectrometer, and the mass spectrometer. For a multi coincidence experiment, the design and instrumentation are to be done carefully by considering the kind of processes and physics to be targeted. For instance, if one uses an electron beam as the projectile, it is important to know the energy of the beam, the electron detection system for the secondary electron, the expected mass of the ion and the resolution and efficiency of the spectrometers. Depending upon these, the design and instrumentation become very critical, particularly when one has to pulse the electron beam as well as mass extraction in a very complicated sequence. Moreover, if the experiment is targeted towards a particular type of process, it requires special considerations. In a typical electron-molecule collision, depending on the energy and momentum transfer to the target molecule below listed processes are possible,

1. $e^- + ABC \rightarrow ABC^* + e^-$ Excitation
2. $e^- + ABC \rightarrow ABC^-$ Electron capture
3. $e^- + ABC \rightarrow ABC^+ + 2e^-$ Direct ionization
4. $e^- + ABC \rightarrow AB^+ + C + 2e^-$ Dissociative ionization/Fragmentation

In this work, the 3rd and 4th processes are the target and in the 4th process, the evaporative processes due to statistical dissociation in the large molecule. The experimental setup for this kind of process requires certain considerations on the projectile beam and the type of target to be used. For example, if one is studying very light molecules and then uses a linear type of mass spectrometer for the mass analysis, the transverse momentum of the fragment or intact ion plays a very important role in deciding the size of the drift

tube [139]. Whereas, in the case of large molecules the transverse momenta are large but the velocities are small and therefore the expected displacement of the particle before hitting the detector at the end is very small. Therefore, the drift tube which is large in diameter is not necessary, and for the same reason, the ion detector need not be a position sensitive detector. The electron impact ionization (e, 2e) is a very useful technique to study the structure and dynamical properties of the molecules like PAHs and PANHs with its simplicity and economic experimental realization.

4.1 e, 2e Experiment

Electron impact ionization procedure usually produces a range of molecular fragments that in most cases, help to elucidate the structure of the molecule. However, although molecular ions are often produced, by knowing the secondary electron energy and angular distribution [140], one can understand the dynamical properties of the molecule, since these properties are related to molecular orbitals. The above listed 3rd and 4th processes, involves the production of secondary electrons and a possible ionic fragment or intact molecular ion. An experiment which uses electron impact, ideally, one should study projectile as well estimate the energy loss to the target. But due to the limitation, right now in this experiment only the secondary electron and recoil ion are measured. This instrument also has the possibility of projectile energy loss measurement once the parallel plate analyzer is assembled as per the plan. This provision will enable us to perform double and triple coincidence measurement in electron-ion coincidence experiment. In the coming section, the details of the experimental setup developed in the Atomic and Molecular Physics lab at IIST, Thiruvananthapuram has been discussed.

4.2 Simulation and Design

In combined electron-ion coincidence experiment, a constant electric field in the interaction region adds difficulty, as the secondary electrons in the low energy regions are very sensitive to the electric field. To understand the sensitivity of electric field in the inter-

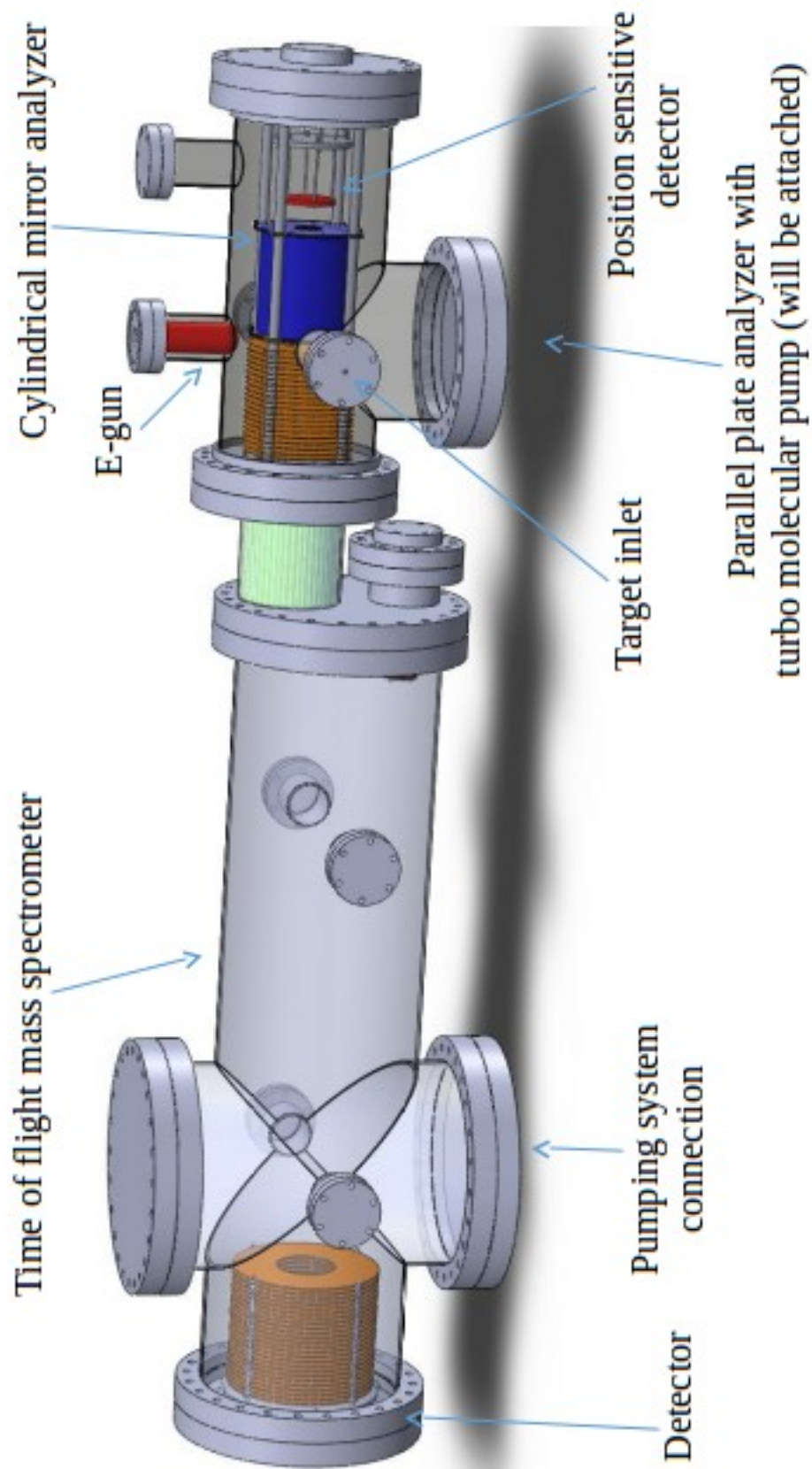


Figure 4.1: 3D view of electron-ion coincidence setup (CAD design with assembly of electron, ion spectrometer and electron gun)

action region as well as particle trajectory through the spectrometer, simulation of the spectrometers and other components were performed. The simulation of the electron gun, cylindrical mirror analyzer, parallel plate analyzer and time-of-flight mass spectrometer is done using SIMION8.0 [141] for optimized geometry as well as voltages for projectile electron beam trajectory, secondary electron energy, and ion trajectory. SIMION8.0 is a software package primarily used to calculate the electric fields and the trajectories of charged particles in those fields. It has the provision to give configuration of electrodes with voltages and particle initial conditions, including optional RF (quasi-static), magnetic field, and collisional effects. Typical electron-ion coincidence experiment is done with the constant electric field in the interaction region, but it requires correction for the projectile beam deflection as well as secondary electron energy [142]. In the electron impact experiment, pulsed extraction of an ion by using a time-varying electric field in the interaction region is used. Moreover, as the timing of the ion extraction for the corresponding electron is critical in this experiment, a complete study of the electron-ion coincidence measurement is done using SIMION8.0. The experimental setup is designed using SOLIDWORKS software package (Figure 4.1). The details of the simulation and construction are described in the following sections.

4.3 Electron Gun

The low energy (few eV) electron gun introduces the complexity in design and operation since it is very sensitive to the stray electric and magnetic field. But for the energy range of few hundreds of eVs to KeVs, it is easy to steer the beam even though it has its own complexity. An electron gun is made by using the emitter section of cathode ray tube (CRT) of a black and white television unit has been used as part of this work. A CRT normally uses magnetic steering, but such a steering is not practical in this experiment since it will affect the secondary electron. Therefore, electrostatic deflectors for the beam steering is used. The electron optics of the electron gun was simulated and optimized using simulation program SIMION8.0 (Figure 4.2). The different operation mode of the gun, namely, afocal, broad, and zoom beam mode, can be accommodated by adjusting various potentials. Separate deflection and beam shaping electrodes are constructed by

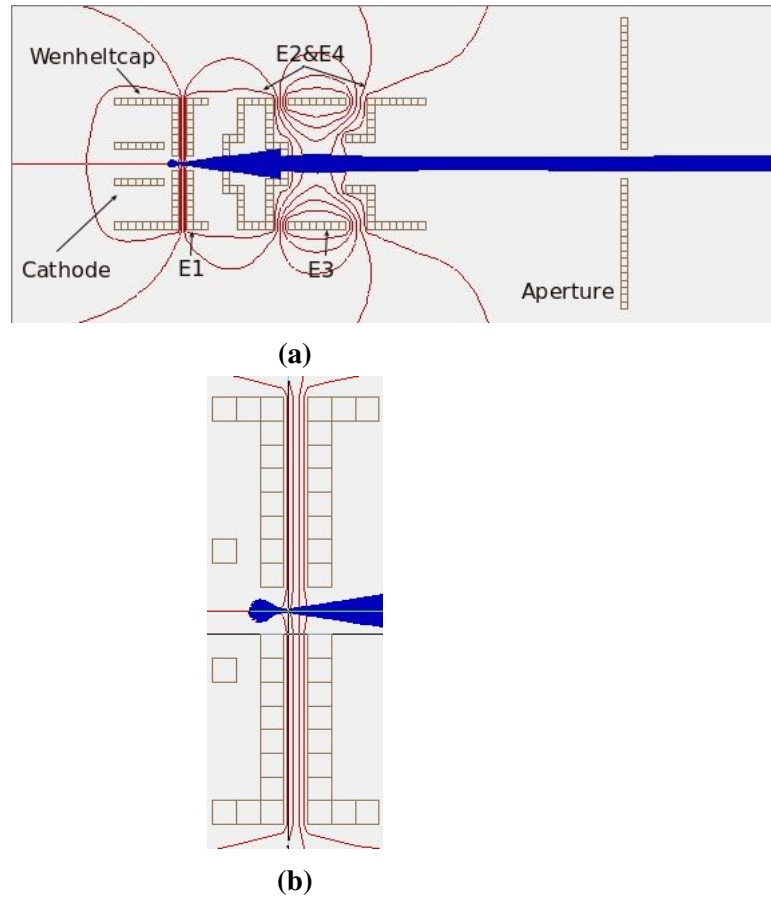


Figure 4.2: Electron gun simulation (a) Trajectory of electron beam (b) Beam source region (Red colour: Electric fields lines, Blue colour: Electron trajectory)

understanding the geometrical parameters from the simulation. The electrostatic focusing of the electron beam is achieved by applying suitable voltages to the lens elements. The indirectly heated cathode is housed in the grid element and both this element and the outer case of the filament are held at a negative potential so that the emitted electrons are accelerated towards the anode electrode. Since the final element on the Einzel lens is held at ground potential, the voltage applied to cathode element determines the energy of the electron beam. When dealing with high energy electron beam, there is a possibility that halo of the beam can hit on the electrodes which in turn produces the secondary electron. These electrons will go in different directions and lead to false coincidence (ionization event with wrong energy and timing). In order to blank the projectile beam during pulsing, two aperture which is located before and between the deflectors respectively (Figure 4.3) is used. A set of X-Y deflector plates are used, and these deflectors allow the beam to be steered horizontally or vertically to correct any misalignment of the filament or the effect

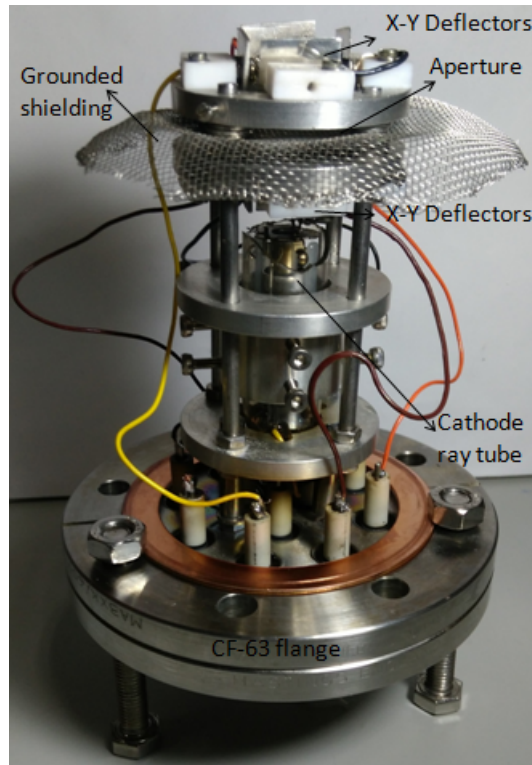
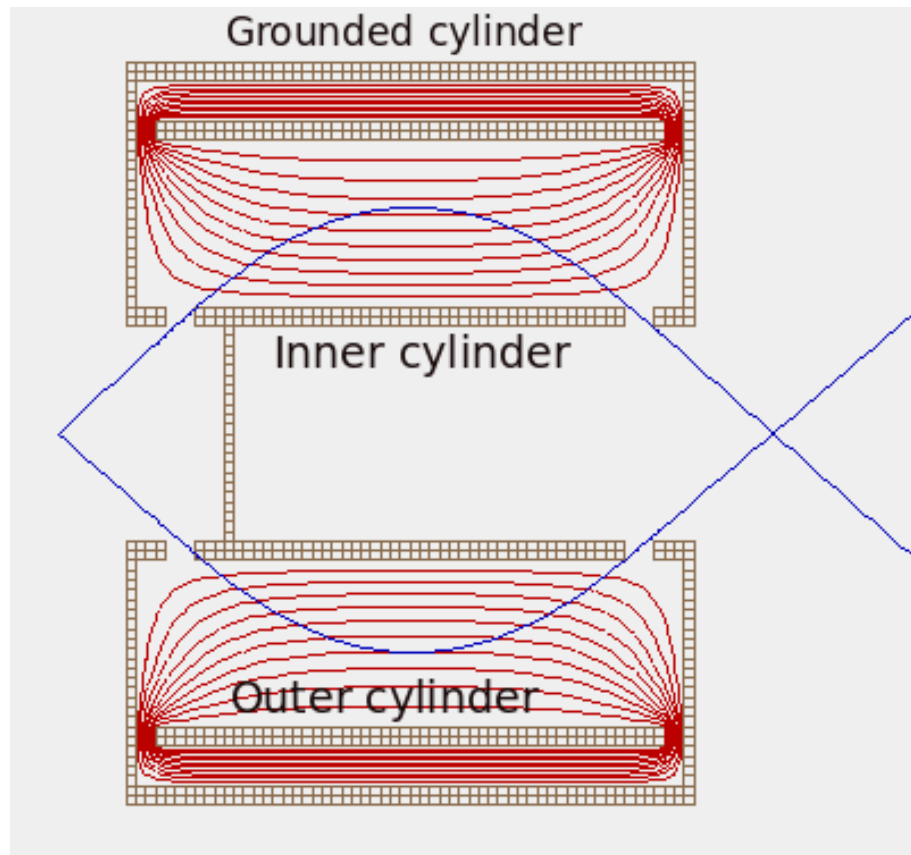


Figure 4.3: Electron gun assembled on CF-63 flange with aperture (0.1 mm) and X-Y deflectors

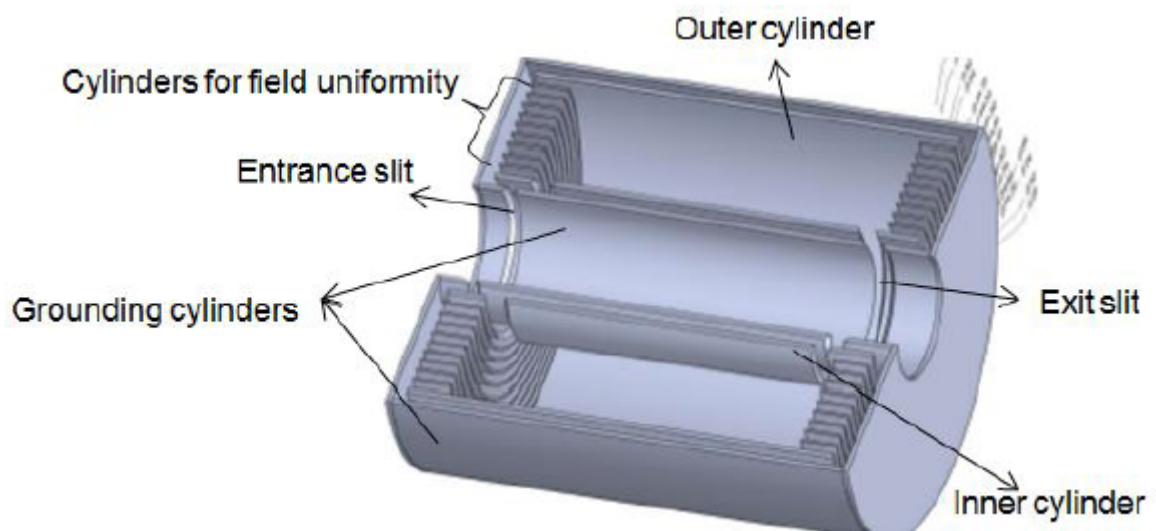
of stray magnetic fields on the electron beam, as well as ensure target collision zone that is well localized in space. Experimental optimization of every potential over the range of relevant kinetic energies is done, by taking all possible combinations of potentials in all electrodes and measuring the beam characteristics, such as the focus spot and the extracted current. A Faraday cup is used to measure the intensity of the electron beam, in which up to 100 microamps is measured for the beam of 2 keV electron energy with 140 mA on the filament. The four-element electron gun described here is designed for (e,2e) experiments, and it may be found to have more general application.

4.4 Electron Spectrometer

Electron spectroscopy involves interrogating the scattered or emitted electrons by detecting them and analyzing its energy. Therefore the efficiency of the method mainly relies on the sensitivity and the energy resolution of the electron spectrometer and proper design of its components. Out of several types of electron spectrometers which have been



(a)



(b)

Figure 4.4: (a) Secondary electron trajectory through CMA (Red colour: Electric fields lines, Blue colour: Electron trajectory) (b) CMA mechanical design

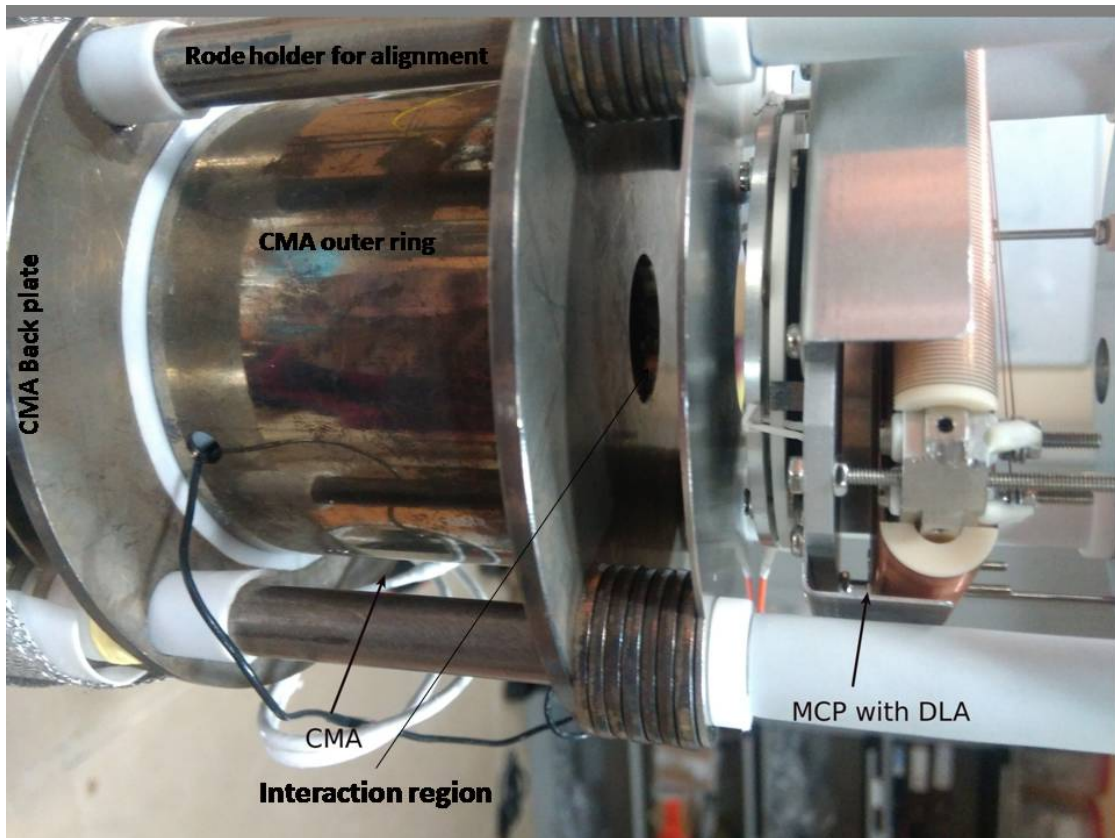


Figure 4.5: CMA assembled with MCP along and delay line anode detector

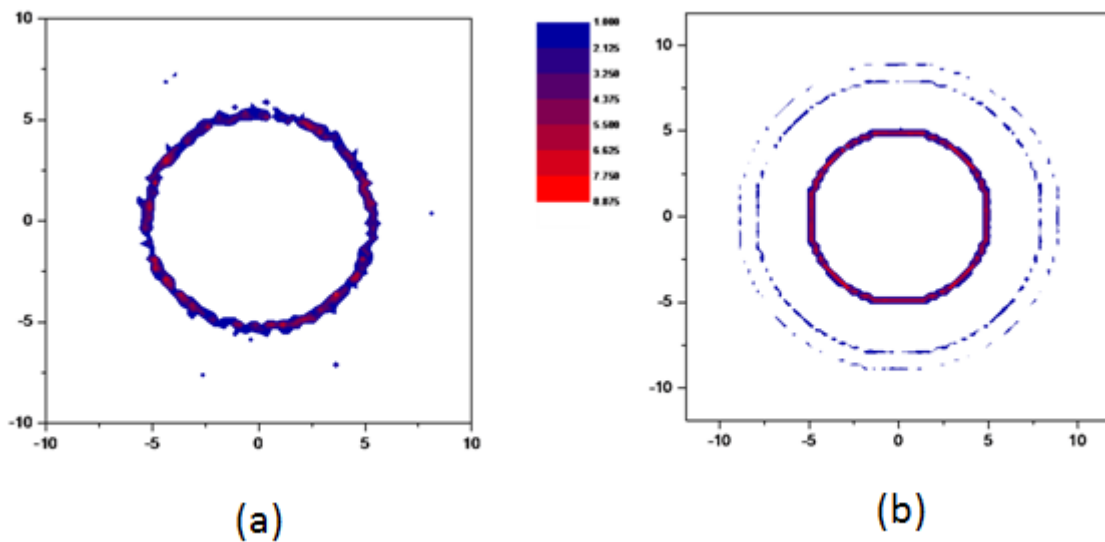


Figure 4.6: Simulated CMA image obtained for electron energy 335 eV with standard deviation 0.42 and FWHM=1, projected at an angle $42^{\circ} 18''$ (a) from a point source (b) from an extended source having diameter of 4 mm

listed previously, cylindrical mirror analyzer and toroidal analyzer are the ones which are of relevance when one wants to do multi-coincidence experiment along with charged particle. These two types of spectrometers sample a conical shell and with a position sensitive detector is used in the focal plane, any asymmetry about this conical shell axis can be detected. Moreover, position sensitive detector has comparatively high resolution and has the ability to show the angular anisotropy present in the chosen cone angle. In this work, cylindrical mirror analyzer is used as the electron spectrometer purely for the reasons of simplicity in construction and collection efficiency in comparison to the toroidal analyzer. There are some advantages of CMA over other energy analyzers, that it focuses the electrons onto a circle if a suitable detector like position sensitive microchannel plate is arranged at the plane before or after the focal point. Moreover, it doesn't require lenses to focus the beam. In the case of e, 2e experiment with the large molecule, high transmission efficiency for higher coincidence rate is necessary, and the energy resolution can be compromised, the processes in this work are like plasmon resonance excitation having very broad energy distribution is of interest in this work. In the case of CMA, energy selection occurs in the field caused by the potential difference $\Delta V = V_1 - V_2$ between two cylinders of radii r_1 and r_2 .

The total projection L_o along the cylinder axis of the flight path between the source and the image slits is given as [143].

$$L_o/r_1 = n \cot \theta_0 + 2 \times \sqrt{(k\pi)} \cos \theta_0 \exp(k \times \sin^2 \theta) \operatorname{erf}(\sqrt{k \sin \theta_0}), \quad (4.1)$$

the geometrical parameter,

$$n = \frac{l_0 + l_1}{r_1} \quad (4.2)$$

where, l_0 and l_1 are, respectively, the distances of the source slit and the image slit from the inner cylinder perpendicular to axis and calibration factor,

$$k = \left(\frac{E_0}{q\Delta V} \right) \ln(r_2/r_1) \quad (4.3)$$

$$L = L_0 + ncot\theta_0 \quad (4.4)$$

The CMA outer cylinder has a diameter of 61 mm and that of the inner cylinder is 23 mm. The total length of the cylinders is 70.4 mm, the distance between two cylinders is 45.2 mm, and the entrance and exit slit distance is 58.2 mm. The electron trajectory through CMA has been simulated using SIMION8.0 as shown in Figure 4.4a for understanding the field sensitivity of the secondary electron as well as angular and energy acceptance of CMA. The estimated calibration factor for electron energy to CMA voltage is $k = 1.3$ which matches well with the experimental value. Mechanical drawing of the same CMA is shown in Figure 4.4b and the CMA assembly is shown in Figure 4.5. Other CMA parameters are $r_1 = 11.5 \text{ mm}$, $r_2 = 36 \text{ mm}$, trajectory $L = 6.139r_1$ and calibration factor $k = 1.3$ which accepts electrons emerging from the interaction region in a cone with $\theta_0 = \pm 42.3^\circ$ opening angle, width of $\pm 3^\circ$, the energy resolution $\frac{\Delta E}{E}$ is 4% and the geometrical efficiency $\approx 10^{-4}$. For the electron energy analysis, the inner cylinder is grounded and a negative potential is applied to the outer cylinder and electrons entering the CMA are energetically analyzed by the electrostatic field generated between the two cylinders. Due to this field electrons of particular energy are focused onto the exit slit for detection. Varying the negative potential of the outer cylinder such that it scans the range in which the energies of the emitted electrons lie, the electron spectrum is generated. The MCP plate of the active area of 40 mm diameter is kept at the exit slit for the detection of the electrons coming out from the CMA. Moreover, the simulation was done to understand the angular distribution as well energy distribution by recording the 2D position of the energetically analyzed secondary electron. Figure 4.6 shows the 2D projection of energetically analyzed electrons from a point source as well as an extended source of 4 mm diameter spherical distribution.

4.5 Mass Spectrometer

Wiley-McLaren type time-of-flight mass spectrometer (ToFMS) [67] is used as the ion spectrometer (Figure 4.7), which is one of the simplest mass analyzing devices, which

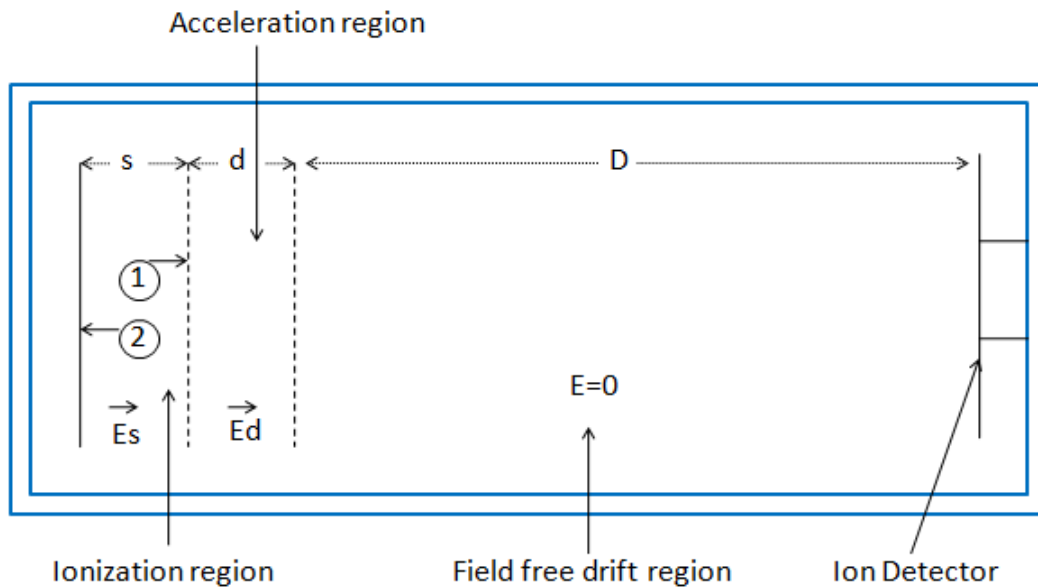


Figure 4.7: Wiley-McLaren type ToF Schematic

separates ions, after their initial acceleration by uniform electric fields, according to their velocities when they drift in a field-free region. The focus condition gave the flight time of ions independent of their generating points in the ionization region to first order. Further, to minimize the effects of velocity distribution on time resolution, ToFMS in 'reflectron' mode is provided, where higher velocity component of the same mass due to initial spatial, velocity spread is corrected by using a reflecting field which ensures the in time arrival for all component for the same mass (as shown in Figure 4.8). Two field Wiley Maclaren type ToFMS with drift tube of 200 mm length, the interaction region of 16 mm and extraction region length of 40 mm is used. The spectrometer can work in pulse mode as well as in coincidence mode.

To derive the flight time of ions, consider an ion created in interaction region having charge q and mass m with initial energy U_0 which increases to U when the ion gets accelerated.

$$U = U_0 + qsE_s + qdE_d \quad (4.5)$$

and time-of-flight,

$$T(U_0, s) = T_s + T_d + T_D, \quad (4.6)$$

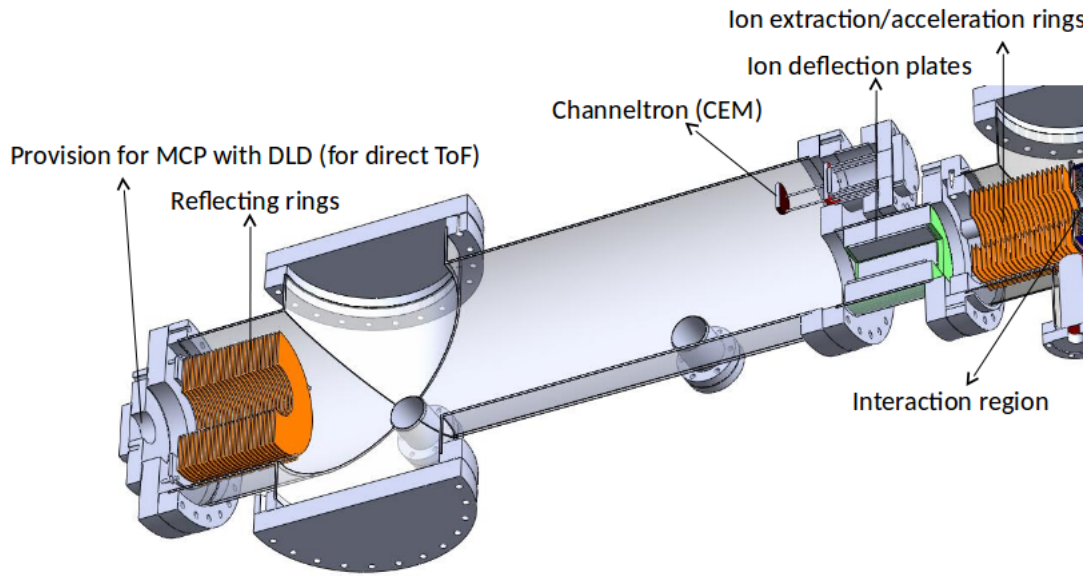


Figure 4.8: Cut view of mechanical design (CAD) of time-of-flight mass spectrometer with provisional reflectron

where, T_s , T_d and T_D are the time-of-flight in interaction region, extraction region and drift tube respectively.

This equation is the general flight time equation in which most of the experimental quantity such as D , s , d , E_s , E_d are known. The time-of-flight is simulated using SIMION8.0 (Figure 4.9) and found to be matching with the experimental value by applying appropriate voltages to the extraction and drift tube and a resolution of, $\frac{m}{\Delta m} = 101$ is achieved. The current ToF mass spectrometer in use is shown in Figure 4.10 .

4.6 Pulsed Extraction ToF

A typical time-of-flight (ToF) spectrometer with permanent extraction electric field could affect the projectile electron beam adversely. Moreover, the secondary electron energy needs to be corrected for the field effect. Therefore, in the electron impact measurement in coincidence, one needs to actively compensate for this effect [142] which in turn can affect the range of usable beam energies. An alternative method is to have pulsed extraction of recoil ions. The technique offers a possibility of having a variable delay between the formation and extraction of the recoil ions. In the case of electron-ion coincidence

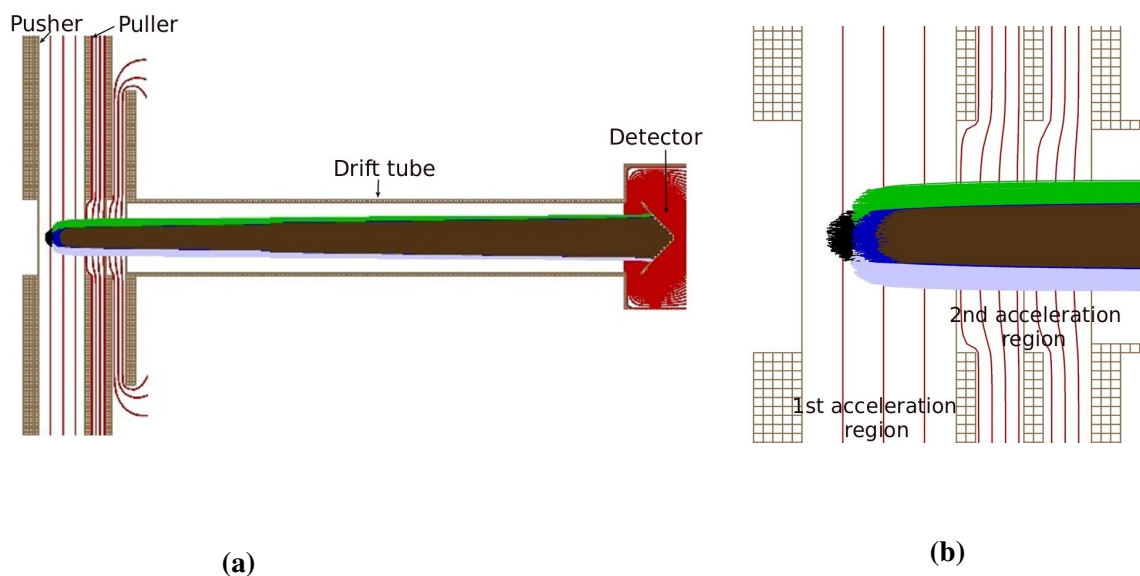


Figure 4.9: (a) Simulated ion trajectories (in colored) through time-of-flight mass spectrometer (Red contours are electric field lines) (b) Interaction and acceleration region of the time-of-flight mass spectrometer shows field uniformity for smooth acceleration of the molecular ions

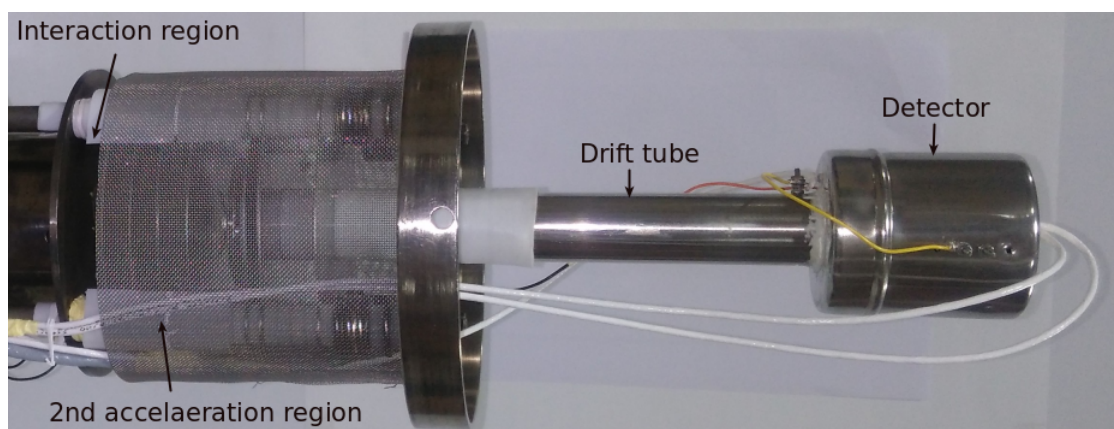


Figure 4.10: Time-of -flight mass spectrometer with ion detector assembled

measurement, the ions that come from the same molecule, like the detected electron, will be called "true ions" and the others will be called "random ions". High true coincidence rate is required for the correlation measurement. So the timing of the electron and corresponding ion measurement are critical. The ion extraction can be delayed due to the detection delay as well as pulse processing electronics. The electron will take typically 50 nanoseconds to reach the detector through the CMA and the typical delay time in detecting ion for an electron start in the current case is about 200 nanoseconds. So it is very important to check the extraction of ions with the delay in time. For this purpose, pulsed extraction of ions with a time-varying electric field in the interaction region is simulated using SIMION8.0 (see Appendix A for the code). The collection efficiency for the different molecular ion with the variable delay time in extraction is also simulated. For example in the case of naphthalene, 99.9% of the ions are expected to have thermal velocities less than 480 micrometers/micro second at room temperature. This implies that the ions can move 2.5 mm in 5 microseconds and the simulations gave us the freedom of shifting the source position of the naphthalene target over the range of 2.5 mm. Hence, 5 microseconds, is considered as the maximum value of the delayed extraction time. The effect of the rise time of the extraction voltage to the molecular velocity spread is numerically calculated and is 20 micrometer/microsecond for naphthalene molecule. So the total spread in the velocity, taking into consideration the spread in thermal velocity as well as the field effect for naphthalene molecule, is expected to be a maximum of 500 micrometer/microsecond. In this case, also the collection efficiency is 100%. By using this provision of the experimental setup, delayed extraction time-of-flight mass spectrometric studies of PAHs and PANHs is performed which will be discussed later.

4.7 Projectile Energy Loss Analyzer

For understanding the complete kinematics of the atomic or molecular target system one needs to know the accurate energy given to the target. For accurate estimation of this energy, it is essential to know the energy of projectile electron before and after interaction with the target. For measuring the projectile energy after the interaction, a parallel plate analyzer with channeltron detector was planned to use. The dimensions of the parallel

plate are 100 mm in length, the distance between the plates is 50 mm, entrance and exit slit width are 1 mm, and all the plates are having 2 mm thickness (mechanical drawing is shown as in figure 4.11).The acceptance angle of this PPA is 45° . The SIMION8.0 simulation is performed to understand the field uniformity and particle trajectory through the parallel plate analyzer and to maintain better uniformity in the electric field inside the spectrometer, the frames were added in between the two plates. Marginal uniformity in the field lines was there in this case even without adding the frames. The electron trajectory simulation parallel plate with different initial energy (colored) is shown in Figure 4.12, and from the simulation, 1 % energy resolution was achieved.

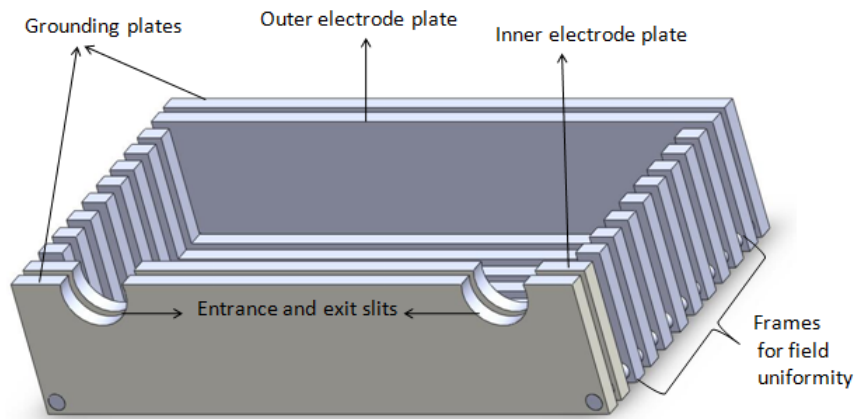


Figure 4.11: 3D cut view of parallel plate electrostatic energy analyser with frames (frame thickness and larger slits are for illustration purpose)

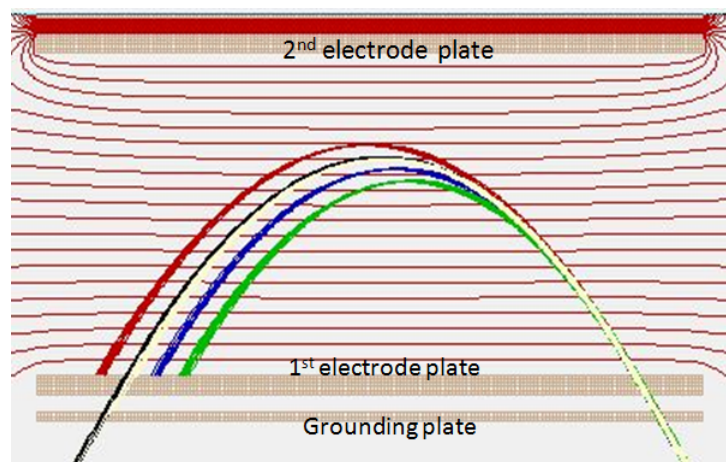


Figure 4.12: Parallel plate electrostatic analyser with electrostatic field lines (shown as red lines) and the particle trajectory (various coloured trajectory corresponds to different initial energies of the electron beam)

4.8 High Voltage MOSFET Switch

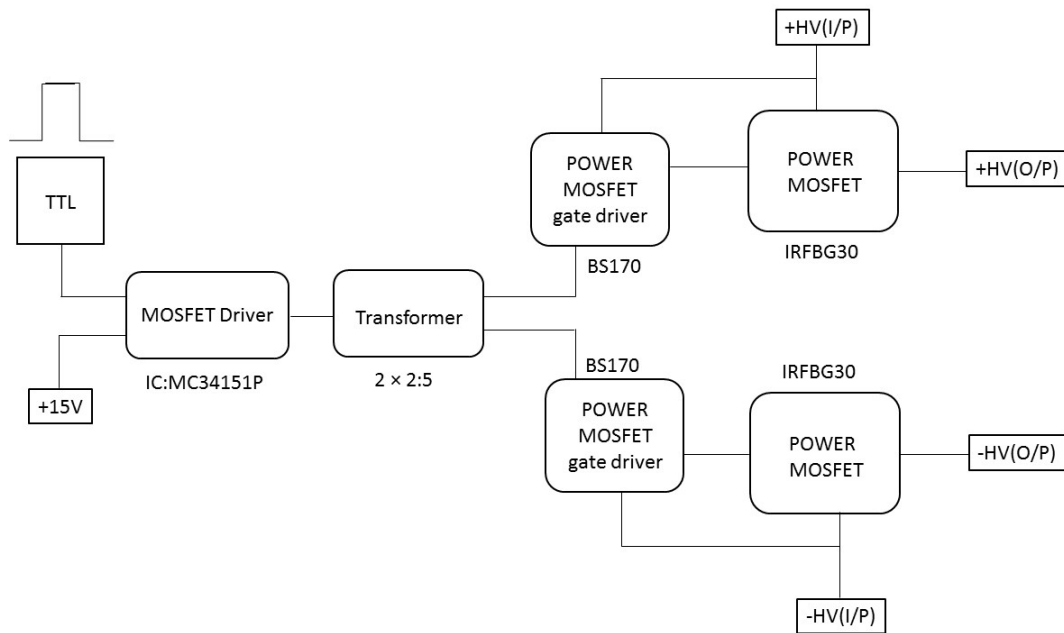


Figure 4.13: High voltage MOSFET switch (push-pull) schematic

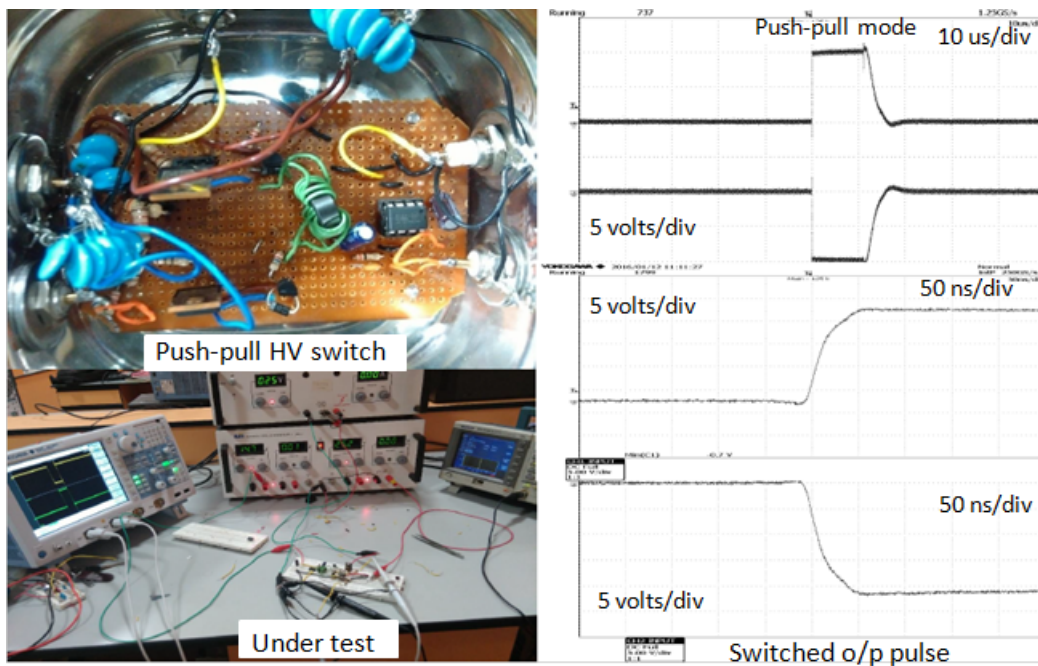


Figure 4.14: High voltage MOSFET switch (push-pull) along with the pulse rise time (<50 ns) and fall time in push-pull mode

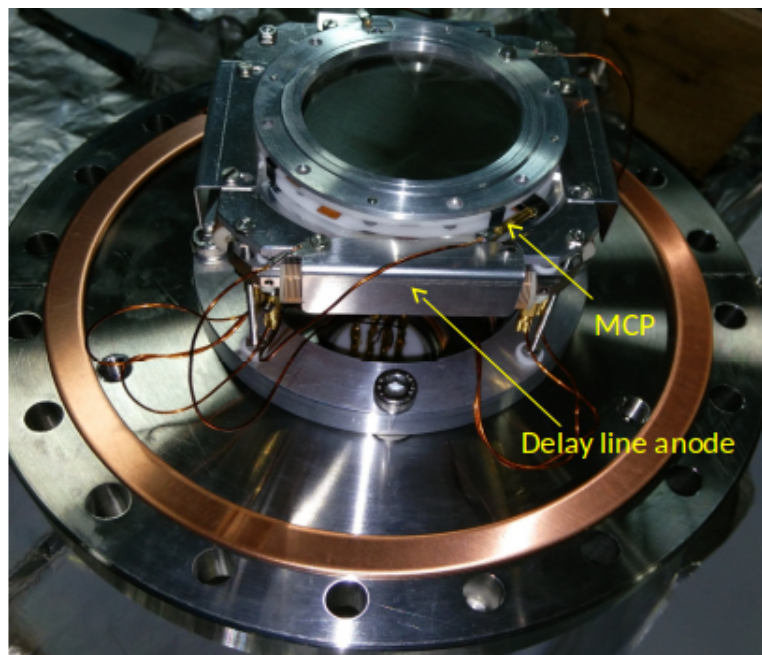
In electron spectroscopy measurement, the interaction region is to be free from both magnetic and electric field, since the secondary electrons trajectories are very sensitive.

But for the ion mass spectrometry experiment, the ions need to be extracted by applying a potential to the electrodes. So when one does the combination of both spectroscopy in coincidence, it is necessary to pulse the extraction field as well as the electron beam. Moreover, during the extraction of the ions, the electron beam must be turned off, otherwise, the deflected beams may hit the electrodes and produce secondary electrons disturbing the experiments. Therefore the present experiment with electron impact ionization requires two sets of fast switches, one for switching electron beam and the other for simultaneous switching of the pusher-puller. The fast switches using commercial off the shelf power MOSFETs is built as part of this work for this switching purpose. Single output switches have been used commonly and a few have been detailed in literature for various applications [144–147]. To control the switching of electron gun as well as extraction of ions accurately, two types of switches are needed, one which can operate in single polarity for switching the electron beam ON or OFF, and the other is a pair of switches working in synchronism but of opposite polarity. First, for the single polarity switch, a pair of fast power MOSFETs triggered in synchronism is used in which 4 MOSFET in series are in use. Each MOSFET is capable of handling ± 800 V and they are all triggered by separate individual MOSFET. A TTL pulse is passed through several logic gates in order to minimize the probability of damage to the external TTL pulse generator due to noise produced by the high voltage section of the circuit. This pulse is then used to trigger a MOSFET driver. The output of the driver is fed to a toroidal transformer with a single primary (2 turns) and a pair of secondary (5 turns each). Each of the two outputs triggers a pair of small signal MOSFETs which in turn control the gate of the main power MOSFET (Figure 4.13). The single polarity switch is tested with voltages as high as ± 3000 V and could achieve rise/fall times of less than 50 nanoseconds with typical capacitive load (Figure 4.14). The fall/rise time at the end of the pulse was about 5 microsecond and was not necessarily to improve as it played no role in the measurement. To apply the simultaneous change of voltage to pusher and puller plates, a bipolar push-pull switch is used, which switches between two voltage states for an electrode with capacitance in the range of few tens of pF , and the rise time of 50 nS. This switch is tested up to ± 300 volts which can operate in a synchronized manner well below sub-microsecond time scale.

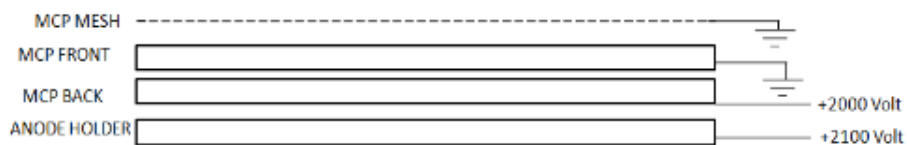
4.9 Electron and Ion Detectors

Electron Detector

The secondary electron detector is a 40 mm diameter MCP which is assembled on CF-60 flange as shown in Figure 4.15, and placed at 5 mm away from the focal point of CMA. This afocal distance can be adjusted, which will ensure the secondary electron distribution projected in a circular shape on the detector, and the intensity distribution on the circle will give us for any angular distribution. The working principle of the MCP has already been discussed in the Chapter 3. Successful strike of a secondary electron produces a cloud of around $10^7 - 10^8$ electrons, which emerges from the rear of the MCP, this electron which falls on the DLA, whereby the position information will also be obtained.



(a)



(b)

Figure 4.15: MCP detector (a) Assembled on CF-160 flange, (b) Electrical connection schematic

Table 4.1

Typical voltage settings used for MCP and DLA (electron detector)

MCP FRONT	0 Volt
MCP BACK	+2000
DLA ANODE HOLDER	+2100
REFERENCE WIRE	+2200
COLLECTING (SIGNAL WIRE)	+2400

Ion Detector

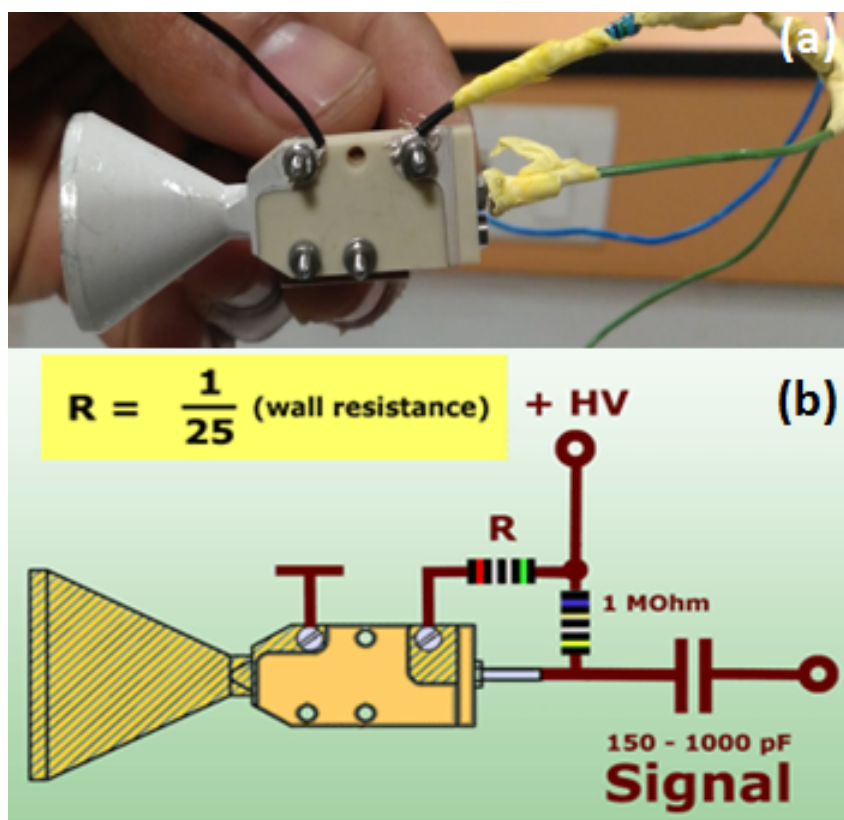


Figure 4.16: CEM detector (a) With electrical connection (b) Standard electrical connection schematic for ion detection

A channel electron multiplier (CEM) with 25 mm active area, as shown in Figure 4.16 is employed for the intact or fragmented ion detection. This detector is assembled at the end of the drift tube, stainless shielding is used to reduce the noise pickup due to any high voltage and time-varying field. Since, the pulsing of high voltage is in use for the electron gun and ion extraction after the detection of the secondary electron on MCP, compared

to electron detection the ion detection is more probable to pick up noise and distort the measurement.

4.10 Electron-Ion Coincidence Experimental Setup

Probing the kinematical changes in molecular dissociation, affected by various ionization mechanisms, requires a combination of different experimental techniques. To reveal the ionization mechanism due to projectile impact on a molecule, the electrons emitted from the molecule are needed to be energetically analyzed in coincidence with molecular ion/fragment yield measurement. A cylindrical mirror analyzer in unison with ToF mass spectrometer is used for this kind of investigation. Schematic of the experimental setup is shown in Figure 4.17.

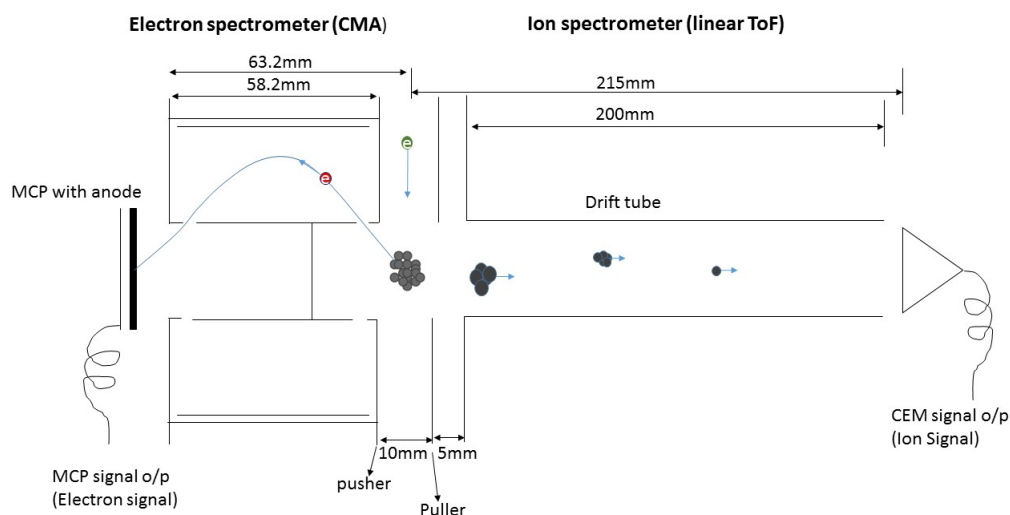


Figure 4.17: Electron-ion coincidence experiment schematic

In this experiment, electron beam produced by electron gun interacts with the target molecule injected in a perpendicular direction to the beam. A Faraday cup is placed at a distance of 50 mm from the exit of the interaction region for projectile electron intensity monitoring and is biased to +36 Volts. The secondary electrons emitted from the molecular ions will be energetically selected by the CMA and detected on microchannel plate (MCP) with position sensitive detector. The MCP signal will trigger the electron gun OFF as well as extraction field for the recoil ions ON simultaneously by using high

voltage MOSFET switch. During extraction, the electron gun will be kept OFF to avoid uncorrelated events.

4.11 Fabrication

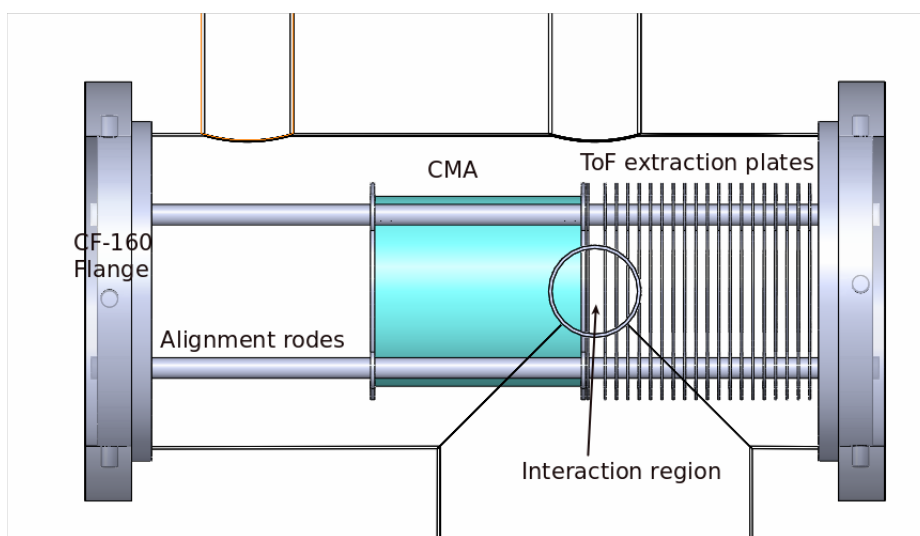


Figure 4.18: Mechanical alignment of the interaction region electron-ion coincidence experiment

With the help of SOLIDWORKS, the full 3D assembly was designed, 2D floor drawings for each component were extracted and the floor drawings were then outsourced for the manufacturing. High vacuum chamber made from SS-304 is used for performing electron-ion coincidence experiment. Ultra high vacuum (UHV) chamber consists of two parts, one is the interaction chamber and another chamber is for the reflectron assembly. Both the chamber are off-axis as shown in Figure 4.1 to meet the reflectron conditions. The alignment of the electron spectrometer, as well as ion spectrometer, interaction region, and electron gun, is very critical. The interaction point will be a crossing point for projectile electron beam, target molecule, the focal point for electron spectrometer and the interaction point for the ion spectrometer (as shown in Figure 4.18). Moreover, the interaction point needs to be well localized for the discrimination of ion spatial distribution, and at the same time, it will be the focal point for the CMA which will decide the acceptance of the secondary electron. The alignment of the electron spectrometer and ion spectrometer is designed in line with a cross electron beam and target gas with 0.1 mm

accuracy. By considering all these matters, the CMA, Reflectron extraction plates and MCP with position sensitive detector are assembled in four rods which are attached to a solid metal ring of the size of the inner diameter of the interaction chamber (as shown in Figure 4.18). With this mechanism, one can insert the whole assembly along with the detectors very accurately and lock its position.

4.12 Operational Modes of the Setup

The setup is designed with very high flexibility so that it can be operated in various modes depending upon the purpose and the requirement of the experiment. The instrument can work as a stand-alone mass spectrometer, electron spectrometer, delayed extraction time of flight mass spectrometer, and the most complex mode of secondary energy analyzed electron coincidence with the recoil ion along with the future possibility of the addition of projectile energy analyzer, it can be easily converted into a triple coincidence instrument. In the present work due to the limitation in time, it has been tested in all the modes except the triple coincidence modes but could use only for two modes of the stand-alone mass spectrometer, simple mass spectrometer in which the synchronized switching and delayed extraction is employed.

Three modes of the pulse processing sequence have been involved in this experiment. Pulse processing and data acquisition system (DAQ) is developed using various electronics modules like an amplifier, constant fraction discriminator (CFD), time to digital converter (TDC) etc. as per the requirements. The data is acquired using a multi-hit time-to-digital converter data acquisition system (Agilent TDC Model: U1051A). The data acquisition program is written with help of Agilent acquires data acquisition programmers manual. The details regarding the pulse processing and data acquisition algorithm for electron spectrum, ion mass spectrum and electron-ion coincidence measurement are discussed below.

4.12.1 Electron Spectrum

For the electron spectrum, in which the energetically selected electrons by CMA is detected on the microchannel plate (MCP) with delay line anode (DLA), which is biased

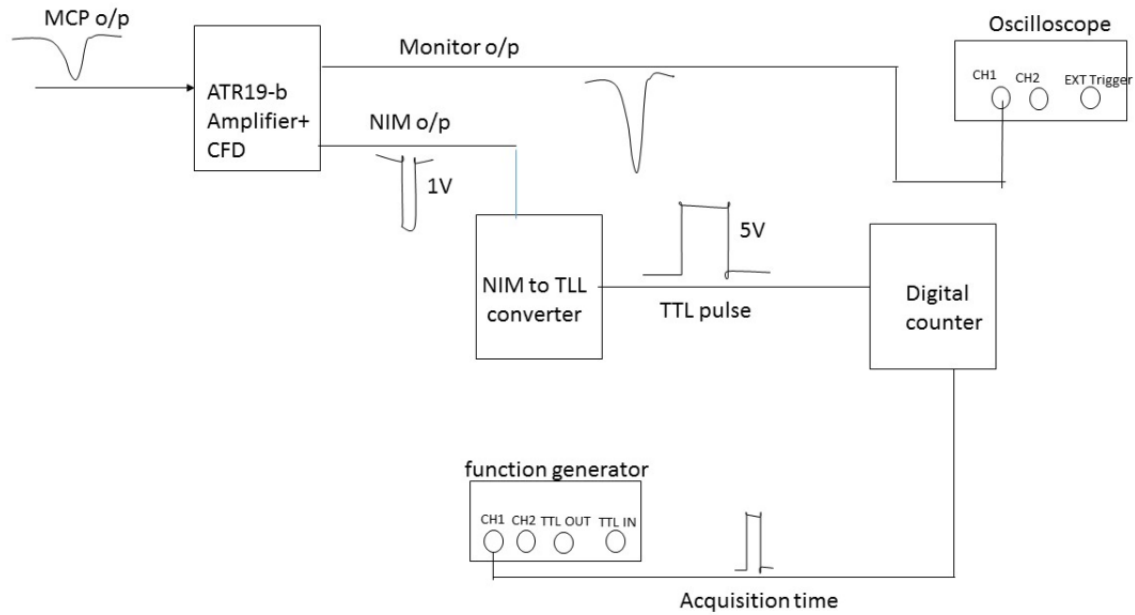


Figure 4.19: Pulse processing schematic for electron energy spectrum using CMA

to +2200 volts. The signal from MCP and DLA will be sent to an amplifier followed by a constant fraction discriminator (CFD) which produces nuclear instrumentation module (NIM) signal (amplitude of -1 volt) for each pulse and reduces the time jitter in each pulse (ATR19b, ROENTDEK is used as the amplifier and CFD). The pulse is then given to a time to digital converter (TDC) with MCP back signal as the trigger for the position measurement (Figure 4.19). The provision to measure the electron intensity directly from MCP back signal by using a programmed ARDUINO DUE is implemented. In this way, the data acquisition for the electron spectrum is automated. The ARDUINO DUE will control the power supply as well as record the number of electrons detected and a program for this automation (see the Appendix B for the code) was written. The 0 to 5 V signal from ARDUINO DUE will be amplified using an operational amplifier (op-amp) (as shown in Figure 4.20) from 0 to 10 V in steps of 0.01 V (the step size is adjustable), which will be given to the power supply as RAMP input control. For each voltage increment, this power supply produces an output from 0 to 1000 V in steps of 1 V (the voltage step size is adjustable). This voltage will be given to CMA for the energy selection of electron and at each voltage setting, the data will be taken for few seconds (acquisition time is adjusted from seconds to hours). The voltage holding time and data acquisition time can be adjustable by changing timing parameter in the coding. So the number of

electrons (data) will be written in the file for each voltage for the given time (can be adjusted in the code). Finally, the voltage is multiplied with a geometric calibration factor of CMA (which will give the electron pass energy), and the energy versus electron intensity (number of counts), which will give the electron spectrum.

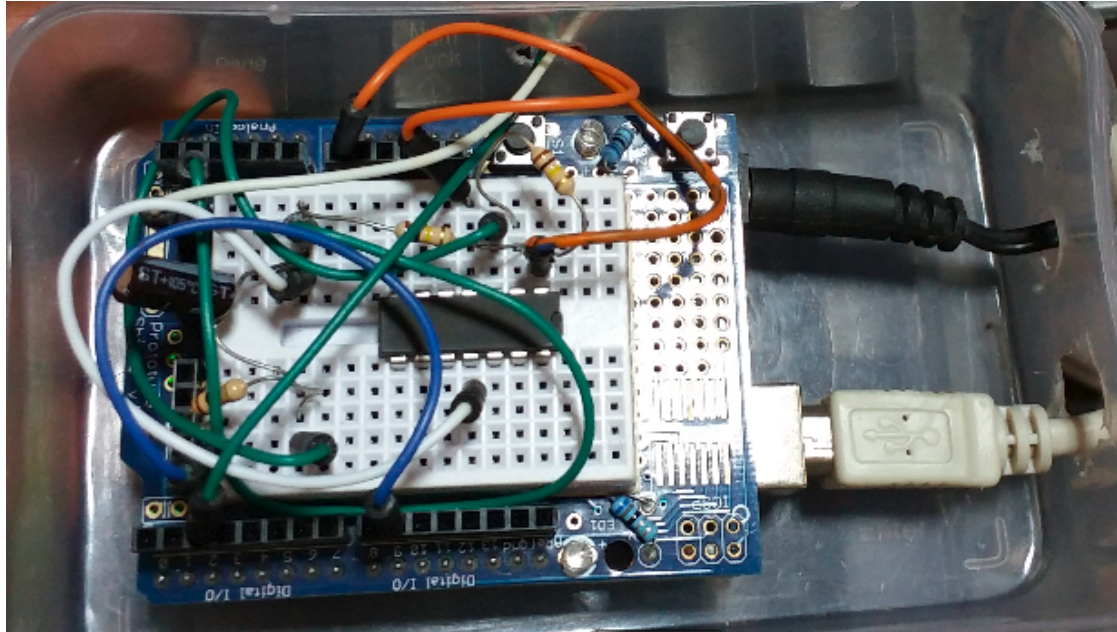


Figure 4.20: ARDUINO DUE with OP-AMP

4.12.2 Mass Spectrum with Synchronized Switching

For the time-of-flight (ToF) of recoil ion, the channeltron (CEM) is biased to -2400 volts. ATR19 (from ROENTDEK) is used to process the signal from CEM, which has an amplifier plus CFD. Here the purpose of CFD is to discriminate the true signal from noise by properly adjusting the threshold value. In the mass spectrometry, as noise signal amplitude will be always less than the true signal, the threshold value should be set in such a way that it will not allow the noise signal to cross that threshold level but the true signal can cross. But sometimes the true signal is too low to cross the threshold and noise signal too high to block. So there will be some true signal loss in this case. The processed signal by ATR19 will be given to TDC, which will convert the timing signal to digital signal and will be recorded using the computer (Figure 4.21). The provision of multi-hit in the ToF DAQ is established.

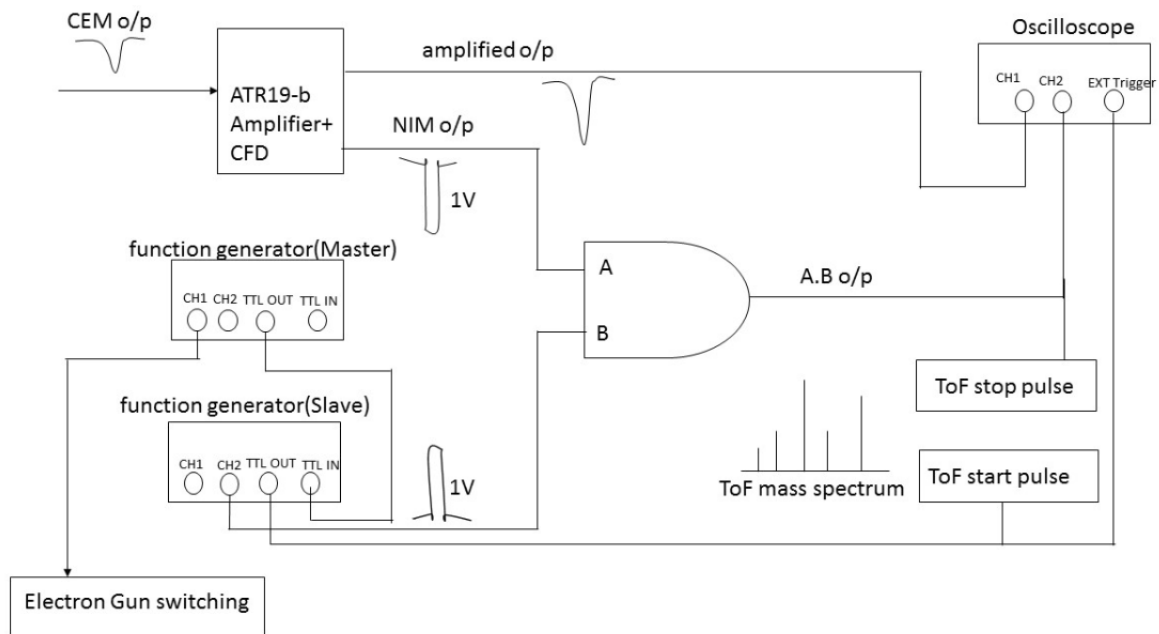


Figure 4.21: Pulse processing schematic for ion ToF

4.12.3 Electron-Ion Coincidence Measurement

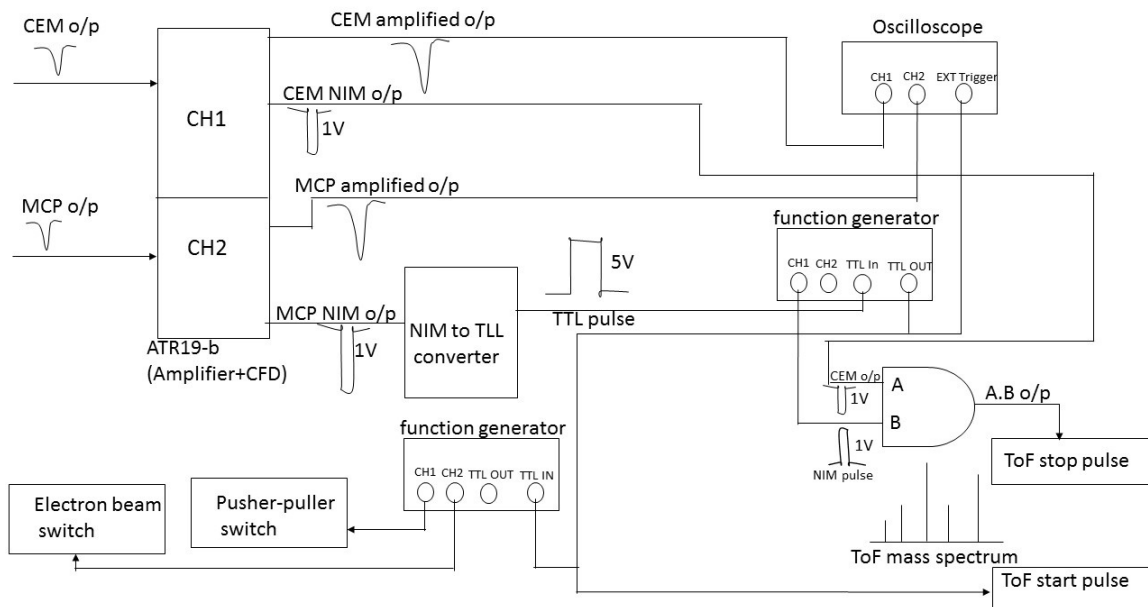


Figure 4.22: Pulse processing electronics for electron-ion coincidence measurement

In the third case, the time-of-flight in coincidence with the secondary electron is measured. The MCP back signal from the energetically selected electron will trigger the position on DLA as well as it will produce a TTL pulse which will be given to electron

gun switch and extraction field switching (pusher-puller switching) (Figure 4.22). The electron gun will be immediately switched OFF once it triggers and the extraction field will be switched ON. By using this pulsing technique the secondary electron will not be affected by any field since the interaction will happen in a field-free region, where the switching of the electron beam as well as extraction field for the recoil ion will start after detection of the secondary electron only. The pulsing schematic for e, 2e measurement is shown in Figure 4.23.

4.13 Data Acquisition System

This acquisition system is capable of measuring the energy and position (x,y) of the secondary electron along with the time of flight (t) of all the recoil ions produced in all modes (as described above Section 4.12). TDC (Model: Agilent Acquiris) consists of 6 channels for input and one common trigger. The time measurement is done with respect to the common trigger. In this coincidence measurement, the common start trigger is the secondary electron pulse. The 32 bit TDC used here has timing resolution 50 picoseconds with pulse pair resolution 10 ns and of unlimited multi-hit capability. So in the TDC, the first channel records the number of electrons for a particular CMA pass energy, and the next four channel records the position of this secondary electron for finding if any angular distribution. The sixth channel in the TDC is used to record the ion mass spectrum with multi-hit analysis provision.

Noise Rejection

The time-varying voltage for the electron beam switching and the similarly time-varying electric field for ion extraction is used, and there is noise picked up by the detector due to this time-varying field. This causes a major problem in the DAQ as it will be difficult to see the lower masses in the mass spectrum when one records it in electron ion-coincidence mode. To solve this problem of noise record, a pulsing sequence was developed (as shown in Figure 4.23) with the help of two function generators. When the electron is detected by the MCP, the processed signal from MCP will go to the TDC for electron counts as well

as the position record of the secondary electron. During this time no time-varying field will be ON so that the secondary electron measurements will not cause noise detection and the same secondary electron signal will send a NIM to TTL converter and this TTL output is given to a function generator which produces a pulse of 5 V amplitude with adjustable delay. This pulse will go to the TDC as the START for the time-of-flight DAQ event record, as well as the START for the ToF extraction switch pulsing. The same signal is given to another function generator and which will be given as VETO (in which data can be recorded with adjustable delay) and this delay will be adjusted such that the time of flight measurement will not have noise.

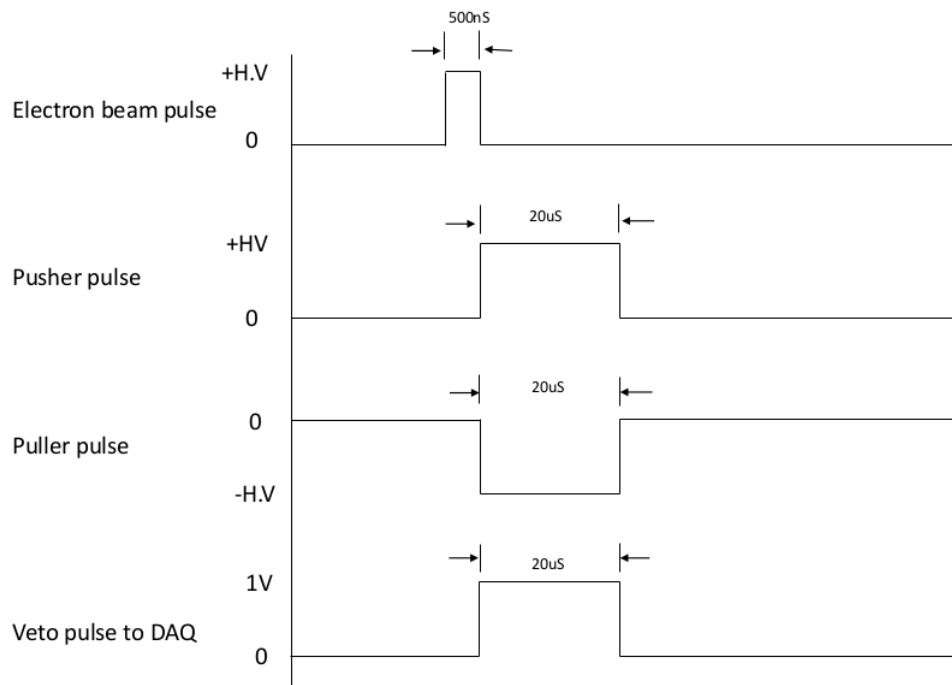


Figure 4.23: Pulsing sequence for electron-ion coincidence measurement

The experimental realization of the setup is constructed along with pulse processing unit as well as data acquisition systems. The whole system is assembled and is kept on a trolley made out of aluminum strut channel as shown in Figure 4.24. There are two separate electrical connections used to power the whole system, one used for the vacuum system (turbo and rotary pumps) and the other is for electronics and related components (power supplies, counters, function generators, logic units, amplifiers etc.), and both are having separate power sources. By providing separate power sources, the precaution for proper power distribution is taken to avoid any damage to individual electronic compo-

nents due to any load or fluctuation in the power. The whole system is movable (by releasing the wheel brake on the aluminum strut channel made trolley) and it can be transported to facilities like synchrotron, high-energy ion source, free electron laser etc. for future experiments. More importantly, only two power sources are required to operate this experimental setup and can be easily assembled in any of the of above-mentioned facilities.

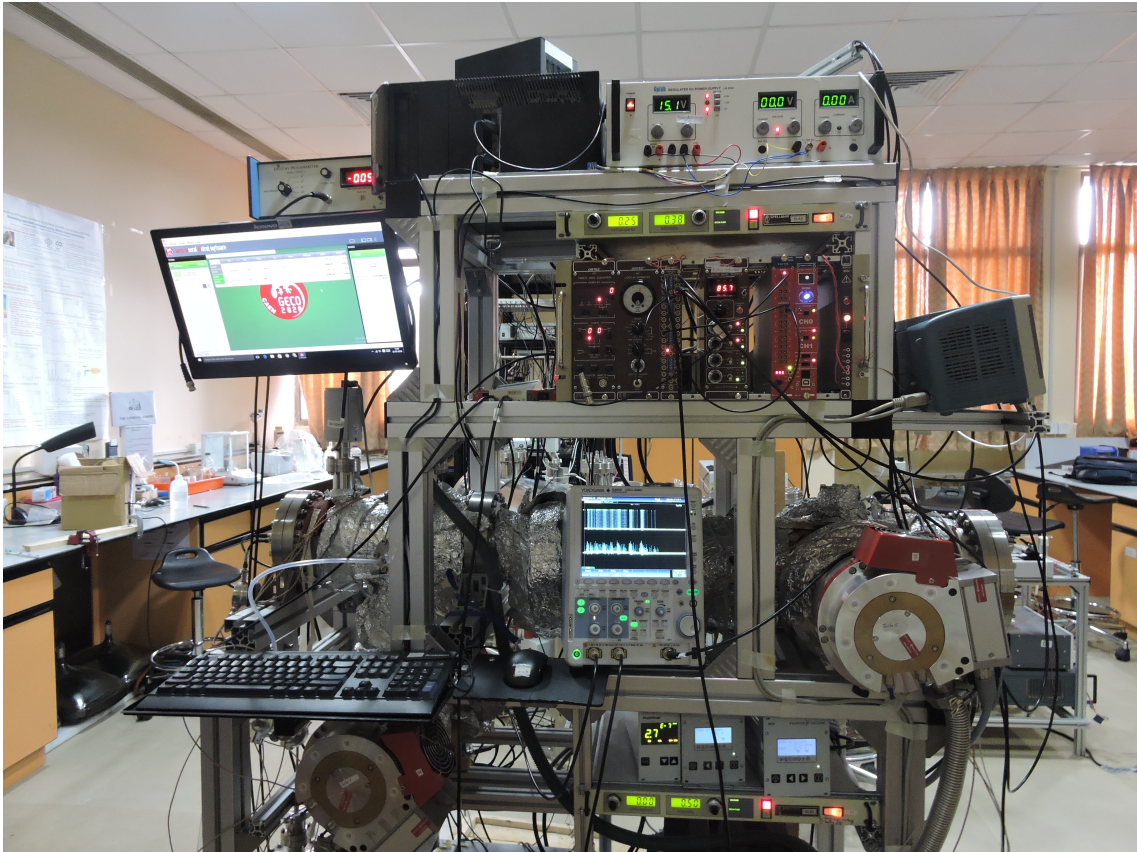


Figure 4.24: Electron-ion coincidence experimental setup with all electronics and DAQ system under working in Atomic and Molecular Physics Lab at IIST, Thiruvananthapuram

Chapter 5

Testing and Calibration

The major part of the works covered in this thesis was the development of the electron coincidence setup, starting from the conceptualization of the instrument, followed by the realization, testing and using it for investigating PAHs and PANHs. The overall complexity in the design of the instrument requires detailed tests and calibration procedures. Particularly in the case of electron spectrometer, the position sensitive electron detection encountered several challenges. Patient modifications and re-wiring of the setup was particularly time-consuming and required intense troubleshooting activity. The whole testing process, though laborious was definitely a learning experience. Since the work involved development of some pulsing electronics, hence these units were tested separately before integration with the setup electronics. The details of such testing of individual subsystems and completed setup in different mode are presented in the following sections.

5.1 Testing for Vacuum

The experimental vacuum chamber consists of the interaction chamber having a diameter of 160 mm and 350 mm length, and reflectron chamber having 200 mm diameter and 800 mm length. The spectrometers are mounted with its axis along the axis of the chamber so that the projectile beam and the spectrometer axis are mutually perpendicular. There are auxiliary ports for pumping, electrical connections, and vacuum gauges. The chamber is pumped by two 700 liters turbomolecular vacuum pumps reaching a minimum pressure of 4.0×10^{-8} mbar without the target. After each venting cycle, the chamber was baked up to a temperature of 60° C for 12 hrs before resuming the experiment. The well-localized reaction volume is achieved by having a projectile-target crossed beam geometry. No heating of target material was required for all the targets (inert gases, naphthalene, quinoline etc.) due to their relatively large vapor pressure at 300 Kelvin. With target vapor, the chamber pressure was maintained at 3.0×10^{-7} mbar.

Detector Testing

When a charged particle or photon hits the front surface of CEM or MCP, which is biased to a high voltage (typically $\sim \pm 2000$ to 3000 Volts), typically a pulse of ~ 20 - 50 mV amplitude will be produced. The rise and fall time of the pulse is generally less than 10 ns. Hence the signal is quite prone to noise and requires to be processed using impedance matched coaxial cables. Special fast amplifiers from Roentdek were used for the pulse processing. The direct pulse from the detector is amplified using these amplifiers and pulse processed and is used as the marker for particle detection. The MCP with delay line anode is used in this experiment as the secondary electron detector, and is biased to $+3000$ V. The typical direct output signal from the detector is shown in Figure 5.1. For the ion detection, a CEM is used with the front cone biased at -2400 V with respect to the tail of the CEM. The testing of the CEM detector is performed with Xe^+ ion, and the MCP is tested with a secondary electron from Xe^+ .



(a)

(b)

Figure 5.1: Detector pulse from (a) CEM for the ion detection (b) MCP for the electron detection

5.2 Fast High Voltage MOSFET Switch Test for Electro-Optic Application

To test the home built high voltage switch, the electro-optic effect in the anisotropic crystal is used as a test case. For such crystals, the refractive index is a function of the application of a dc or low-frequency electric field. A field applied to an anisotropic electro-optic material modifies its refractive indices and thereby its effect on polarized light (Figure 5.2). Electro-optic devices are widely used for beam modulation, amplitude modulation as well as in Q-switching. SBN:61 (Strontium Barium Niobate ($\text{Sr}_{0.61}\text{Ba}_{0.39}\text{Nb}_2\text{O}_6$)) is an excellent optical and photorefractive material due to its photorefractive, electro-optic, non-linear optic, and dielectric properties. SBN crystal has a very large electro-optic coefficient up to 1400 pm/V and is a potential crystal for new generation electro-optic devices. The sample used in this work was one with dimension 5x20x5 mm. In a linear electro-optic modulator (following Pockel effect [148]) the electric field is linearly proportional to voltage applied as given as,

$$E = V/l \quad (5.1)$$

where V is the applied voltage and l is the length of the crystal. The refractive index of the crystal is given as,

$$n(E) \approx n - \frac{1}{2}rn^3E \quad (5.2)$$

where r is the electro-optic coefficient and the typical values of r lie in the range $10^{-12} \sim 10^{-10}$ m/V (1 to 100 pm/V). For $E = 10^6$ V/m (10 kV applied across a cell of thickness 1 cm), changes in the refractive index induced by electric fields are indeed very small. But, its effect on an optical wave propagating a distance much greater than the wavelength of light in the medium can be significant. If the refractive index increases by 10^{-5} , for example, an optical wave propagating a distance of 10^5 wavelengths will experience an additional phase shift of 2π .

As mentioned above, this electro-optic device requires a high voltage with low current power supply (HVPS) in order to have electro-optic effect in the crystal. High voltage

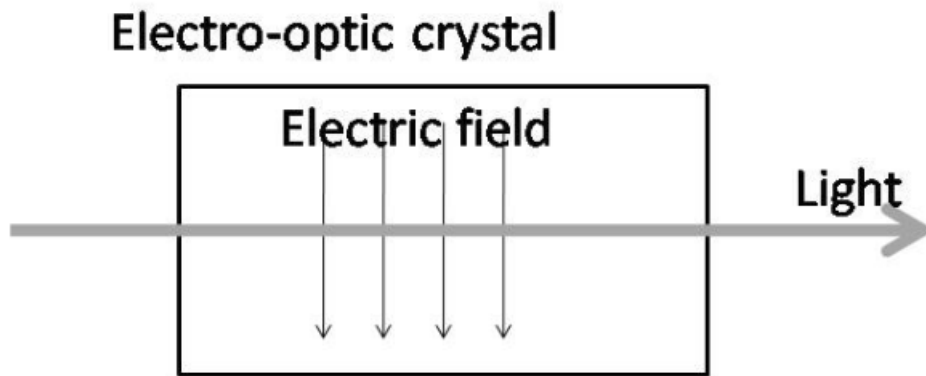


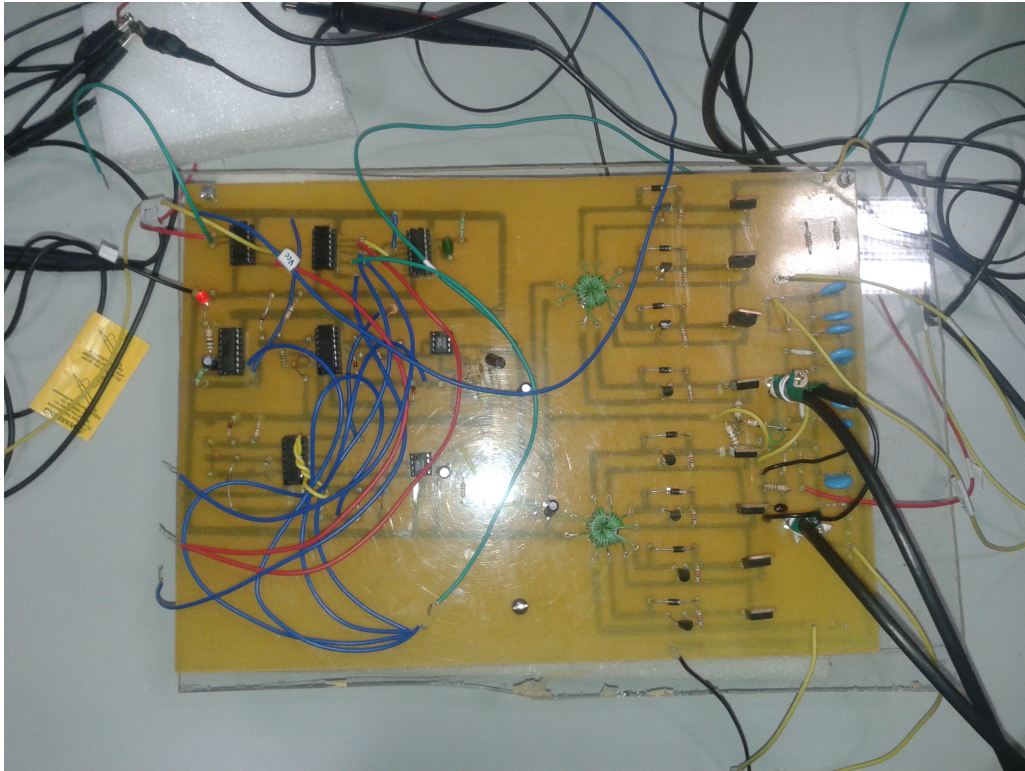
Figure 5.2: A steady electric field applied to an electro-optic material changes its refractive index

square pulse generator with both nanosecond rise and fall times is desirable. Additionally, the generator should have a powerful current driving ability with a capacitive load, for the electro-optic effect in the crystal with a capacitive load. The single polarity HVF MOS switch, which uses a pair of fast power MOSFETs triggered in synchronism with 4 MOSFET series are used for this purpose (as shown in Figure 5.3a). The working principle of the HVF MOS has described in Section 4.8 of Chapter 4. It has been tested to voltages as high as ± 3000 V and could achieve rise/fall times of less than 50 nanoseconds with typical capacitive load (testing of the HVF MOS is shown Figure 5.3b).

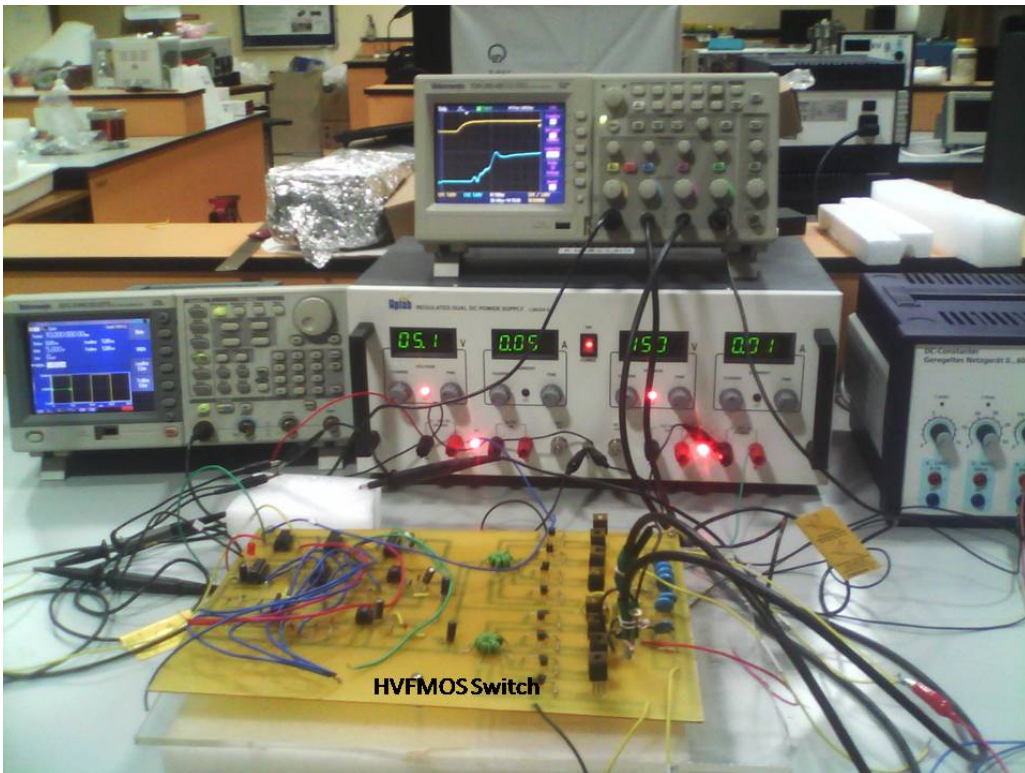
5.2.1 Electro-Optic Modulator Experiment

A He-Ne laser of 633 nm wavelength and related optics along with SBN crystal for the electro-optic modulator experimental setup is shown as in Figure 5.4b. The schematic of the experimental setup is shown in Figure 5.4a. The He-Ne laser light here is a vertically polarized one. Initially, the vertically polarized light passes through a polarizer and then through the SBN crystal. The outgoing beam from the crystal is sending to a sensitive photodetector for the intensity measurement. A polarizer and analyzer combination before and after the SBN crystal is used to study the polarization effect and optoelectric effect of the crystal.

When the DC switched voltage is applied to the crystal by using HVFMS, it will act as a capacitive load and the refractive index of this crystal will change as per the eqn. 5.1

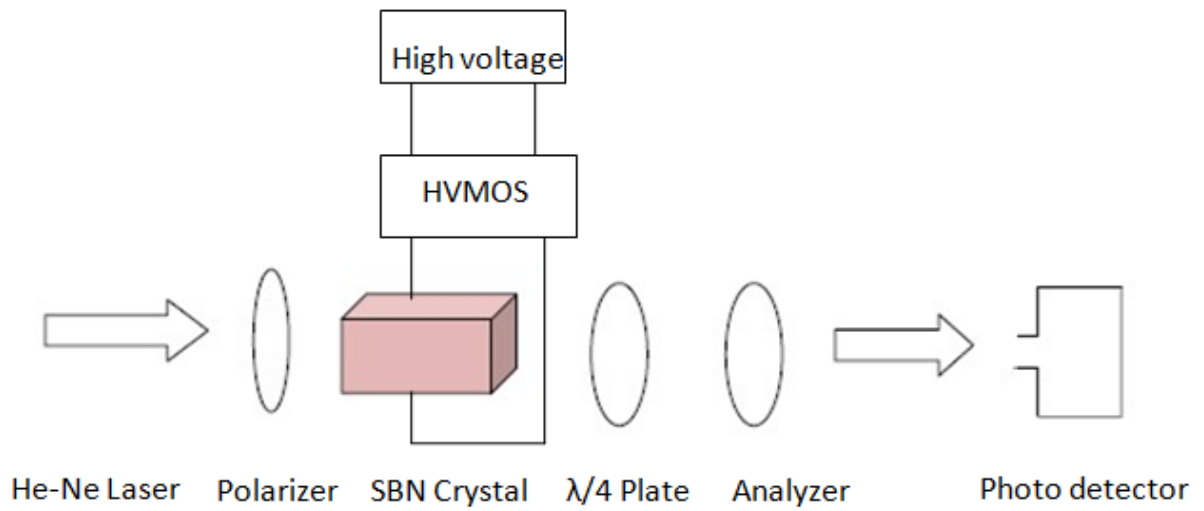


(a)



(b)

Figure 5.3: Image of (a) Single polarity HVFMOS (b) Single polarity HVFMOS under test

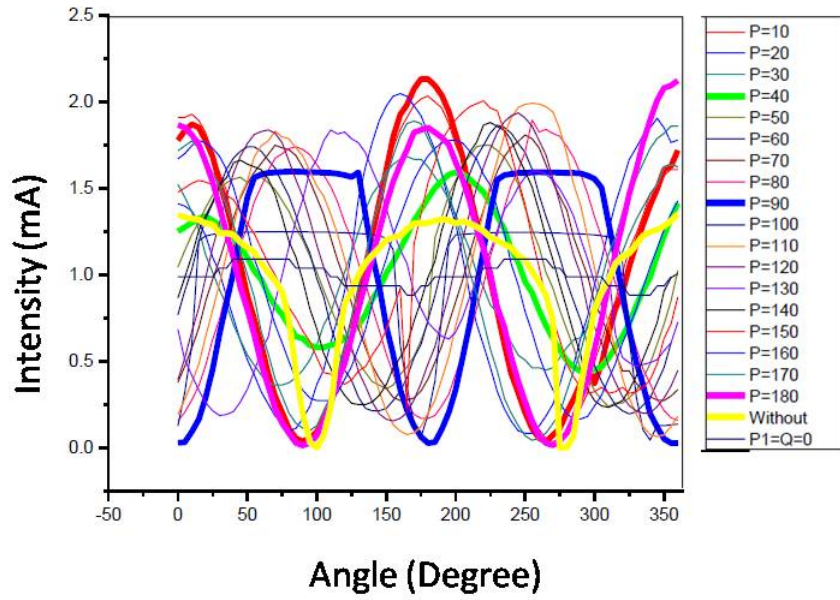


(a)

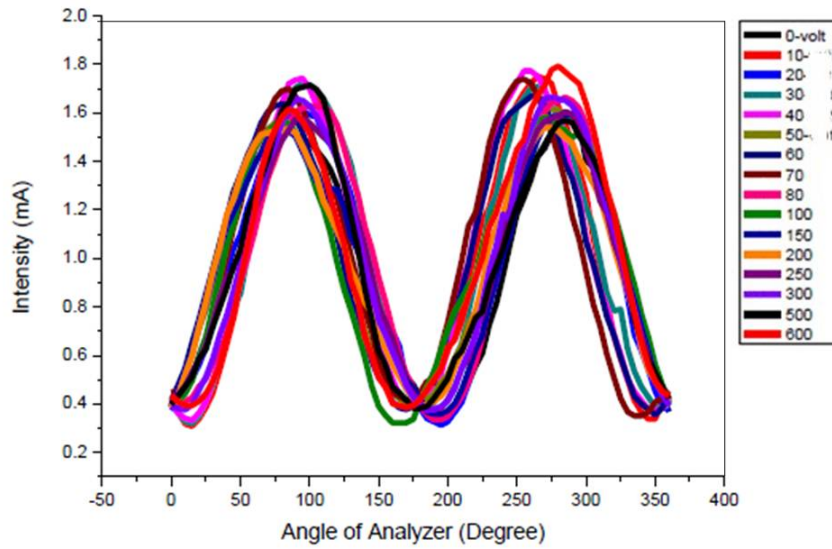


(b)

Figure 5.4: Electro-optic modulator (a) Schematic (b) Experimental setup



(a)



(b)

Figure 5.5: (a) Optic axis of SBN crystal is found to be 40° (the intensity without crystal (yellow) matches with SBN crystal 40° (green) data) (b) Angle and voltage graph for finding the proper operation of the setup

and eqn. 5.2. Thus the light beam coming through the SBN crystal become switched ON and OFF depending on the TTL pulse generator input of the HVFMOS. Thus the intensity of the beam is measured by using photodetector, and the width and frequency of this switching are controlled by TTL of HVFMOS. The setup can also be called as the transverse electro-optic modulator as the voltage is applied to opposite direction of propagation of light. The SBN crystal is aligned with its optical axis in line with the propagation direction of the light beam and is uniaxial with no external electric field present. Due to the birefringence of the crystal material, a properly constructed Pockels cell behaves as an optical retardation plate. Linearly polarized light entering the crystal is split into ordinary and extraordinary rays, each with different indices of refraction and therefore have different wavelengths in the crystal medium. The phase relationship, and hence the polarization of the light as it exits the crystal, can be determined by the length of the crystal.

At a particular axis, the two components of light travel with the same velocity. Here the change in the refractive index does not occur, and different crystal has different nature of optic axis. For finding optic axis, initially, the output light by the photodetector is observed without crystal. After that, the intensity of output beam is studied with crystal at the different angle of the polarizer. The graph of intensity versus polarizer angle is drawn to obtain the optic axis of the SBN crystal used, and is found to be 40° (Figure 5.5a).

For finding the appropriate switching voltage applied to the crystal, the transmission at different voltage and angle of the polarizer is studied. The angle scan has done by rotating the analyzer at the different angle. This procedure is repeated for different voltage and angle, and at a particular voltage and angle the intensity reaches its peak value [5.5b].

After finding the angle and operating voltage, the switching effect on the crystal in a transverse mode of operation is studied, in which the applied field is applied normal to the direction of propagation. The reason for this mode is that the field electrodes do not interfere with the optical beam, and the retardation being directly proportional to the product of the field. The switching action of laser light has been observed on the oscilloscope (Figure 5.6). The phase of laser light could change in two ways. First, by changing the angle of the analyzer. The intensity of switching of the beam can be

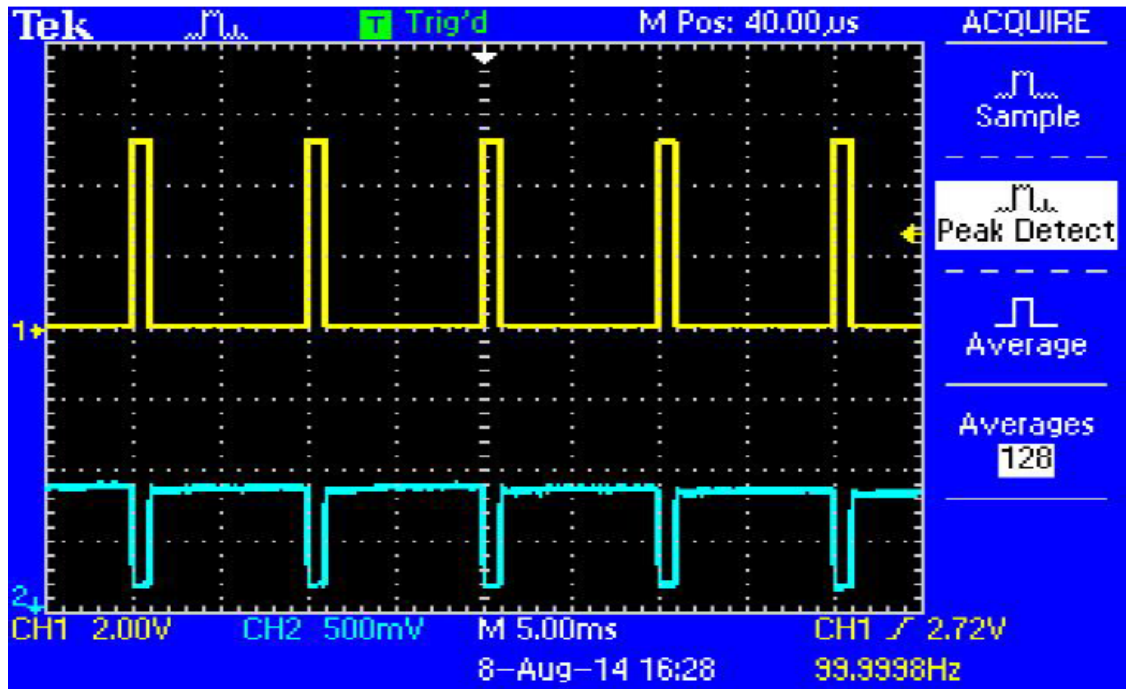


Figure 5.6: Switching performance (yellow color represents the output of HVFMS and blue color gives the output of switching of laser beam)

controlled by the change in the angle of the polarizer. At an angle 40° the maximum intensity of laser switch was achieved. Second, to change the phase of switching of light is to change the voltage. At different voltages, different phase of the laser beam is achieved. This is explained as wave coupling for linear electro-optic effect [149]. The frequency and width of switched laser light are same as the frequency and width of the electronic switch. Thus the rise time and fall time of optical switching in nanosecond range are achieved. So, this switch can be used for the electro-optic modulator and also for the different optical application like Q-switching.

5.2.2 Calibration and Testing of Cylindrical Mirror Analyser

Calibration of the spectrometer requires a knowledge of the absolute voltage, the slope, and the linearity of the scan. For this purpose, it is useful to have convenient standards spanning a range of kinetic energies by which these quantities can be measured. Electron kinetic energy spectra are typically obtained by measuring the counting rate of the electrons detected in the spectrometer as a function of the voltage applied to the spectrometer.

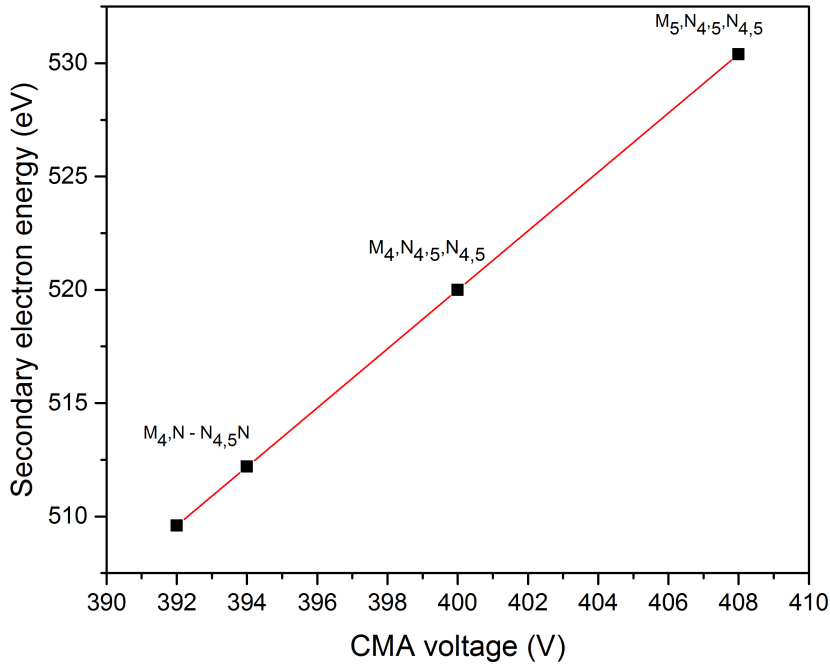


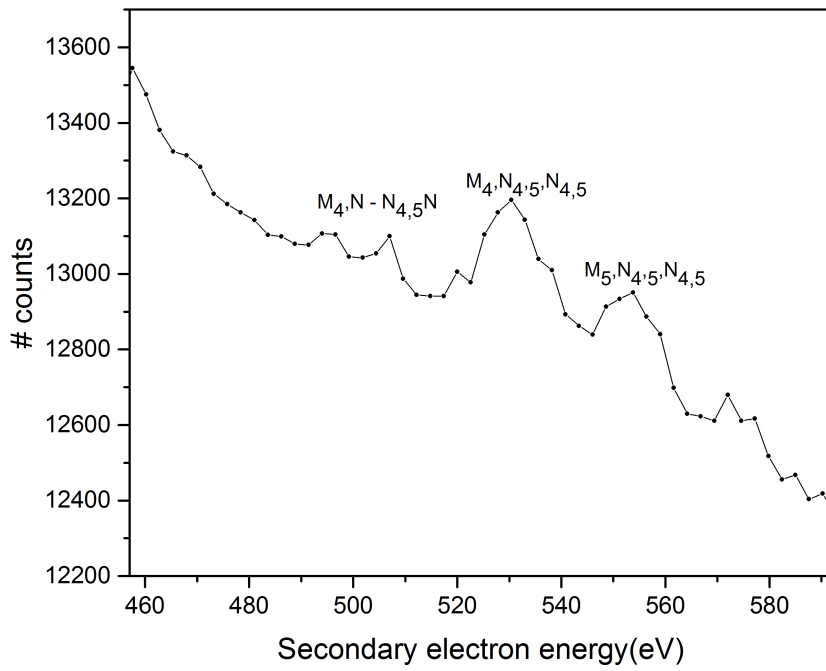
Figure 5.7: Calibration curve for CMA drawn from Auger electron spectrum of Xenon

Ideally, the kinetic energy is linearly related to this voltage with unit slope. In the real world, however, it is possible (and even likely) that the slope is not exactly one, that the scale is not exactly linear, and there is an offset between the true and apparent kinetic energy scales. In typical systems, the offset can be greater than 1 eV. In a cylindrical mirror analyzer, the pass energy E_0 directly depends on the potential difference ∇V , applied between the cylindrical electrodes and is given as,

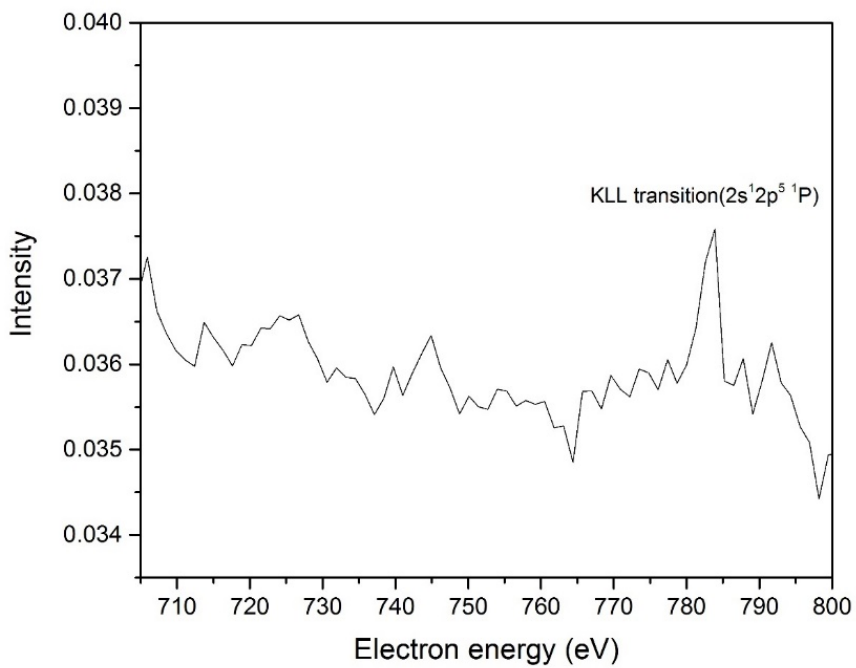
$$E_0 = kV, \quad (5.3)$$

where k is the calibration factor, a function of the geometry and dimensions of the device, and the CMA, $k= 1.3$. The Auger process of inert gases (Ar, Ne, Xe) has been utilized to calibrate the system. CMA calibration drawn for the Auger electron of Xenon is shown in Figure 5.7.

The high-energy electron Auger process for Xenon has been chosen because low energy Auger electrons can interfere with background electrons. M_{4,5}NN Auger of Xenon [150]

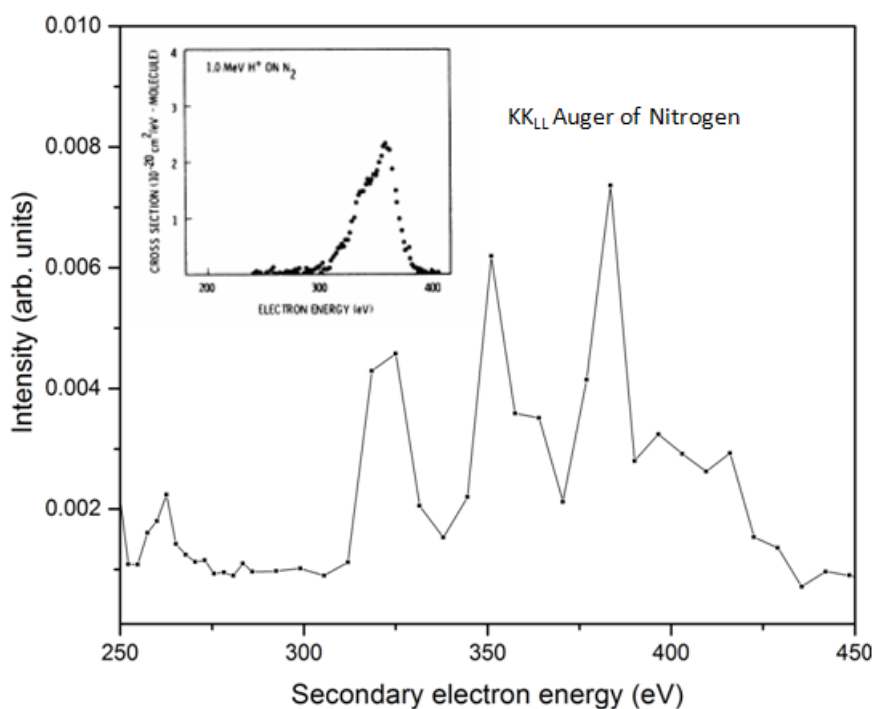


(a) Auger electron spectrum of Xenon



(b) Auger electron spectrum of Neon

Figure 5.8: Secondary electron (Auger) spectrum of atomic targets

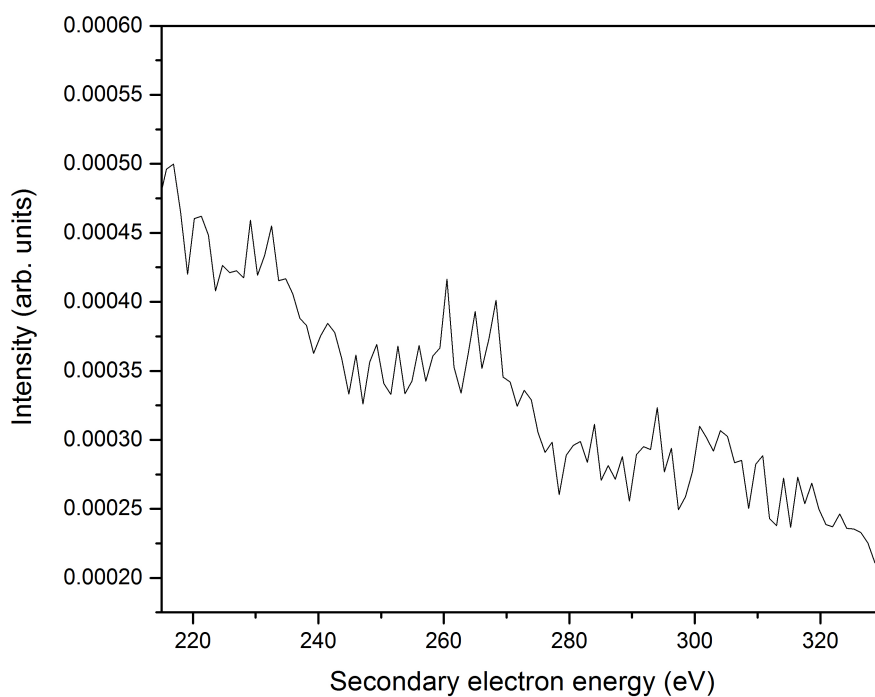


(a) Secondary electron spectrum of Nitrogen

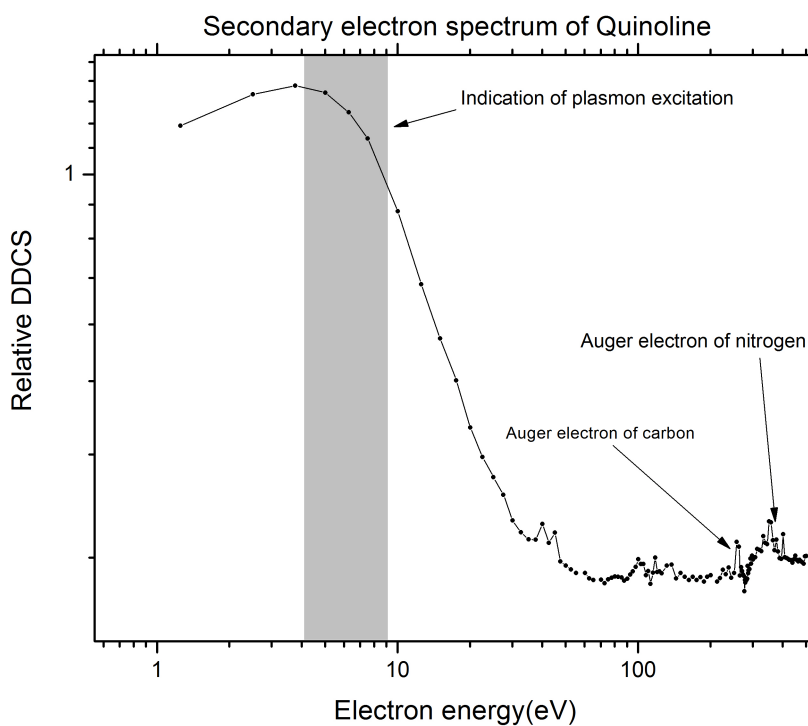
Figure 5.9: Secondary electron spectrum of diatomic molecular target (KLL Auger reported in the literature)

and is a good source for calibration. The corresponding energy for this Auger are at 509 eV, 525 eV, and 545 eV, and the secondary electron from Xe shows a significant enhancement in the intensity as compared to the energies nearby from the electron spectrum (Figure 5.8a). A one to one peak comparison with the high-resolution reported [150] data is not possible in this case since the resolution is 4.5%, which is moderate. The resolution with comparatively large entrance and exit slit for high transmission is compromised. The Auger electron spectrum of atoms (e.g. Neon Figure 5.8) and diatomic molecules (e.g. N_2 Figure 5.9a) has been studied. The electron spectrum of large molecules like Benzene (C_6H_6), Quinoline (C_9H_7N) are shown in Figure 5.10a, Figure 5.10b as the preliminary test. The quinoline electron spectra shows the regular rapid decrease in the cross sections as a function of the energy but a pronounced broad peak is observed approximately 8 eV. Similar feature is observed in the case of DDCS measurement in coronene ($C_{24}H_{12}$) nearly to 17 eV which is associated to collective (plasmon) electronic excitation [151, 152].

The energy angular distribution of the secondary electron will be available when the electron with its position is recorded. The 2D projection of the electron on the detector

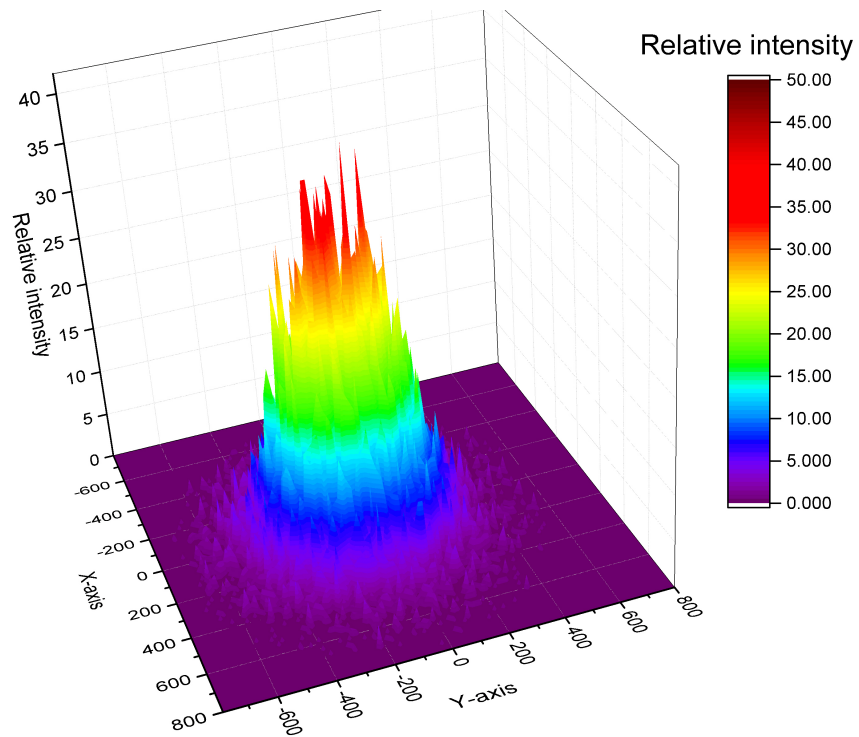


(a) Secondary electron spectrum of Benzene under 1000 eV electron impact

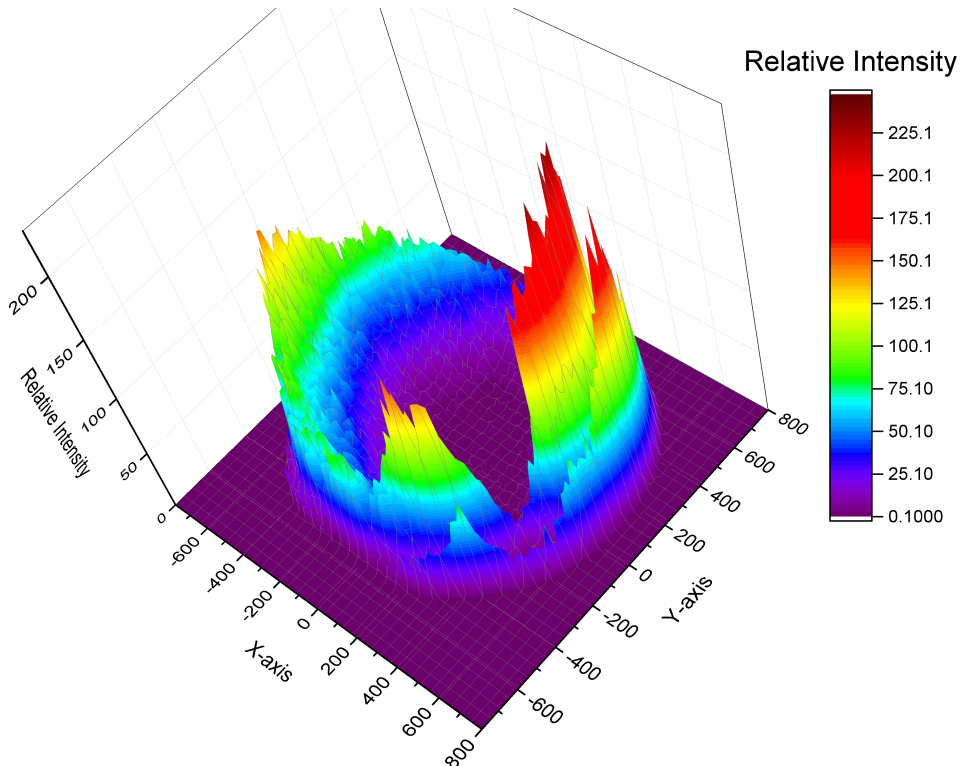


(b) Secondary electron spectrum of Quinoline under 1000 eV electron impact

Figure 5.10: Secondary electron spectrum of molecular targets

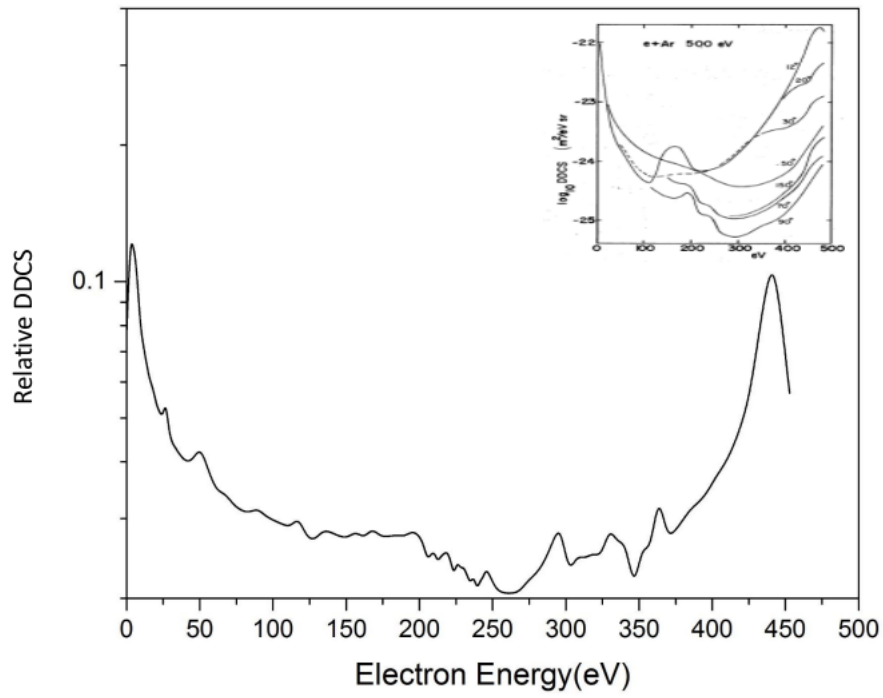


(a)

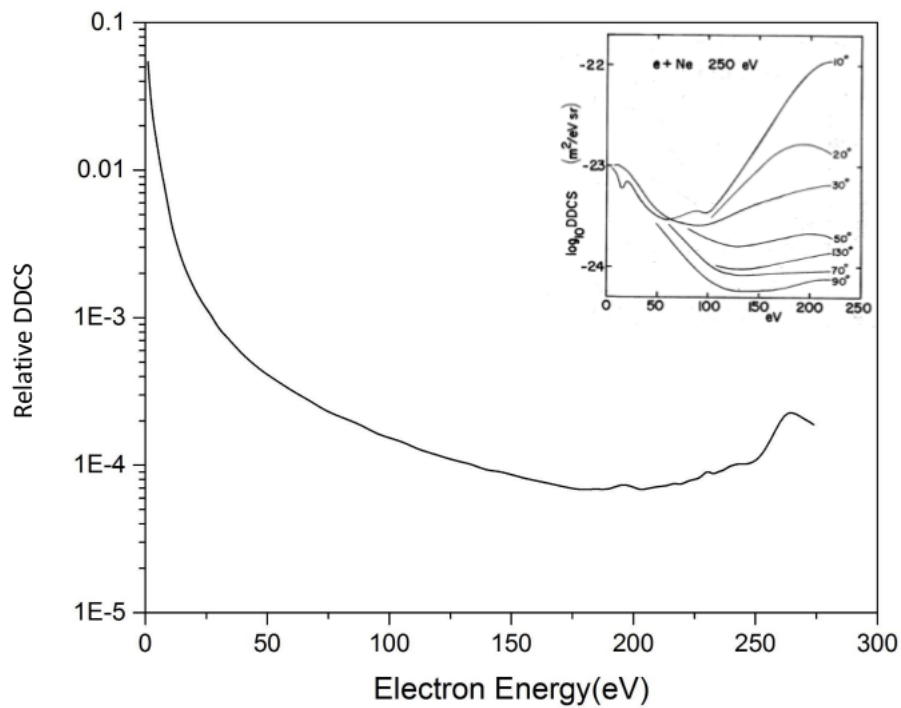


(b)

Figure 5.11: Secondary electron spectrum from Xe projected on PSD kept at (a) Focal point of CMA (b) 10 mm away from focal point of CMA



(a)



(b)

Figure 5.12: Differential cross section for Argon at (a) 500 eV electron impact (b) 300 eV electron impact (inset data are the DDCS of argon reported)

will form a circular ring, and if projected as the intensity, it will have intensity variation as per the angular distribution, if the emission of secondary electron prefers any particular angle. The position of Xenon secondary electron is recorded with position sensitive detector (PSD) at the focal point of the CMA (Figure 5.11a) as well as 10 mm far away from the focal point of CMA (Figure 5.11b). In the first case, even though the secondary electron is focused at the PSD center, it will not give any angular and energy distribution. For that, the detector needs to be kept away from the focal point as explained.

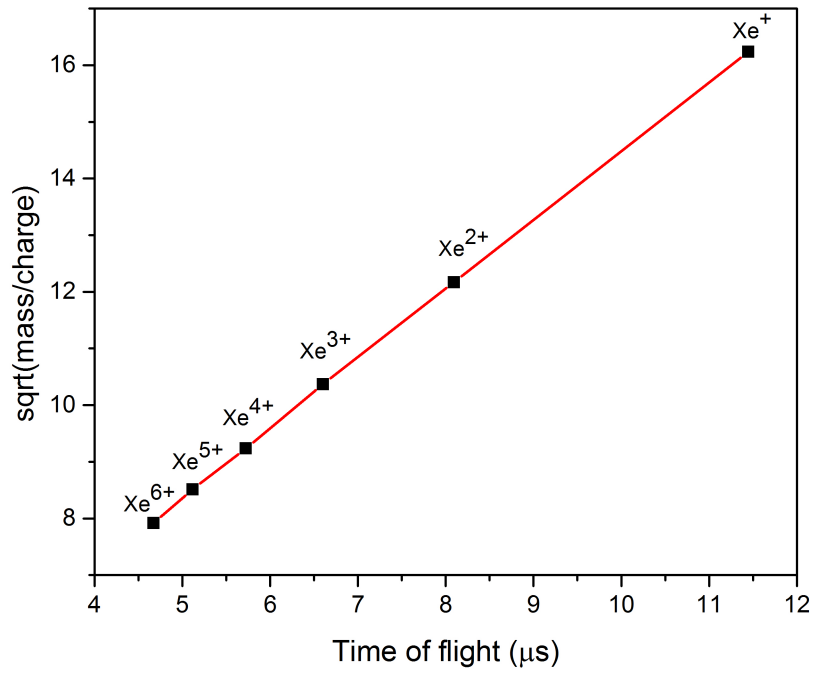
The CMA is used as the electron spectrometer for the study of the secondary electron differential cross section of argon (Figure 5.12a, Figure 5.12b) and the angles of emission were 43° . Relative differential cross sections for argon were measured for selected secondary electron energies by manually adjusting the analyzing voltage and recording the scattered signals. These results match with the published results [153]. Often the count rate had to be kept low to avoid secondary electron emission from the components. This led to the requirement to take several scans of the electron spectra under the same condition. The electron beam tuning and the rest of the system were made very stable to maintain steady count rate under fixed conditions. Then the Arduino based simple pulse counting and spectrometer voltage scanning system were used in subsequent tests. This arrangement helped in taking good quality data with sufficient statistics.

5.2.3 Calibration and Testing of Time-of-Flight Mass Spectrometer

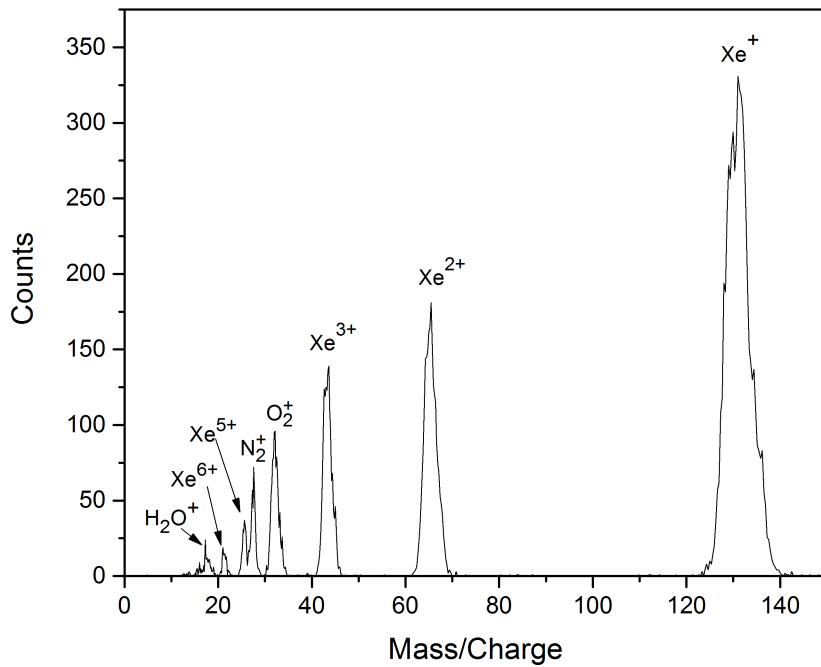
The accurate linearity between the time of arrival of various atomic and molecular ion, and fragments, and the corresponding mass spectra is tested by a proper calibration of time-of-flight mass spectrometer. For calibration purposes, the Xenon time-of-flight spectrum is recorded and the calibration curve (Figure 5.13a). calibration equation obtained after the linear fit is given as,

$$\sqrt{\frac{m}{q}} = 1.21206 \times \text{time of flight} + 2.36318 \quad (5.4)$$

A typical ToF spectrum of Xe produced by collision with the electron at 1000 eV is shown in Figure 5.13b. A maximum of six-fold ionization of Xe was obtained. The main

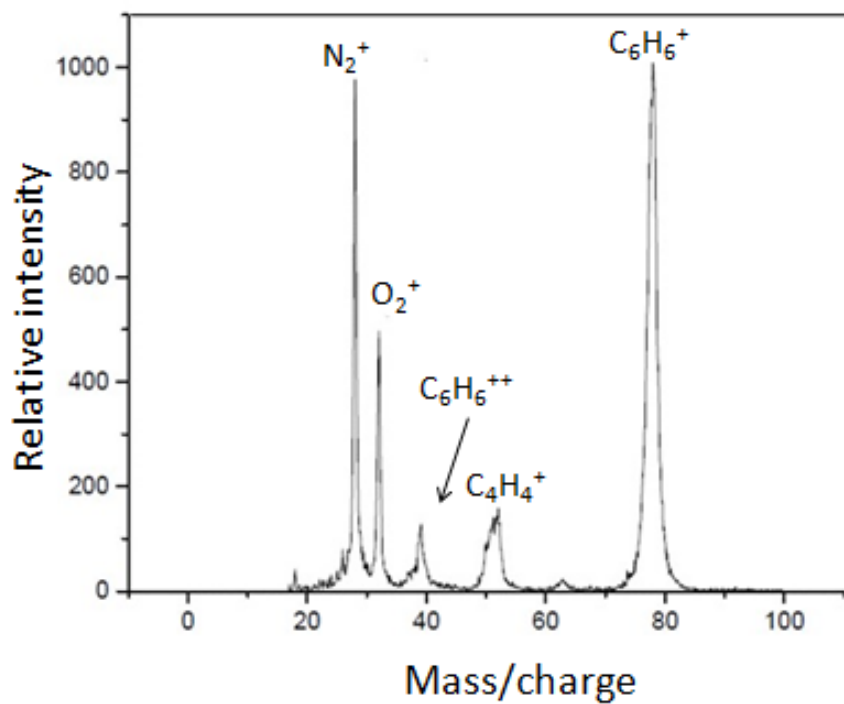


(a)

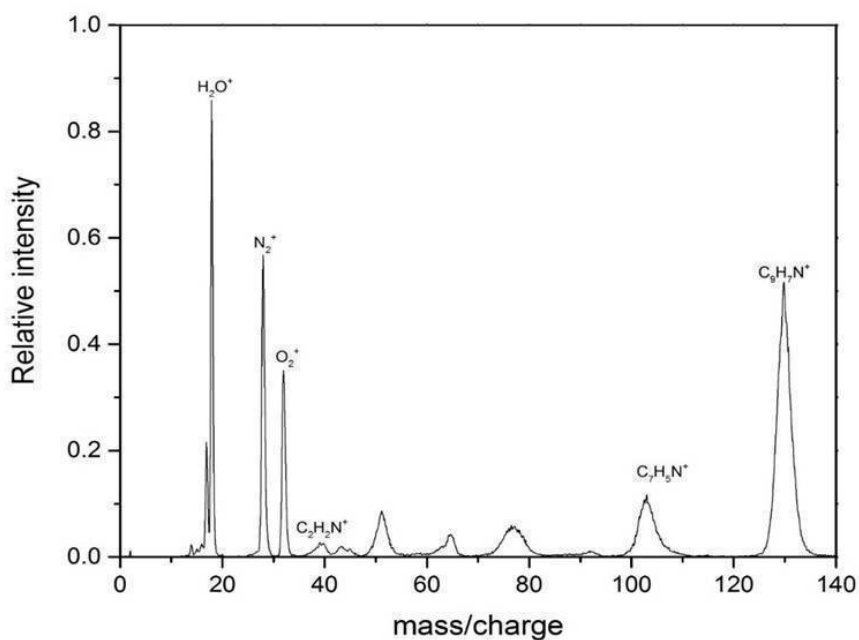


(b)

Figure 5.13: (a) Calibration curve for ToFMS drawn from Xenon (Xe⁺ – Xe⁶⁺) time of flight (b) ToF mass spectrum of Xe under 1000 eV electron impact



(a) ToF Mass spectrum of Benzene at 1000 eV electron impact



(b) ToF mass spectrum of Quinoline under 1000 eV electron impact

Figure 5.14: ToF mass spectrum of molecular targets

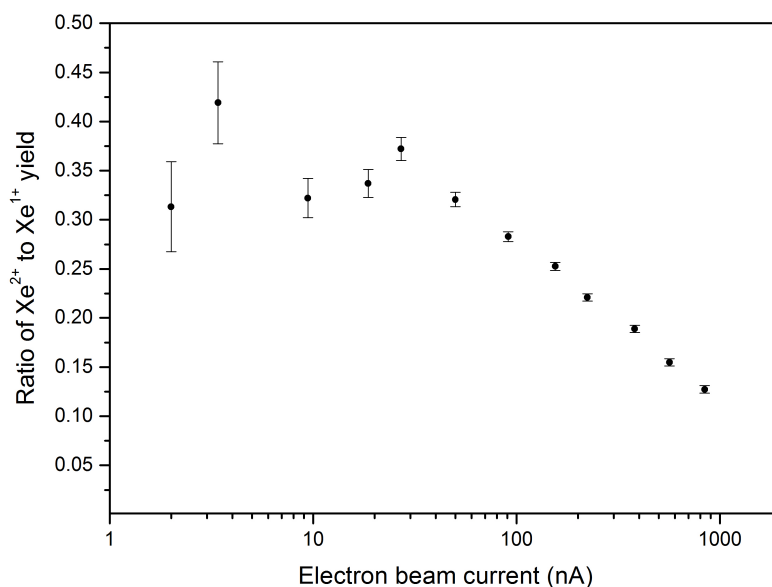


Figure 5.15: $\frac{Xe^{2+}}{Xe^{1+}}$ as a function of projectile electron beam current

characteristic of the ToF-MS is its mass resolution $\frac{\Delta m}{m} = \frac{1}{101}$ with 60 V/cm extraction field. The ToF of the molecules like benzene, quinoline is taken as the preliminary test (Figure 5.14a, Figure 6.3b) The ToF-MS under delayed extraction of molecular ions is tested and the details will be discussed in Chapter 6.

Electron beam energy distribution over beam current is an important information to reduce the halo of the beam. The ToF of Xe as a function of beam current and is plotted and the yield of $\frac{Xe^{2+}}{Xe^{1+}}$ (Figure 5.15) is studied for this purpose. At higher beam current, the production of Xe^{1+} is higher because the halo of the projectile beam can hit any of the electrode plates and cause low energy secondary electron production. These low-energy electrons will interact with the Xe target and produce Xe^{1+} .

5.3 Multi Coincidence Experiment

The last critical test was to demonstrate the actual functionality of the setup with energy analyzed electron detected in coincidence with the correlated ion. This was very essential for the success of this work. The count rates on the two detectors are highly dissimilar under the best of the condition. This caused severe problems due to chance coincidence.

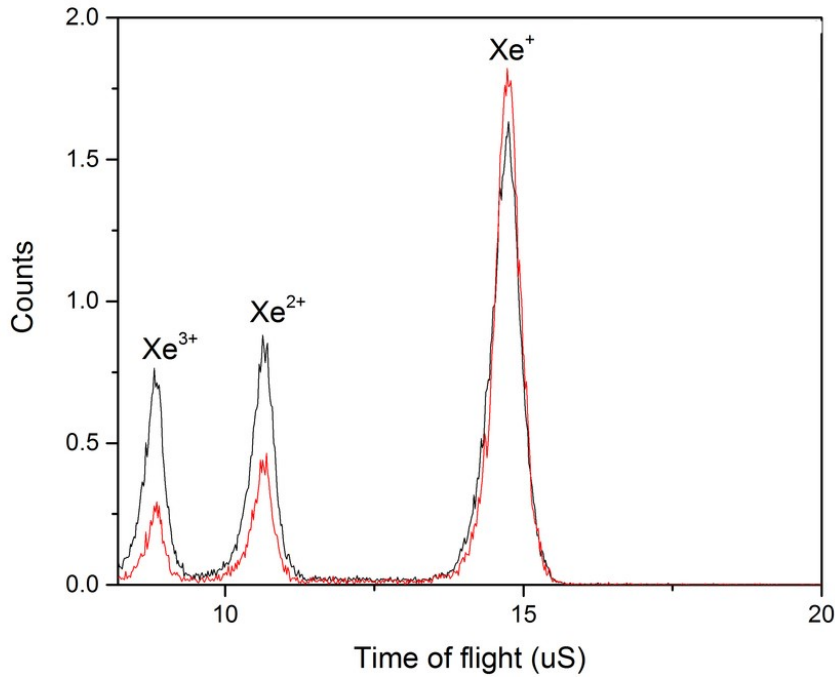
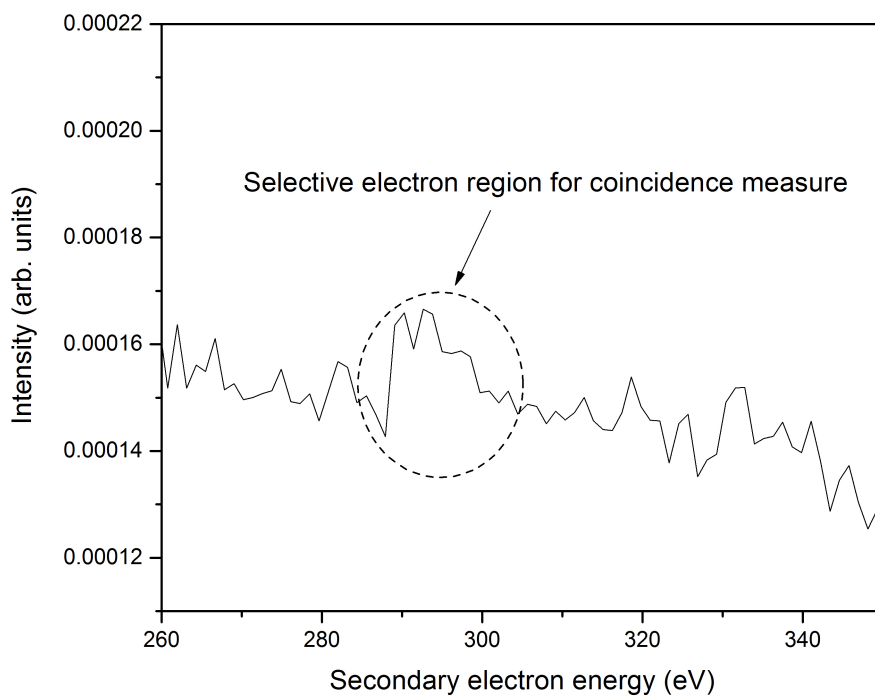


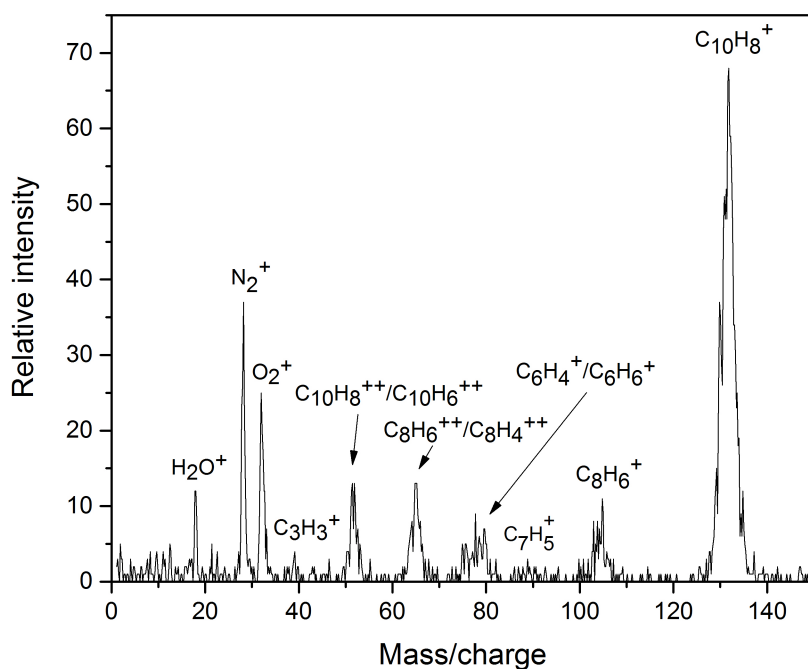
Figure 5.16: ToF mass spectrum of Xenon in coincidence with secondary electron

Typically, a coincidence rate of about 10 Hz is desirable to avoid too much chance coincidence. The effect of such coincidence using Xe as the target is demonstrated here.

The coincident data was acquired with each event being characterized by five timing signals, one giving the time-of-flight of the ion w.r.t. the start-off trigger and the remaining four contains the X-Y position information of the energy analyzed electron. Since the electron detection pulse is not only recorded but also is used to trigger extraction of the recoil ion, it was essential to arrange complex logic sequence to avoid contamination of the data with pulsing noise. The details of the DAQ scheme is discussed previously (Section 4.12.3). The mass spectra in coincidence with random trigger pulses are recorded and compared with the mass spectra at one of the Auger peaks (520 eV). As one can expect at the Auger peak the intensity of the double or triple ionization will enhance in the mass spectra over singly charged Xe. Due to moderate resolution, the Auger peaks were not very well resolved in the studied energy range. Hence the yields of multiply charged Xenon ions vary according to auger process (shown in Figure 5.16) is observed. The random electron-coincidence spectra are shown in the same graph. As a preliminary



(a)



(b)

Figure 5.17: Naphthalene (C_{10}H_8) (a) Secondary electron spectrum (b) ToF mass spectrum in coincidence with energy selective secondary electron

test, the electron-ion coincidence measurement is done for naphthalene (Figure 5.17). Furthermore, when CMA and ToF-MS are used in unison, the information regarding the dissociation dynamics, preferred channels of dissociation is obtained when a secondary electron of specific energy is emitted. More importantly, this instrument has the provision to measure the fragmented ion in coincidence with position and energy of the secondary electron along with the projectile electron energy loss. This makes this instrument to work in a complicated triple coincidence system. Currently, the study of the correlation between secondary electron emission and fragmentation dynamics of large molecules is in progress.

Chapter 6

Electron Impact on PAHs and PANHs

Electron impact ionization is one of the oldest mass spectrometric tools which focuses on identifying the possible ionization and fragmentation channels of molecules. In past, several electron impact ionization investigations have been done mainly on inert gases, diatomic or triatomic molecular gases within the range of 70 - 100 eV beam energy [154]. Several experiments and modeling attempts have been made for such studies with electron energy up to a few keV [155–157]. But such studies are very rare for larger molecules due to the complexity from numerous decay channels and difficulties in separating direct and indirect ionization processes. Target specific energy loss modeling in charged particle interaction with molecules has been attempted in some specific cases [158].

The complexity of mass spectrometric studies in polyatomic molecules arises from the fact that several indirect ionization/fragmentation channels are present in such molecules [59, 159]. Such indirect processes span a large range of decay time constants and are often nested, leading to difficulties in identification of a channel and interpretation [160]. In the context of PEPICO spectroscopy, the excess energy left in the molecule after the photoionization process plays a vital role in deciding the decay pathways of the molecular ions [59]. Similarly, in the case of charged particle interactions, the mechanism of energy loss decides the internal energy of the recoil ions and possible decay channels [14, 161]. In the past few years, plasmon excitation in fullerene and PAHs have been shown to be a very prominent indirect ionization channel [35, 161]. For fullerene, the plasmon excitation is centered around 21 eV energy and is shown to cause the ionization of C₆₀ molecule [35]. The residual energy is shared between the outgoing electron and the internal heating of the fullerene molecule. In the case of PAHs, the plasmon excitation peak is at 17 eV and it has been shown recently to cause internal heating of the molecule by an amount of 8 to 9 eV [14, 161]. It is also seen that acetylene C₂H₂ loss comes as a by-product of such plasmon excitation with a very specific range of decay constants.

Electronic delocalization plays a crucial role in deciding the stability of aromatic molecules. This delocalization gives rise to very interesting properties in molecules like polycyclic aromatic hydrocarbons (PAHs) and is the reason behind their abundant existence in the interstellar medium as well as in the earth's atmosphere [162, 163]. Therefore any radiation damages to such molecules cannot be assessed without taking into account the spread in the electron density for a given molecular orbital and, in some cases resulting in the collective behavior [27, 35, 60, 161, 164]. Photoinduced ionization and dissociation remain the most selective measurement in terms of the internal energy deposited into the molecules by the radiation. Most commonly known techniques for such measurements are the PEPICO and T-PEPICO spectroscopy [36]. In these experiments with the help of the energy analysis of emitted electrons, a precise value of the internal energy and therefore a very narrow range of decay constants can be experimentally obtained for a given statistical dissociation channel [59, 160]. On the other hand charged projectiles would deposit a broad range of energies, hence making the process of estimating the internal energy very complex, even if the secondary electron energy is tracked. Thus it becomes impractical to use conventional ToF mass spectroscopy techniques to study the dynamics of statistical decay in charged particle collisions.

A molecular system with a given internal energy is prone to decay by statistical decay process. This process is usually modeled as an Arrhenius type unimolecular dissociation process. The decay constant for such evaporation channel is given as,

$$k = Ae^{\left(\frac{E_a}{k_B T}\right)}, \quad (6.1)$$

where A is the frequency factor, E_a is the barrier energy for decay, k_B is Boltzmann constant and T is the temperature due to the internal energy of the molecule. For a given internal energy of the molecule, the decay curve will be exponential in time. But for a range of internal energies, the decay function will be a more complex combination of multiple exponential decays due to a range of decay constants.

In this work, an attempt is made to investigate the interaction of high-energy electron beam with PAH and PANHs, then assess the time dependence of C_2H_2 evaporation in comparison with the other channels using a TOF mass spectrometer. In electron im-

compact experiment, permanent extraction field for recoil ion is to be compensated, since it could affect the projectile beam adversely [142], which in turn can affect the range of usable beam energies. Pulsed extraction of recoil ion is an alternate method, which offers a possibility of having a variable delay between the formation and extraction of recoil ion. But the main disadvantage of this method is the relatively poor mass resolution [165] owing to which the technique is applied less often. A few systematic measurements using this technique in the electron-molecule collision have been reported recently [166], in which delayed extraction time-of-flight (DEToF) was employed in order to measure kinetic energy distributions of electron-molecules collision products and disentangle different fragmentation pathways and moieties with the same mass-to-charge ratio. We have implemented the same technique of DEToF here, to investigate the time-dependent population of the produced fragments in high-energy electron-PAH collision.

6.1 Delayed Extraction Time-of-Flight

The versatility of our electron-ion coincidence experimental set-up enables us to explore a rather uncommon technique of delayed extraction time-of-flight (DEToF) [Figure 6.1]. The pulsed extraction of ions in a ToF setup can be used to analyze the evolution of a time-dependent population of various fragmentation channels of PAHs and PANHs. If the decay constants are in the range of $10^5 - 10^6$, then it becomes possible to probe the system within sufficient time so that the thermal velocity dispersion does not affect the collection efficiency. Though such a system has limited applicability, it has helped in the present investigation to assess the evaporative loss from a PAH/PANH molecule due to electron impact. The instrumentation presented here is very effective under such conditions.

Astro-biologically important statistical dissociation channels of the PAHs and PANHs are probed using DEToF. We choose naphthalene as our PAH sample, its two derivatives quinoline, and isoquinoline as PANHs since it exhibits all the properties of large PAHs/PANHs even though it is the smallest in that class. Generally, for naphthalene and its nitrogen-containing derivatives, the loss of H and C_2H_2/HCN are the most dominant

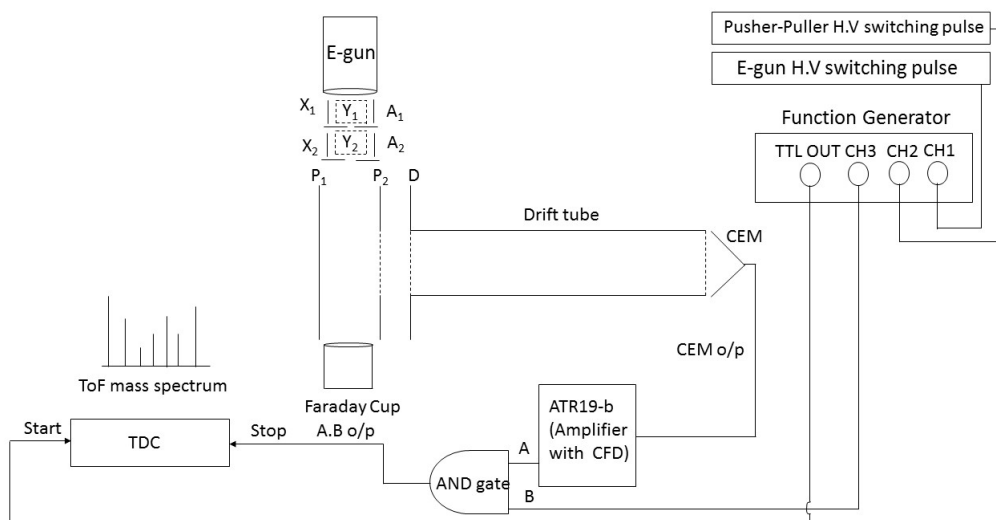


Figure 6.1: DEToF experimental schematic (first acceleration region: region between P_1 and P_2 , second acceleration region: region between P_2 and D)

statistical dissociation channels. Statistical decay channels show increasing the yield of daughter ions as a function of extraction delay in the order of 10^6 s^{-1} decay constant, whereas the yields due to fast dissociation channels were observed to decrease as a function of extraction delay. On the basis of the projectile beam energy dependence of the yield, the effect of plasmon excitation in quinoline and isoquinoline is shown for the first time.

6.2 DEToF Experimental Setup Details

We use a Wiley-McLaren-type ToF mass spectrometer [167] with the pulsed extraction technique for detection of the product-ions. The schematic diagram of the experimental set-up with the data acquisition module is shown in Figure 6.1. The spectrometer consists of a pusher (P_1) as well as puller (P_2) plate of thickness 1 mm and an outer diameter of 105 mm. The puller plate has an opening diameter of 26 mm and is covered with a nickel mesh characterized by 16 lines per cm, for field uniformity. This allows a transmission efficiency of 95% of the ions. For the field-free drift of ions, we have a drift tube of length 200 mm with an opening of 25 mm covered by a nickel mesh for field uniformity, which is identical in characteristics to the one used for covering the opening of the puller plate.

The gap between the pusher (P_1) and puller plates (P_2) is 16 mm while that between the puller and the drift tube is 5 mm. A home-built, low current high energy (1-5 keV) electron gun is used for ionizing the target molecule. The filament produces electrons via thermionic emission with a heating current of about 180 mA. Two sets of XY deflectors are mounted beyond the focusing lens. We use two apertures (A_1 , A_2), one between the two deflector sets (A_1) and the other after the deflectors (A_2), to avoid the secondary electrons from the internal scattering of the beam to reach the interaction region. The energy of the electron beam is decided by the floating voltage of the whole electron gun assembly. The electron gun operates in a pulsed mode with a variable ON time width. For pulsed extraction ToF, we have used home-built high voltage MOSFET switches, which can switch the high voltage in the push-pull mode with a 50 ns rise and fall time. A cylindrical shaped Faraday cup of length 100 mm and radius of 25 mm, biased to +36 Volts is used to collect the projectile electrons. The target molecule is introduced into the interaction zone that is well localized in space through a fine capillary of internal diameter 300 microns and length of 15 mm. The capillary exit is kept nearly 5 mm away from the center of the ToF interaction region to avoid any possible secondary electron emission due to the electron beam colliding with the capillary. We have used a channeltron (CEM) for the detection of ions, with a bias voltage of -2600 Volts. In addition, we pulse the electron gun and the pusher-puller plates for delayed ToF mass spectrometry as per the pulsing sequence is shown in Figure 6.2. Ions produced in the interaction region (region between P_1 and P_2) are accelerated by the electric field and compensated for the spatial spread in the second region (region between P_2 and D) before entering the field-free drift tube followed by the ion detector. The data is acquired using a multi-hit time-to-digital converter data acquisition system (Agilent TDC Model: U1051A). A gate pulse is used to filter out the switching noise picked up by the detector channel.

The target sample vapor was introduced into the setup at room temperature in which the RMS velocity of the molecules is $\sim 240 \mu\text{m}/\mu\text{s}$. Thus, it is very important to design the ToF in such a way that the drift of target molecules between the electron pulse and the extraction pulse do not reduce the collection efficiency. It is important to account for the extraction pulse rise time in order to have a constant collection efficiency over different extraction delays. This was achieved by using high extraction field of 125 V/cm

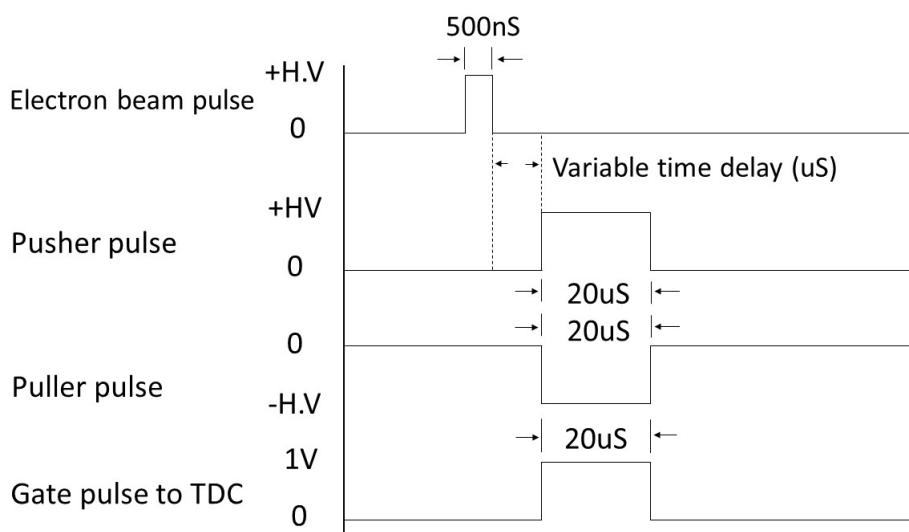


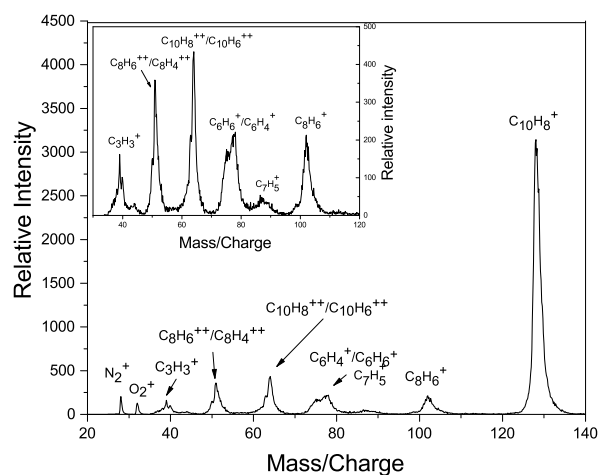
Figure 6.2: Pulsing sequence for DEToF

(interaction region). By doing an ion trajectory simulation with the help of SIMION8.0 we arrived at these settings. To check the collection efficiency, the simulations are done with all the three molecules by a spherical distribution of the source of diameter 6 mm and an RMS velocity twice as large as the value at 300 K, that is $480 \mu\text{m}/\mu\text{s}$ as the worst case scenario.

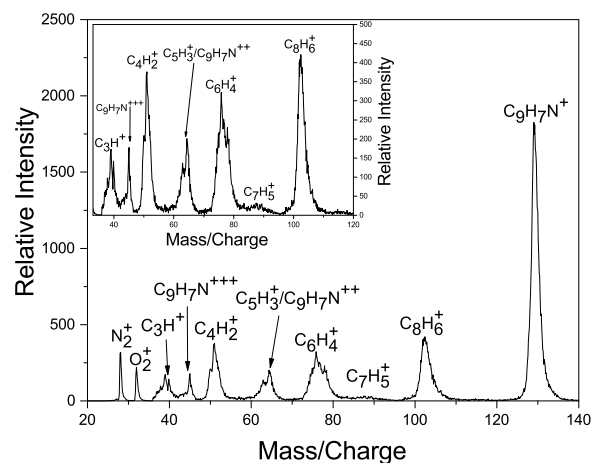
6.3 Analysis and Results

The typical mass spectra for the three cases are shown in Figure 6.3. The major mass peak groups can be identified with appropriate carbon and nitrogen-containing fragments. Due to the proximity of nitrogen and carbon mass in the ToF and considering the possibilities of multiple H atoms attached to a fragment, it becomes very important to distinguish the exact mass value with an error that is better than 0.5 amu at 64.5 amu and 1 amu at 129 amu, particularly for the doubly charged channels. In order to achieve this and in the absence of higher resolution mass spectral data of these molecules we used our own mass spectra measured in a separate experiment at high energy proton beam collisions with naphthalene, quinoline, and isoquinoline (not shown here). With the help of these mass spectra, we ascertain the possible decay channels in the mass spectra to be expected.

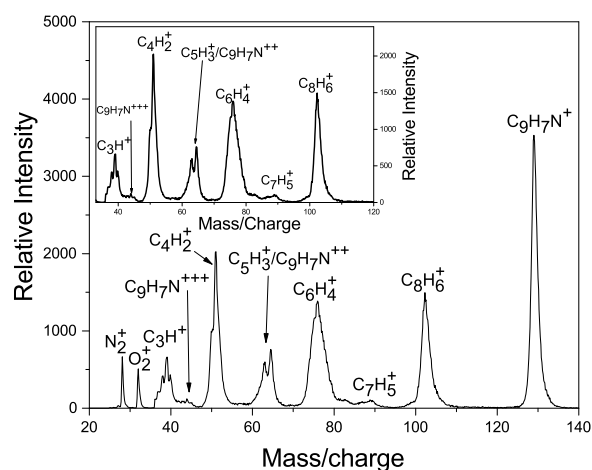
We have considered the following groups of decay channels for our analysis. The



(a)



(b)



(c)

Figure 6.3: Typical Mass Spectrum of (a) Naphthalene ($C_{10}H_8$) (b) Quinoline (C_9H_7N) (c) isoquinoline (C_9H_7N) at 1000 eV electron impact (Inset: in figure (a) fragments of naphthalene, (b) fragments of quinoline, (c) fragments of isoquinoline)

yields are obtained from the mass spectra of each of the mass groups. The other possible channels are generally of negligible intensity and hence they are not expected to affect the yield ratios for a given group.

I) Naphthalene

1. $C_{10}H_8 + e^- \rightarrow C_{10}H_8^+ + 2e^-$

2. $C_{10}H_8 + e^- \rightarrow C_8H_6^+ + C_2H_2 + 2e^-$
 $C_{10}H_8 + e^- \rightarrow C_8H_5^+ + C_2H_2 + H + 2e^-$

3. $C_{10}H_8 + e^- \rightarrow C_6H_6^+ + C_4H_2 + 2e^-$
 $C_{10}H_8 + e^- \rightarrow C_6H_5^+ + C_2H_2 + C_2H + 2e^-$
 $C_{10}H_8 + e^- \rightarrow C_6H_4^+ + C_4H_4(2 \times C_2H_2) + 2e^-$

4. $C_{10}H_8 + e^- \rightarrow C_5H_3^+ + C_2H_2 + C_3H_3 + 2e^-$

5. $C_{10}H_8 + e^- \rightarrow C_4H_4^+ + C_4H_2 + C_2H_2 + 2e^-$
 $C_{10}H_8 + e^- \rightarrow C_4H_3^+ + 2 \times C_2H_2 + C_2H + 2e^-$
 $C_{10}H_8 + e^- \rightarrow C_4H_2^+ + 3 \times C_2H_2 + 2e^-$

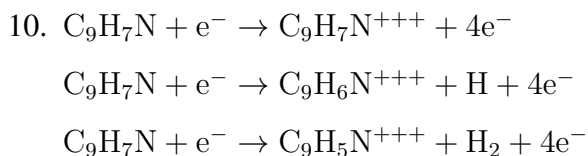
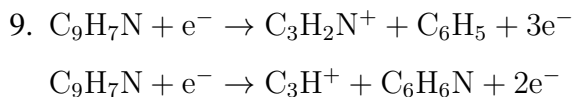
6. $C_{10}H_8 + e^- \rightarrow C_3H_3^+ + C_3H_3 + C_4H_2 + 2e^-$

7. $C_{10}H_8 + e^- \rightarrow C_{10}H_8^{++} + 3e^-$
 $C_{10}H_8 + e^- \rightarrow C_{10}H_6^{++} + 2H/H_2 + 3e^-$

8. $C_{10}H_8 + e^- \rightarrow C_8H_6^{++} + C_2H_2 + 3e^-$
 $C_{10}H_8 + e^- \rightarrow C_8H_4^{++} + C_2H_2 + 2H/H_2 + 3e^-$

II) Quinoline and Isoquinoline

- $C_9H_7N + e^- \rightarrow C_9H_7N^+ + 2e^-$
- $C_9H_7N + e^- \rightarrow C_8H_6^+ + HCN + 2e^-$
 $C_9H_7N + e^- \rightarrow C_8H_5^+ + H_2CN + 2e^-$
- $C_9H_7N + e^- \rightarrow C_7H_5N^+ + C_2H_2 + 2e^-$
 $C_9H_7N + e^- \rightarrow C_7H_5^+ + C_2H_2N^+ + 3e^-$
- $C_9H_7N + e^- \rightarrow C_6H_3^+ + C_3H_4N + 2e^-$
 $C_9H_7N + e^- \rightarrow C_6H_2^+ + C_3H_5N + 2e^-$
- $C_9H_7N + e^- \rightarrow C_5H_2N^+ + C_4H_4 + H + 2e^-$
 $C_9H_7N + e^- \rightarrow C_5H_2N^+ + 2 \times C_2H_2 + H + 2e^-$
 $C_9H_7N + e^- \rightarrow C_5H_2^+ + C_4H_5N + 2e^-$
- $C_9H_7N + e^- \rightarrow C_9H_7N^{++} + 3e^-$
 $C_9H_7N + e^- \rightarrow C_9H_6N^{++} + H + 3e^-$
 $C_9H_7N + e^- \rightarrow C_9H_5N^{++} + H_2 + 3e^-$
- $C_9H_7N + e^- \rightarrow C_6H_6^+ + C_3H_2N + 2e^-$
 $C_9H_7N + e^- \rightarrow C_6H_4^+ + C_5H_4N + 2e^-$
- $C_9H_7N + e^- \rightarrow C_4H_2^+ + C_5H_5N + 3e^-$



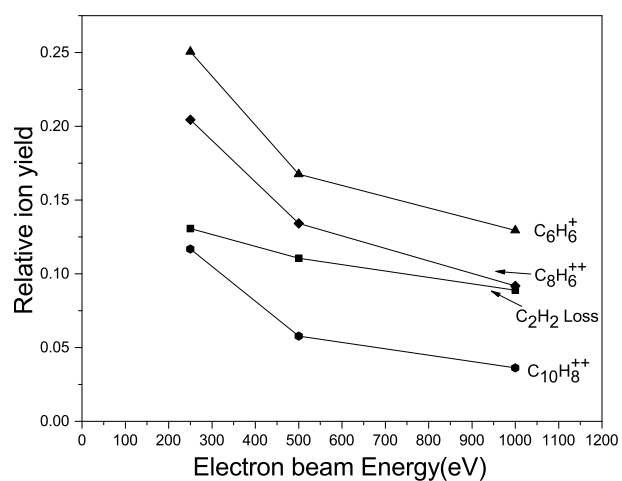
Generally, for PAHs and PANHs, the loss of H and C₂H₂/HCN are the most dominant statistical dissociation channels. The CEM detection efficiency, which strongly depends on the velocity of the ion hitting the detector, causes a lower detection efficiency as a function of increasing the mass of the fragment [168]. Hence the actual HCN loss intensity is higher than what appears in the mass spectrum. Since our main goal here is to compare relative yields of identical mass fragments with different targets, the efficiency correction is not expected to affect the analysis. Compared to PANHs, naphthalene clearly shows much higher stability with the fragmentation yields in comparison with the low stability of fragmentation yields of singly charged ions. Similarly, the second ionization yield is larger compared to adjacent fragment peaks in naphthalene highlighting the stability of naphthalene di-cation over the other two targets. The C₂H₂ loss channel is important in naphthalene whereas HCN loss is an important channel in the other two PANHs. The activation barrier for the C₂H₂/HCN loss has been reported for naphthalene, quinoline and isoquinoline to be 4.13 eV [160], 4.17±0.05 eV and 4.03±0.05 eV [12] respectively. The kinetic shift, i.e. the excess energy required to have the decay constant in the order of 10⁶ s⁻¹ for C₂H₂ loss in naphthalene is about 4.2 eV whereas for the HCN loss in the PANHs considered here it is about 2.7 to 3 eV, which is calculated using the Rice-Ramsperger-Kassel-Marcus quasi-equilibrium theory (RRKM/QET) [160]. Thus, it is expected that the PANHs show a much larger yield of HCN loss compared to the C₂H₂ loss in naphthalene. For the *decay channel no. 5*, in this time scale, the mechanism of formation is less clear and hence it is hard to associate it with any individual decay process. The other fragments are much stronger in PANHs. The most significant observation is a higher tendency of isoquinoline compared to quinoline towards fragmentation. Both PANHs show a H₃ loss in the double ionization peak as the prominent channel. The origin

of this channel is difficult to ascertain. A similar peak is seen in naphthalene but with the H_2 loss. The intensity of H_2 or H_3 loss at the double ionization peak is quite significant. $C_6H_4^+$ region shows a clear difference in the peak shape across the three examples. This indicates a difference in the decay channel which again could be related to the location of the nitrogen atom in the ring.

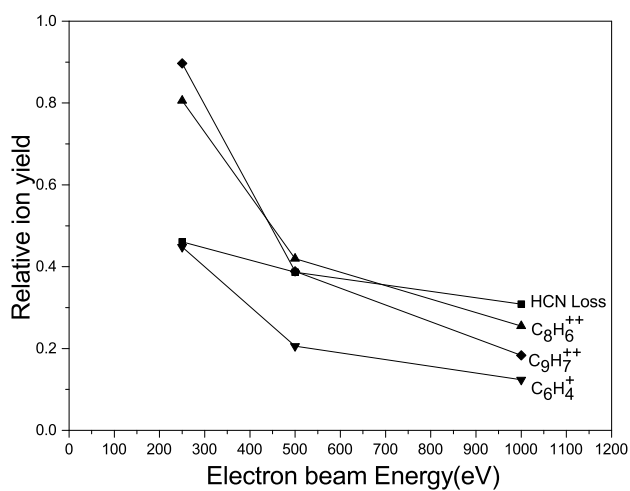
6.3.1 Normalisation and Beam Energy Dependence

HCN loss shows the strongest intensity compared to adjacent mass peaks in quinoline and isoquinoline hence other channels in this mass group are neglected in the rest of the analysis. The yields in each spectrum are normalized with the total area of the single ionization peak, including neutral H loss. The total counts in each area were much larger than 10000. Thus, the systematic errors are canceled due to self-normalization with the single ionization peak and the statistical error was much smaller than the symbol size used in all the subsequently shown figures. First, we compare the relative yields as a function of the impact energy in all the three targets. This trend is shown in Figure 6.4a, 6.4b and 6.4c. Here we notice the first indication that C_2H_2 /HCN loss is different from the other channels. It is very clear that C_2H_2 and HCN channel in naphthalene and (iso)quinoline, respectively show a much slower change in the yield as compared to all the other channels. The other channels show almost an identical variation of rapid decrease within a given target species. This effect has also been observed with ion impact on naphthalene and is attributed to plasmon excitation process [34]. We observed similar features in the nitrogen derivatives as well. This shows that the presence of one nitrogen atom does not affect the collective excitation process.

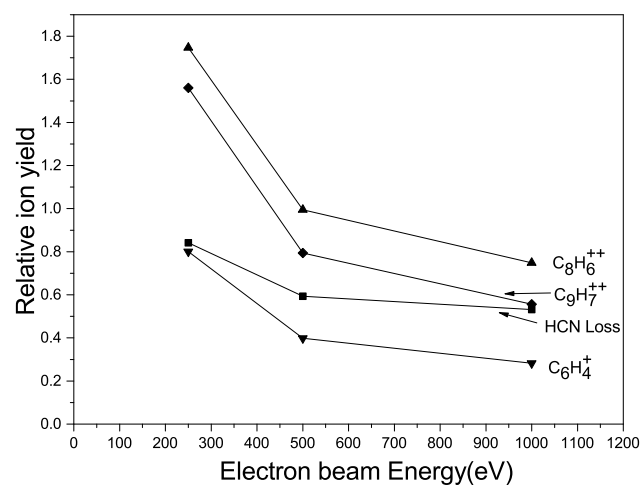
The mass spectra are recorded and the relative yields in the target and incident beam energy combinations are plotted as a function of the extraction delay for each individual channel. Figure 6.6 shows the data for naphthalene at a beam energy of 250 eV. The relative yields clearly show two types of decay channels. One set shows a systematic decrease in magnitude as we increase the delay and the other shows either a constant or small increase in intensity that stabilizes within 5 microsecond time scale. A similar behavior is seen in all the other beam energies. In the case of naphthalene, these slow changing or



(a)

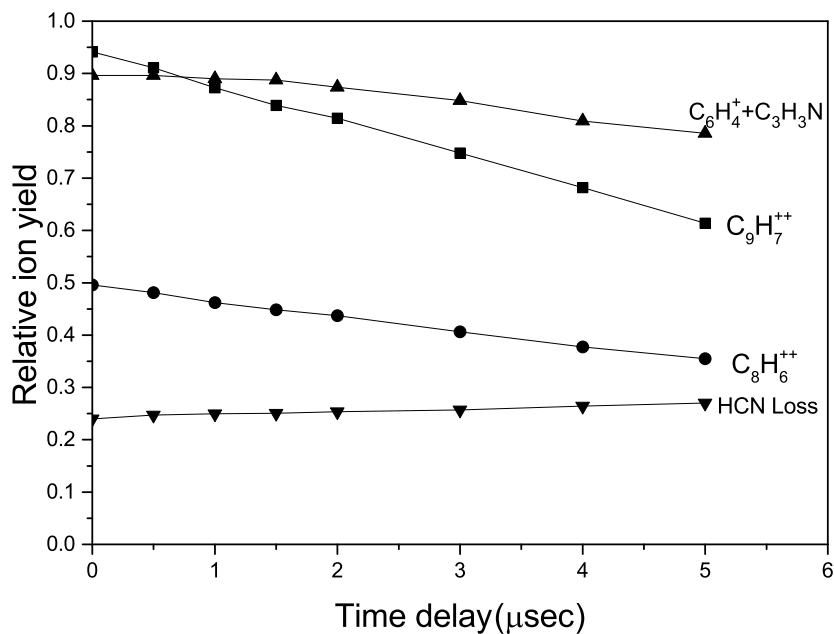


(b)

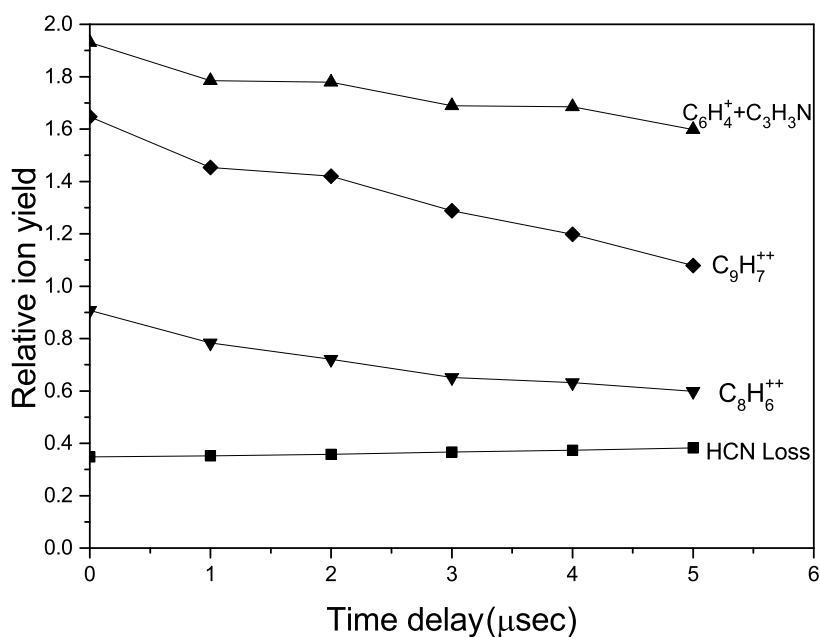


(c)

Figure 6.4: Energy dependence of different decay channels with zero delay time extraction (a) Naphthalene (b) Quinoline (c) Isoquinoline molecules



(a)



(b)

Figure 6.5: Various dissociative and violent decay channels with delay time extraction (a) Quinoline (b) Isoquinoline molecules under 250 eV electron impact

increasing channels are clearly related to the statistical dissociation channels [87, 160]. Figure 6.5a and 6.5b, show the similar measurements for quinoline and isoquinoline at 250 eV. Here, the behavior is again similar to naphthalene except that the relative yields for corresponding channels are higher and the time evolution of the two slow channels is different. The statistical channels for naphthalene have been reported in the literature

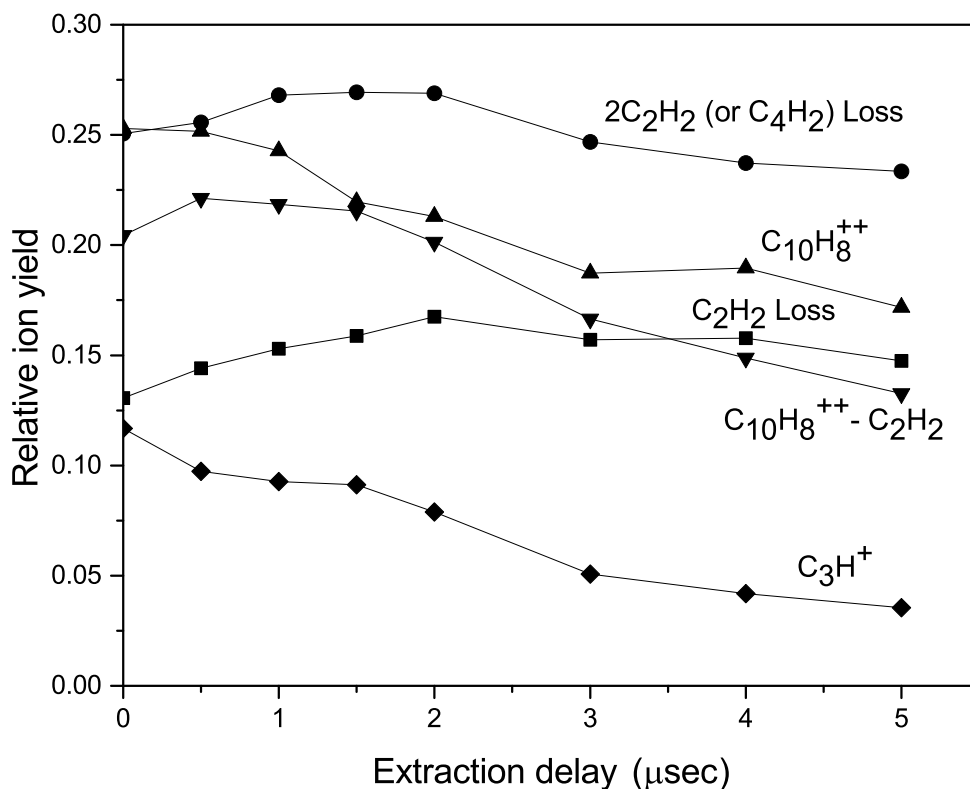


Figure 6.6: Various violent and dissociative decay channels with delayed extraction time for naphthalene under 250 eV electron impact

but for quinoline and isoquinoline, such detailed studies are not available. Bouwman *et al.* (2015) have discussed H loss and HCN loss in one of the recent photodissociation studies for the two cases but the second slow channel seen here is not discussed in the literature [104]. Using the list of decay channels and their mechanisms it is easy to identify that the HCN loss and C₃H_nN are the dissociation channels with microsecond timescale whereas all other channels decay at a much faster rate with sufficiently large kinetic energy release (KER) to diffuse from the interaction region rapidly. In particular, the doubly charged species (decay channel) is likely to further dissociate to smaller singly charged fragments. Consequently, the population of the intact dication and dication-HCN also decrease rapidly as seen in the data. We compare our results with the NIST data taken at 70 eV [107]. The mass spectra show the same decay channels as our case but with a strong variation in the yields. For both PANHs the mass spectra are almost identical yields for respective decay channels at 70 eV. In contrast, we observe clearly that isoquinoline is more prone to decay by fragmentation than quinoline.

6.3.2 HCN Loss Channel in Quinoline and Isoquinoline

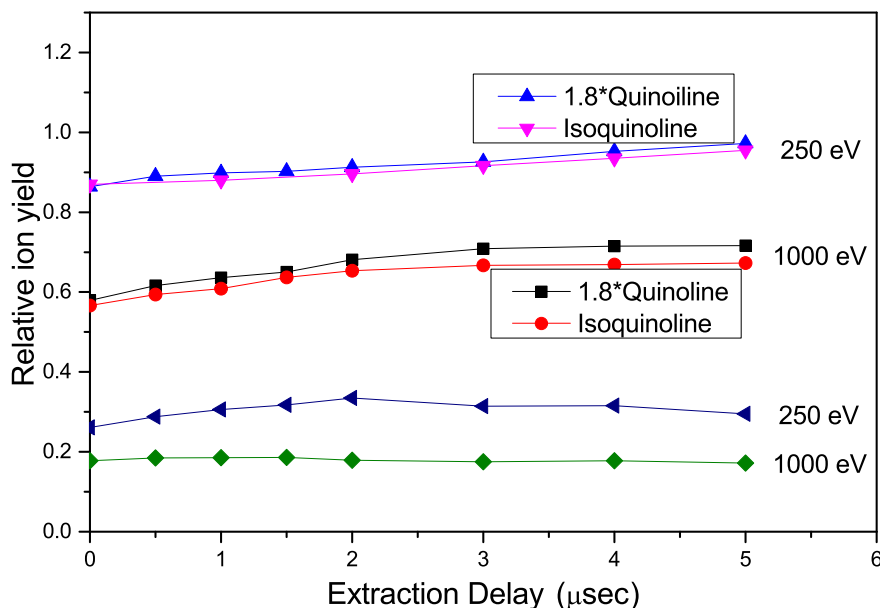


Figure 6.7: HCN/C₂H₂ loss channel in naphthalene, quinoline and isoquinoline

The HCN elimination process in both the PANHs studied here is known to depend on the pairing of the nitrogen atom with the nearest carbon atom. In the case of quinoline at 70 eV electron impact, 33% yield of HCN was seen to arise from one of the adjacent carbon atoms [12]. The other atom in one of the shared carbon between two rings was not found to contribute significantly. On the other hand, for isoquinoline, the nitrogen position was found to help in pairing with either of the two carbons, contributing to nearly 70% of the HCN yield [13]. Moreover, at low energy neutral impact, the process was entirely governed by pairing with the adjacent carbon atoms and the carbon randomization was found to be absent [12, 13]. This work directly demonstrates that the relative yield of HCN loss for quinoline is approximately half (0.555) of that from isoquinoline. On the other hand, we found that the decay constants for HCN loss are of the order of 10^6s^{-1} and are almost identical in both PANHs.

At all the three beam energies, the HCN loss channel in quinoline and isoquinoline show a strong similarity in the evolution of the relative yield which follows exactly the same time scale as shown in Figure 6.7. This highlights very clearly that the mechanism of formation of HCN in the two cases must be identical. A detailed discussion regarding the elimination of HCN from these two species can be found in the very recent work

by Bouwman et al [104]. The observations here are consistent with their experimental results on photodissociation. Having noted this, the two examples drastically differ in the magnitude of the relative yields. As shown in Figure 6.7 the HCN loss yield in quinoline is multiplied by a factor of 1.8 to match with that of the isoquinoline, which clearly shows that the possibility of losing HCN from quinoline is approximately half of that of from isoquinoline as shown by the structure calculations in Section 2.1 in the Chapter 2. This factor remains the same for all the beam energies. Such a comparison of yields under identical conditions is not reported so far to the best of our knowledge.

6.3.3 HCN+C₂H₂ Loss Channel in Quinoline and Isoquinoline

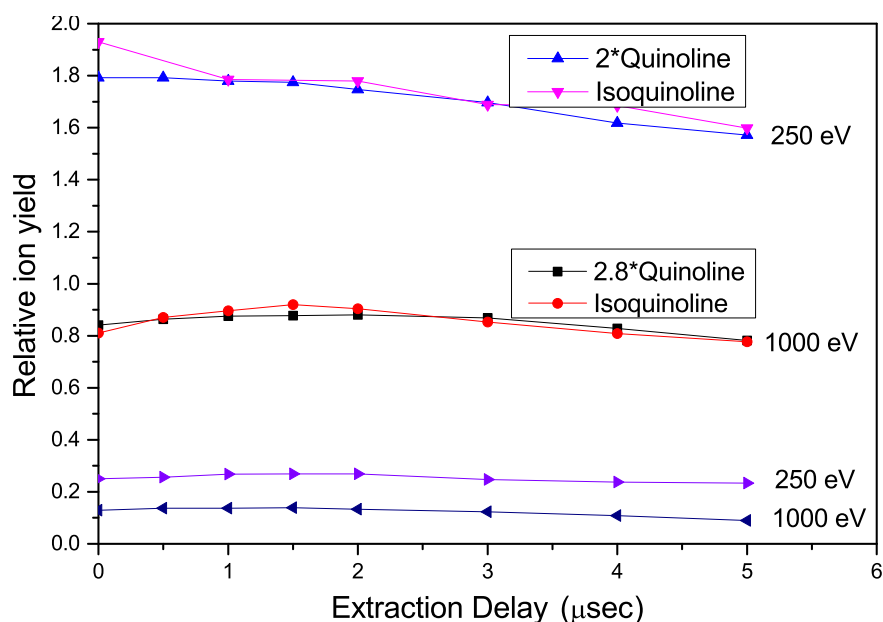


Figure 6.8: HCN+C₂H₂ loss channel in quinoline and isoquinoline

In the case of naphthalene, the loss of diacetylene and 2 times the loss of C₂H₂ are competing channels with the diacetylene loss being the significantly larger channels as seen in figure 6.3. Structurally, both the rings in naphthalene can produce diacetylene fragment. In quinoline and isoquinoline, on the other hand, 76 amu has a higher intensity than 78 amu. The minimal intensity of 79 amu indicates diacetylene loss is negligible. This leaves the ring with nitrogen to produce the neutral fragment with the corresponding ion at 76 and 78 amu. There are two possibilities in this mass region, first is the loss of HCN + C₂H₂, giving rise to the fragment of mass 76. The other possibility is the loss

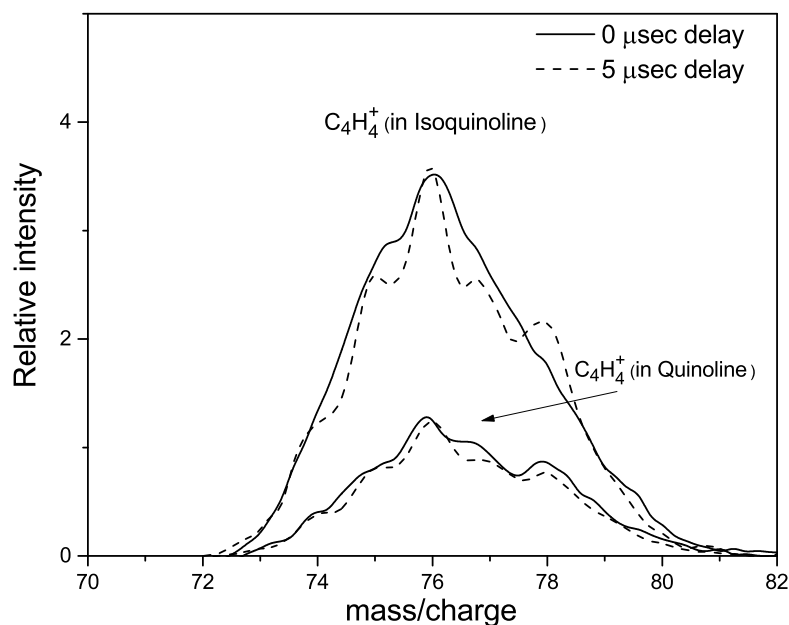


Figure 6.9: HCN+C₂H₂ loss channel overlapped mass spectrum in quinoline and isoquinoline

of propiolonitrile (C₃NH) resulting in a fragment of mass 78. Due to the lack of previous investigations towards this aspect, it has not been possible to quantify and compare these two channels energetically. As we can see in Figure 6.3, quinoline shows a higher intensity of 76 mass compared to rest of the fragments in the vicinity. This is in contrast to isoquinoline spectrum. Considering the structure of propiolonitrile (C₃NH), it is expected that quinoline should have a higher probability of HCN + C₂H₂ loss compared to isoquinoline. In terms of time evolution, this channel shows an initial increase up to 1.5 microseconds and thereafter a rapid decrease for isoquinoline at 1000 eV beam energy. For quinoline, this change is much slower and it peaks at about 3 microseconds. The yield variation is as much as 20% from the zero delay to the peak yield for isoquinoline and about 12% for quinoline at 1000 eV. At 250 eV on the other hand, the decrease is very rapid in both the targets as can be seen in Figure 6.8.

To this end, it is observed that the shape of the peak in this channel also evolves with the extraction time for isoquinoline. Figure 6.9 shows the mass overlapped mass spectra for quinoline and isoquinoline in the mass range of the fragment in the discussion. It is evident that the isoquinoline structure develops sharper peaks due to the fast diffusion of higher energy fragments from the interaction region thus improving the resolution of the

mass spectrum. This behavior is very weak in quinoline. Similar to HCN loss channel, this channel also shows a variation in the magnitude of the yield between quinoline and isoquinoline. The factor to be multiplied with quinoline yield to match with the isoquinoline magnitude is about 2 at 250 eV and 2.8 at 1000 eV.

The statistical decay channels of naphthalene, quinoline, and isoquinoline were observed to show a slow microsecond range decay time constant. A similar trend was seen with C_4H_2 and C_2H_2+HCN loss channel in naphthalene and (iso)quinoline, respectively. The rest of the channels show a gradual decrease in intensity as a function of delay due to rapid dispersion following a violent fragmentation. Thus the DEToF technique is used to separate the fast and slow decay channels after electron impact. A detailed analysis of HCN loss showed identical time scales in quinoline and isoquinoline but nearly twice the yield in favor of isoquinoline. We correlate this with the position of the nitrogen and the corresponding bond properties using a simplistic interpretation. A Hartree-Fock level structure calculation with GAUSSIAN09 with 3-21G basis set is used to assess the bond length variations of the targets. The observed yield variation is explained on the basis of the results. A similar analysis of diacetylene/ propiolonitrile channels shows the statistical nature of this dissociation dominating at higher electron impact energy.

Chapter 7

Ion Impact on PAHs and PANHs

In contrast with the electron impact processes, a positive charge projectile leads to additional complexities. This is mainly due to the availability of bound states. The dynamics of ion-molecule collision is very complex as it involves numerous processes occurring simultaneously such as direct (multiple) ionization, fragmentation, inner shell ionization preceding Auger effect, autoionization, transfer ionization and electron capture process. Generally, electron or photon impact mass spectroscopy measurements on PAHs are dominated by single or multiple ionization, while fragmentation channels remain dormant. On the other hand, in ion-PAH collisions, the fragmentation channels play a prominent role due to substantial energy deposition in the electronic and vibrational modes. In this chapter we are discussing the positively charged particle interaction on PAHs and PANHs, where we have used H^+ as our projectile.

We have chosen the experimental conditions in which we will be able to probe the molecule in the time scales of the microsecond. The higher sensitivity of the projectile electron below 250 eV restricted our ability to do measurement below 4 a.u. of the velocity of the charged particle. Therefore, to probe the energy loss in this velocity regime where we expect the charged particle to deposit more energy in electronic energy loss model, we perform the experiment with proton beam at lower velocity. But when we do this, proton beam itself introduces additional complications due to the electron capture (EC) and capture ionization(CI) processes. Using multi-coincidence technique we have isolated as many possible contributions as possible. The data helped in identifying the extent to which structural randomisation can happen at a given projectile velocity. This method has also helped to compare the rate of evaporation from mono and dication.

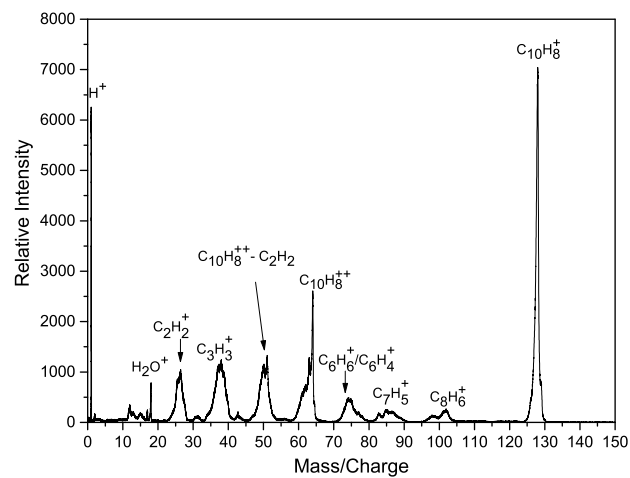
7.1 Experimental Details

The proton-PAH/PANH experiment was carried out at the Low Energy Ion Beam Facility, Inter-University Accelerator Centre, New Delhi, using an electron cyclotron resonance (ECR) ion source. Proton beams of energy between 50 and 150 keV were made to collide with naphthalene, quinoline and isoquinoline target. Target samples were effusing from a needle placed perpendicular to the projectile beam path in the collision chamber. The chamber pressure was 5×10^{-7} Torr during the experiment. There was no contamination seen in the time-of-flight (TOF) spectrum due to impurities in the sample. A linear two-field TOF mass spectrometer (TOFMS) with a position-sensitive microchannel plate detector was used to detect the recoiled naphthalene ions after interaction with the proton beam. The electrons ejected in the process were extracted in a direction opposite the TOFMS and detected by a channeltron. The proton beam was allowed to interact with the target and then using extra electrostatic deflector after interaction section of ToF, the neutralized proton beam was separated and the neutral hydrogen was produced by the electron capture process and detected using the third detector. Post-collision, the charged projectiles were deflected away from this detector using an electrostatic deflector. The NIM triggers from the ejected electron and neutralized projectile were delayed and gated with OR condition. This signal was delayed by enough time to use as the common stop. Since the capture cross sections are much lower, by adding extra delay a priority was given to projectile stop. The individual start signals were taken from the microchannel plate detector in the ToF. Multi coincidence measurements were carried out in both EE and EC mode by a CAMAC based multihit data acquisition system (DAQ) employing LeCroy time-to-digital converter (model 3377 TDC). A very sophisticated multi-coincidence technique is employed to isolate the electron capture and capture ionization process from pure electron emission (EE) process in proton PAH and PANH collision. A relatively high energy proton beam ranging from 50 keV to 200 keV was used, which gave us velocity in between 1.42 a.u. to 2.46 a.u. The data was written in list mode, where the full coincidence information was preserved. Out of this information, we selectively took out the correlated processes like EC, EE, and CI. The detailed layout of the experimental setup and DAQ is described elsewhere [169].

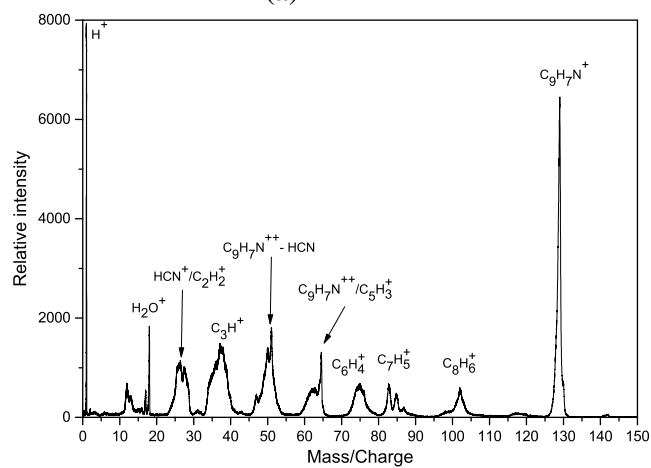
7.2 Mass Spectrum

The proton impact data has three modes, EE, EC and CI mode respectively. One typical example of each set is shown in Figure 7.1, 7.2, 7.3. Our electron impact data shows relatively higher fragmentation yield compared to EE or EC mode data. This is mainly due to two different detectors being used for two experiment. The proton impact data clearly shows very sharp peak resulting from pure ionization and ionization plus neutral evaporation process, whereas the broader peaks are assumed to be due to more violent multi-fragmentation. Areas of individual group peaks were extracted and were normalized to singly charged parent ion, except for sharp peaks like dication, dication with C_2H_2/HCN loss, dication- H_2/H_3 where individual peaks could be integrated. While extracting the data under EE, EC and CI conditions there are possibilities of contamination due to small detection efficiency for the emitted electron as well as the neutralized projectile. In the present experiment, they both were less than 10 %. Moreover, the main conclusions drawn in this work are based on only singly charged parent ions and their evaporative daughter ions which are not affected by it. The conclusions for dication are also independent of such cross-contamination. In the case of proton impact, it was found that the electron capture process had very low cross-section compared to the pure EE mode. This was already known in the case of naphthalene [60]. Therefore, even if the capture process is causing any contamination in our measurement it would cause a very little correction.

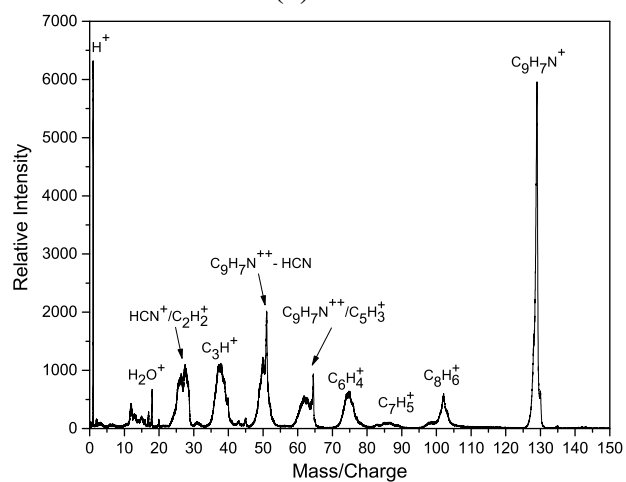
We extract the EE mode data and EC mode data by putting the condition in the software and then we normalize to the single molecular ionized peak. But in the case of CI, singly charged parent ion peak was seen due to chance coincidence and was not correlated with the different channel, so we normalized it with doubly charged parent ion. This analysis is done purely for comparison of all the three processes. Compared to EE, capture cross-section was one order of magnitude less; so also in the case of EC, CI was one order magnitude less. Thus the error due to chance coincidence could affect only the highly energetic fragmentation process these errors will be visible only in the highly energetic fragmentation process and that too only a few percentage. So such contamination can be neglected and therefore we can separate the electronic energy loss dynamics from the pure capture dynamics and capture ionization. This is particularly true for evaporative



(a)

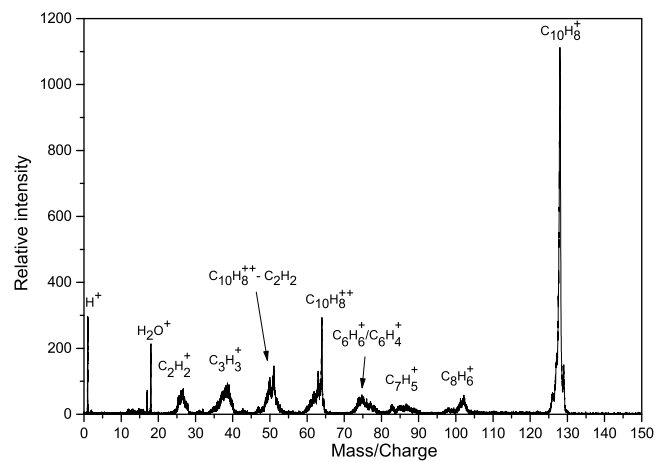


(b)

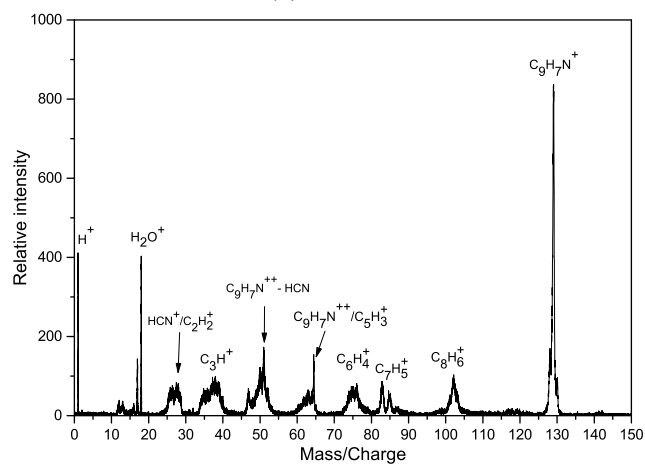


(c)

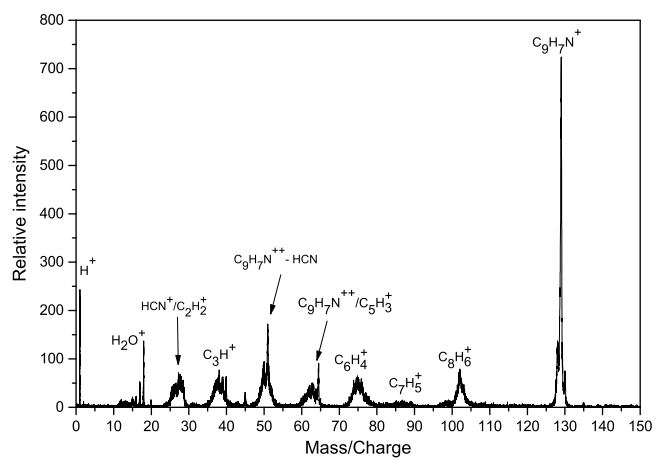
Figure 7.1: Typical Mass Spectrum of (a) Naphthalene ($C_{10}H_8$) (b) Quinoline (C_9H_7N) (c) isoquinoline (C_9H_7N) at 50 keV proton impact in EE mode



(a)

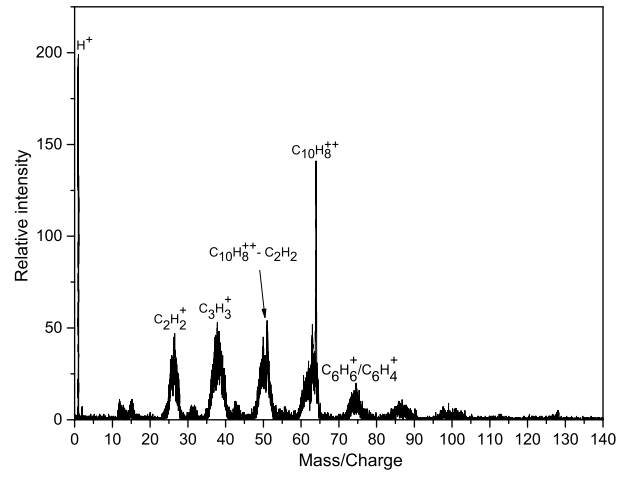


(b)

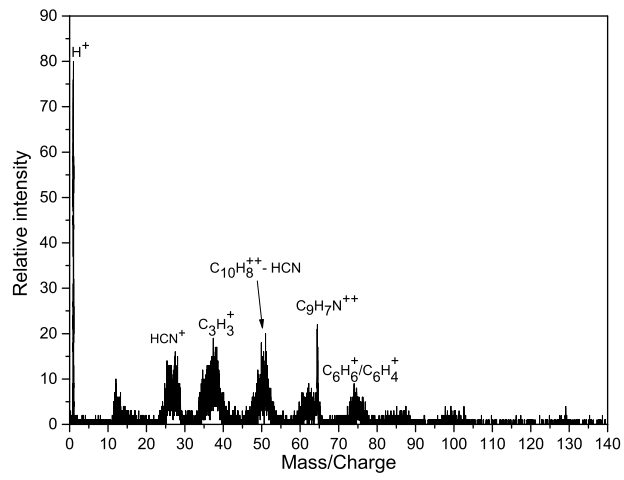


(c)

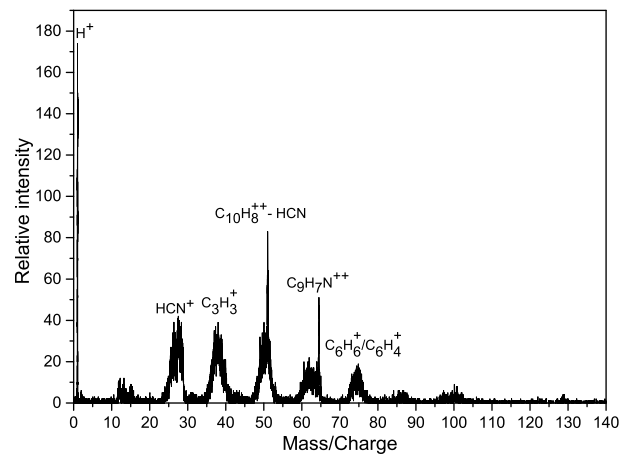
Figure 7.2: Typical Mass Spectrum of (a) Naphthalene ($C_{10}H_8$) (b) Quinoline (C_9H_7N) (c) isoquinoline (C_9H_7N) at 50 keV proton impact in EC mode



(a)



(b)



(c)

Figure 7.3: Typical Mass Spectrum of (a) Naphthalene ($C_{10}H_8$) (b) Quinoline (C_9H_7N) (c) isoquinoline (C_9H_7N) at 50 keV proton impact in CI mode

losses of C₂H₂/HCN.

Each mass spectra contained a small though noticeable water ion peak. We use this information to obtain the neutralized projectile and secondary electron detector efficiencies as well as the ratio of the absolute cross-section. Due to too high uncertainty in the vapor pressure of the target molecules and the limitation in collecting the projectile beam post interaction it was not possible to do absolute normalization. Since the data was taken with multi-coincidence in list mode for a given set of beam energies and target combination, the number density of target and projectile flux was identical for EE, EC, and CI mode. We use the ratio of dication intensity in CI mode and EC mode to obtain absolute secondary electron detection efficiency. This was possible because we are using a proton projectile and we neglect double capture process. We use the published total and partial cross-section of production of the monocation of H₂O under pure ionization and pure capture for proton projectile energies studied here [170–172]. Using this we obtain the ratio of neutral projectile detection efficiency to electron detection efficiency. Thus we have the absolute electron detection efficiency which was found to be identical within error bars for all the runs as expected from the setup geometry. The neutralized projectile detection, on the other hand, was found to be very different for different projectile energies. This is due to the different tuning conditions. With the help of this information, we found out the ratio of single ionization cross-section to single electron capture cross-section by using the equation:

$$\left(\frac{I_+^i}{I_+^c}\right)_{H_2O} = \left(\frac{\sigma^i}{\sigma^c}\right)_{H_2O} \times \left(\frac{\varepsilon_e}{\varepsilon_p}\right) \quad (7.1)$$

$$\frac{I_{2+}^i}{I_{2+}^c} = \frac{1}{\varepsilon_e} - 1 \quad (7.2)$$

where, I_+^i is the area of H₂O⁺ in EE mode, I_+^c is the area of H₂O⁺ in EC mode, σ^i is the cross-section for H₂O⁺ in EE mode data [170–172], σ^c is the cross-section for H₂O⁺ in EC mode data [170–172], I_{2+}^i is the area of dication of respective molecule in EE mode, I_{2+}^c is the area of dication of respective molecule in EC mode, ε_e is the electron detection efficiency and ε_p is the projectile detection efficiency.

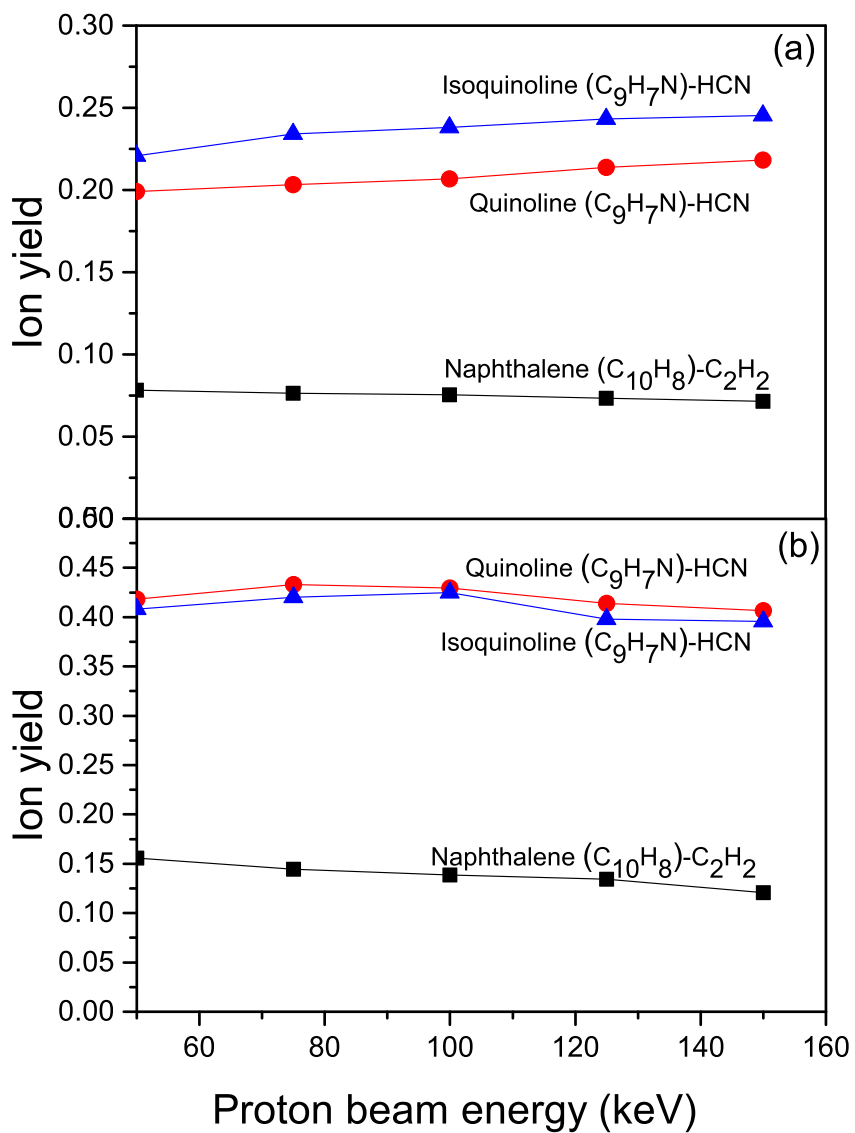


Figure 7.4: Projectile proton beam energy dependence of C_2H_2 loss channel in naphthalene, HCN loss channel in quinoline and isoquinoline in (a) EE mode (b) EC mode

We found that for all the targets the ratio of ionization to capture cross-section varied from 3 to 40 for corresponding proton energy of 50 keV to 150 keV (Figure 7.5). This is expected by considering that the projectile velocity is beyond 1 a. u., thus surpassing the required velocity matching condition and therefore decreasing in the partial cross-section as a function of velocity for electron capture. The emission cross-section is also known to decrease in this energy range as well but the decrease in capture cross-section is much faster [34]. The most important observation is that the three molecules follow the same ratio. But considering the fact that the electron capture and electron emission process are two distinct processes changing rapidly in this energy range, this similarity in the ratio clearly proves that both the ionization and capture processes are identical and the presence, as well as the position of nitrogen in PANHs, have very little effect on the cross-section for capture as well as electron emission. No significant effect of evaporation process over the yield of single and double ionization is observed. The ratio of ionization to capture cross-section, as well as the ratio of double ionization to capture ionization, are independent of the presence and position of Nitrogen in PAHs (Figure 7.5).

Earlier studies on anthracene $C_{14}H_{10}$, acridine $C_{13}H_9N$ and phenazine $C_{12}H_8N_2$ ions colliding with He, Ne, Ar, or Xe at 5 keV shows that the total fragmentation cross section is the same for all three molecules for a given target gas [173]. It is known that in naphthalene the skeletal structure is much more stable as observed in our electron impact as well as proton impact studies. In the case of quinoline and isoquinoline, on the other hand, it has been reported in the past that under collision induced excitation processes there is a possibility that there can be some amount of structural randomization. If this randomization process is of carbon and nitrogen atoms in the skeleton, they lose their positional identity. Due to the structural difference between quinoline and isoquinoline we expect that the ratio of HCN loss should double in case of isoquinoline compared to quinoline if there is no randomization. Structure calculations on these molecules also highlight the identical nature of respective C-C and C-N bonds when we compare quinoline and isoquinoline.

For the EE mode and EC mode, the C_2H_2 or HCN loss yield was plotted as a function of projectile energy (Figure 7.4). Several similarities were observed between electron impact and proton impact in EE mode. First of all, the contribution from C_2H_2 and HCN

from PAHs and PANHs and other branching processes was found to be less compared to electron impact. This is in agreement with what has been reported with photodissociation also; in the case of quinoline and isoquinoline, C_2H_2 loss was found to be minimal compared to HCN loss and it has been clearly established that HCN loss is the dominant channel [104]. Since these are two different setups, detectors used were different, so the detection efficiency will be different. So, the absolute value of the ratio may not be compared quantitatively, but a qualitative behavior as a function of projectile velocity can be obtained.

In the case of capture ionization, we observe a small amount of singly charged molecular ion, which comes due to chance coincidence. There are peaks with 6, 7 or 8 carbon atoms which are seen due to fragmentation of dication decay in which the smaller fragment is not detected. We see a sharp dication and very prominent dication minus HCN or C_2H_2 (Figure 7.7). At the outset, it is very clear that naphthalene dication is much more stable than both quinoline and isoquinoline, from the fact that the naphthalene doubly charged molecular ion is the strongest peak and there are other peaks but much smaller in amount, which includes a sharp peak due to C_2H_2 loss and due to H loss or H_2 loss as well as broad peaks due to fragments. In the case of quinoline and isoquinoline, on the other hand, the HCN loss peak is also quite prominent. Surprisingly, in the case of isoquinoline, the dication is prominent compared to HCN loss and in quinoline, it is the other way (Figure 7.6). The relative yield of dication in EE mode less by a factor of 2 compared to yield in the case of EC mode; it indicates the extra monocation intensity in EE mode coming from plasmon excitation. As expected, the yield of dication is highest for naphthalene and lowest for isoquinoline for both the cases (Figure 7.6).

7.3 Plasmon Excitation in Charged Particle Collision

Charged particle collision in electronic energy loss regime can cause local electronic energy loss and thus electronic excitation, such collective excitations are called plasmon excitations. The plasmon excitation is a prominent collective excitation mode in PAHs and PANHs. Planar PAH's happened to have the energy of about 17 eV. The photoion

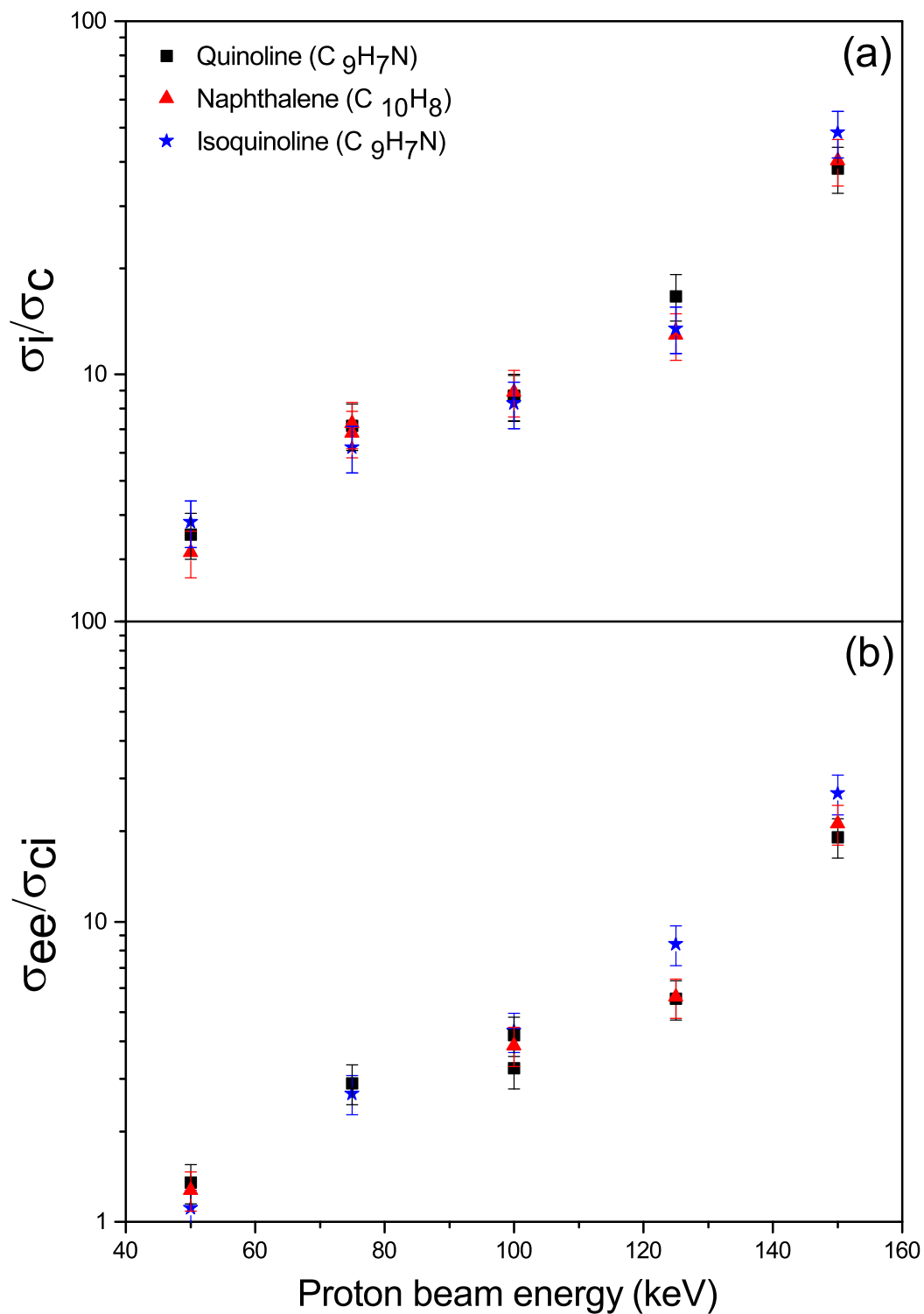


Figure 7.5: The ratio of partial cross-section for (a) ionisation (σ_i) to capture (σ_c) (b) double ionisation (σ_{ee}) to capture ionisation (σ_{ci}) for naphthalene (C₁₀H₈) quinoline (C₉H₇N) isoquinoline (C₉H₇N) with different proton beam energies

yield measurements performed over a large range of PAH has clearly shown plasmon excitation at 17 eV [36, 41]. To the best of our knowledge similar photoion yield measurements are not done in quinoline and isoquinoline and therefore it is not possible to assess how strong the excitation will be in these molecules comparative to naphthalene. It is known that collective excitation states due to inner valence shell electrons could exist for PAHs along with many single particle excited states and the collective excitation is expected to couple to intramolecular vibrational distributions via such single particle states [32]. Such coupling is strongly dependent on the symmetry and aromaticity of the molecule.

It is already known as well as observed in this study that naphthalene shows a very strong effect of this excitation mode. In naphthalene, C_2H_2 loss channel was used to demonstrate this effect in collisions with protons as well as with electrons [34, 174]. Thus we observe similar effect with PANHs in our present study as well. The energetics, on the other hand, is different due to the structural isomers of PANHs used here. Compare electron impact and proton impact with respect to Bohr adiabaticity parameter for plasmon [175, 176]. For larger impact parameters the collision interaction times become longer and it becomes possible for the projectile to couple strongly with the various collective excitations in the molecule. Still, at larger impact parameters, the excitation probability drops off again because (a) the Coulomb interaction becomes weaker, and (b) the collision times become large compared to the period of the excitation and the interaction becomes adiabatic. An estimate of the impact parameter at which this occurs is Bohr's adiabatic distance [175], $b_0 = \gamma \hbar \nu / E$, where γ is the usual relativistic parameter, ν is the projectile velocity, and E is the energy of the excitation. So at 1 a.u., the velocity of the projectile, it is 1.6 a.u. and at 4 a.u. velocities of the projectile, it is 6.4 a.u., assuming the plasmon excitation energy is 17 eV for naphthalene, quinoline, and isoquinoline.

More interestingly, just like in the case of electron impact we observe C_2H_2 loss, as well as HCN loss channel, evolve very slowly with the projectile energy (Figure 7.4). We found that the loss of $C_2H_2 + HCN$ in the case of quinoline and isoquinoline and loss of C_4H_2 in the case of naphthalene follow approximately $1/v$ dependence, where v is the velocity of the projectile, clearly showing that the origin of this process is due to the electronic energy loss. The C_2H_2 loss and HCN loss showing the very weak dependence

on the projectile velocity matches the behavior as shown in the case of plasmon excitation [60]. We observe that for naphthalene, C_2H_2 loss is constant within the error bar. But in quinoline and isoquinoline, HCN loss shows a small variation larger than naphthalene C_2H_2 loss. The behavior of naphthalene is understood to be the effect of plasmon excitation which deposits approximately identical amount of energy independent of projectile velocity. The variation is mainly due to the broad shape of plasmon excitation as well as a small contribution for the normal electron stopping. The second contribution is mainly due to the fact that for substantial electronic stopping the projectile must pass very close to the molecular electron cloud, on the other hand, plasmon being a collective excitation, it can occur at large impact parameters. Thus for quinoline and isoquinoline, the deviation from the constant nature of HCN loss process is understood on the basis of the fact that the reduced symmetry which will reduce plasmon excitation oscillator strength and hence the normal electronic stopping due to localized electron interaction will contribute more in comparison with naphthalene target. Therefore in contrast with naphthalene, C_{60} or coronene, which has been shown by different studies that it is a purely plasmon dominated process [35, 60, 151] the nitrogen-containing PAH derivatives show relatively less effect of the plasmon. Moreover, we see that as the projectile velocity increases in case of quinoline and isoquinoline the HCN loss was increasing (Figure 7.4). Thus we conclude that not only the plasmon resonance effect but also other energy loss processes participate in producing HCN loss. Since the dissociation barrier for quinoline and isoquinoline to loose HCN(2.7-3 eV) is lower than naphthalene to loose C_2H_2 (4.2 eV) as reported by Bouman et. al [104], secondary processes will lead to depletion of HCN loss daughter ions within the ToF time scales. Such secondary processes will decrease in proportion as we go to higher projectile velocities and hence cause the observed increase of yield as a function of projectile velocity. As we go to higher velocity, the average energy deposited by the projectile into the target is lower and therefore if there is any secondary process after losing HCN due to extra energy available in the molecule, that probability is decreasing. And therefore HCN yield appears to be increasing as a function of projectile velocity. So the effect is not due to increase in HCN loss population, but it is due to the decrease in the secondary processes which were happening after HCN loss.

The evaporation of C_2H_2 or HCN is used as a temperature measuring means in this

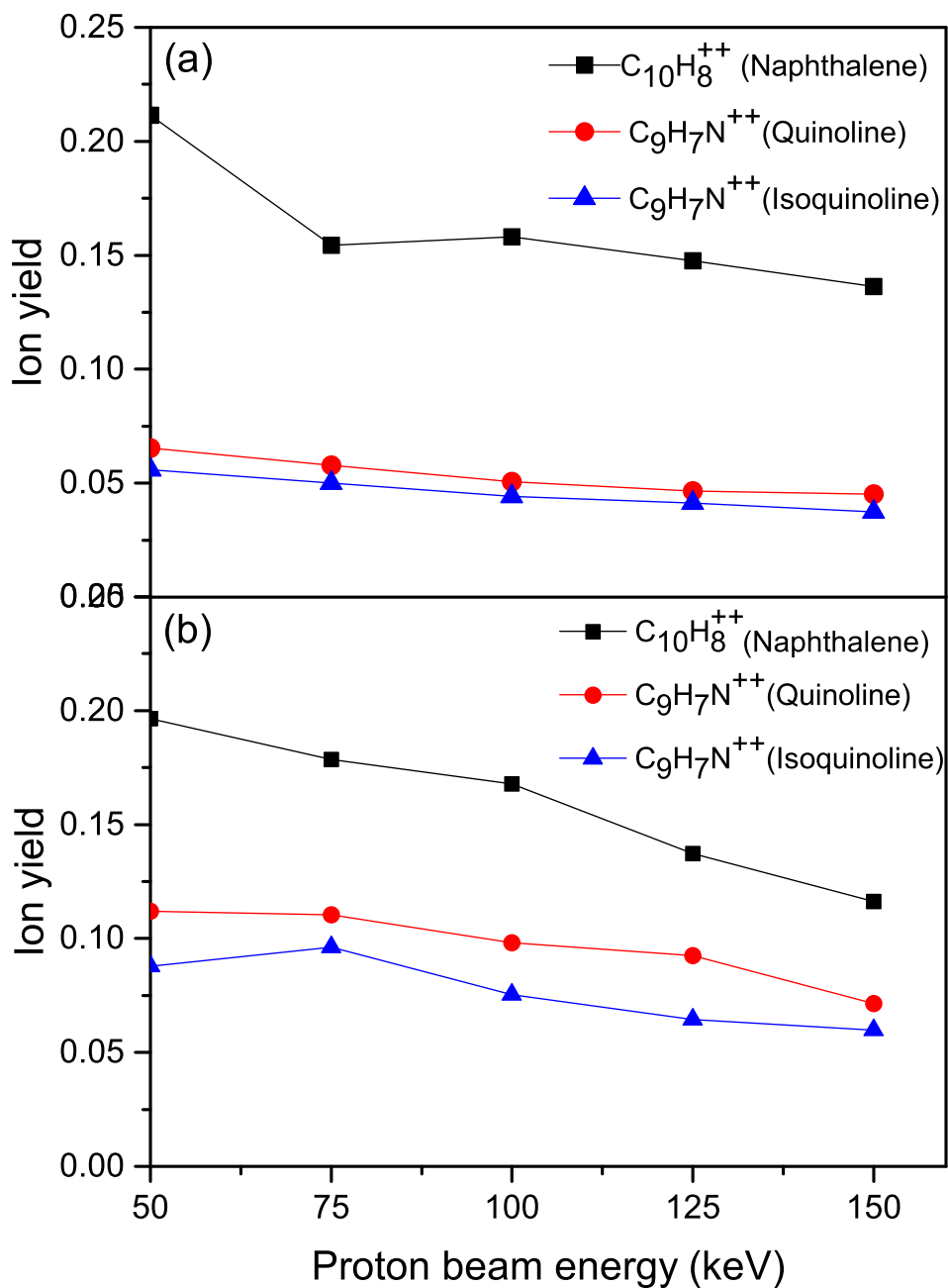


Figure 7.6: Projectile proton beam energy dependence of $C_{10}H_8^{++}$ channel in naphthalene, $C_9H_7N^{++}$ channel in quinoline and isoquinoline in (a)EE mode (b) EC mode

work. Hence the relative yield of C_2H_2 / HCN loss is plotted as a function of beam energy in EE and EC mode shown in Figure 7.4. A similar analysis was done for electron impact. In addition, in the case of electron impact, a delayed extraction study was also conducted, details of which can be found elsewhere [177]. In the case of electron impact at 4 a. u. or more velocity, it is observed that the ratio of HCN loss in isoquinoline to quinoline is not exactly double as expected from the structure calculations but it is 1.8 times. This indicates that there is a small fraction of the population of ionized parent ion which undergoes randomization of the structure and HCN loss happened after the randomization. Since the extraction time scale in our ToF setup is about few microseconds such rearrangement and evaporation must be accomplished in that time to be able to get detected. By implementing delayed extraction time-of-flight (DEToF) technique, we could identify the evaporation time scale down to 0.5 microseconds and hence the randomization must occur within time scales shorter than that. But since only a small fraction of the population of parent ion sees the randomization effect we can not identify the exact timescale of randomisation. Whereas in the case of proton impact and EE mode we observe this ratio to be 1.2 times. The same feature is seen in EC mode with the ratio approaching unity. So the fact that in the case of EE mode the yield of HCN is more and that this ratio is higher for EC mode shows there is much more structural randomization in EC mode compared to EE mode and this is because of higher internal energy deposition to the target molecule. So both these facts point to a marginally larger electronic energy loss in the case of EC mode compared to EE mode. This is also consistent with the fact that the EC cross section is more than one order of magnitude lower than EE cross-sections thus requiring the projectile to approach closed impact parameters for EC to take place leading to additional electronic energy loss.

The energy loss process in charged particle interaction is very different than in the case of photoexcitation. Since this process effects in many different and nested channels, direct connection of multifragmentation to one particular sequence of fragmentation is almost impossible. But the end result in the form of evaporation or fragmentation yields as a function of projectile velocity provides a method to assess the possible origin of the fragment species. Thus we plot various decay product relative intensities as a function of projectile energy. Two distinct effects are observed, one in which the fragmented prod-

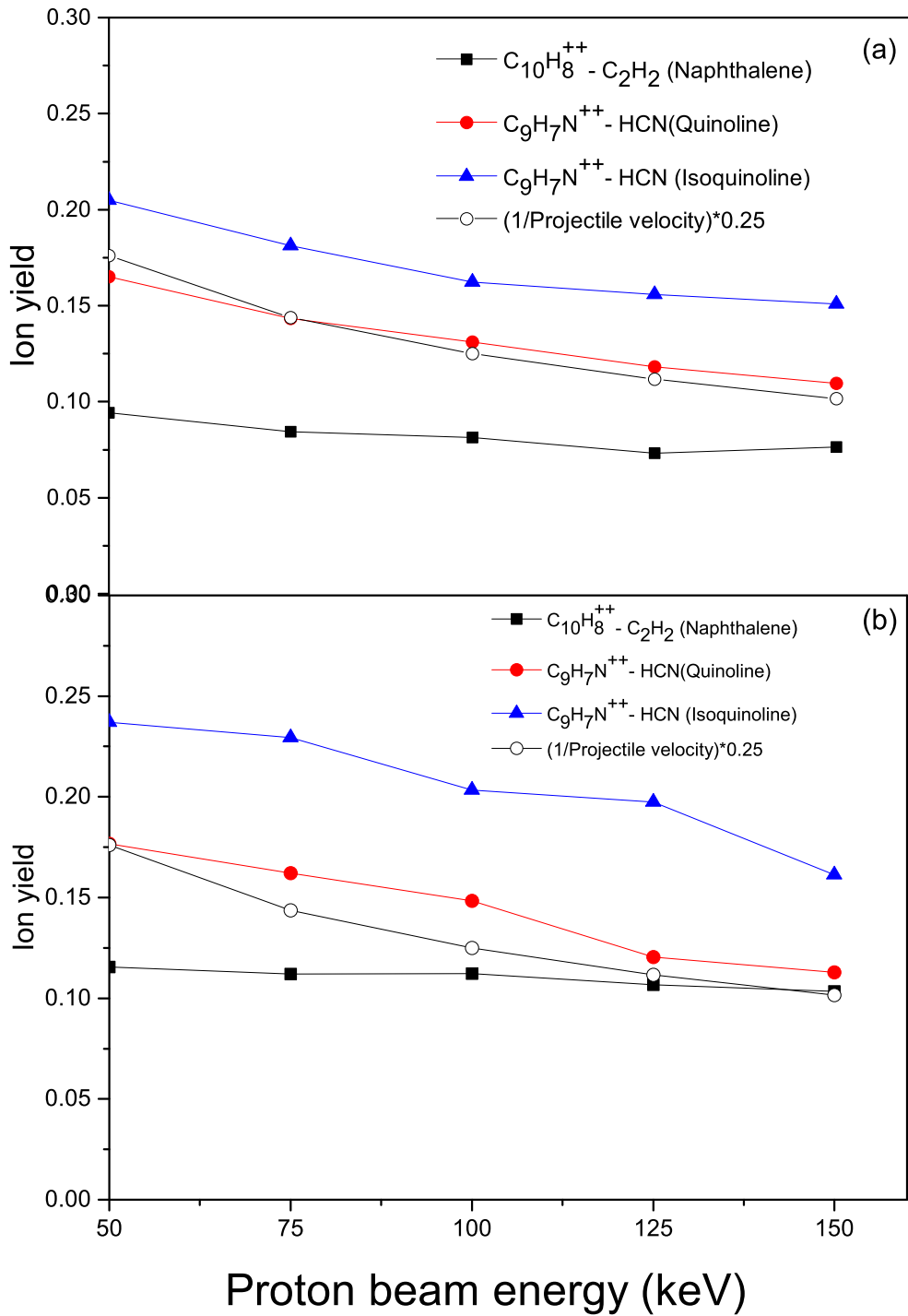


Figure 7.7: Projectile proton beam energy dependence of $C_{10}H_8^{++} - C_2H_2$ channel in naphthalene, $C_9H_7N^{++} - HCN$ channel in quinoline and isoquinoline in (a) EE mode (b) EC mode

uct has a decreasing yield as the function of projectile energy and the other where they roughly follow a $1/v$ or exponential decrease with velocity. We correlate this with the similar effect seen in C_{60} using experiments as well as molecular dynamics (MD) simulations. But this study was in 1 a. u. velocity regime or less [178, 179]. We expect that the effect will be similar in our proton projectile case as well. More recently proton beam interaction with biomolecules has been studied and the energy loss values were estimated by Tan et. al. in 2008 [180]. The energy loss of amino acids is observed to increase in the study's range of proton energy here. We assume a similar behavior with PAH and PANH due to the similar elemental composition. Thus we explain the multifragmentation channels on the basis of electron stopping. Whereas the processes particularly C_2H_2 and HCN loss process are clearly of a different origin and hence can be attributed to plasmon excitation. The relative intensity of the evaporation products was found to be nearly twice in case of isoquinoline compared to quinoline under low internal energy deposition, which can be explained on the basis of the skeletal structure effect. This picture is altered when we have charged particle with lower velocities.

The projectile energy dependence of the electron impact ionization process is very commonly known to peak at about 70 eV to 100 eV, particularly for low-Z targets like hydrocarbons. At higher energy, the cross section varies as $\ln E/E$ [174]. When we compare the relative yields as a function of the electron impact energy in all the three targets we notice the first indication that C_2H_2 /HCN loss is different from the other channels. It is very clear that C_2H_2 and HCN channel in naphthalene and isoquinoline, respectively show a much slower reduction in the yield as compared to all the other channels. The other channels show almost identical variation with a given target species. This effect has also been observed with ion impact on naphthalene and is attributed to plasmon excitation process [34]. We observed similar features in the nitrogen derivatives as well. This shows that the presence of one nitrogen atom does not affect the collective excitation process drastically.

7.4 Stability of PAHs and PANHs under Charged Particle Interaction

Structural stability of PAHs or PANHs molecules can be studied using electron as well as proton as the projectile by separating statistical and non-statistical decay channels. The present work explores structural and dynamical implications of nitrogen substitution in naphthalene as well as the position dependence of the same. Intriguingly enough the presence and the position of nitrogen have no observable effect as far as the ratio of ionization to capture is concerned. Thus the single ionization causing processes for both electron emission as well as capture mode are unaltered in the three target molecule in this proton energy range. The relative intensity of the statistical evaporative channels on the other hand show very different picture. Projectile velocities higher than 1 a. u. are expected to have decreasing mean electronic stopping in the type of target considered here. Therefore statistical as well as non-statistical channels should have shown decreasing trend in yields. With electron as well as proton as the projectile, all the three target molecules show the expected behavior as a function of projectile velocity except the evaporative channels like C_2H_2 or HCN loss both from mono as well as dication. As reported earlier for the case of naphthalene, the multifragmentation channels which are expected to be non-statistical were observed to follow $1/v$ dependence. Similar behavior was also seen in the case of C_{60} fragmentation but with lower proton velocities than the one used here. Thus for naphthalene, quinoline and isoquinoline the multifragmentation channel yields found to decrease with the velocity for both electron as well as proton projectile ranging from 1 a. u. to 4 a. u. HCN/ C_2H_2 evaporation channel from monocation, on the other hand, shows almost a constant yield or even more interestingly an increasing intensity as a function of projectile velocity. Dication, on the other hand, is found to have higher yield in case of quinoline due to its higher stability compared to isoquinoline. Moreover, in electron emission as well as electron capture mode the yields show a marginal decrease in the intensity. Finally, HCN loss from the dication is observed to have approximately $1/v$ dependence in the yield. Thus the HCN loss process from monocation must have a contribution from energy loss mechanisms other than pure localized electronic stopping. This contribution is namely plasmon excitation for EE mode and electron capture from inner

valence shell in EC as shown in the case of naphthalene under similar conditions. The projectile energy dependence and subsequent analysis of evaporative processes provide us with a method to quantify the structural randomization process and positional identity of carbon and nitrogen, in collision-induced excitation in case of quinoline and isoquinoline.

The highlight of this work is the observation of the systematic evolution of acetylene or HCN evaporation in comparison with structural isomerization. A clear signature of structural isomerization is obtained by comparing the HCN evaporation yields of quinoline and isoquinoline under different impact energy conditions. We observe that at 4 a. u. and higher velocities, the ratio approaches the expected value as per the preliminary structure calculation. At lower velocities, on the other hand, a combination of plasmon excitation and electronic stopping is observed to cause the higher amount of internal energy deposition which in turn increases the decay rate as well as the rate of isomerization. But we observe that the rate constant of isomerization is faster than the rate constant of HCN evaporation. From previous reported Monte Carlo simulation the expected average internal energy deposited due to electronic stopping is approximately 50 eV. This may or may not be accompanied by additional loss due to plasmon excitation. In the case of electron capture, the ratio of HCN loss in both isomers is seen to be identical. Moreover, the relative yield of HCN loss is also seen to be higher compared to the pure electron emission mode.

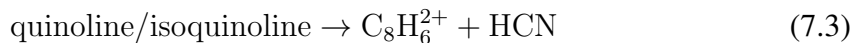
The dication of quinoline and isoquinoline are also observed to loose HCN with high propensity. As expected from the structure, HCN loss from isoquinoline is almost 50% higher than in the case of quinoline (40 percentage in EE mode and 30 percentage in EC mode). Here again, the evaporative yields are higher for the EC mode compared to EE mode corroborating the observation made in the case of mono cation in terms of relatively higher internal energy. Moreover, the HCN loss from dication of quinoline and isoquinoline evolves with $1/v$ of the projectile beam.

It is known that energetically, quinoline is more stable than isoquinoline and therefore it is also expected that in the interstellar medium, the proportion of isoquinoline is much less than quinoline. And therefore one may expect the role of quinoline to be more important in the prebiotic chemistry. But our work shows that sufficient internal energy leads to

rapid rearrangement and the contribution from both isomers would become equally significant. As studied in the past the collision of the proton, particularly at a lower energy in the medium the shockwaves of supernova play a significant role in biological interest in ISM. And in such collisions center of mass energies far greater than 50 eV are expected and experimentally observed. Therefore we conclude in spite of being of the much lower population in ISM, isoquinoline might play a significant role as quinoline.

7.5 Metastable Decay Dynamics of PANHs upon HCN Loss

Earlier studies have focused on understanding the product formation from neutral and mono-cationic PANHs [181]. However, the product formation from dicationic PANHs (present in interstellar medium) species has received far less attention. Moreover, understanding the dissociation of these metastable states may give us a hint regarding how the association reactions could have progressed to form these intact dications. Thus, to understand the mechanisms involved in the metastable dicationic species, simplest of PANHs quinoline (C_9H_7N) (and its isomer isoquinoline (C_9H_7N)) have been chosen. Even though the loss of C_2H_2 or HCN is feasible from these species, it has been shown that HCN is energetically favorable. In this article, we report metastable intermediate states that could be involved in the formation of $C_7H_3^+$, which belongs to $C_{2n+1}H_3$ class and unlike their analogs C_3H_3 and C_5H_3 less explored. We report $C_7H_3^+$ from quinoline and isoquinoline through an intermediate $C_8H_6^{2+}$ which possess a metastable state.



Earlier reports have obtained $C_8H_6^{2+}$ in the time of flight spectrum [182] since only a single hit information is obtained, it was attributed to be a stable species. Field et al. [183] have shown that the intensity variation of the difference of the time of flight(TOF) of the

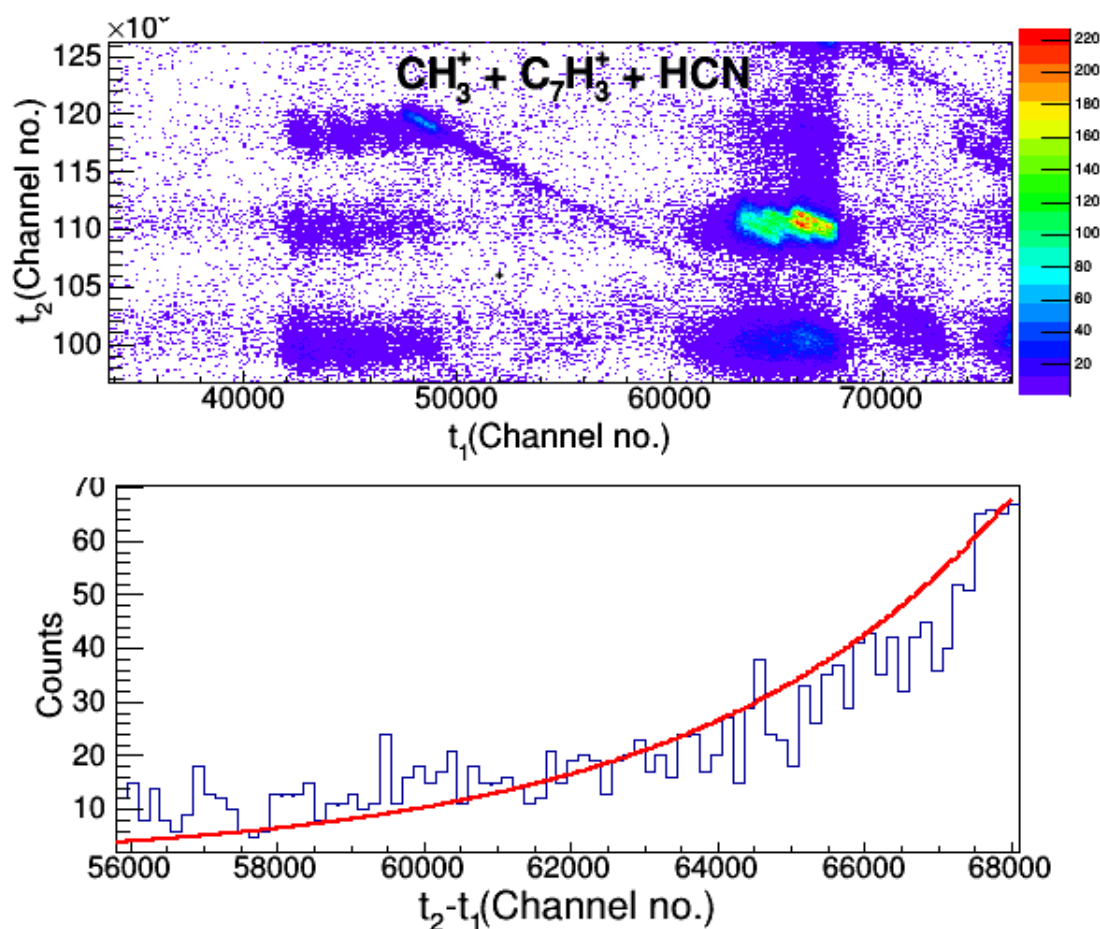


Figure 7.8: Top: The tail structure shown is formed when lifetime of parent $C_8H_6^{2+}$ has lifetime comparable to the time of flight of the fragments. Bottom: Shows the experimental intensity distribution as the function of ToF difference.

two ions in the tail region can give us a quantitative estimate regarding the lifetimes of the metastable species as shown in Eqn 7.5.

$$I(t_2 - t_1) = A \exp\left(-\frac{m_1 + m_2}{m_1 - m_2} \frac{t_2 - t_1}{2\tau}\right) \quad (7.5)$$

Here, m_1 and m_2 denote the mass of the two fragments the metastable state is dissociating into, τ denotes the lifetime. This function is fit [see Appendix C for the code] to obtain the time difference in ToF. This function is fit (red line in Figure 7.8) with Eqn 7.5 giving lifetime (τ) of $C_8H_6^{2+}$ as ~ 75 ns. It should be noted that the $C_7H_3^+$ molecule and its isomers are linear in their ground state. Moreover, removal of CH_3^+ is not energetically favored from the ring structures of $C_8H_6^{2+}$.

Chapter 8

Conclusion and Future Scope

Electron impact ionization of atoms and molecules is one of the most basic processes in physics, with fundamental applications in different areas like astrophysics, plasma physics, fusion physics, surface science, etc. Recent theoretical and experimental investigations have greatly contributed to the understanding of the scattering processes. Single and double differential electron emission cross sections are very vital in understanding the nature of the atomic and molecular state, and their interactions in nature. Sensitive nature of electron energy and angular distribution measurement puts several stringent requirements on the development of experimental setup. Moreover, the complexity of various excitation processes demands very advanced theoretical models to interpret the data. Complementary information on the mass of recoil ions generally improves the fidelity of the measurement but brings in its own stringent requirements. As one probe from atomic target to di or tri-atomic molecules the complexity in the measurements increases and this type generally titled as PEPICO for photon projectile and $e, 2e$ for electron impact, which grows substantially. This is mainly due to complex nature of molecular wavefunction and the requirement to capture the recoil ion mass as well as momentum information accurately to complete the picture. Thus the experimental setups for such measurements are quite elaborate and complex to design and build.

For larger molecules, the recoil ion momentum measurement becomes impractical due to their large mass and numerous fragmentation channels. But the electron emission cross-sections in correlation with mass brings in very elucidating details of the molecular properties. The main goal of the present work was to establish a system with capabilities to perform electron spectroscopy and recoil ion mass spectrometry in coincidence, specially tuned for large molecular targets. PAHs are the focus of this development due to their very intriguing behavior and their importance in nature. The astronomical significance of PAHs and PANHs can be assessed and understood only in the light of molecular structure and dynamics of individual PAHs or PANHs. The size of the family of PAHs

and PANHs compels us to perform molecular physics investigations on a few representative molecules and extend the understanding to the full spectrum of PAHs and PANHs. Considering large time scales of the order of millions of years, molecular dynamics is dominated by statistical dissociation processes. In such studies, it becomes extremely important to have an extensive quantum chemical structure calculation supported equally complex experimental apparatus.

As part of this work, an electron-ion coincidence experimental set-up was built. The development work involved full design fabrication and testing of the vacuum system and components hardware. Paralelly, full electronics, partly using modular electronics units off the shelf and partly by complete design and fabrication of vital electronics, was established. The pulsing techniques, as well as data acquisition for electron-molecule interaction with energy selective secondary electron-ion coincidence study, was then tested in various operational modes. The setup was then used to probe C_2H_2 /HCN evaporation process in naphthalene and two of its nitrogen-containing derivatives under high-energy electron impact. These measurements were used to assess the rate of structural randomisation vis-a-vis HCN evaporation process. These results are of vital importance in understating the C_2H_2 and HCN population in ISM since they play an important role in astrobiological modeling. The results were complemented with the proton impact studies in the same velocity range. The results were compared to two ionizing modes, electron transfer, and electron emission mode. The work also took into account the plasmon contribution in all the cases.

8.1 Instrumentation and Setup Development

Setup was developed using SIMION8.0 simulations and the whole hardware was designed as a modular unit with high mobility and flexibility. This is needed since the full strength of the system can be realized with the angular distribution of the emitted electron measured using PSD. But this can be done only with photon impact which needs synchrotron radiation source (SRS). Hence the setup can be transported to an SRS beam line and can be used. The setup has several modes including a high mass resolution reflectron mode for

future use. A modular electron gun is built from cathode ray tube CRT of black and white television unit as an excitation source. Separate deflection and beam shaping electrodes are constructed by understanding the geometrical parameters from the simulation. The electron gun performance is tested with the different operation mode of the gun, afocal, broad, and zoom beam mode. In such type of e, 2e systems, the pulsing of high voltage plays a very important role. Hence two types of pulsing units were developed using commercial off the shelf power MOSFETs as part of this work. A single polarity high voltage pulser in which a pair of fast power MOSFETs triggered in synchronism for switching the electron beam ON or OFF was used. For the extraction of the molecular ion from the interaction region, a bipolar pulser is used which is a pair of switches working in synchronism but of opposite polarity. Both the switches were tested for the mass spectrometric and the possible electro-optic switching applications.

Multi-coincidence measurements invariably require a complex pulse processing and logic. Moreover, in this works the logic including the complex pulsing sequence of HV units to pulse the electron beam and pulse the mass spectrometer. The whole pulsing and processing sequence was realized as a part of this work. Moreover, the pulsing sequence was made modular to use the setup in different modes. A complete pulse processing and DAQ system were also developed as a part of this work.

8.2 Calibration and Testing

To understand the operating parameters the spectrometers were calibrated. For the calibration of CMA, the known Auger electrons were used, and the calibration graph was drawn for the detected electron as a function of the voltage applied to the CMA. The DDCS spectra of various atoms and molecules as a preliminary test. The position of Xenon secondary electron with a PSD at the focal point as well as away from the focal point of the CMA was shown to demonstrate the energy and angular distribution.

A similar calibration curve is drawn for ToF with Xenon ion, up to a charge state of Xe^{6+} . ToF spectra of various atoms and molecules are shown as the preliminary test results. The ToF unison with CMA was tested for the energy selective secondary electron-

ion coincidence measurement by using Xenon and naphthalene as the test sample.

8.3 Investigation of Structural Effects in Naphthalene and its Derivatives

The DEToF technique was implemented to investigate the time scales of fragmentation channels of the target molecules, and this technique is used to separate the fast and slow decay channels after electron impact. A detailed analysis of HCN loss showed identical time scales in quinoline and isoquinoline but nearly twice the yield in favor of isoquinoline. All these results were correlated with Arrhenius decay constant, internal energy and plasmon excitation energy.

Structural stability of this class of molecules is studied using electron as well as proton as the projectile by separating statistical and non-statistical decay channels. It is observed that in the case of electron impact at high velocity, as expected, the internal energy deposited to the molecule on an average is less and therefore the number of times C_2H_2/HCN loses is also decided by the structure, whereas structural alteration plays a very limited role. But in proton impact or at a lower velocity charge particle interaction, as expected, the internal energy deposited is more and therefore there arises more structural randomization. Now this work warrants even further exploration of a continuous variation of very low energy proton and very high energy proton as well as very low energy electron studies. To confirm this, due to practical difficulties, experiments could not be done with very high energy proton impact as well as very low energy electron impact, as both require a different machine. The metastable state of intermediate $C_8H_6^{2+}$ in naphthalene, quinoline and isoquinoline after C_2H_2/HCN loss was explored by using time-of-flight technique under proton impact. The similarities and differences in the structural properties of three molecules of PAHs and PANHs through theoretical calculation and a conclusion of the experimental results were drawn with the help of quantum chemistry calculation performed using HF method. This work has identified a method to study the structural randomization depending upon the internal energy of the molecule and a clear signature of the same has been seen in the case of naphthalene, quinoline, and

isoquinoline.

8.4 Future Scope

The electron-ion coincidence experimental set-up will be used with time-of-flight mass spectrometer in reflectron mode for mass resolution improvement. In addition, a parallel plate analyzer will be used for energy loss measurement of the projectile beam. By doing this kind of measurement we will be knowing the energy deposition to the target under charge particle collision and the following decay processes can be known. So a complete energetic study of the target molecule is possible. The experimental setup is made compact and modular, and it can be transported to facilities like synchrotron, high-energy ion source, free electron laser etc. for future experiments. For a complete understanding of PAHs and PANHs class of molecule, this study can be continued to other molecules apart from naphthalene and its two nitrogen derivatives. It will be a unique method and this work can be extended to more complex and important systems like biomolecules, aggregates, and clusters.

Appendix A

LUA Program Code Used in SIMION8.0 for Time Varying Electric Field

```
simion.workbench_program()
    adjustable switch_time = 17
    adjustable plate_voltage = 10
    functionsegment.tstep_adjust()
    if ion_time_of_flight < switch_time then
        ion_time_step = min(ion_time_step, switch_time- ion_time_of_flight)
    end
end
functionsegment.fast_adjust()
if ion_time_of_flight < switch_time then
    adj_elect02 = plate_voltage
else adj_elect02 = 0
end
end
do
    functionsegment.other_actions()
    if switch_time == ion_time_of_flight then
        sim_update_pe_surface = 1
    end
end
end
```

Appendix B

Arduino Program for Electron Spectrometer Operation and DAQ Automation

```
// Set 'TOP' for PWM resolution. Assumes 16 MHz clock.

const unsigned int TOP = 0xFFFF; // 16-bit resolution. 244 Hz PWM
// const unsigned int TOP = 0x7FFF; // 15-bit resolution. 488 Hz PWM
// const unsigned int TOP = 0x3FFF; // 14-bit resolution. 976 Hz PWM
// const unsigned int TOP = 0x1FFF; // 13-bit resolution. 1953 Hz PWM
// const unsigned int TOP = 0x0FFF; // 12-bit resolution. 3906 Hz PWM
// const unsigned int TOP = 0x07FF; // 11-bit resolution. 7812 Hz PWM
// const unsigned int TOP = 0x03FF; // 10-bit resolution. 15624 Hz PWM

define pwmPin 9

long pulseCount = 0;

float inputVoltage = 0;

float delayTime = 120; // Delay time in seconds

void PWM16Begin()

// Stop Timer/Counter1

TCCR1A = 0; // Timer/Counter1 Control Register A
TCCR1B = 0; // Timer/Counter1 Control Register B
TIMSK1 = 0; // Timer/Counter1 Interrupt Mask Register
TIFR1 = 0; // Timer/Counter1 Interrupt Flag Register
ICR1 = TOP;

OCR1A = 0; // Default to 0
OCR1B = 0; // Default to 0
```

```

// Set clock prescale to 1 for maximum PWM frequency TCCR1B |= (1 << CS10);
// Set to Timer/Counter1 to Waveform Generation Mode 14: Fast PWM with TOP set
by ICR1
TCCR1A |= (1 << WGM11);
TCCR1B |= (1 << WGM13) | (1 << WGM12) ;
void PWM16EnableA()

// Enable Fast PWM on Pin 9: Set OC1A at BOTTOM and clear OC1A on OCR1A
compare
TCCR1A |= (1 << COM1A1);
pinMode(9, OUTPUT);

inline void PWM16A(unsigned int PWMValue)
OCR1A = constrain(PWMValue, 0, TOP);

void setup()
Serial.begin(9600);
PWM16Begin();

// On the Arduino UNO T1A is Pin 9 and T1B is Pin 10
PWM16A(0); // Set initial PWM value for Pin 9
PWM16EnableA(); // Turn PWM on for Pin 9
attachInterrupt(0, handlePulse, RISING); //Connect the pulse counter to pin 2
Serial.begin(9600);
Serial.println(); //Required to start
void loop()
//testingCounts();

//Serial.print statements are for debugging ( except last one )
if(Serial.available())
inputVoltage = Serial.parseFloat();
//Serial.print("Voltage Input: ");

```

```

//Serial.println(inputVoltage,4);
long pwm = (long)(inputVoltage*65535/10);
//Serial.print("Pwm: ");
//Serial.println(pwm);
PWM16A(pwm);
//analogWrite(pwmPin,pwm);
delay(2000);//Required for the voltage output through RC filter to reach steady state
//Serial.println("Output voltage set. Now counting pulses");
//Now start counting pulses
pulseCount = 0;
delay(delayTime*1000); //Total time delay. Pulses are being counted during this time
Serial.print(""); //Required for some reason we dont know
Serial.println(String(pulseCount));
void testingCounts()
Serial.println(pulseCount);
delay(10);
void handlePulse()
pulseCount = pulseCount +1;

```

MATLAB Code for DAQ:

This sends voltage commands to Arduino for electron spectroscopy experiment, and receives the counts detected

```

close all; clear all;
s = serial('COM8');
set(s,'BaudRate',9600);
fopen(s);
V_array = 3.7:0.01:4.3;

```

```
counts_array = 0 * V_array ;
fgetl(s);
for i = 1 : length(V_array)
fprintf(s, num2str(V_array(i)));
pause(20);
counts_array(i) = str2num(fgetl(s));
end
fclose(s);
delete(s);
dlmwrite('xenon210220171718.txt', [V_array'counts_array'])
```

Appendix C

Function Fit Program for Metastable Decay Life-time Measurement

```
float timetochannel=ROOT::TMath::Power(10,-12)*25;

float mass1=15.0;

float mass2=87.0;

float tau=150*ROOT::TMath::Power(10,-9);

float tauchannel=tau/timetochannel;

//(1/(160*1000))*70;

TF1 f2 ( "f2","exp(-(x/[2])*(([0]+[1])/([0]-[1])))" ,45000,68000); //function

f2->SetParameter(0,mass1);

f2->SetParameter(1,mass2);

f2->SetParameter(2,tauchannel);

float constant=f2->GetMaximum();

float counts=68;

TF1 f ( "f",("[4]/[3])*exp(-(x/[2])*(([0]+[1])/([0]-[1])))" ,45000,68000); //function

f->SetParameter(0,mass1);

f->SetParameter(1,mass2);

f->SetParameter(2,tauchannel);

f->SetParameter(3,constant);

f->SetParameter(4,counts);
```

Bibliography

- [1] M. De Becker, “Astrochemistry: the issue of molecular complexity in astrophysical environments,” *arXiv preprint arXiv:1305.6243*, 2013.
- [2] P. Ehrenfreund, M. Spaans, and N. G. Holm, “The evolution of organic matter in space,” *Philosophical Transactions of the Royal Society of London A: Mathematical, Physical and Engineering Sciences*, vol. 369, no. 1936, pp. 538–554, 2011.
- [3] J. J. Thomson, “XI. cathode rays,” *The London, Edinburgh, and Dublin Philosophical Magazine and Journal of Science*, vol. 44, no. 269, pp. 293–316, 1897.
- [4] J. Thomson, “Xlvii. on rays of positive electricity,” *The London, Edinburgh, and Dublin Philosophical Magazine and Journal of Science*, vol. 13, no. 77, pp. 561–575, 1907.
- [5] E. Rutherford, H. Nagaoka, H. Schmidt, and H. Geiger, “Rutherford 1913,” *Phil. Mag*, vol. 21, p. 669, 1911.
- [6] S. D. Price, “Investigating the gas-phase chemical reactions of molecular dications,” *Physical Chemistry Chemical Physics*, vol. 5, no. 9, pp. 1717–1729, 2003.
- [7] R. Thissen, O. Witasse, O. Dutuit, C. S. Wedlund, G. Gronoff, and J. Lilensten, “Doubly-charged ions in the planetary ionospheres: a review,” *Physical Chemistry Chemical Physics*, vol. 13, no. 41, pp. 18 264–18 287, 2011.
- [8] M. T. D., “Fundamental aspects of electron impact ionization,” *Int. J. Massspectrom. Ion Phys.*, vol. 45, pp. 125–145, 1982.
- [9] M. E. Wacks and V. H. Dibeler, “Electron impact studies of aromatic hydrocarbons. i. benzene, naphthalene, anthracene, and phenanthrene,” *The Journal of Chemical Physics*, vol. 31, no. 6, pp. 1557–1562, 1959.

- [10] M. E. Wacks, "Electron-impact studies of aromatic hydrocarbons. ii. naphthacene, naphthaphene, chrysene, triphenylene, and pyrene," *The Journal of Chemical Physics*, vol. 41, no. 6, pp. 1661–1666, 1964.
- [11] R. J. Van Brunt and M. E. Wacks, "Electron-impact studies of aromatic hydrocarbons. iii. azulene and naphthalene," *The Journal of Chemical Physics*, vol. 41, no. 10, pp. 3195–3199, 1964.
- [12] M. A. Baldwin, Langley, and G. John, "Identification of two separate mechanisms for hcn loss from gas phase quinoline cations," *Journal of Mass Spectrometry*, vol. 21, no. 1, pp. 29–31, 1986.
- [13] M. A. Baldwin, J. Gilmore, and M. N. Mruzek, "Unexpected structural integrity of gas phase isoquinoline cations that eliminate hcn," *Journal of Mass Spectrometry*, vol. 18, no. 3, pp. 127–129, 1983.
- [14] P. Mishra, J. Rajput, C. Safvan, S. Vig, and U. Kadhane, "Velocity dependence of fragmentation yields in proton–naphthalene collision and comparison with electronic energy loss calculation," *Journal of Physics B: Atomic, Molecular and Optical Physics*, vol. 47, no. 8, p. 085202, 2014.
- [15] L. Andersen, P. Hvelplund, H. Knudsen, S. Møller, K. Elsener, K.-G. Rensfelt, and E. Uggerhøj, "Single and double ionization of helium by fast antiproton and proton impact," *Physical review letters*, vol. 57, no. 17, p. 2147, 1986.
- [16] R. DuBois, L. Toburen, and M. E. Rudd, "Multiple ionization of rare gases by h+ and he+ impact," *Physical Review A*, vol. 29, no. 1, p. 70, 1984.
- [17] A. de Barros, J. Lecointre, H. Luna, M. Shah, and E. Montenegro, "Energy distributions of h+ fragments ejected by fast proton and electron projectiles in collision with h₂o molecules," *Physical Review A*, vol. 80, no. 1, p. 012716, 2009.
- [18] R. Browning and H. Gilbody, "Fragmentation of molecular gases by 5–45 kev protons," *Journal of Physics B: Atomic and Molecular Physics*, vol. 1, no. 6, p. 1149, 1968.

- [19] J.-P. Champeaux, P. Çarçabal, M. Sence, P. Moretto-Capelle, and P. Cafarelli, “A simple statistical approach for fragmentation studies of doubly ionized cytosine, thymine and uracil bases,” *Journal of Physics B: Atomic, Molecular and Optical Physics*, vol. 44, no. 4, p. 045205, 2011.
- [20] L. Chen, R. Bredy, J. Bernard, G. Montagne, A. Allouche, and S. Martin, “Fragmentation of singly charged adenine induced by neutral fluorine beam impact at 3 keV,” *The Journal of chemical physics*, vol. 135, no. 11, p. 114309, 2011.
- [21] B. Coupier, B. Farizon, M. Farizon, M. Gaillard, F. Gobet, N. de Castro Faria, G. Jalbert, S. Ouaskit, M. Carré, B. Gstyr *et al.*, “Inelastic interactions of protons and electrons with biologically relevant molecules,” *The European Physical Journal D-Atomic, Molecular, Optical and Plasma Physics*, vol. 20, no. 3, pp. 459–468, 2002.
- [22] S. Ptasińska, P. Candori, S. Denifl, S. Yoon, V. Grill, P. Scheier, and T. Märk, “Dissociative ionization of the nucleosides thymidine and uridine by electron impact,” *Chemical physics letters*, vol. 409, no. 4, pp. 270–276, 2005.
- [23] B. Boudaïffa, P. Cloutier, D. Hunting, M. A. Huels, and L. Sanche, “Resonant formation of dna strand breaks by low-energy (3 to 20 eV) electrons,” *Science*, vol. 287, no. 5458, pp. 1658–1660, 2000.
- [24] H. Abdoul-Carime, J. Langer, M. Huels, and E. Illenberger, “Decomposition of purine nucleobases by very low energy electrons,” *The European Physical Journal D-Atomic, Molecular, Optical and Plasma Physics*, vol. 35, no. 2, pp. 399–404, 2005.
- [25] T. Märk, “Cross section for single and double ionization of N₂ and O₂ molecules by electron impact from threshold up to 170 eV,” *The Journal of Chemical Physics*, vol. 63, no. 9, pp. 3731–3736, 1975.
- [26] F. Alvarado, S. Bari, R. Hoekstra, and T. Schlathölter, “Interactions of neutral and singly charged keV atomic particles with gas-phase adenine molecules,” *The Journal of chemical physics*, vol. 127, no. 3, p. 034301, 2007.

- [27] J. Postma, S. Bari, R. Hoekstra, A. Tielens, and T. Schlathölter, “Ionization and fragmentation of anthracene upon interaction with keV protons and α particles,” *The Astrophysical Journal*, vol. 708, no. 1, p. 435, 2009.
- [28] D. Bordenave-Montesquieu, P. Moretto-Capelle, A. Bordenave-Montesquieu, and A. Rentenier, “Scaling of c60 ionization and fragmentation with the energy deposited in collisions with h⁺, h₂⁺, h₃⁺ and he⁺ ions (2-130 keV),” *Journal of Physics B: Atomic, Molecular and Optical Physics*, vol. 34, no. 5, p. L137, 2001.
- [29] B. Forsberg, J. D. Alexander, T. Chen, A. Pettersson, M. Gatchell, H. Cederquist, and H. Zettergren, “Ions interacting with planar aromatic molecules: Modeling electron transfer reactions,” *The Journal of chemical physics*, vol. 138, no. 5, p. 054306, 2013.
- [30] A. I. Holm, H. Zettergren, H. A. Johansson, F. Seitz, S. Rosen, H. T. Schmidt, A. Ławicki, J. Rangama, P. Rousseau, M. Capron *et al.*, “Ions colliding with cold polycyclic aromatic hydrocarbon clusters,” *Physical review letters*, vol. 105, no. 21, p. 213401, 2010.
- [31] S. Martin, L. Chen, R. Brédy, G. Montagne, C. Ortega, T. Schlathölter, G. Reitsma, and J. Bernard, “Statistical fragmentation of doubly charged anthracene induced by fluorine-beam impact at 3 keV,” *Physical Review A*, vol. 85, no. 5, p. 052715, 2012.
- [32] H. Jochims, E. Rühl, H. Baumgärtel, S. Tobita, and S. Leach, “Vuv peaks in absorption spectra and photoion yield curves of polycyclic aromatic hydrocarbons and related compounds,” *International journal of mass spectrometry and ion processes*, vol. 167, pp. 35–53, 1997.
- [33] I. Hertel, H. Steger, J. De Vries, B. Weisser, C. Menzel, B. Kamke, and W. Kamke, “Giant plasmon excitation in free c 60 and c 70 molecules studied by photoionization,” *Physical review letters*, vol. 68, no. 6, p. 784, 1992.
- [34] P. M. Mishra, J. Rajput, C. P. Safvan, S. Vig, and U. Kadhane, “Electron emission and electron transfer processes in proton-naphthalene collisions at intermediate velocities,” *Phys. Rev. A*, vol. 88, p. 052707, Nov 2013.

- [35] U. Kadhane, D. Misra, Y. Singh, and L. C. Tribedi, "Effect of collective response on electron capture and excitation in collisions of highly charged ions with fullerenes," *Physical review letters*, vol. 90, no. 9, p. 093401, 2003.
- [36] H. Jochims, H. Baumgärtel, and S. Leach, "Structure-dependent photostability of polycyclic aromatic hydrocarbon cations: Laboratory studies and astrophysical implications," *The astrophysical journal*, vol. 512, no. 1, p. 500, 1999.
- [37] G. Baldwin and G. Klaiber, "Photo-fission in heavy elements," *Physical Review*, vol. 71, no. 1, p. 3, 1947.
- [38] I. Kaplan, "Giant resonances in atoms, atomic clusters, fullerenes, condensed media, and nuclei," *Zeitschrift für Physik D Atoms, Molecules and Clusters*, vol. 40, no. 1, pp. 375–380, 1997.
- [39] I. G. Kaplan, "Comparative discussion of the giant resonance phenomenon in nuclei, atoms, atomic clusters, and condensed media," *Czechoslovak journal of physics*, vol. 48, no. 6-7, pp. 763–768, 1998.
- [40] G. F. Bertsch, A. Bulgac, D. Tománek, and Y. Wang, "Collective plasmon excitations in c 60 clusters," *Physical review letters*, vol. 67, no. 19, p. 2690, 1991.
- [41] Y. Ling and C. Lifshitz, "Plasmon excitation in polycyclic aromatic hydrocarbons studied by photoionization," *Chemical physics letters*, vol. 257, no. 5-6, pp. 587–591, 1996.
- [42] U. Kadhane, A. Kelkar, D. Misra, A. Kumar, and L. C. Tribedi, "Effect of giant plasmon excitations in single and double ionization of c 60 in fast heavy-ion collisions," *Physical Review A*, vol. 75, no. 4, p. 041201, 2007.
- [43] M. T. D., "Electron impact ionization, in gaseous ion chemistry and ms, futrell," *Int. J. Massspectrom. Ion Phys.*, pp. 61–93, 1986.
- [44] M. A. Baldwin and K. J. Welham, "Charge localization by molecular orbital calculations. i. urea and thiourea," *Rapid Communications in Mass Spectrometry*, vol. 1, no. 1, pp. 13–15, 1987.

- [45] W. Baldwin, Michael. A. and K. J., “Charge localization by molecular orbital calculations. ii. formamide, thioformamide and n-methylated analogues,” *Journal of Mass Spectrometry*, vol. 23, no. 5, pp. 425–428, 1988.
- [46] R. Weinkauff, F. Lehrer, E. Schlag, and A. Metsala, “Investigation of charge localization and charge delocalization in model molecules by multiphoton ionization photoelectron spectroscopy and dft calculations,” *Faraday discussions*, vol. 115, pp. 363–381, 2000.
- [47] S. Denifl, B. Sonnweber, J. Mack, L. Scott, P. Scheier, K. Becker, and T. Märk, “Appearance energies of singly, doubly, and triply charged coronene and corannulene ions produced by electron impact,” *International Journal of Mass Spectrometry*, vol. 249, pp. 353–358, 2006.
- [48] A. Ławicki, A. I. Holm, P. Rousseau, M. Capron, R. Maisonnay, S. Maclot, F. Seitz, H. A. Johansson, S. Rosén, H. T. Schmidt *et al.*, “Multiple ionization and fragmentation of isolated pyrene and coronene molecules in collision with ions,” *Physical Review A*, vol. 83, no. 2, p. 022704, 2011.
- [49] M. Gatchell, M. Stockett, P. Rousseau, T. Chen, K. Kulyk, H. Schmidt, J. Chesnel, A. Domaracka, A. Méry, S. Maclot *et al.*, “Non-statistical fragmentation of paphs and fullerenes in collisions with atoms,” *International Journal of Mass Spectrometry*, vol. 365, pp. 260–265, 2014.
- [50] M. H. Stockett, H. Zettergren, L. Adoui, J. Alexander, U. Bērziņš, T. Chen, M. Gatchell, N. Haag, B. Huber, P. Hvelplund *et al.*, “Nonstatistical fragmentation of large molecules,” *Physical Review A*, vol. 89, no. 3, p. 032701, 2014.
- [51] M. Stockett, L. Adoui, E. Anderson, T. Chen, J. Chesnel, N. De Ruelle, M. Gatchell, L. Giacomozzi, B. Huber, K. Kulyk *et al.*, “Non-statistical fragmentation of large molecules in collisions with atoms,” in *Journal of Physics: Conference Series*, vol. 635, no. 1. IOP Publishing, 2015, p. 012036.
- [52] T. Chen, M. Gatchell, M. H. Stockett, J. D. Alexander, Y. Zhang, P. Rousseau, A. Domaracka, S. Maclot, R. Delaunay, L. Adoui *et al.*, “Absolute fragmentation

- cross sections in atom-molecule collisions: scaling laws for non-statistical fragmentation of polycyclic aromatic hydrocarbon molecules,” *The Journal of chemical physics*, vol. 140, no. 22, p. 224306, 2014.
- [53] Y. A. Dyakov, C.-K. Ni, S. Lin, Y. Lee, and A. Mebel, “Ab initio and rrmk study of photodissociation of azulene cation,” *Physical Chemistry Chemical Physics*, vol. 8, no. 12, pp. 1404–1415, 2006.
- [54] J. Schirmer, L. Cederbaum, W. Domcke, and W. Von Niessen, “Strong correlation effects in inner valence ionization of n₂ and co,” *Chemical Physics*, vol. 26, no. 1, pp. 149–153, 1977.
- [55] J. Schirmer, L. S. Cederbaum, W. Domcke, and W. Von Niessen, “Complete breakdown of the quasiparticle picture for inner-valence electrons: Hydrogen cyanide and formic acid,” *Chemical Physics Letters*, vol. 57, no. 4, pp. 582–587, 1978.
- [56] L. Cederbaum and W. Domcke, “Theoretical aspects of ionization potentials and photoelectron spectroscopy: A green’s function approach,” *Adv. Chem. Phys.*, vol. 36, pp. 205–344, 1977.
- [57] L. Cederbaum, W. Domcke, J. Schirmer, W. Von Niessen, G. Diercksen, and W. Kraemer, “Correlation effects in the ionization of hydrocarbons,” *The Journal of Chemical Physics*, vol. 69, no. 4, pp. 1591–1603, 1978.
- [58] W. von Niessen, “Application of a green’s function method to the calculation of photoelectron spectra,” *Butlletí de les Societats Catalanes de Física, Química, Matemàtiques i Tecnologia*, pp. 227–262, 1991.
- [59] M. Alagia, P. Candori, S. Falcinelli, F. Pirani, M. S. P. Mundim, R. Richter, M. Rosi, S. Stranges, and F. Vecchiocattivi, “Dissociative double photoionization of benzene molecules in the 26–33 eV energy range,” *Physical Chemistry Chemical Physics*, vol. 13, no. 18, pp. 8245–8250, 2011.
- [60] P. Mishra, J. Rajput, C. Safvan, S. Vig, and U. Kadhane, “Electron emission and electron transfer processes in proton-naphthalene collisions at intermediate velocities,” *Physical Review A*, vol. 88, no. 5, p. 052707, 2013.

- [61] J. Ullrich, R. Moshhammer, R. Dörner, O. Jagutzki, V. Mergel, H. Schmidt-Böcking, and L. Spielberger, “Recoil-ion momentum spectroscopy,” *Journal of Physics B: Atomic, Molecular and Optical Physics*, vol. 30, no. 13, p. 2917, 1997.
- [62] R. Doerner, V. Mergel, L. Spielberger, M. Achler, K. Khayyat, T. Vogt, H. Bräuning, O. Jagutzki, T. Weber, J. Ullrich *et al.*, “Kinematically complete experiments using cold target recoil ion momentum spectroscopy,” *Nuclear Instruments and Methods in Physics Research Section B: Beam Interactions with Materials and Atoms*, vol. 124, no. 2-3, pp. 225–231, 1997.
- [63] F. M. Penning, “Die glimmentladung bei niedrigem druck zwischen koaxialen zylindern in einem axialen magnetfeld,” *physica*, vol. 3, no. 9, pp. 873–894, 1936.
- [64] W. Paul and M. Raether, “Das elektrische massenfilter,” *Zeitschrift für Physik A Hadrons and Nuclei*, vol. 140, no. 3, pp. 262–273, 1955.
- [65] W. Paul, H. Reinhard, and U. Von Zahn, “Das elektrische massenfilter als massenspektrometer und isotopentrenner,” *Zeitschrift für Physik A Hadrons and Nuclei*, vol. 152, no. 2, pp. 143–182, 1958.
- [66] M. Guilhaus, “Special feature: Tutorial. principles and instrumentation in time-of-flight mass spectrometry. physical and instrumental concepts,” *Journal of Mass Spectrometry*, vol. 30, no. 11, pp. 1519–1532, 1995.
- [67] A. J. de Haas, J. Oomens, and J. Bouwman, “Time of flight mass spectrometer with improved resolution,” *Review of Scientific Instruments*, 1993.
- [68] A. G. Tielens, “Interstellar polycyclic aromatic hydrocarbon molecules,” *Annu. Rev. Astron. Astrophys.*, vol. 46, pp. 289–337, 2008.
- [69] H. Yu, “Environmental carcinogenic polycyclic aromatic hydrocarbons: photochemistry and phototoxicity,” *Journal of Environmental Science and Health, Part C*, vol. 20, no. 2, pp. 149–183, 2002.
- [70] V. Dryza, J. A. Sanelli, E. G. Robertson, and E. J. Bieske, “Electronic spectra of gas-phase polycyclic aromatic nitrogen heterocycle cations: Isoquinoline⁺ and

- quinoline+,” *The Journal of Physical Chemistry A*, vol. 116, no. 17, pp. 4323–4329, 2012.
- [71] A. Mattioda, D. M. Hudgins, C. Bauschlicher, M. Rosi, and L. Allamandola, “Infrared spectroscopy of matrix-isolated polycyclic aromatic compounds and their ions. 6. polycyclic aromatic nitrogen heterocycles,” *The Journal of Physical Chemistry A*, vol. 107, no. 10, pp. 1486–1498, 2003.
- [72] H. A. Galué, O. Pirali, and J. Oomens, “Gas-phase infrared spectra of cationized nitrogen-substituted polycyclic aromatic hydrocarbons,” *Astronomy & Astrophysics*, vol. 517, p. A15, 2010.
- [73] B. Klærke, A. Holm, and L. H. Andersen, “Uv action spectroscopy of protonated pah derivatives-methyl substituted quinolines,” *Astronomy & Astrophysics*, vol. 532, p. A132, 2011.
- [74] Z. Peeters, O. Botta, S. Charnley, Z. Kisiel, Y.-J. Kuan, and P. Ehrenfreund, “Formation and photostability of n-heterocycles in space-i. the effect of nitrogen on the photostability of small aromatic molecules,” *Astronomy & Astrophysics*, vol. 433, no. 2, pp. 583–590, 2005.
- [75] S. Soorkia, C. A. Taatjes, D. L. Osborn, T. M. Selby, A. J. Trevitt, K. R. Wilson, and S. R. Leone, “Direct detection of pyridine formation by the reaction of ch (cd) with pyrrole: a ring expansion reaction,” *Physical Chemistry Chemical Physics*, vol. 12, no. 31, pp. 8750–8758, 2010.
- [76] J. E. Elsila, M. R. Hammond, M. P. Bernstein, S. A. Sandford, and R. N. Zare, “Uv photolysis of quinoline in interstellar ice analogs,” *Meteoritics & Planetary Science*, vol. 41, no. 5, pp. 785–796, 2006.
- [77] P. G. Stoks and A. W. Schwartz, “Nitrogen-heterocyclic compounds in meteorites: significance and mechanisms of formation,” *Geochimica et Cosmochimica Acta*, vol. 45, no. 4, pp. 563–569, 1981.
- [78] A. Landera and A. M. Mebel, “Mechanisms of formation of nitrogen-containing polycyclic aromatic compounds in low-temperature environments of planetary at-

- mospheres: A theoretical study,” *Faraday discussions*, vol. 147, pp. 479–494, 2010.
- [79] A. Tielens, “The molecular universe,” *Reviews of Modern Physics*, vol. 85, no. 3, p. 1021, 2013.
- [80] C. S. Hansen, S. J. Blanksby, and A. J. Trevitt, “Ultraviolet photodissociation action spectroscopy of gas-phase protonated quinoline and isoquinoline cations,” *Physical Chemistry Chemical Physics*, vol. 17, no. 39, pp. 25 882–25 890, 2015.
- [81] G. Portella, J. Poater, J. M. Bofill, P. Alemany, and M. Sola, “Local aromaticity of [n] acenes,[n] phenacenes, and [n] helicenes (n= 1- 9),” *The Journal of organic chemistry*, vol. 70, no. 7, pp. 2509–2521, 2005.
- [82] C. Koper, L. W. Jenneskens, and M. Sarobe, “Externally-fused cyclopenta moieties in non-alternant cp-pahs act as peri-substituents,” *Tetrahedron letters*, vol. 43, no. 21, pp. 3833–3836, 2002.
- [83] A. Jones, A. Tielens, D. Hollenbach, and C. McKee, “Grain destruction in shocks in the interstellar medium,” *The Astrophysical Journal*, vol. 433, pp. 797–810, 1994.
- [84] A. Jones, A. Tielens, and D. Hollenbach, “Grain shattering in shocks: The interstellar grain size distribution,” *The Astrophysical Journal*, vol. 469, p. 740, 1996.
- [85] E. Micelotta, A. Jones, and A. Tielens, “Polycyclic aromatic hydrocarbon processing in interstellar shocks,” *Astronomy & Astrophysics*, vol. 510, p. A36, 2010.
- [86] Y. Gotkis, M. Oleinikova, M. Naor, and C. Lifshitz, “Time-dependent mass spectra and breakdown graphs. xvii: Naphthalene and phenanthrene,” *Journal of physical chemistry*, vol. 97, no. 47, pp. 12 282–12 290, 1993.
- [87] B. West, C. Joblin, V. Blanchet, A. Bodi, B. Sztáray, and P. M. Mayer, “On the dissociation of the naphthalene radical cation: new ipepico and tandem mass spectrometry results,” *The Journal of Physical Chemistry A*, vol. 116, no. 45, pp. 10 999–11 007, 2012.

- [88] J. Poveda, A. Guerrero, I. Alvarez, and C. Cisneros, "Multiphoton ionization and dissociation of naphthalene at 266, 355, and 532nm," *Journal of Photochemistry and Photobiology A: Chemistry*, vol. 215, no. 2, pp. 140–146, 2010.
- [89] B. Lohmann, "Electron–auger electron coincidence experiments: Current status and future prospects," *Australian journal of physics*, vol. 49, no. 2, pp. 365–374, 1996.
- [90] B. Brehm and E. von Puttkamer, "Koinzidenzmessung von photoionen und photoelektronen bei methan," *Zeitschrift für Naturforschung A*, vol. 22, no. 1, pp. 8–10, 1967.
- [91] J. H. Eland, "Predissociation of triatomic ions studied by photo-electron-photoion coincidence spectroscopy and photoion kinetic energy analysis: I. CO_2^+ ," *International Journal of Mass Spectrometry and Ion Physics*, vol. 9, no. 4, pp. 397–406, 1972.
- [92] P. Morin, M. Simon, C. Miron, N. Leclercq, and D. Hansen, "Electron-ion spectroscopy: a probe of molecular dynamics," *Journal of electron spectroscopy and related phenomena*, vol. 93, no. 1, pp. 49–60, 1998.
- [93] D. Céolin, C. Miron, M. Simon, and P. Morin, "Auger electron-ion coincidence studies to probe molecular dynamics," *Journal of electron spectroscopy and related phenomena*, vol. 141, no. 2, pp. 171–181, 2004.
- [94] E. Fainelli, F. Maracci, and R. Platania, "Auger electron–ion coincidence experiment on nitrogen molecule excited by electron impact," *The Journal of chemical physics*, vol. 101, no. 8, pp. 6565–6569, 1994.
- [95] E. Fainelli, F. Maracci, R. Platania, and L. Avaldi, "The fragmentation of CCl_4 dications studied by auger electron-ion coincidence experiments," *Journal of Electron Spectroscopy and Related Phenomena*, vol. 119, no. 1, pp. 81–93, 2001.
- [96] M. Born and R. Oppenheimer, "Zur quantentheorie der molekeln," *Annalen der Physik*, vol. 389, no. 20, pp. 457–484, 1927.

- [97] K. Capelle, “A bird’s-eye view of density-functional theory,” *Brazilian Journal of Physics*, vol. 36, no. 4A, pp. 1318–1343, 2006.
- [98] P. Hohenberg and W. Kohn, “Inhomogeneous electron gas,” *Physical review*, vol. 136, no. 3B, p. B864, 1964.
- [99] A. Becke, “Density-functional thermochemistry. iii. the role of exact exchange,” *J. Chem. Phys.*, vol. 98, pp. 5648–5652, 1993.
- [100] J.-D. Chai and M. Head-Gordon, “Long-range corrected hybrid density functionals with damped atom–atom dispersion corrections,” *Physical Chemistry Chemical Physics*, vol. 10, no. 44, pp. 6615–6620, 2008.
- [101] Y. Zhao and D. G. Truhlar, “A new local density functional for main-group thermochemistry, transition metal bonding, thermochemical kinetics, and noncovalent interactions,” *The Journal of chemical physics*, vol. 125, no. 19, p. 194101, 2006.
- [102] S. Grimme, “Density functional theory with london dispersion corrections,” *Wiley Interdisciplinary Reviews: Computational Molecular Science*, vol. 1, no. 2, pp. 211–228, 2011.
- [103] M. Frisch, G. Trucks, H. Schlegel, G. Scuseria, M. Robb, J. Cheeseman, G. Scalmani, V. Barone, B. Mennucci, G. Petersson *et al.*, “Gaussian 09, revision d. 01,” 2009.
- [104] J. Bouwman, B. Sztal^ÀAray, J. Oomens, P. Hemberger, and A. Bodi, “Dissociative photoionization of quinoline and isoquinoline,” *The Journal of Physical Chemistry A*, vol. 119, no. 7, pp. 1127–1136, 2015.
- [105] M. J. Frisch, G. W. Trucks, H. B. Schlegel, G. E. Scuseria, M. A. Robb, J. R. Cheeseman, G. Scalmani, V. Barone, B. Mennucci, G. A. Petersson, H. Nakatsuji, M. Caricato, X. Li, H. P. Hratchian, A. F. Izmaylov, J. Bloino, G. Zheng, J. L. Sonnenberg, M. Hada, M. Ehara, K. Toyota, R. Fukuda, J. Hasegawa, M. Ishida, T. Nakajima, Y. Honda, O. Kitao, H. Nakai, T. Vreven, J. A. Montgomery, Jr., J. E. Peralta, F. Ogliaro, M. Bearpark, J. J. Heyd, E. Brothers, K. N. Kudin, V. N. Staroverov, R. Kobayashi, J. Normand, K. Raghavachari, A. Rendell, J. C. Burant,

- S. S. Iyengar, J. Tomasi, M. Cossi, N. Rega, J. M. Millam, M. Klene, J. E. Knox, J. B. Cross, V. Bakken, C. Adamo, J. Jaramillo, R. Gomperts, R. E. Stratmann, O. Yazyev, A. J. Austin, R. Cammi, C. Pomelli, J. W. Ochterski, R. L. Martin, K. Morokuma, V. G. Zakrzewski, G. A. Voth, P. Salvador, J. J. Dannenberg, S. Dapprich, A. D. Daniels, Ā. Farkas, J. B. Foresman, J. V. Ortiz, J. Cioslowski, and D. J. Fox, “GaussianĀĹij09 Revision E.01,” gaussian Inc. Wallingford CT 2009.
- [106] K. D. Dobbs and W. Hehre, “Molecular orbital theory of the properties of inorganic and organometallic compounds. 6. extended basis sets for second-row transition metals,” *Journal of computational chemistry*, vol. 8, no. 6, pp. 880–893, 1987.
- [107] P. J. Linstrom and W. G. Mallard, *NIST Chemistry WebBook, NIST Standard Reference Database Number 69*. Gaithersburg MD, 20899: National Institute of Standards and Technology, Jun. (2016).
- [108] A. Modelli and L. Mussoni, “Rapid quantitative prediction of ionization energies and electron affinities of polycyclic aromatic hydrocarbons,” *Chemical physics*, vol. 332, no. 2, pp. 367–374, 2007.
- [109] P. Mishra and U. Kadhane, “Monte carlo simulation of electronic energy loss for proton impact on nucleobases,” *Nuclear Instruments and Methods in Physics Research Section B: Beam Interactions with Materials and Atoms*, vol. 336, pp. 12–18, 2014.
- [110] F. Elder, R. Langmuir, and H. Pollock, “Radiation from electrons accelerated in a synchrotron,” *Physical Review*, vol. 74, no. 1, p. 52, 1948.
- [111] C. Pellegrini, “The history of x-ray free-electron lasers,” *The European Physical Journal H*, vol. 37, no. 5, pp. 659–708, 2012.
- [112] D. R. Hamilton and L. Gross, “An electrostatic beta-spectrograph,” *Review of Scientific Instruments*, vol. 21, no. 11, pp. 912–917, 1950.
- [113] J. A. Simpson, “Design of retarding field energy analyzers,” *Review of Scientific Instruments*, vol. 32, no. 12, pp. 1283–1293, 1961.

- [114] M. Satir, F. Sik, E. Turkoz, and M. Celik, "Design of the retarding potential analyzer to be used with burfit-80 ion thruster and validation using pic-dsmc code," in *Recent Advances in Space Technologies (RAST), 2015 7th International Conference on.* IEEE, 2015, pp. 577–582.
- [115] G. Harrower, "Measurement of electron energies by deflection in a uniform electric field," *Review of Scientific Instruments*, vol. 26, no. 9, pp. 850–854, 1955.
- [116] J. Rubio-Zuazo and G. Castro, "First principle study of the properties of a cylindrical sector analyzer: Complete calculation of the electron trajectory," *Journal of Electron Spectroscopy and Related Phenomena*, vol. 184, no. 8, pp. 440–451, 2011.
- [117] J. S. Risley, "Design parameters for the cylindrical mirror energy analyzer," *Review of Scientific Instruments*, vol. 43, no. 1, pp. 95–103, 1972.
- [118] X. Zhou, C. Xu, Z. Wei, W. Liu, J. Li, X. Chen, J. Williams, and K. Xu, "Angle and energy dispersive multichannel electron energy spectrometer for surface analysis," *Journal of Electron Spectroscopy and Related Phenomena*, vol. 165, no. 1, pp. 15–19, 2008.
- [119] F. Toffoletto, R. Leckey, and J. Riley, "Design criteria for an angle resolved electron spectrometer of novel toroidal geometry," *Nuclear Instruments and Methods in Physics Research Section B: Beam Interactions with Materials and Atoms*, vol. 12, no. 2, pp. 282–297, 1985.
- [120] S. Helmut and P. Wolfgang, "Apparatus for separating charged particles of different specific charges," Jun. 7 1960, uS Patent 2,939,952.
- [121] R. Ali, V. Frohne, and C. Cock, "M. st ockli, s. cheng, and l. raphaelian," *Phys. Rev. Lett*, vol. 69, p. 2491, 1992.
- [122] J. L. Wiza, "Microchannel plate detectors," *Nuclear Instruments and Methods*, vol. 162, no. 1-3, pp. 587–601, 1979.
- [123] L. M. Hirvonen and K. Suhling, "Wide-field tcspc: methods and applications," *Measurement Science and Technology*, vol. 28, no. 1, p. 012003, 2016.

- [124] J. G. Mainprize and M. J. Yaffe, “The effect of phosphor persistence on image quality in digital x-ray scanning systems,” *Medical physics*, vol. 25, no. 12, pp. 2440–2454, 1998.
- [125] M. Ameloot, B. Valeur, N. Boens *et al.*, “Pitfalls and their remedies in time-resolved fluorescence spectroscopy and microscopy,” *Journal of fluorescence*, vol. 15, no. 3, pp. 377–413, 2005.
- [126] P. Hoess and K. Fleder, “Response of very-fast-decay phosphors in image intensifier tubes for ccd readout devices,” in *24th International Congress on High-Speed Photography and Photonics*, vol. 4183. International Society for Optics and Photonics, 2001, pp. 127–133.
- [127] W. Augustyniak, W. Brown, and H. Lie, “A hybrid approach to two dimensional charged particle position sensing preserving energy resolution,” *IEEE Transactions on Nuclear Science*, vol. 19, no. 3, pp. 196–200, 1972.
- [128] M. Lampton and F. Paresce, “The ranicon: A resistive anode image converter,” *Review of Scientific Instruments*, vol. 45, no. 9, pp. 1098–1105, 1974.
- [129] M. Lampton and R. Malina, “Quadrant anode image sensor,” *Review of Scientific Instruments*, vol. 47, no. 11, pp. 1360–1362, 1976.
- [130] Y. Prokazov, E. Turbin, M. Vitali, A. Herzog, B. Michaelis, W. Zuschratter, and K. Kemnitz, “Reborn quadrant anode image sensor,” *Nuclear Instruments and Methods in Physics Research Section A: Accelerators, Spectrometers, Detectors and associated Equipment*, vol. 604, no. 1, pp. 221–223, 2009.
- [131] K. Kemnitz, L. Pfeifer, R. Paul, and M. Coppey-Moisan, “Novel detectors for fluorescence lifetime imaging on the picosecond time scale,” *Journal of Fluorescence*, vol. 7, no. 1, pp. 93–98, 1997.
- [132] K. Kemnitz, L. Pfeifer, and M. Ainbund, “Detector for multichannel spectroscopy and fluorescence lifetime imaging on the picosecond timescale,” *Nuclear Instruments and Methods in Physics Research Section A: Accelerators, Spectrometers, Detectors and Associated Equipment*, vol. 387, no. 1-2, pp. 86–87, 1997.

- [133] C. Martin, P. Jelinsky, M. Lampton, R. Malina, and H. Anger, “Wedge-and-strip anodes for centroid-finding position-sensitive photon and particle detectors,” *Review of Scientific Instruments*, vol. 52, no. 7, pp. 1067–1074, 1981.
- [134] O. Siegmund, S. Clothier, J. Thornton, J. Lemen, R. Harper, I. Mason, and J. Culhane, “Application of the wedge and strip anode to position sensing with microchannel plates and proportional counters,” *IEEE Transactions on Nuclear Science*, vol. 30, no. 1, pp. 503–507, 1983.
- [135] H. Anger, “Survey of radioisotope cameras.” Univ. of California, Berkeley, Tech. Rep., 1966.
- [136] O. Jagutzki, V. Mergel, K. Ullmann-Pfleger, L. Spielberger, U. Spillmann, R. Dörner, and H. Schmidt-Böcking, “A broad-application microchannel-plate detector system for advanced particle or photon detection tasks: large area imaging, precise multi-hit timing information and high detection rate,” *Nuclear Instruments and Methods in Physics Research Section A: Accelerators, Spectrometers, Detectors and Associated Equipment*, vol. 477, no. 1, pp. 244–249, 2002.
- [137] A. Oelsner, O. Schmidt, M. Schicketanz, M. Klais, G. Schönhense, V. Mergel, O. Jagutzki, and H. Schmidt-Böcking, “Microspectroscopy and imaging using a delay line detector in time-of-flight photoemission microscopy,” *Review of Scientific Instruments*, vol. 72, no. 10, pp. 3968–3974, 2001.
- [138] O. Jagutzki, V. Dangendorf, R. Lauck, A. Czasch, and J. Milnes, “A position-and time-sensitive photon-counting detector with delay-line read-out,” *arXiv preprint physics/0703186*, 2007.
- [139] V. Sharma and B. Bapat, “An apparatus for studying momentum-resolved electron-impact dissociative and non-dissociative ionisation,” *The European Physical Journal D-Atomic, Molecular, Optical and Plasma Physics*, vol. 37, no. 2, pp. 223–229, 2006.
- [140] S. T. Manson and A. F. Starace, “Photoelectron angular distributions: energy dependence for s subshells,” *Reviews of Modern Physics*, vol. 54, no. 2, p. 389, 1982.

- [141] D. Gahl, "Simion 3d version 6.0," ASMS, East Lansing, MI (United States), Tech. Rep., 1995.
- [142] K. Saha, S. Banerjee, and B. Bapat, "A combined electron-ion spectrometer for studying complete kinematics of molecular dissociation upon shell selective ionization," *Review of Scientific Instruments*, vol. 84, no. 7, p. 073101, 2013.
- [143] S. Aksela, "Analysis of the energy distribution in cylindrical electron spectrometers," *Review of Scientific Instruments*, vol. 42, no. 6, pp. 810–812, 1971.
- [144] R. Baker and B. Johnson, "Series operation of power mosfets for high-speed, high-voltage switching applications," *Review of scientific instruments*, vol. 64, no. 6, pp. 1655–1656, 1993.
- [145] W. Jiang, "Fast high voltage switching using stacked mosfets," *IEEE Transactions on Dielectrics and Electrical Insulation*, vol. 14, no. 4, 2007.
- [146] P. Chappell and K. Campden, "Switching performance of power mosfets with capacitive loads at high frequency and high voltage for square wave generators," *Measurement Science and Technology*, vol. 3, no. 4, p. 356, 1992.
- [147] M. T. Bernius and A. Chutjian, "High-voltage, full-floating 10-mhz square-wave generator with phase control," *Review of Scientific Instruments*, vol. 60, no. 4, pp. 779–782, 1989.
- [148] F. C. A. Pockels, *Lehrbuch der kristallogoptik*. BG Teubner, 1906, vol. 19.
- [149] W. She and W. Lee, "Wave coupling theory of linear electrooptic effect," *Optics communications*, vol. 195, no. 1, pp. 303–311, 2001.
- [150] L. O. Werme, T. Bergmark, and K. Siegbahn, "The high resolution l2, 3 mm and m4, 5 nn auger spectra from krypton and m4, 5 nn and n4, 5 oo auger spectra from xenon," *Physica Scripta*, vol. 6, no. 2-3, p. 141, 1972.
- [151] S. Biswas and L. Tribedi, "Plasmon-mediated electron emission from the coronene molecule under fast ion impact," *Physical Review A*, vol. 92, no. 6, p. 060701, 2015.

- [152] S. Biswas, C. Champion, and L. C. Tribedi, "Differential electron emission from polycyclic aromatic hydrocarbon molecules under fast ion impact," *Scientific Reports*, vol. 7, 2017.
- [153] R. DuBois and M. E. Rudd, "Absolute doubly differential cross sections for ejection of secondary electrons from gases by electron impact. ii. 100-500-ev electrons on neon, argon, molecular hydrogen, and molecular nitrogen," *Physical Review A*, vol. 17, no. 3, p. 843, 1978.
- [154] P. J. Linstrom and W. Mallard, "Nist chemistry webbook; nist standard reference database no. 69," 2001.
- [155] Y.-K. Kim and M. E. Rudd, "Binary-encounter-dipole model for electron-impact ionization," *Physical Review A*, vol. 50, no. 5, p. 3954, 1994.
- [156] H. Deutsch, D. Margreiter, and T. Märk, "A semi-empirical approach to the calculation of absolute inner-shell electron impact ionization cross sections," *Zeitschrift für Physik D Atoms, Molecules and Clusters*, vol. 29, no. 1, pp. 31–37, 1994.
- [157] C. Vallance, P. W. Harland, and R. G. Maclagan, "Quantum mechanical calculation of maximum electron impact single ionization cross sections for the inert gases and small molecules," *The Journal of Physical Chemistry*, vol. 100, no. 37, pp. 15 021–15 026, 1996.
- [158] W. Hwang, Y.-K. Kim, and M. E. Rudd, "New model for electron-impact ionization cross sections of molecules," *The Journal of Chemical Physics*, vol. 104, no. 8, pp. 2956–2966, 1996.
- [159] B. Erk, D. Rolles, L. Foucar, B. Rudek, S. W. Epp, M. Cryle, C. Bostedt, S. Schorb, J. Bozek, A. Rouzee *et al.*, "Ultrafast charge rearrangement and nuclear dynamics upon inner-shell multiple ionization of small polyatomic molecules," *Physical review letters*, vol. 110, no. 5, p. 053003, 2013.
- [160] Y. Gotkis, M. Oleinikova, M. Naor, and C. Lifshitz, "Time-dependent mass spectra and breakdown graphs. xvii: Naphthalene and phenanthrene," *Journal of physical chemistry*, vol. 97, no. 47, pp. 12 282–12 290, 1993.

- [161] P. M. Mishra, L. Avaldi, P. Bolognesi, K. C. Prince, R. Richter, and U. R. Kadhane, "Valence shell photoelectron spectroscopy of pyrene and fluorene: Photon energy dependence in the far-ultraviolet region," *The Journal of Physical Chemistry A*, vol. 118, no. 17, pp. 3128–3135, 2014.
- [162] F. Salama and L. Allamandola, "Electronic absorption spectroscopy of matrix-isolated polycyclic aromatic hydrocarbon cations. i. the naphthalene cation (c₁₀h₈)," *The Journal of chemical physics*, vol. 94, no. 11, pp. 6964–6977, 1991.
- [163] J. Fulara, D. Lessen, P. Freivogel, and J. Maier, "Laboratory evidence for highly unsaturated hydrocarbons as carriers of some of the diffuse interstellar bands," *Nature*, vol. 366, no. 6454, pp. 439–441, 1993.
- [164] G. Reitsma, H. Zettergren, L. Boschman, E. Bodewits, R. Hoekstra, and T. Schlathölter, "Ion–polycyclic aromatic hydrocarbon collisions: kinetic energy releases for specific fragmentation channels," *Journal of Physics B: Atomic, Molecular and Optical Physics*, vol. 46, no. 24, p. 245201, 2013.
- [165] L. Sigaud, V. de Jesus, N. Ferreira, and E. Montenegro, "A novel double-focusing time-of-flight mass spectrometer for absolute recoil ion cross sections measurements," *Review of Scientific Instruments*, vol. 87, no. 8, p. 083112, 2016.
- [166] N. Ferreira, L. Sigaud, and E. Montenegro, "Molecular fragmentation by electron impact investigated using a time delayed spectroscopic technique," in *Journal of Physics: Conference Series*, vol. 488, no. 1. IOP Publishing, 2014, p. 012042.
- [167] W. C. Wiley and I. H. McLaren, "Time-of-flight mass spectrometer with improved resolution," *Review of Scientific Instruments*, vol. 26, pp. 39–441, 1993.
- [168] C. N. Burrous, A. J. Lieber, and V. T. Zaviantseff, "Detection efficiency of a continuous channel electron multiplier for positive ions," *Review of Scientific Instruments*, vol. 38, pp. 1477–1481, 1967.
- [169] A. Kumar, J. Rajput, T. Sairam, M. Jana, L. Nair, and C. Safvan, "Setup for measuring angular anisotropies in slow ion-molecule collisions," *International Journal of Mass Spectrometry*, vol. 374, pp. 44–48, 2014.

- [170] M. E. Rudd, T. Goffe, R. DuBois, and L. Toburen, “Cross sections for ionization of water vapor by 7–4000-keV protons,” *Physical Review A*, vol. 31, no. 1, p. 492, 1985.
- [171] F. Gobet, B. Farizon, M. Farizon, M. Gaillard, M. Carré, M. Lezius, P. Scheier, and T. Märk, “Total, partial, and electron-capture cross sections for ionization of water vapor by 20–150 keV protons,” *Physical review letters*, vol. 86, no. 17, p. 3751, 2001.
- [172] F. Gobet, S. Eden, B. Coupier, J. Tabet, B. Farizon, M. Farizon, M. Gaillard, M. Carré, S. Ouaskit, T. Märk *et al.*, “Ionization of water by (20–150)-keV protons: Separation of direct-ionization and electron-capture processes,” *Physical Review A*, vol. 70, no. 6, p. 062716, 2004.
- [173] M. H. Stockett, M. Gatchell, J. D. Alexander, U. Bērziņš, T. Chen, K. Farid, A. Johansson, K. Kulyk, P. Rousseau, K. Støchkel *et al.*, “Fragmentation of anthracene c 14 h 10, acridine c 13 h 9 n and phenazine c 12 h 8 n 2 ions in collisions with atoms,” *Physical Chemistry Chemical Physics*, vol. 16, no. 40, pp. 21 980–21 987, 2014.
- [174] P. Najeeb and U. Kadhane, “Delayed extraction time-of-flight mass spectrometer with electron impact for PAH studies,” *Journal of Instrumentation*, vol. 12, no. 03, p. P03009, 2017.
- [175] K. D. V. N. Bohr, “The penetration of atomic particles through matter,” *Mat. Fys. Medd*, vol. 18 (8), p. 144, 1948.
- [176] S. Cheng, H. Berry, R. Dunford, H. Esbensen, D. Gemmell, E. Kanter, T. LeBrun, and W. Bauer, “Ionization and fragmentation of C₆₀ by highly charged, high-energy xenon ions,” *Physical Review A*, vol. 54, no. 4, p. 3182, 1996.
- [177] P. K. Najeeb and U. Kadhane, “Relative stability of naphthalene, quinoline and isoquinoline under high energy electron impact,” *International Journal of Mass Spectrometry*, vol. 414, no. 03, pp. 23–30, 2017.

- [178] T. Schlathölter, O. Hadjar, J. Manske, R. Hoekstra, and R. Morgenstern, “Electronic versus vibrational excitation in he^+ collisions with fullerenes,” *International journal of mass spectrometry*, vol. 192, no. 1, pp. 245–257, 1999.
- [179] T. Schlathölter, O. Hadjar, R. Hoekstra, and R. Morgenstern, “Strong velocity effects in collisions of he^+ with fullerenes,” *Physical review letters*, vol. 82, no. 1, p. 73, 1999.
- [180] Z. Tan, Y. Xia, X. Liu, and M. Zhao, “Proton inelastic mean free path in amino acids and protein over the energy range of 0.05–10mev,” *Nuclear Instruments and Methods in Physics Research Section B: Beam Interactions with Materials and Atoms*, vol. 268, no. 17, pp. 2606–2610, 2010.
- [181] A. J. de Haas, J. Oomens, and J. Bouwman, “Facile pentagon formation in the dissociation of polyaromatics,” *Physical Chemistry Chemical Physics*, 2017.
- [182] J. Roithová and D. Schröder, “Bond-formation versus electron transfer: C–c-coupling reactions of hydrocarbon dications with benzene,” *Physical Chemistry Chemical Physics*, vol. 9, no. 6, pp. 731–738, 2007.
- [183] T. A. Field and J. H. Eland, “Lifetimes of metastable molecular doubly charged ions,” *Chemical physics letters*, vol. 211, no. 4-5, pp. 436–442, 1993.

Publications Based on the Thesis

■ Refereed International Journals

1. P. K Najeeb and U. Kadhane, Relative stability of naphthalene, quinoline and isoquinoline under high energy electron impact, *International Journal of Mass Spectroscopy* **414**, 23-30 (2017).
2. P. K Najeeb and U. Kadhane, Delayed extraction time-of-flight mass spectrometer with electron impact for PAH studies, *Journal of Instrumentation* **12**, 03009 (2017).
3. P. K. Najeeb, T Sairam, M. V Vinitha, Sarita Vig, Anudit Kala, U. Kadhane, Pragya Bhat and C. P Safvan, Exploring metastable decay dynamics of polycyclic aromatic nitrogen containing hydrocarbons upon HCN evaporation, *Journal of Physics Conference Series* **875**, 2004 (2017).
4. P. K. Najeeb, M. V Vinitha, Sarita Vig, Anudit Kala, U. Kadhane, Pragya Bhat and C. P Safvan, Structural effects on naphthalene and its derivative in collision with fast electrons and protons, (*Under review, Physical Review A (Ref. No. AN11343)*).
5. P. K. Najeeb, M. J. Anitha and U. Kadhane, High voltage fast MOSFET switch for electro-optical applications, (*To be submitted*).
6. P. K. Najeeb and U. Kadhane, Performance of an electron impact ionisation (e,2e) experimental setup for electron-ion coincidence measurement of large molecules, (*Under preparation*).

■ Conference Presentations

1. P. K. Najeeb, U. Kadhane, Design and construction of experimental set-up to study electron impact ionization (e,2e) processes in large molecules by using coincidence method, *20th National conference on atomic and molecular physics (NCAMP-XX), IIST, Thiruvananthapuram, India, 9-12 December 2014.*

2. P. K. Najeeb, U. Kadhane, Energetics of Electron Impact Excitation of PAH's (Polyaromatic Hydrocarbons), *International symposium on "Global Human Resource Program Bridging across Physics and Chemistry"*, TMU, Tokyo, Japan, 29th January 2016.
3. P. K. Najeeb, U. Kadhane, Developments of electron-ion coincidence set-up for e, 2e process measurements, 21st National conference on atomic and molecular physics (NCAMP-XXI), PRL, Ahmedabad, India, 03-06 January 2017.
4. P. K. Najeeb, U. Kadhane, Relative stability of naphthalene, quinoline and isoquinoline under high-energy electron impact, 21st National conference on atomic and molecular physics (NCAMP-XXI), PRL, Ahmedabad, India, 03-06 January 2017.
5. P. K. Najeeb, U. Kadhane, Structural studies of large molecule under electron impact with delayed extraction time-of-flight mass spectrometry, 29th Kerala Science Congress, Mar Thoma College, Thiruvalla, Kerala, India, 28-30 January 2017.
6. P. K. Najeeb, T. Sairam, M. V Vinitha, Sarita Vig, Anudit Kala, U. Kadhane, Pragya Bhat and C. P Safvan, Exploring metastable decay dynamics of polycyclic aromatic nitrogen-containing hydrocarbons upon HCN evaporation, 30th International Conference on Photonic Electronic and Atomic Collisions (ICPEAC-XXX), Cairns, Australia, 26 July - 1 August 2017.
7. P. K. Najeeb, U. Kadhane, Electron-ion coincidence set-up for large molecule spectroscopy, 19th International Symposium on Polarisation and Correlation in Electronic and Atomic Collisions (e, 2e), Palmcove, Australia, 1-4 August 2017.
8. P. K. Najeeb, U. Kadhane, Stability of polycyclic aromatic hydrocarbons and polycyclic nitrogen heterocycles under electron impact, 19th International Symposium on Polarization and Correlation in Electronic and Atomic Collisions (e, 2e), Palmcove, Australia, 1-4 August 2017.